UCTEA Turkish Chamber of Civil Engineers
TMMOB İnşaat Mühendisleri Odası

Turkish Journal of Civil Engineering

formerly
Teknik Dergi

Volume 35
Issue 3
May 2024

Turkish Journal of Civil Engineering (formerly Teknik Dergi) Publication Principles

Turkish Journal of Civil Engineering (TJCE), a non-profit, open access scientific and technical periodical of UCTEA Chamber of Civil Engineers, publishes papers reporting original research work and major projects of interest in the area of civil engineering. TJCE annually publishes six issues and is open to papers in English and Turkish. It should be noted that TJCE (formerly, Teknik Dergi/ Technical Journal of Turkish Chamber of Civil Engineers) is being published regularly for more than 30 years since 1990. Main publication principles of TJCE are summarized below:

1. Articles reporting original scientific research and those reflecting interesting engineering applications are accepted for publication. To be classified as original, the work should either produce new scientific knowledge or add a genuinely new dimension to the existing knowledge or develop a totally new method or substantially improve an existing method.
2. Articles reporting preliminary results of scientific studies and those which do not qualify as full articles but provide useful information for the reader can be considered for publication as technical notes.
3. Discussions received from the readers of the published articles within three months from publication are reviewed by the Editorial Board and then published together with the closing remarks of the author.
4. Manuscripts submitted for publication are evaluated by two or three reviewers unknown to the authors. In the light of their reports, final decision to accept or decline is taken by the Editorial Board. General policy of the Board is to get the insufficient manuscripts improved in line with the reviewers' proposals. Articles that fail to reach the desired level are declined. Reasons behind decisions are not declared.
5. A signed statement is taken from the authors, declaring that the article has not been published as a "journal article or book chapter". In case the Editorial Board is in the opinion that the article has already been published elsewhere with minor changes or suspects plagiarism or a similar violation of ethics, then not only that article, but none of the articles of the same authors are published.
6. Papers reporting works presented as conference papers and developed further may be considered for publication. The conference it was presented to is given as a footnote in the first page.
7. Additionally, a document signed by all authors, transferring the copyright to UCTEA Chamber of Civil Engineers is submitted together with the manuscript.

UCTEA Turkish Chamber of Civil Engineers
TMMOB İnşaat Mühendisleri Odası

Turkish Journal of Civil Engineering

formerly
Teknik Dergi

Volume 35
Issue 3
May 2024

UCTEA Turkish Chamber of Civil Engineers
TMMOB İnşaat Mühendisleri Odası
Necatibey St. No: 57, Kızılay 06440 Ankara, Turkey
Tel: +90.312.294 30 00 - Faks: +90.312.294 30 88
E-mail: imo@imo.org.tr - www.imo.org.tr

Publisher *(Sahibi)*:
Nusret SUNA
On behalf of UCTEA Turkish Chamber of Civil Engineers

Administrative Officer *(Yazı İşleri Müdürü)*:
Bülent TATLI

Volume 35 - Issue 3 - May 2024 *(Cilt 35 - Sayı 3 - Mayıs 2024)*
Published bi-monthly. Local periodical. *(İki ayda bir yayınlanır, yerel süreli yayın)*
Date of Print: May 1, 2024 *(Baskı Tarihi: 1 Mayıs 2024)*
Number of copies: 800 *(800 adet basılmıştır)*

ISSN: 2822-6836

Turkish Journal of Civil Engineering (formerly Teknik Dergi) is indexed by
- Science Citation Index Expanded
- Scopus
- Journal Citation Reports / Science Edition
- Engineering Index
- Concrete Abstracts (American Concrete Institute)
- National Technical Information Service (US NTIS)
- CITIS
- Ulrich's International Periodical's Directory
- Google Scholar
- TR Index

Turkish Journal of Civil Engineering (formerly Teknik Dergi) is a peer reviewed open access periodical publishing papers of original research and interesting practice cases. It addresses both the research community and the practicing engineers.

Printed by *(Baskı)*:
Ziraat Gurup Matbaacılık Ambalaj San. Tic. A.Ş.
Bahçekapı Mah. 2534 Sok. No: 18 Şaşmaz, Etimesgut / Ankara
Tel: 0.312.384 73 44 - Faks: 0.312.384 73 46

Reviewers:

This list is renewed each year and includes reviewers who served in the last two years of publication.

Şükran AÇIKEL
Kamil Bekir AFACAN
Bülent AKBAŞ
Sami Oğuzhan AKBAŞ
Zülal AKBAY ARAMA
Rıfat AKBIYIKLI
Sarven AKCELYAN
Burcu AKÇAY ALDANMAZ
Cihan Taylan AKDAĞ
Bekir AKGÖZ
Cem AKGÜNER
Fevziye AKÖZ
Erkan AKPINAR
Muhammet Vefa AKPINAR
Atakan AKSOY
Hafzullah AKSOY
Tülay AKSU ÖZKUL
Uğurhan AKYÜZ
Alper ALDEMİR
Cenk ALHAN
Gülay ALTAY
Sinan ALTIN
Adlen ALTUNBAŞ
Yalçın ALVER
Mustafa M. ARAL
Davit ARDITI
Yalın ARICI
Deniz ARTAN İLTER
Deepankar Kumar ASHISH
Ayşegül ASKAN GÜNDOĞAN
Ali Osman ATAHAN
Hakan Nuri ATAHAN
Güzide ATASOY ÖZCAN
Ali Osman ATEŞ
Özgür AVŞAR
Cem AYDEMİR
Metin AYDOĞDU
Ülker Güner BACANLI
Selim BARADAN
Eray BARAN
Özgür Uğraş BARAN
Türkay BARAN
Efe BARBAROS
Bekir Oğuz BARTIN
Zeynep BAŞARAN BUNDUR
Mustafa Gökçe BAYDOĞAN
Cüneyt BAYKAL
Mehmet BERİLGEN
Katrin BEYER
Niyazi Özgür BEZGİN
Ozan BİLAL
Senem BİLİR MAHÇİÇEK
İlknur BOZBEY
Ali BOZER
Mehmet Bakır BOZKURT
Zafer BOZKUŞ
Zekai CELEP
Cihan CENGİZ
Halim CEYLAN
Joao Ramoa CORREIA
Ali Fırat ÇABALAR
Barlas Özden ÇAĞLAYAN
Ferit ÇAKIR
Melih ÇALAMAK
Gülben ÇALIŞ
Umut ÇALIŞKAN
Süheyla Pelin ÇALIŞKANELLİ
Mehmet Alper ÇANKAYA
Serdar ÇARBAŞ
Dilay ÇELEBİ
Tevfik Kutay ÇELEBİOĞLU
Ahmet Ozan ÇELİK
Oğuz Cem ÇELİK
Ozan Cem ÇELİK
Hilmi Berk ÇELİKOĞLU
Kemal Önder ÇETİN
Mecit ÇETİN
Elif ÇİÇEK
Emin ÇİFTÇİ
Hüseyin ÇİLSALAR
Erdal ÇOKÇA
Semra ÇOMU
Turgay ÇOŞGUN
Atilla DAMCI
Yakup DARAMA
Kutlu DARILMAZ
Tayfun DEDE
Cem DEMİR
Selçuk DEMİR
Uğur DEMİR
Ender DEMİREL
Mehmet Cüneyd DEMİREL
Murat DİCLELİ
Seyyit Ümit DİKMEN
Ahmet Anıl DİNDAR
Mustafa DOĞAN
Marco DOMANESCHİ
Gökhan DÖK
Cemalettin DÖNMEZ
İsmail DURANYILDIZ
Cengiz DÜNDAR
Nurhan ECEMİŞ ZEREN
Özgür EKİNCİOĞLU
Serkan ENGİN
Murat Altuğ ERBERİK
Ali ERCAN
Barış ERDİL
Sinan Turhan ERDOĞAN
Şakir ERDOĞDU
Esin ERGEN PEHLEVAN
Yusuf Çağatay ERŞAN
Kağan ERYÜRÜK
Esra Ece ESELLER BAYAT
Tuğba ESKİŞAR TEFÇİ
Burak FELEKOĞLU
Mahmut FIRAT
Onur GEDİK
Abdullah GEDİKLİ
Ergun GEDİZLİOĞLU
Ahmet Talha GEZGİN
Sadık Can GİRGİN
Zehra Canan GİRGİN
Saadet Gökçe GÖK
Tansu GÖKÇE
Serdar GÖKTEPE
Semih GÖNEN
Rahmi GÜÇLÜ
Ali GÜL
Fazlı Erol GÜLER
Ilgın GÜLER
M. Fethi GÜLLÜ
Adil GÜLTEKİN
Fırat GÜMGÜM
Gürkan GÜNAY
Taylan GÜNAY
Murat GÜNAYDIN
Samet GÜNER
Burcu GÜNEŞ
Oğuz GÜNEŞ
Mehmet Şükrü GÜNEY
Tuba GÜRBÜZ BÜYÜKKAYIKÇI
Aslı Pelin GÜRGÜN
Tefarruk HAKTANIR
Soner HALDENBİLEN
Murat HAMDERİ
Ingo A. HANSEN
Umut HASGÜL
Emre HASPOLAT
Mustafa HATİPOĞLU
Lucas HOGAN
Zeynep IŞIK
Sabriye Banu İKİZLER
Okan İLHAN
Erol İSKENDER
Medine İSPİR ARSLAN
Recep İYİSAN
Nuray Işık KABDAŞLI
Volkan KALPAKÇI
Muhammet KAMAL
Reza KAMGAR
Hakan Alper KAMİLOĞLU
Elif Çağda KANDEMİR
Tanay KARADEMİR
Hüseyin Faruk KARADOĞAN
Ümit KARADOĞAN
Mustafa Erkan KARAGÜLER
Halil KARAHAN
Oğuz KAYABAŞI
İlker KAZAZ
Saeid KAZEMZADEH AZAD
Mustafa Kubilay KELEŞOĞLU
Elçin KENTEL
Hadi KHANBABAZADEH
Ufuk KIRBAŞ
Veysel Şadan Özgür KIRCA
Mehmet Anıl KIZILASLAN
Esat Selim KOCAMAN
Salih KOÇAK
Baha Vural KÖK
Mete KÖKEN
Özgür KURÇ
Hasan KURTARAN
Murat KURUOĞLU
Akif KUTLU
Merih KÜÇÜKLER
Abdullah KÜRKÇÜ
Todd LİTMAN
Faqih MAARİF
Müslüm Murat MARAŞ
Halit Cenan MERTOL
Mahmoud MIARI
Mehmet Murat MONKUL
Nihat MOROVA
Yetiş Şazi MURAT
Sepanta NAİMİ
Salih OFLUOĞLU
Fuad OKAY
Didem OKTAY
Derviş Volkan OKUR
Sezan ORAK
Engin ORAKDÖĞEN
Şeref ORUÇ
Okan ÖNAL
Akın ÖNALP
Bihrat ÖNÖZ
Cihan ÖSER
Yiğit ÖZÇELİK
Gökhan ÖZDEMİR
Zuhal ÖZDEMİR
Murat ÖZEN
Pelin ÖZENER
Ekin ÖZER
Hasan ÖZER
Hakkı Oral ÖZHAN
Mehmet Fatih ÖZKAL
Zeynep Huri ÖZKUL BİRGÖREN
Aşkın ÖZOCAK
Sadık ÖZTOPRAK
Turan ÖZTURAN
Gözde Başak ÖZTÜRK
Mustafa ÖZUYSAL
Tolga Yılmaz ÖZÜDOĞRU
Atilla ÖZÜTOK
Nilüfer ÖZYURT ZİHNİOĞLU
Erhan Burak PANCAR
Seval PINARBAŞI ÇUHADAROĞLU
Elişan Filiz PİROĞLU
Bora POLATSU
Shehata E. Abdel RAHEEM
Selçuk SAATÇİ
Selman SAĞLAM
Mehmet SALTAN
Altuğ SAYGILI
Serdar SELAMET
Nuri SERTESER
Halil SEZEN
Alper SEZER
Metin SOYCAN
Kurtuluş SOYLUK
Serdar SOYÖZ
Rifat SÖNMEZ
Tayfun Altuğ SÖYLEV
Haluk SUCUOĞLU
Erol ŞADOĞLU
Yuşa ŞAHİN
Zekai ŞEN
Burak ŞENGÖZ
Gülüm TANIRCAN
Serhan TANYEL
Mucip TAPAN
Ergin TARI
Yüksel TAŞDEMİR
Ali Şahin TAŞLIGEDİK
Hasan TATLI
Gökmen TAYFUR
Serdal TERZİ
Berrak TEYMUR
Hüseyin Onur TEZCAN
Mesut TIĞDEMİR
Salih TİLEYLİOĞLU
Onur Behzat TOKDEMİR
Nabi Kartal TOKER
Ali TOPAL
Cem TOPKAYA
Kamile TOSUN FELEKOĞLU
Gökçe TÖNÜK
Erkan TÖRE
Kemal Dirgen TÖZER
Nursu TUNALIOĞLU
Gürsoy TURAN
Hasan Nuri TÜRKMENOĞLU
Cüneyt TÜZÜN
Eren UÇKAN
Latif Onur UĞUR
Mehmet Baran ULAK
Dilay UNCU
Berna UNUTMAZ
Mehmet UTKU
Volkan Emre UZ
İbrahim Mert UZUN
Deniz ÜLGEN
Mehmet Barış Can ÜLKER
Yurdanur ÜNAL
Ali ÜNAY
Cüneyt VATANSEVER
Ahmet YAKUT
Erkut YALÇIN
Aslı YALÇIN DAYIOĞLU
Mustafa Sinan YARDIM
Anıl YAZICI
Gökhan YAZICI
Halit YAZICI
Cem YENİDOĞAN
Mehmet YETMEZ
İrem Zeynep YILDIRIM
Berivan YILMAZER POLAT
Ercan YÜKSEL
Yeliz YÜKSELEN AKSOY
Ahmet Şahin ZAİMOĞLU
Abdullah Can ZÜLFİKAR

Turkish Journal of Civil Engineering (formerly Teknik Dergi)

Volume 35 Issue 3 May 2024

CONTENTS

RESEARCH ARTICLE

Turkish Journal of Civil Engineering, 2024 1-20, Paper 767, ***Research Article***

Bearing Capacity Equation for Shallow Foundations on Unsaturated Soils

Ali Reza BAGHERIEH[1*]
Ozer CINICIOGLU[2]

ABSTRACT

For shallow foundations resting on unsaturated soils, matric suction increases effective stresses, resulting in enhanced bearing capacity. However, this boost in bearing capacity is ignored in practice for the sake of simplicity, thus compromising economy. That is why this study aims to consider the beneficial effect of unsaturated conditions on bearing capacity. This is achieved by applying limit analysis using the finite element method on unsaturated soils and investigating the problem parametrically for shallow foundations. The suction effect is taken into account in the formulation of the limit analysis based on effective stress principle. The numerical outcomes are verified by comparing them with available experimental data from the literature. The findings from the parametric study emphasize that the influence of suction on bearing capacity is determined by the friction angle. Moreover, the effects of a varying suction profile are contingent on the foundation width. Based on the results derived from the numerical analyses, a modified bearing capacity equation is introduced. This equation showcases a very good coefficient of determination, effectively encompassing the effects of the soil suction profile. Consequently, the proposed procedure can be considered as a convenient yet precise tool for estimating bearing capacity in engineering practice.

Keywords: Bearing capacity, effective stress, unsaturated soil, matric suction, finite element limit analysis.

1. INTRODUCTION

Design of shallow foundations involve the consideration of ultimate and serviceability limit states. The main problem corresponding to an ultimate limit is the bearing capacity. That is why there are a number of seminal studies for calculating bearing capacity [1-4]. The general

Note:
- This paper was received on February 6, 2023 and accepted for publication by the Editorial Board on November 13, 2023.
- Discussions on this paper will be accepted by July 31, 2024.
- https://doi.org/10.18400/tjce.1248220

1 Malayer University, Department of Civil Engineering, Malayer, Iran
bagheri@malayeru.ac.ir - https://orcid.org/0000-0003-2181-3636

2 Boğaziçi University, Department of Civil Engineering, İstanbul, Türkiye
ozer.cinicioglu@boun.edu.tr - https://orcid.org/0000-0001-9334-6956

* Corresponding author

practice in bearing capacity calculations is to assume either saturated or dry conditions for the underlying soil layers, even though unsaturated soils account for almost 40% of Earth's land surface. As bearing capacity of unsaturated soils are greater, this practice yields uneconomic results. Therefore, accounting for unsaturation in bearing capacity computations would be economically beneficial.

The most common analytical methods used in the determination of bearing capacity are limit equilibrium, limit analysis and method of characteristic lines. Among these, limit analysis involves the upper bound and the lower bound theorems based on the classical theory of plasticity. Use of limit analysis method for analyzing stability is difficult when geometry and loading conditions are complex [5]. Therefore, combining the advantages of finite element method (FEM) with the theory of limit analysis presents a powerful option for evaluating stability and failure problems. The theoretical basis of finite element limit analysis method was originated from the studies of Lysmer [6] and Bottero et al. [7]. Subsequently, Sloan [5, 8] presented a new numerical scheme for solving lower bound and upper bound limit analysis problems using FEM and linear programming. Kim et al. [9] introduced pore water pressure into FELA formulation and applied it to the analysis of slope stability problems. This formulation can be straightforwardly extended to unsaturated soils with the aid of effective stress principle.

Mechanical behavior of unsaturated soils started to attract the attention of researchers around 1950s and the primary focus was on the applicability of effective stress principle. Researchers questioned the applicability of effective stress principle in some features of soil behavior like collapse [10-12]. These arguments were predominately based on an equivalent linear elastic theoretical background [13]. Therefore, up until early 2000s most models were based on two independent stress variables, until it was reasoned that collapse involves non-recoverable deformations and therefore arguments questioning the validity of effective stress principle are incorrect [14].

Over the recent two decades, experimental measurements of the bearing capacity of shallow foundations resting on unsaturated soils have been reported by several researchers [15-19]. However, due to the complexity of the problem and the relatively small number of experiments reported so far, as well as to the fact that existing experiments are generally performed on small scale footings, comprehensive understanding of the behavior of foundations on unsaturated soils is still lacking.

Fredlund et al. [20] proposed a relationship for calculating shear strength of unsaturated soils as a function of independent stress variables of net stress (σ - u_a) and suction (u_a - u_w) as:

$$\tau = c' + (\sigma - u_a)\tan\phi' + (u_a - u_w)\tan\phi^b \quad (1)$$

where c' is cohesion, ϕ' is friction angle, and ϕ^b is the friction angle of the unsaturated soil because of the contribution of suction. Moreover, σ is total stress, u_a and u_w are air and water pressures, respectively.

Yet there has been limited research on unsaturated bearing capacity. Oloo et al. [21] modified Terzaghi's general bearing capacity equation and adjusted the cohesion term to consider the effect of matric suction on the ultimate bearing capacity (q_{ult}), as given in Eq. (2).

$$q_{ult} = [c' + (u_a - u_w)\tan\phi^b]N_c + qN_q + 0.5B\gamma N_\gamma \quad (2)$$

where q is the overburden pressure, B is the width of the footing, γ is soil unit weight, and N_c, N_q, N_γ are bearing capacity factors.

This method is referred to as total cohesion concept. Similarly, Oh and Vanapalli [22] adopted a similar approach and modified the cohesion term to account for the contribution of matric suction. More recent effective-stress based works use cohesion correction strategy to consider suction effects [23, 24]. Their general form of bearing capacity equation is as follows:

$$q_{ult} = [c' + \chi(u_a - u_w)\tan\phi']C_f N_c + qN_q + 0.5B\gamma N_\gamma \quad (3)$$

However, the majority of available methods often need a number of tuning or fitting parameters such as C_f which require material-specific calibration (Akbari Garkani et al., [24]) and this drawback limits their efficiency and practicality. On the other hand, Vo and Russell [25] solved the problem of bearing capacity of shallow foundations on unsaturated soils using Slip Line Method and proposed dimensionless bearing capacity charts. Inspired by apparent cohesion concept Vo and Russell [25] used dimensionless parameters which are originally defined by Martin [26] for soils with depth dependent cohesion values. Likewise, the effective-stress based relation of Tang et al. [27] modifies cohesion by considering the frictional contribution of suction.

Recently, Ghasemzadeh and Akbari [28] developed a limit equilibrium solution based on independent stress variables approach. Simultaneous with the modification of soil cohesion to take the influence of soil suction into account, a new term is introduced into Terzaghi's bearing capacity equation to consider the contribution of suction.

On the other hand, Jahanandish et al. [29] calculated the bearing capacity of foundations resting on unsaturated soils by the method of Zero Extension Lines based on the principle of effective stress. To account for the effect of unsaturation, empirical relations were proposed to adjust Nγ as a function of suction. Similarly, Ajdari and Esmail-Pour [19] performed experiments on small-scale physical model footings and then adjusted Nγ for different magnitudes of suction to fit the experimental data. Much like numerous other existing methods, this approach requires the utilization of fitting parameters specific to the soil being studied.

Clearly, the influence and contribution of suction to bearing capacity need to be well understood and methods based on numerical analyses provide a powerful medium for this purpose.

Accordingly, present work adopts a numerical approach and utilizes Finite Elements Limit Analysis (FELA) which is a powerful yet effective tool. The most important advantage of FELA over nonlinear stress-strain analyses is that it can directly determine the capacity with low computational effort. For this purpose, Optum G2 [30] software is used in this study. The optimal limit solution is determined by incorporating the Mohr-Coulomb yield criterion. After determining the trend of bearing capacity boost induced by matric suction, the bearing capacity equations are modified to take the effects of suction into account.

2. METHOD OF ANALYSIS

Kim et al. [9] introduced steady-state pore-water pressures to the formulation of FELA based on the effective stress principle. Both in lower-bound and upper-bound formulations, pore pressures were introduced as auxiliary nodal variables. In lower-bound analysis, effective stresses were used for applying yielding constraints, while total stresses were applied for imposing stress boundary conditions. As an example, two-dimensional differential equations of equilibrium are as follows:

$$\frac{\partial \sigma_x}{\partial x} + \frac{\partial \tau_{xy}}{\partial y} = \frac{\partial \sigma_x'}{\partial x} + \frac{\partial u_w}{\partial x} + \frac{\partial \tau_{xy}}{\partial y} = 0 \tag{4a}$$

$$\frac{\partial \sigma_y}{\partial y} + \frac{\partial \tau_{xy}}{\partial x} = \frac{\partial \sigma_y'}{\partial y} + \frac{\partial u_w}{\partial y} + \frac{\partial \tau_{xy}}{\partial x} = \gamma \tag{4b}$$

In which, u_w is pore-water pressure and stress variables with prime superscript denote effective stress variables while those without prime are total stresses.

Correspondingly, Kim et al. [9] employed effective stresses to enforce yield condition and flow rule in upper bound solutions. They also considered the work done by pore-pressure in the formulation. The procedure suggested by Kim et al. [9] can be easily extended to unsaturated soils using Bishop's [31] equation of effective stress.

$$\sigma' = (\sigma - u_a) + \chi(u_a - u_w) = (\sigma - u_a) + \chi s \tag{5}$$

Here, χ denotes the effective stress parameter under partially saturated conditions and *s* is suction. Analogous to Terzaghi's [1] bearing capacity equation in unsaturated state, u_w in Eq. 3 is replaced with $u_a - \chi s$ as given below:

$$\frac{\partial \sigma_x}{\partial x} + \frac{\partial \tau_{xy}}{\partial y} = \frac{\partial \sigma_x'}{\partial x} + \frac{\partial (u_a - \chi s)}{\partial x} + \frac{\partial \tau_{xy}}{\partial y} = 0 \tag{6a}$$

$$\frac{\partial \sigma_y}{\partial y} + \frac{\partial \tau_{xy}}{\partial x} = \frac{\partial \sigma_y'}{\partial y} + \frac{\partial (u_a - \chi s)}{\partial y} + \frac{\partial \tau_{xy}}{\partial x} = \gamma \tag{6b}$$

The bearing capacity of shallow foundations were evaluated using the upper and lower bound theorems of plasticity in finite element simulations (FELA). The analyses were performed using OptumG2 [30] software which uses second order cone programming (SOCP) to solve the optimization problems of limit analysis. Originally Optum G2 [30] that the effective stress parameter (χ) is equal to the degree of saturation (S_r). However, in the present research, Khalili and Khabbaz [32] relation is preferred which empirically determines the magnitude of χ as function of suction ratio:

$$\chi = \begin{cases} \left(\frac{(u_a - u_w)}{(u_a - u_w)_b}\right)^{-0.55} & \text{if } (u_a - u_w) > (u_a - u_w)_b \\ 1 & \text{if } (u_a - u_w) < (u_a - u_w)_b \end{cases} \tag{7}$$

where, $(u_a - u_w)_b$ is the air-entry suction for drying paths or the air-expulsion suction for wetting paths.

3. VALIDATION

For the purpose of validation, bearing capacities obtained by the FELA analyses conducted in this study are compared with the results of model footing tests available in literature. Rojas et al. [15] conducted in-situ plate load tests in seven test pits on lean clay using a steel plate with a diameter of 0.31m. In those tests, matric suction was measured by tensiometers that are installed at depths of 0.1m, 0.3m, 0.6m and 0.9m below the model footing. These experiments are modeled as axis-symmetric problems in OptumG2. The footing was modeled as a weightless rigid element, whereas the soil obeys the Mohr-Columb yielding criterion. The initial number of elements was 1000 which was eventually increased to 5000 using adaptive meshing.

The boundary conditions utilized in this study align with what are commonly referred to as "standard fixities". Specifically, along the vertical boundaries of the domain, tangential forces are released while normal forces exist. On the contrary, the bottom boundary permits the presence of both tangential and normal forces. A multiplier distributed force was applied at the surface of the foundation. Its magnitude was determined through an optimization procedure. The resulting optimized distributed load represents the bearing capacity of the foundation. Table 1 summarizes the geometrical dimensions and material properties used in these analyses.

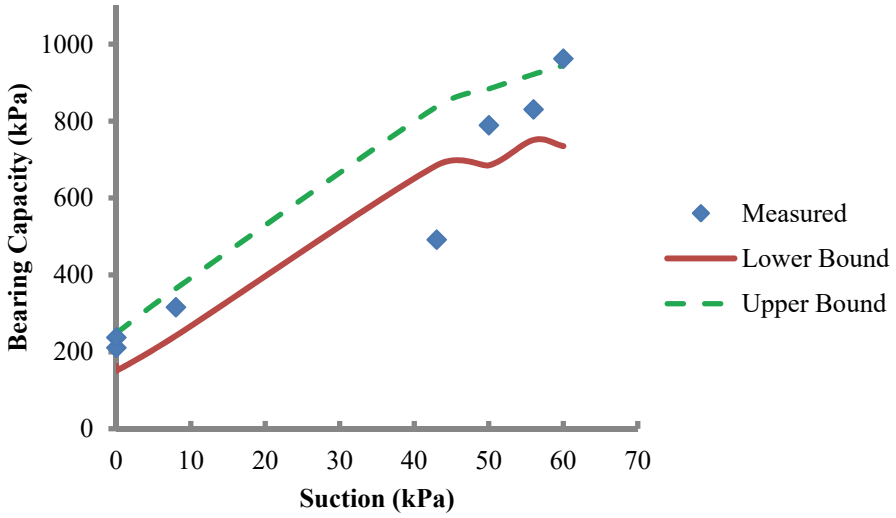

Figure 1 - The measured bearing capacities together with upper-bound and lower bound analysis results

Table 1 - Details of bearing capacity test and material properties

Footing Diameter (m)	0.31
Footing Depth (m)	0
Air entry suction (kPa)	18
Angle of internal friction of soils (degrees)	26
Cohesion (kPa)	3
Dry unit weight of soil (kN/m^3)	15.6

Bearing capacities obtained from lower-bound and upper bound limit analyses are compared with the results of the model tests in Figure 1. Apparently, there is good agreement between experimental results and numerical calculations since the measured test results are located between lower and upper bounds as expected. Figure 2 shows a zoomed view of shear dissipation as a typical example of the resulting failure mechanism in axisymmetric lower bound finite element analyses.

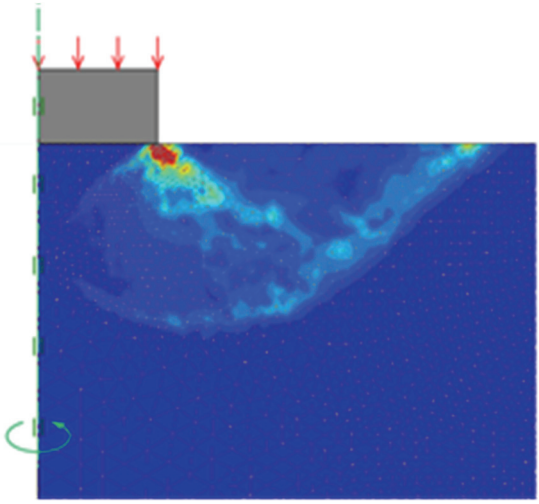

Figure 2 - Shear dissipation contour in axisymmetric lower-bound analysis of validation experiments

4. PARAMETRIC ANALYSIS

Once the method of analysis is validated, it is used for a parametric study of unsaturated bearing capacity of shallow foundations. For this purpose, lower bound analyses are preferred as the results obtained by lower-bound FELA are strictly lower bound and therefore safe. To consider the influence of the differing suction profiles on the results, analyses are performed for two different suction profiles. These are uniform and linear suction profiles and the obtained results are presented in the following two sections.

4.1. Uniform Suction Profile

In order to determine the effect of matric suction on bearing capacity, initially a uniform suction profile is assumed for the zone of influence below the foundation (Figure 3a). A parametric study was conducted with the assumed suction profile in which effective friction angle (ϕ'), cohesion (c') and χs are varied. The magnitudes of parameters used in the parametric study are given in Table 2. View of a typical failure mechanism of strip foundation overlain by refined mesh are shown in Figure 4.

Table 2 - The values of the parameters that are varied in the analyses

Parameter	Values used in the analyses
ϕ' (deg)	5°, 10°, 15°, 20°, 25°, 30°, 35°, 40°, 45°
c' (kPa)	0, 10, 20, 30, 40, 50, 75, 100
χs_0 (kPa)	0, 50,100, 150, 200, 250, 300, 350, 400, 450, 500, 550, 600
ρ (kN/m^2)	-5, -4, -3, -2, -1, 0, 1, 2, 3, 4, 5, 6, 7, 8, 9, 10
B (m)	1, 2, 3, 4, 5

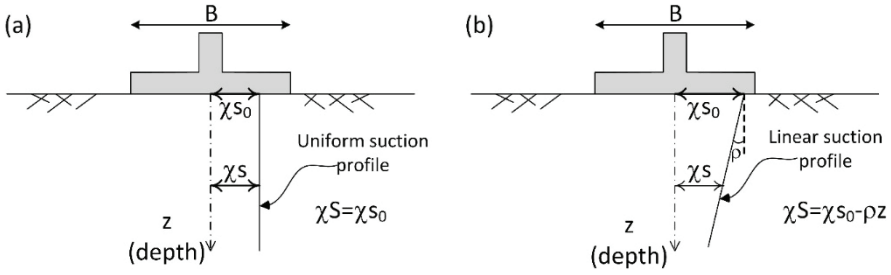

Figure 3 - Suction (χs) profiles under a footing (a) uniform suction profile (b) linear suction profile

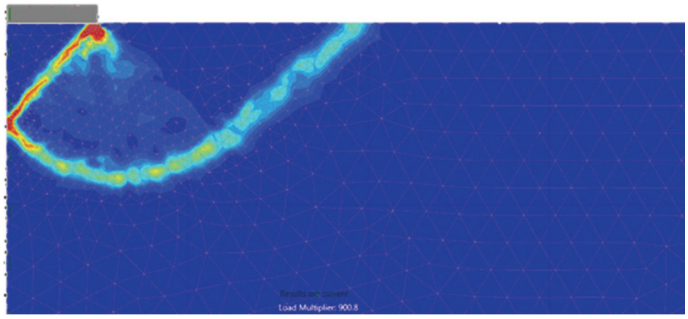

Figure 4 - Failure pattern (total dissipation) in the case of ϕ'=10, c'=100 kPa, χs=50 kPa

The concentration of present study on strip foundations stems from their widespread practical use, particularly in scenarios where the problem can be simplified as a plain strain situation. Additionally, it is important to note that many established bearing capacity equations for saturated soils were originally developed specifically for strip foundations. These equations were subsequently extended to encompass other foundation shapes like rectangular or circular by incorporating shape correction factors.

For uniform suction profiles, Figure 5 presents the results of the parametric study in the form of χs versus q_{ult} relationships for specific magnitudes of ϕ′ and c′. It is observed that for constant values of ϕ′ and c′, relationships between χs and q_{ult} are linear. Moreover, it is important to note that the slopes of these linear χs-q_{ult} relationships are the same when ϕ′ is kept constant and is not affected by the magnitude of cohesion.

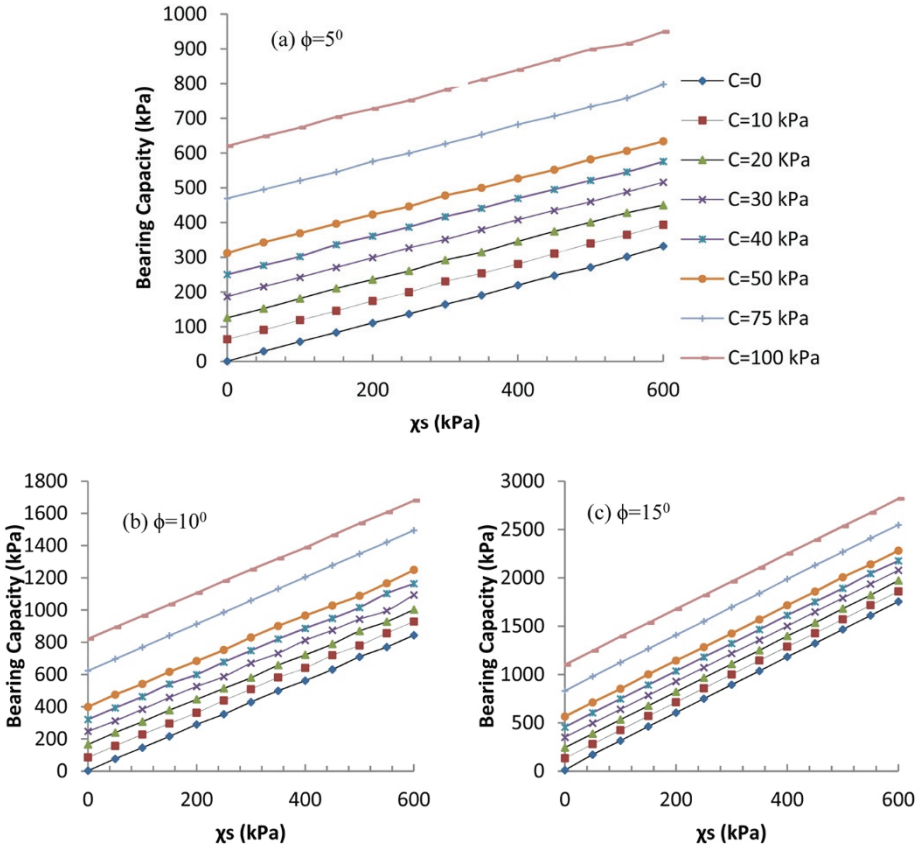

Figure 5 - The variations of bearing capacity versus suction for a constant suction profile and different combinations of c′ and ϕ′.

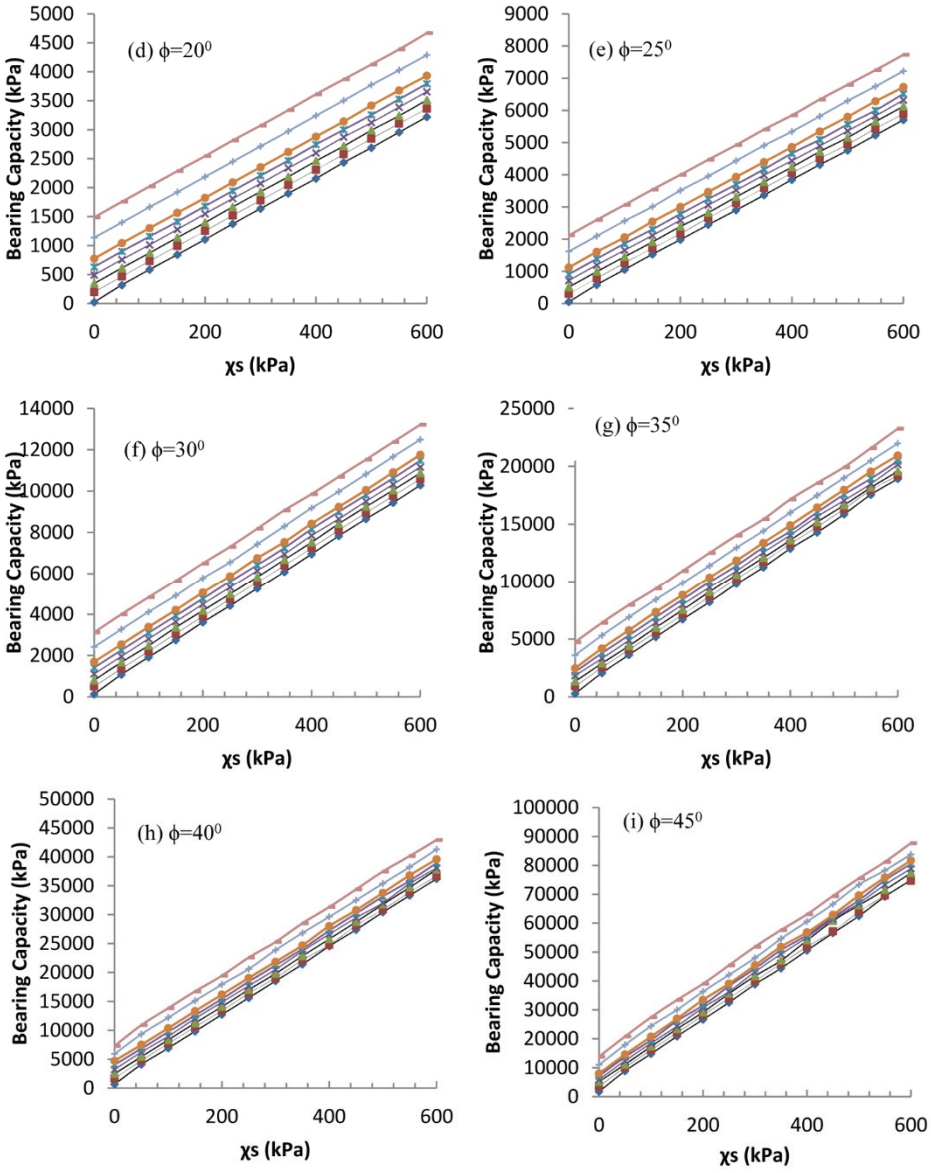

Figure 5 - The variations of bearing capacity versus suction for a constant suction profile and different combinations of c′ and ϕ′. (continue)

It is possible to separate q_{ult} into its components based on the source of contribution, as shown in Eq. 8:

$$q_{ult} = q_0 + q_s \tag{8}$$

where q_o is the bearing capacity when χs is zero and q_s is the contribution of matric suction to bearing capacity. Then using the results of the parametric study, the magnitudes of q_s ($= q_{ult} - q_o$) are determined and plotted against their respective χs values in Figure 6. It is observed in Figure 6 that q_s-χs relationships for all magnitudes of ϕ′ are linear and they all pass through the origin. In other words, the amount of cohesion has no effect on the magnitude of q_s.

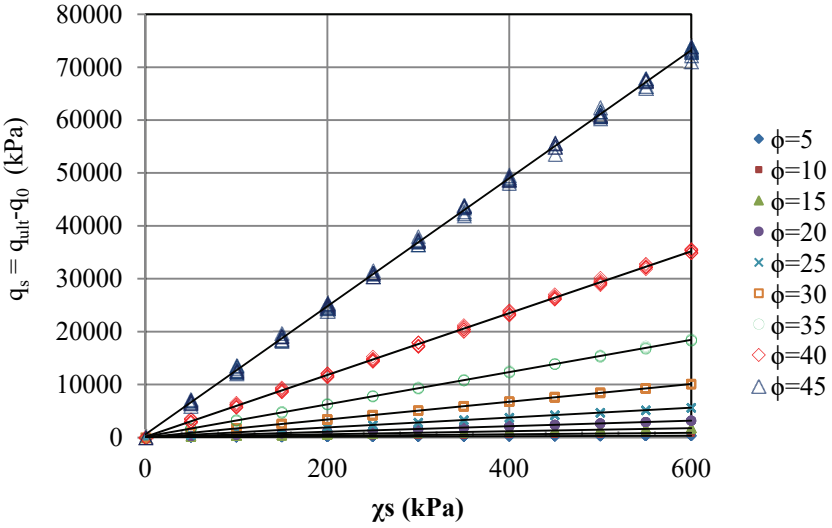

Figure 6 - The variation of q_s with χs for different values of the friction angle for a soil layer with constant χs profile

Table 3 - Slopes of the q_s-χs lines($N_{\chi s}$)at various friction angle values

ϕ′	N_c*	$N_{\chi s}$	$N_c \times \tan \phi'$
5	6.20	0.55	0.54
10	8.20	1.43	1.44
15	10.81	2.88	2.90
20	14.50	5.28	5.28
25	20.40	9.33	9.51
30	29.64	16.80	17.11
35	43.02	30.51	30.12
40	64.79	59.03	54.36
45	116.17	121.47	116.17
			R^2=0.999

* Computed through Lower Bound Finite Element Analysis in the current study

The slopes of the q_s-χs lines at different friction angle values ($N_{\chi s}$), as ascertained through the performed parametric analysis, are detailed in Table 3. This table also includes the N_c values, which are also determined from the findings of the current research, albeit under conditions of zero suction. The values of N_c multiplied by tanϕ are also presented in the table. It is evident from the table that the $N_{\chi s}$ values closely align with the respective Nc × tanϕ values, exhibiting a high coefficient of determination ($R^2 = 0.999$).

Hence, $N_{\chi s}$, which determines the contribution of χs to bearing capacity, can be expressed as follows:

$$N_{\chi s} = N_c \times \tan \phi' \tag{9}$$

Clearly, q_s can be computed using the formula provided in Eq. 10:

$$q_s = \chi s \, N_c \, tan\phi' \tag{10}$$

Consequently, in the case of a constant suction profile, the bearing capacity can be determined as:

$$q_{ult} = [c' + \chi s \tan \phi']N_c + qN_q + 0.5B\gamma N_\gamma \tag{11}$$

Clearly, the present research outcomes arising from a comprehensive array of parametric analyses have yielded valuable insights. As expounded in the introduction, a notable gap existed in the comprehensive understanding of adapting the bearing capacity equation to account for the effects of suction. Previous researchers harbored varying viewpoints on which specific bearing capacity term necessitated modification and how to implement adjustments for suction. The present study bridges this gap and establishes that, for a consistent suction profile, adjusting cohesion relative to suction proves sufficient.

Moreover, while certain researchers concentrated on the cohesion term and employed specific tuning parameters tailored to individual materials, this approach significantly curtailed their practical applicability and user-friendliness. However, the findings of the present research indicate that no distinct tuning parameter is required. Instead, incorporating χs tanϕ' into the effective cohesion (c'), as delineated in Equation 11, proves to be satisfactory. Thus, the most significant advantage of the proposed method lies in its simplicity: obtaining an accurate measurement of χs stands as the sole prerequisite, negating the need to incorporate adaptive strength parameters for unsaturated conditions.

4.2. Linear Suction Profile

A soil profile with linearly varying χs is assumed (Figure 3b) to consider the influence of a variable suction profile on bearing capacity. Vo and Russell [25] found that when there is infiltration or evaporation at ground surface, χs profile could be approximated by a linear function within the zone of influence, and the errors associated with this approximation are negligible. Accordingly, the value of χs at any depth can be calculated as follows:

$$\chi s = \chi s_0 - \rho z \tag{12}$$

where, χs_0 is the value of χs at ground surface and ρ is the rate of decrease of χs with depth. Positive ρ values signify a decline in soil suction as depth increases. This arises when the groundwater level is beneath the surface and infiltration is absent. Conversely, negative ρ values correspond to scenarios where the soil faces surface infiltration. Consequently, points nearer to the surface exhibit lower suction compared to those at greater depths.

In order to assess the effect of suction variation on bearing capacity, numerous analyzes are performed and bearing capacities for different magnitudes of ρ are determined (q_ρ). These are later compared with the bearing capacities measured in models with uniform suction profiles (ρ=0) that have the same c'-ϕ'-χs_0 combinations ($q_{\rho=0}$). Then, the reduction in the magnitude of bearing capacity due to the variability of the suction profile (δq) can be expressed as follows:

$$\delta q = q_\rho - q_{\rho=0} \tag{13}$$

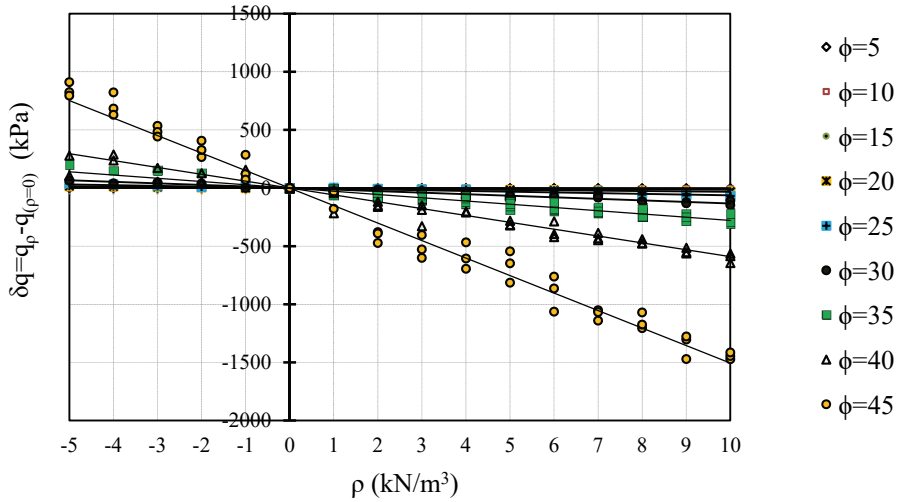

Figure 7 - Bearing capacity variations relative to χs gradient (ρ), (B=1 m)

Figure 7 illustrates the values of δq (for the foundation width B=1 m) plotted against ρ for various magnitudes of ϕ'. In addition to the data presented in Figure 7, further analyses were conducted, and while these analyses yield consistent trends, they are omitted here to prevent overcrowding. Evidently, the relationship between δq and ρ can be accurately described by a linear function with a zero intercept where the slope depends on the value of ϕ'. To investigate the influences of cohesion and χs_0 on the gradient of the parametric relationship between δq and ρ, a series of analyses were conducted. As illustrative instances, Figures 8 and 9 are presented. Upon observing Figure 8, it becomes evident that the cohesion value

does not exert any discernible impact on the gradient of δq – ρ. Similarly, Figure 9 underscores the consistent nature of the gradient across various values of χs_0. Consequently, it can be deduced that the slope of δq – ρ remains unaffected by both cohesion and χs_0 values.

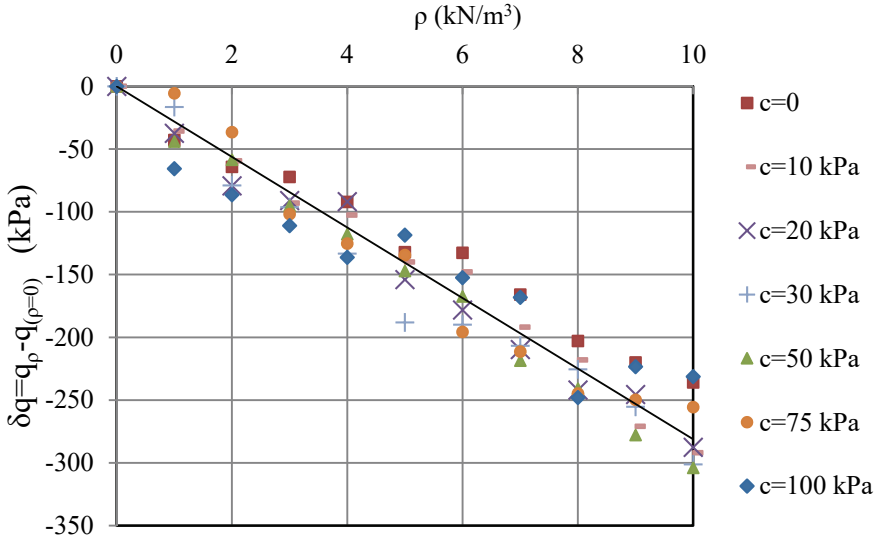

Figure 8 - Sensitivity analysis of the effect of cohesion value on δq – ρ relationship (ϕ′=35°, χs₀=50 kPa, B=1 m)

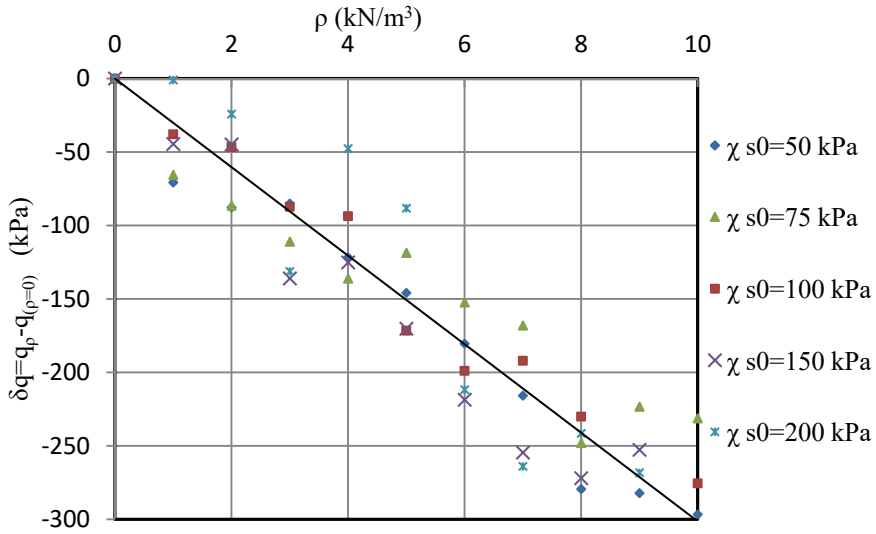

Figure 9 - Sensitivity analysis of the effect of χs_0 on δq – ρ relationship (ϕ′=35°, c=100 kPa, B=1 m)

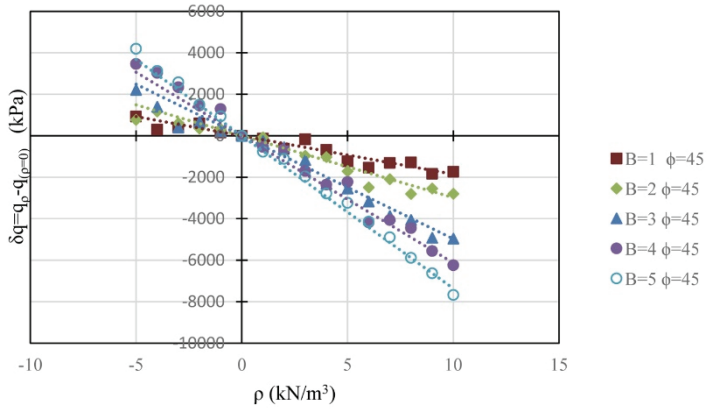

(a) $\phi'=45^o$

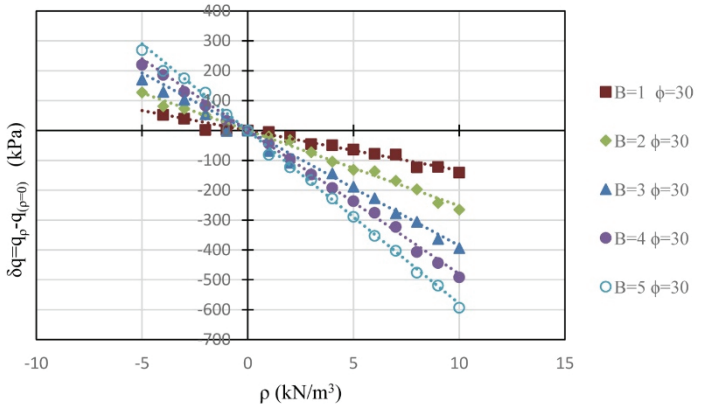

(b) $\phi'=30^o$

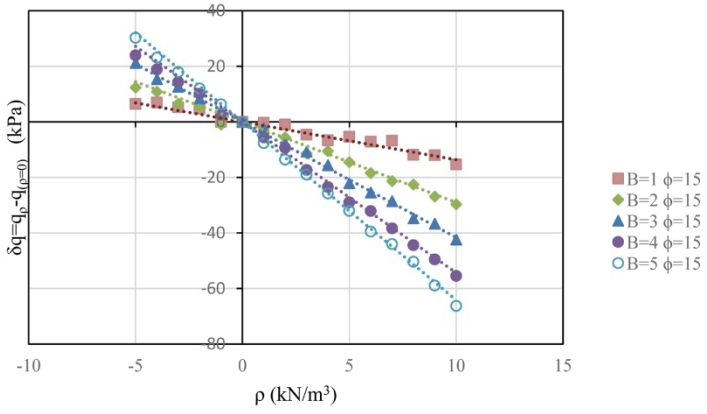

(c) $\phi'=15^o$

Figure 10 - The changes in bearing capacity (δq) versus the gradient of χs (ρ) for different foundation widths (a) $\phi'=45^o$, (b) $\phi'=30^o$, (c) $\phi'=15^o$

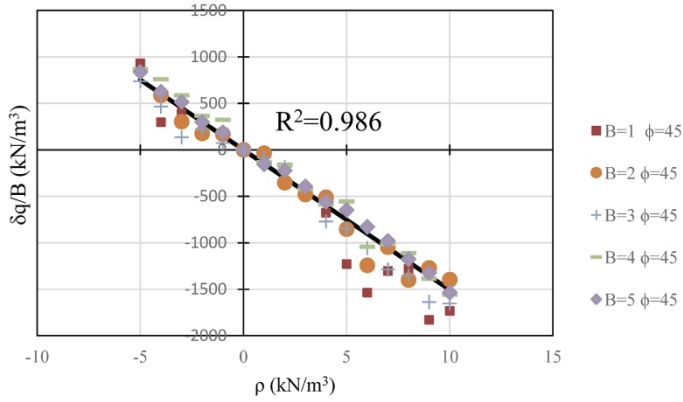

(a) ϕ′=45°

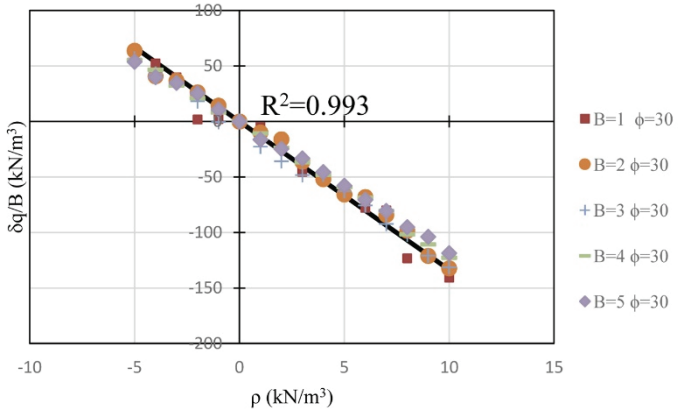

(b) ϕ′=30°

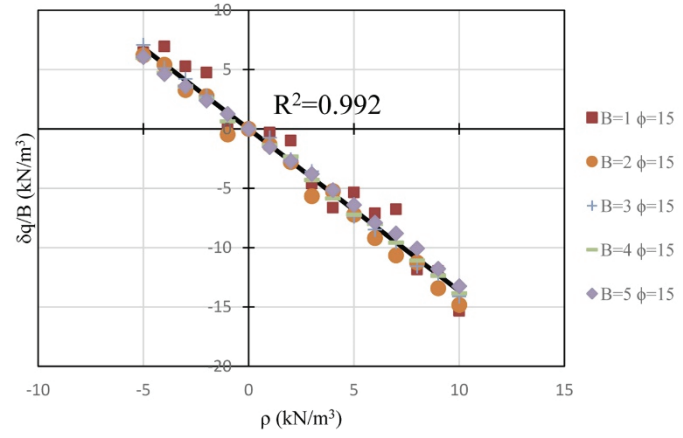

(c) ϕ′=15°

Figure 11 - The changes in normalized bearing capacity ($\frac{\delta q}{B}$) versus ρ for different foundation widths a) ϕ′=45°, (b) ϕ′=30°, (c) ϕ′=15°

To evaluate the impact of the footing width (B) on the relationship between δq and ρ, supplementary analyses were conducted for varying B values. Figure 10 presents the correlations between δq and ρ across different B values. This figure highlights that an increase in the foundation width (B) leads to an augmentation in the slope of the δq – ρ relationship. Consequently, when dealing with foundations situated in areas with varying suction profiles in depth, the width of the foundation becomes a significant factor in influencing the contribution of matric suction to bearing capacity. As a result, it is imperative to incorporate foundation width into relevant formulations.

However, when the values of δq are divided by the foundation width (δq / B) and plotted against ρ, a notable observation can be made, as depicted in Figure 11. Across a constant ϕ value, all data points become normalized and coalesce along a singular line. This signifies that the slope of the δq/B – ρ relationship remains consistent for a specific ϕ value, which is denoted as Nρ. Consequently, it can be formulated as follows:

$$N_{\rho}(\phi') = \frac{\frac{\delta q}{B}}{\rho} \tag{14}$$

Consequently, if $N_{\rho}(\phi)$ values corresponding to the friction angle (ϕ) are accessible, it becomes possible to calculate the impact of a varying suction profile on the bearing capacity (δq) using the equation:

$$\delta q = \rho B\, N_{\rho}(\phi') \tag{15}$$

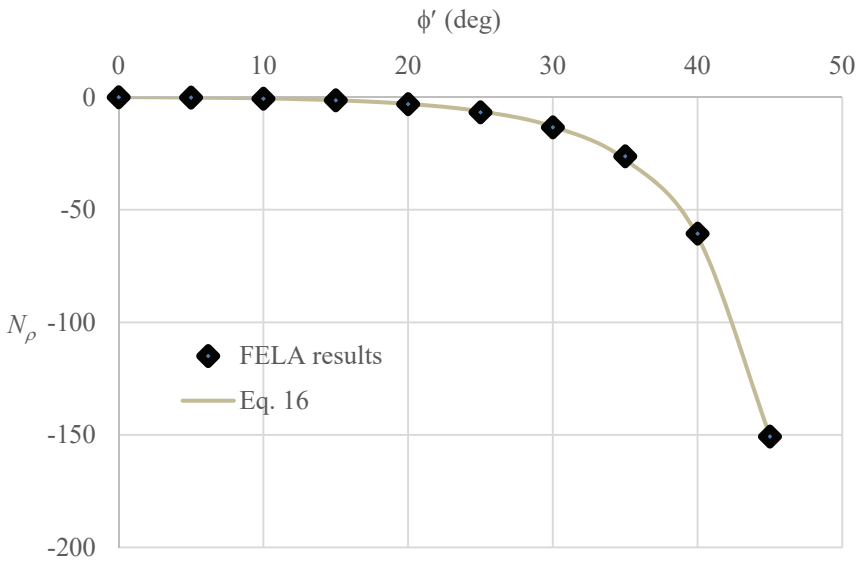

Figure 12 - The values of N_ρ versus ϕ'

The symbolic regression technique was used to develop an empirical relation for N_ρ as:

$$N_\rho = N_\rho(\phi') = tan\phi' \times \left(1 - 1.86e^{(4.4\tan\phi')}\right) \quad (16)$$

The comparison of values of N_ρ obtained by LBFE analyses and calculated using Eq. 16 are shown in Figure 12.

The bearing capacity equation for a shallow continuous foundation resting on an unsaturated soil profile becomes:

$$q_{ult} = [c' + \chi s \tan\phi']N_c + \rho B\, N_\rho + qN_q + 0.5B\gamma N_\gamma \quad (17)$$

5. CONCLUSIONS

The principle of effective stress together with FELA was used to parametrically investigate the influence of different suction profiles on bearing capacity shallow strip footings. The effectiveness of the employed numerical analysis was evaluated by comparing the obtained results with existing experimental data, revealing a notable concurrence.

A comprehensive parametric analysis was conducted by varying factors such as friction angle, cohesion, suction, rate of suction change with depth, and foundation width. The outcomes of these parameter variations indicated that cohesion does not impact the extent of increase in bearing capacity caused by suction. Instead, the primary influencing factor is the friction angle. Enhancing the friction angle leads to an amplified contribution of suction to the bearing capacity.

The research discovered that the augmentation in bearing capacity due to suction can be incorporated by modifying the conventional bearing capacity equations to consider the attributes of the suction distribution. The findings demonstrated that the influence of suction can be predicted by adjusting the cohesion term with respect to suction in the bearing capacity equation. This approach enables a highly accurate prediction of the bearing capacity. For linear suction profiles, the significant factors are the rate of suction variation with depth, friction angle, and foundation width. The equation proposed in this study effectively predicts the contribution of variable suction profiles on bearing capacity.

Although Khalili and Khabaz [32] relationship is preferred by the authors and used to determine the effective stress parameter (χ) to validate the numerical analyses, the method proposed in this study for calculating the bearing capacity of unsaturated soils is independent of how effective stress parameter is calculated.

Contrary to earlier equations presented so far, the proposed extended equation does not need additional calibration and soil specific material parameters. Therefore, the proposed method is practical and can be used for calculating bearing capacity of shallow footings resting on unsaturated soils provided that the distributions of suction and effective stress parameter are known.

A notable aspect of the proposed method is its reliance on effective stress parameters, allowing the continued applicability of saturated strength parameters. This characteristic

underscores the practical simplicity of the method, as it obviates the need for measuring separate strength parameters in unsaturated conditions, making its application notably straightforward.

Acknowledgements

The authors would like to express gratitude to the anonymous reviewers whose insightful comments contributed in enhancing the quality of paper.

References

[1] Terazaghi, K., Theoretical soil mechanics. John Wiley and Sons, 1943.

[2] Meyerhof, G., The ultimate bearing capacity of foudations. Geotechnique. 2(4), 301-332, 1951.

[3] Vesić, A.S., Analysis of ultimate loads of shallow foundations. Journal of the Soil Mechanics and Foundations Division. 99(1), 45-73, 1973.

[4] Hansen, J.B., A revised and extended formula for bearing capacity, in Bulletin No.28. Danish Geotechnical Institute: Copenhagen. 5–11, 1970.

[5] Sloan, S., Lower bound limit analysis using finite elements and linear programming. International Journal for Numerical and Analytical Methods in Geomechanics. 12(1), 61-77, 1988.

[6] Lysmer, J., Limit analysis of plane problems in soil mechanics. Journal of the Soil Mechanics and Foundations Division. 96(4), 1311-1334, 1970.

[7] Bottero, A., R. Negre, J. Pastor, and S. Turgeman, Finite element method and limit analysis theory for soil mechanics problems. Computer Methods in Applied Mechanics and Engineering. 22(1), 131-149, 1980.

[8] Sloan, S., Upper bound limit analysis using finite elements and linear programming. International Journal for Numerical and Analytical Methods in Geomechanics. 13(3), 263-282, 1989.

[9] Kim, J., R. Salgado, and H. Yu, Limit analysis of soil slopes subjected to pore-water pressures. Journal of Geotechnical and Geoenvironmental Engineering. 125(1), 49-58, 1999.

[10] Jennings, J.E.B. and J.B. Burland, Limitations to the Use of Effective Stresses in Partly Saturated Soils. Géotechnique. 12(2), 125-144, 1962.

[11] Matyas, E.L. and H.S. Radhakrishna, Volume Change Characteristics of Partially Saturated Soils. Géotechnique. 18(4), 432-448, 1968.

[12] Fredlund, D.G. and N.R. Morgenstern, Stress state variables for unsaturated soils. Journal of the geotechnical engineering division. 103(5), 447-466, 1977.

[13] Khalili, N., F. Geiser, and G.E. Blight, Effective Stress in Unsaturated Soils: Review with New Evidence. International Journal of Geomechanics. 4(2), 115-126, 2004.

[14] Loret, B. and N. Khalili, A three-phase model for unsaturated soils. International journal for numerical and analytical methods in geomechanics. 24(11), 893-927, 2000.

[15] Rojas, J.C., L.M. Salinas, and C. Seja. Plate-load tests on an unsaturated lean clay. in Experimental unsaturated soil mechanics. 2007. Springer.

[16] Li, X., Laboratory studies on the bearing capacity of unsaturated sands. University of Ottawa (Canada), 2008.

[17] Wuttke, F., B. Kafle, Y. Lins, and T. Schanz, Macroelement for statically loaded shallow strip foundation resting on unsaturated soil. International Journal of Geomechanics. 13(5), 557-564, 2013.

[18] Vanapalli, S.K. and F.M. Mohamed, Bearing capacity and settlement of footings in unsaturated sands. GEOMATE Journal. 5(9), 595-604, 2013.

[19] Ajdari, M. and A. Esmail Pour, Experimental evaluation of the influence of the level of the ground water table on the bearing capacity of circular footings. Iranian Journal of Science and Technology Transactions of Civil Engineering. 39(C2+), 497-510, 2015.

[20] Fredlund, D.G., N.R. Morgenstern, and R.A. Widger. The shear strength of unsaturated soils. Canadian Geotechnical Journal. 15(3): 313-321, 1978.

[21] Oloo, S.Y., D. Fredlund, and J.K. Gan, Bearing capacity of unpaved roads. Canadian Geotechnical Journal. 34(3), 398-407, 1997.

[22] Oh, W.T. and S.K. Vanapalli, Interpretation of the bearing capacity of unsaturated fine-grained soil using the modified effective and the modified total stress approaches. International Journal of Geomechanics. 13(6), 769-778, 2013.

[23] Vahedifard, F. and J.D. Robinson, Unified method for estimating the ultimate bearing capacity of shallow foundations in variably saturated soils under steady flow. Journal of Geotechnical and Geoenvironmental Engineering. 142(4), 04015095, 2016.

[24] Akbari Garakani, A., H. Sadeghi, S. Saheb, and A. Lamei, Bearing capacity of shallow foundations on unsaturated soils: analytical approach with 3D numerical simulations and experimental validations. International Journal of Geomechanics. 20(3), 04019181, 2020.

[25] Vo, T. and A.R. Russell, Bearing capacity of strip footings on unsaturated soils by the slip line theory. Computers and Geotechnics. 74, 122-131, 2016.

[26] Martin, C., ABC–Analysis of bearing capacity. University of Oxford 77, 2004.

[27] Tang, Y., H.A. Taiebat, and K. Senetakis, Effective stress based bearing capacity equations for shallow foundations on unsaturated soils. Journal of GeoEngineering. 12(2) 2017.

[28] Ghasemzadeh, H. and F. Akbari, Determining the bearing capacity factor due to nonlinear matric suction distribution in the soil. Canadian Journal of Soil Science. 99(4), 434-446, 2019.

[29] Jahanandish, M., G. Habibagahi, and M. Veiskarami, Bearing capacity factor, Nγ, for unsaturated soils by ZEL method. Acta Geotechnica. 5(3), 177-188, 2010.

[30] Optum-G2. Finite Element Program for Geotechnical Analysis. 2020; Available from: www.optumce.com.

[31] Bishop, A.W., The principal of effective stress. Teknisk ukeblad. 39, 859-863, 1959.

[32] Khalili, N. and M. Khabbaz, A unique relationship for χ for the determination of the shear strength of unsaturated soils. Geotechnique. 48(5), 681-687, 1998.

Turkish Journal of Civil Engineering, 2024 21-46, Paper 768, ***Research Article***

Ultrasonic Characterization of Polymer Based Sille Stone Powder Composite Mortars

Ahmet Cihat ARI[1*]
Mustafa TOSUN[2]
Imran ORAL[3]
Yasin Ramazan EKER[4]

ABSTRACT

The Sille stone mined in the Sille Region of Konya province in Turkiye, is an andesitic rock. This stone is a material used in the construction of traditional and modern buildings. The Sille stone is cut for use in buildings. The Sille stone powder (SSP) is formed during this cutting process. The SSPs cause environmental pollution. This study was carried out to produce durable and eco-friendly new restoration mortars from the SSP that can be used in the restoration of historical buildings. The SSP composites were prepared by contributing SSP into epoxy and polyester resins in varied ratios such as 60–75 wt.%. The effect of resin types and SSP contribution ratios on the elastic properties of epoxy resin (ER)/SSP and polyester resin (PR)/SSP composites was investigated by the ultrasonic pulse-echo method. Additionally, the morphology of these composites was investigated by scanning electron microscopy (SEM). Experimental results indicated that both the longitudinal and shear wave velocity values of the PR/SSP composites were higher than those of the ER/SSP composites. Furthermore, a linear increase in the elastic properties of the obtained composites was observed with increasing amounts of SSP.

Keywords: Polymer materials, Sille stone powder, ultrasonic, nondestructive testing, restoration.

Note:
- This paper was received on May 16, 2023 and accepted for publication by the Editorial Board on November 24, 2023.
- Discussions on this paper will be accepted by July 31, 2024.

• https://doi.org/10.18400/tjce.1297882

1 Yozgat Bozok University, Department of Architecture and Urban Planning, Yozgat, Türkiye
a.cihat.ari@bozok.edu.tr - https://orcid.org/0000-0002-4690-8968

2 Konya Technical University, Department of Architecture, Konya, Türkiye
mtosun@ktun.edu.tr - https://orcid.org/0000-0002-0718-4100

3 Necmettin Erbakan University, Department of Physics Education, Konya, Türkiye
oralimran@erbakan.edu.tr - https://orcid.org/0000-0002-5299-5068

4 Necmettin Erbakan University, Department of Basic Sciences, Konya, Türkiye
Necmettin Erbakan University, Science and Technology Research and Application Center (BITAM), Konya, Türkiye
yeker@erbakan.edu.tr - https://orcid.org/0000-0001-7395-4364

* Corresponding author

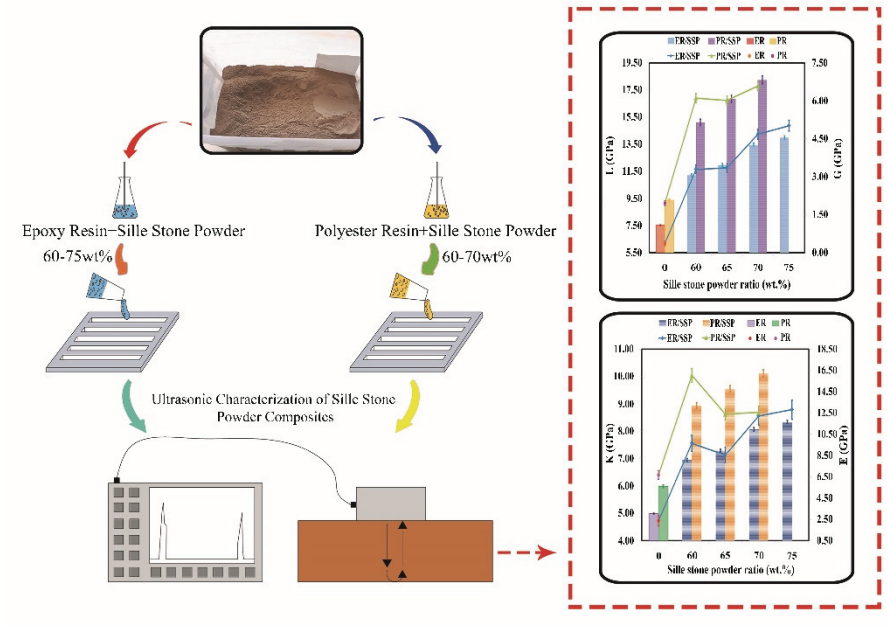

Graphical Abstract

1. INTRODUCTION

Polymers have been preferred over traditional materials due to their application in various fields. In the preference for polymers over traditional materials; the fact that they can be processed, have high strength, and are economical has been effective [1]. Additionally, the many properties of materials could be improved by adding fillers into polymer resins such as polyester, vinyl ester, and epoxy. Fillers provide volume to the material, reduce cost, and provide aesthetic properties [2]. Composite materials developed with polymer resins have been used in different fields such as aviation, maritime, automobile industries, and construction sectors. Nowadays, the potential of polymer materials has been recognized in the construction industry for the reinforcement of structures and their use as repair materials [3]. For example, by mixing polymer resins with concrete, high-performance concrete and modified mortars with high tensile strength, compressive strength, and corrosion protection have been developed [4, 5]. Polymer-modified mortars are used as repair materials in the construction industry and public works because they have a longer life, provide good insulation against moisture on the wall, have good adhesion properties, and are resistant to the negative effects of the environment [6]. Since the aggregates used in mortars affect the durability of the mortar, the demand for aggregates is increasing with the rapid development of the construction industry. The inadequacy of aggregates such as river sand used in buildings in the construction sector also damages the natural environment of the land in aggregate mining. For this reason, recycled aggregates from waste materials have had an important place in meeting the increasing demand for aggregates in the construction industry [7]. The use of waste materials in the development of new materials allows both to protect the environment and to produce more economical materials. Therefore, recycling waste

materials contributes to the reduction of environmental pollution caused by the construction industry to the whole world and to sustainable development. Also, using the waste materials in polymer mortars helps improve the many properties of materials [8-11].

Sille stone is mined in the Sille region of Konya in Turkey. Sille stone is known as "Sulutas Volcanic". However, this stone contains dacite, rhyodacite, and andesite [12]. The stones in the Sille region are gray, brown, and pink [13, 14]. The different colors and high strength of this stone are used in the construction of buildings in and around Konya and the restoration of historical buildings. However, for this stone to be used in buildings, it must be cut to certain dimensions. In Sille quarries, stones are cut into blocks with different methods. These stones, processed for decorative purposes, are made economically valuable. However, a large amount of stone powder is formed during the cutting process of Sille stones. The use of Sille stone powder, which is formed during the cutting of the stone, as a repair mortar in the repair and strengthening of structures is important both in terms of environmental protection and economically.

The durability of building materials affects the lifetime of the buildings. Deteriorations and damage occur due to external effects such as corrosion, humidity, and earthquakes during the usage period of the buildings. The material used in the construction of the structures is important in providing resistance to these external effects. The use of polymers in the construction industry has become increasingly common recent years. Epoxy and polyester resins draw attention due to their good mechanical properties, low viscosity, and fast curing [15, 16]. Therefore, many epoxy and polyester resin-based composites have been extensively studied in engineering applications recently [15-21].

One of the most common non-destructive testing methods used to determine the material's properties is the ultrasonic testing (UT) technique [22, 23]. One of the most important advantages of the UT method is the non-destructive determination of the width of the cracks formed by the wear of the materials, the location of the cracks, and the compressive strength of the materials. Thus, the UT method has proven useful in determining the structural behavior, microstructure, and mechanical properties of polymer composites [24-26]. UT method is used to evaluate composites' elastic properties and microstructures [27]. For example, it has been used to estimate the strength of rock [28], concrete [29], brick [30], and steel [31] by the UT method. Also, the UT method enables the determination of the defects and damaged areas of the composite materials as well [32]. For instance, Sun and Zhu [33], used the UT technique to detect internal defects of steel plates in thick concrete walls. They determined that the UT technique can be used to evaluate the early and late age conditions of three connecting rods with different bonding conditions in concrete. Additionally, the UT method has been used to determine the mechanical properties of composite mortars used in historical and ancient buildings as well [34-38]. For example, in the study conducted by Branco et al. [35], the binding properties of lime mortars, masonry structures, and wall coverings in historical buildings were investigated. In addition, the compressive and flexural strengths and ultrasonic velocities of the mortars were also measured. Since it is not possible to take core samples from historical buildings, the mechanical properties of the materials used in the repair of historical buildings should be known. Therefore, it is extremely important to determine the mechanical properties of the materials used in the repair of historical buildings with the UT method [22, 39]. In the literature, many studies have been published on the use of the stone, such as the mechanical properties of Sille stone [40-42],

the effect of salt crystallization on historical buildings and monuments [43], the effects of the freeze-thaw (F–T) cycle of rocks [44], the sulfate effect of building stones [45], on the use of stone in floor tiles [46] and the physicochemical properties of heat-treated Sille stone [47]. However, the development of repair mortar to be used in the repair of Sille stone structures and cultural assets in Konya has not been mentioned in the literature. Moreover, as far as we know, no studies have been conducted on the use of Sille stone powder (SSP) with epoxy and polyester resins and the ultrasonic characterization of the epoxy resin (ER)/SSP and polyester resin (PR)/SSP composites. Therefore, this study was carried out to produce durable and environmentally friendly new restoration mortars from SSP that can be used in the restoration of traditional structures (for example: houses, mansions, etc.) built with Sille stone in Konya and determine the elastic properties of these composite mortars by the UT method. Moreover, this study was conducted to reduce the cost of raw materials in the preparation of mortars and evaluate the waste products generated during the processing of natural stones.

2. MATERIALS AND METHODS

2.1. Materials

Commercial bisphenol-A type epoxy resin (BRTR Kimya A.Ş., Turkiye), and polyester resin containing 0.2% by weight of Cobalt octoate 6% accelerator (Kompozit Pazarı, Turkiye) were used to produce composite materials in the study. Cycloaliphatic polyamine (BRTR Kimya A.Ş., Turkiye) and methyl ethyl ketone peroxide (MEK-P) (Kompozit Pazarı, Turkiye) were used as hardeners. The properties of epoxy resin, polyester resin, and SSP used in this research are given in Table 1. In addition, Sille stone powder (SSP), which was used as a filling material in the study, was obtained from the quarry in the Sille region (Konya, Turkiye). The chemical content of the SSP is given in Table 2.

Table 1 - Some features of matrix systems and SSP used in this research [40, 48-50].

Used Materials	Features of Matrices and SSP	
Epoxy resin (ER)	Color and appearance	: Transparent and Glossy
	Density (g.cm^{-3} at 25°C)	: 1.10
	Mixing Ratio	: 5/3
	Mixture Life at 25°C (Minutes)	: 30
	Drying Time at 25°C (Hours)	: 12
Polyester resin (PR)	Color	: Yellowish
	Density (g.cm^{-3} at 20 °C)	: 1.12 – 1.14
	Viscosity (cps, at 20 °C)	: 550 – 650
	Gelation time (Minutes)	: 4 – 8
	Exothermic warming (°C)	: 160 – 200
	Boiling point (°C)	: 145.2 °C

Table 1 - Some features of matrix systems and SSP used in this research [40, 48-50]. (continue)

Sille stone powder (SSP)	Color	: Pink
	Density (g.cm^{-3} at 20 °C)	: 2.26 – 2.35
	Water absorption (%, at 23 °C)	: 3.9
	Melting point(°C)	: 2000
	Fineness (μm)	: < 150

Table 2 - Chemical content of the SSP.

Content of the SSP	SiO_2	Al_2O_3	K_2O	Na_2O	MgO	CaO	Fe_2O_3	TiO_2	ZrO_2
%	66.67	13.24	4.11	4.94	1.09	5.07	3.66	0.52	0.39

2.2. Preparation of the ER/SSP, and the PR/SSP Composites

Within the scope of this research, two types of composite series were produced. For the first type of composite series, a cycloaliphatic polyamine hardener was added to the neat ER at a ratio of 5:3 by weight to obtain a hardened neat ER sample. Then, the SSP was added to neat ER in 75, 70, 65, and 60 wt.% ratios. Each mixture of the ER/SSP obtained was mixed for 3

Figure 1 - Production stage of composite mortars.

minutes, and after that, cycloaliphatic polyamine hardener was added to each of the ER/SSP mixtures at a ratio of 5:3 by weight. Finally, each of the ER/SSP composite mortar mixtures obtained was mixed for 3 minutes as well. For the second type of composite series, a methyl ethyl ketone peroxide hardener was added to the polyester resin containing cobalt octoate accelerator in 1.5 % by weight and mixed for 3 minutes to obtain the hardened neat PR sample. The SSP has added to neat PR in 75, 70, 65, and 60 wt. % ratios for obtaining the PR/SSP composite mortars. Then each mixture of the PR/SSP obtained was mixed for 3 minutes. Then, methyl ethyl ketone peroxide hardener was added to each of the PR/SSP composite mortar mixtures at 1.5% by weight and mixed for 3 minutes as well (Figure 1 and Table 3). The ER/SSP and PR/SSP composite mortar mixtures were poured into 20x20x20 mm molds made of polymethyl methacrylate (PMMA) by ASTM D638-14[51] standard, using the traditional hand lay-up process. Finally, all the obtained composite mortars were dried at 25±1°C for 24 hours. After completing the mechanical strength of the composite mortars in 7 days, ultrasonic measurements of the samples were carried out. However, unlike the ER/SSP composites, when the PR and SSP were mixed at a ratio of 25:75 by weight, it was observed that a suitable structure was not formed between them.

Table 3 - The abbreviations and ingredients of composite mortars.

Composite mortars' abbreviations	Combination ratio of resin type/SSP
ER	100:0
ER/SSP-1	40:60
ER/SSP-2	35:65
ER/SSP-3	30:70
ER/SSP-4	25:75
PR	100:0
PR/SSP-1	40:60
PR/SSP-2	35:65
PR/SSP-3	30:70

2.3. Density and Ultrasonic Wave Velocity Measurements

Density measurements were carried out by an analytical balance (Radwag AS220/C/2, capacity 220 g, readability 0.1 mg, Poland) and a density kit (Radwag 220, Poland) at room temperature (25°C).

Ultrasonic wave velocity measurements of composite samples were carried out by ultrasonic pulse-echo method using the flaw detector given in Figure 2a (Epoch-XT-Panametrics Olympus).

Before measuring the ultrasonic velocities of the composite samples, the thicknesses of the samples were measured using an analog micrometer (Somet, Czechoslovakia).

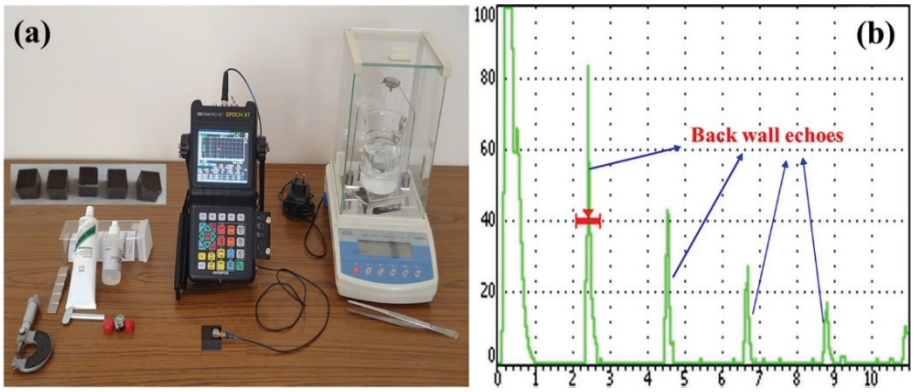

Figure 2 - a: Tools used for density and ultrasonic wave velocity measurements, b: A-scan signals of back wall echoes.

The appropriate frequency was determined as 5 MHz for both longitudinal and shear wave velocity measurements. Therefore, both the longitudinal wave velocity and shear wave velocity measurements were carried out at 5 MHz frequencies. Longitudinal wave velocity measurements were carried out using a longitudinal mode transducer (5 MHz, V116-Panametrics Olympus, USA), while shear wave velocity measurements were carried out using a shear mode transducer (V155-Panametrics Olympus, USA). At the interface between two environments with different acoustic impedances, most of the energy of the sound waves coming from the first environment is reflected before they pass to the second environment due to the impedance difference. In this case, clear peaks cannot be obtained on the oscilloscope screen since the sound wave energy coming back from the second environment is very low. This not only makes ultrasonic measurement difficult but also prevents sensitive measurements from being taken. Thus, coupling fluids are used as impedance matches [52]. The coupling fluids used nowadays can pass only 10-15% of the sound wave energy sent from the first medium to the second medium. Glycerin is one of the best coupling fluids, and it can pass up to 15% of the sound wave energy coming into it to the second medium [53]. Therefore, glycerin (BQ-Panametrics Olympus, USA) and shear wave coupling (SWC-Panametrics Olympus, USA) were used in ultrasonic longitudinal and shear wave measurements, respectively. Additionally, a constant force was applied to the ultrasonic transducer to have a stable layer at the interface of the sample. Ultrasonic wave velocity measurements were repeated 10 times to ensure the accuracy of the results.

During the ultrasonic longitudinal and shear wave velocities measurements, errors such as micro voids in the examined material can be detected by the extra peaks appearing between the peaks of two consecutive back wall echoes. Normally, in the ultrasonic pulse-echo method, the time (Δt) between two consecutive back wall echoes (for example, the 1st and 2nd, 2nd and 3rd or 3rd and 4th back wall echoes) is determined on the oscilloscope screen (Figure 2b). Ultrasonic waves pass through the material thickness twice in the time between two consecutive back wall echoes in the ultrasonic pulse-echo method. The velocity is measured by substituting these obtained values into Equation (1) below. Meanwhile, in this research, velocity measurements were carried out at points that did not give error peaks between back wall echoes as much as possible.

$$V = \frac{2\Delta d}{\Delta t} \tag{1}$$

where *V, Δd,* and *Δt* are the velocity of sound, the thickness of the sample, and the time-of-flight between subsequent backwall signals on the oscilloscope, respectively.

2.4. Determination of Elastic Constants

The elastic modulus is related to the interatomic forces. Therefore, the elastic modulus of the materials expresses the maximum strength that can be achieved. There is a direct mathematical relationship between the elastic modulus, ultrasonic longitudinal, and shear wave velocities [54]. The elastic properties of composites obtained were determined using Equations (2-8) which are used for isotropic composite materials [55].

$$L = \rho V_L^{\,2} \tag{2}$$

$$G = \rho V_S^{\,2} \tag{3}$$

$$K = L - \frac{4}{3}G \tag{4}$$

$$\mu = \frac{L - 2G}{2(L - G)} \tag{5}$$

$$E = 2G(1 + \mu) \tag{6}$$

$$H = \frac{(1 - 2\mu)E}{6(1 + \mu)} \tag{7}$$

$$Z = \rho V_L \tag{8}$$

Where ρ, V_L, V_s, L, G, K, E, μ, H, and Z are the density, longitudinal wave velocity, shear wave velocity, longitudinal modulus, shear modulus, bulk modulus, Young's modulus, Poisson's ratio, ultrasonic micro-hardness, and the characteristic acoustic impedance of composites samples, respectively.

3. RESULTS AND DISCUSSIONS

The ultrasonic testing technique is widely used in the construction industry, as it provides a non-destructive evaluation of the changes in the microstructure of various materials, the locations of damages, and their mechanical properties [56]. Particularly in the construction

industry, in the characterization of building materials, the ultrasonic testing technique gives reliable results in the evaluation of mechanical properties without damaging the material compared to destructive methods. For example, many studies have been conducted in the characterization of traditional materials such as wood [57], stone [58], and brick [59] and in the characterization of today's materials such as cement mortars [60], concrete [61] and steel [62] using UT methods. Ultrasonic studies on SSP and polymer material are insufficient in the literature. Therefore, the elastic properties of ER/SSP and PR/SSP composite mortars were determined using the ultrasonic pulse-echo method. The experimental results were given in Tables (4-6) and plotted in Figures (3-10).

3.1. Morphological Results

SEM micrographs of the ER/SSP and PR/SSP composites and the morphology of the composites are shown in Figure 3 and Figure 4. As shown in Figures 3 and 4, SSP particles

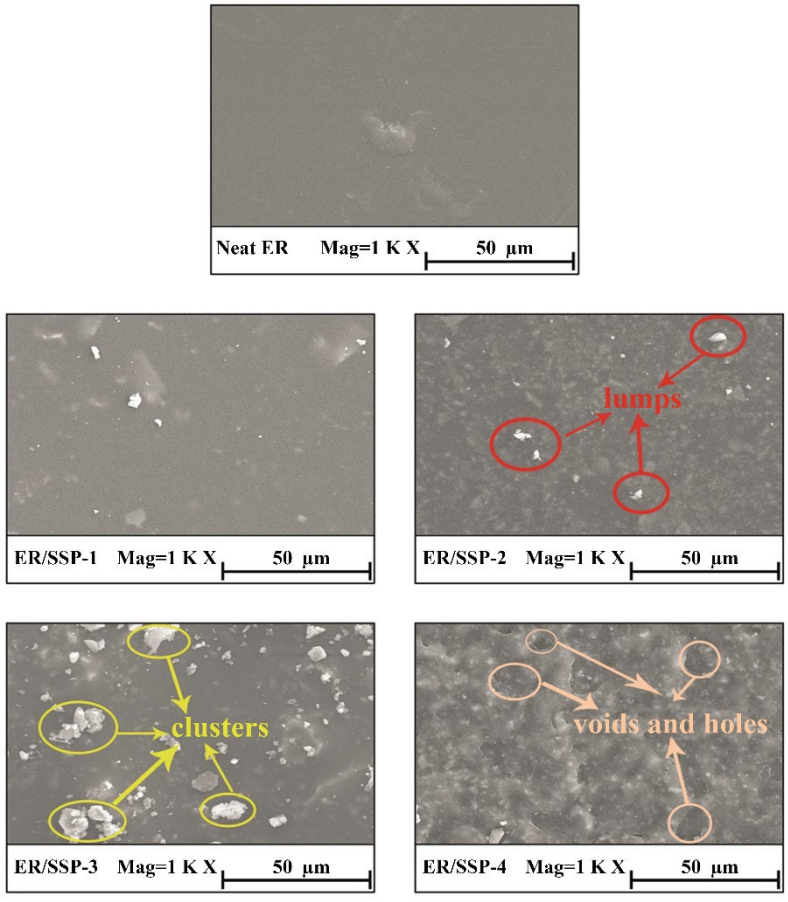

Figure 3 - SEM images of the ER/SSP composites (Magnification of 1.00 K X, 50 µm).

are homogeneously dispersed in the ER and PR matrix. However, lumps occur in composite samples due to the increase in the amount of SSP filler. As stated in studies in the literature, polyester, and epoxy resins have a glassy, brittle, and smooth surface. Therefore, the addition of SSP fillers to the polymer matrix enables the composite to form rough surfaces and the material to have a more durable structure.

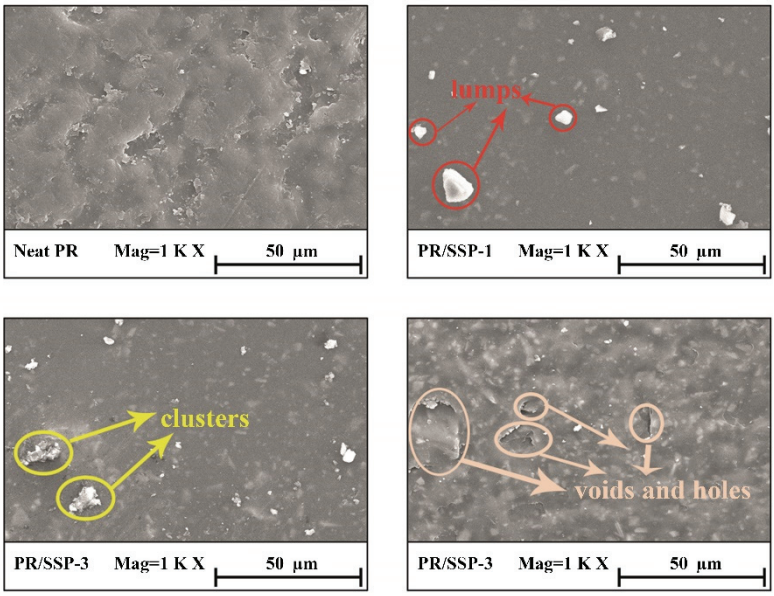

Figure 4 - SEM images of the PR/SSP composites (Magnification of 1.00 K X, 50 µm).

In the ER/SSP-2 and PR/SSP-2 composites, SSP particles agglomerate when interacting with the matrix, these composites do not form a good bond with the polymer matrix. Additionally, in all composites, the number of voids and holes in the material increases due to the increase in the amount of SSP filler.

In the ER/SSP-4 and PR/SSP-3 composites, it is seen that there is a better adhesion in the composites with the homogeneous distribution of the SSP particles with the matrix (See Figures 3 and 4).

3.2. Densities and Ultrasonic Wave Velocities

As can be seen in Table 4 and Figure 5, the density values of the ER/SSP and PR/SSP composites ranged from 1607.12 to 1757.16 kg.m^{-3}, and 1784.24 to 1873.24 kg.m^{-3}, respectively.

The density values measured for obtained the ER/SSP and PR/SSP composite mortars are in good agreement with related literature [36, 38, 63]. For example, Aggelakopoulou et al. [63]

produced restoration mortars to be used on historical walls by mixing metakaolin and hydrated lime with sand, and the density values of the restoration mortars they obtained were measured between 1850–1900 $kg.m^{-3}$. The density values of all the ER/SSP and PR/SSP composites are found higher than the density values of neat ER and PR, respectively. Additionally, the highest density value among all composite mortars was determined as 1873.24 $kg.m^{-3}$ for the PR/SSP-3 sample. When PR/SSP and ER/SSP composites were compared, it was determined that PR/SSP composites had higher densities than ER/SSP composites. As a result, the density values of ER/SSP and PR/SSP composites increase linearly with the addition of SSP.

Table 4 - Density (ρ) and ultrasonic wave velocities (V_L and V_S) values of materials obtained in this research.

Samples' ID	Composition ratio (wt.%)	ρ ($kg.m^{-3}$)	V_L ($m.s^{-1}$)	V_S ($m.s^{-1}$)
ER	100:0	1109.84±7.59	2360.80±12.04	991.20±7.99
ER/SSP-1	40:60	1607.12±5.22	2692.20±8.73	1381.00±5.48
ER/SSP-2	35:65	1653.72±11.08	2666.20±4.12	1448.00±5.87
ER/SSP-3	30:70	1742.32±23.47	2858.80±64.53	1564.80±8.38
ER/SSP-4	25:75	1757.16±7.98	2907.40±88.20	1610.20±13.42
PR	100:0	1216.32±8.34	2743.40±38.19	1303.60±21.08
PR/SSP-1	40:60	1784.24±5.90	3078.00±9.80	1698.60±3.14
PR/SSP-2	35:65	1843.16±4.87	3012.40±13.16	1815.60±19.62
PR/SSP-3	30:70	1873.24±9.57	3081.60±45.92	1909.20±29.29

According to the results given in Table 4 and Figure 6, both ultrasonic longitudinal and shear wave velocities of the composites are higher than that of ER. The longitudinal wave velocity values of the ER/SSP composites vary between 2666.20 and 2907.40 $m.s^{-1}$ while the shear wave velocity values vary between 1381.00 and 1610.20 $m.s^{-1}$. The longitudinal ultrasonic wave velocity value of all ER/SSP was increased with the addition of SSP compared to neat ER. However, as can be seen from Table 4 and Figure 6, when the amount of SSP was increased from 60% to 65% by weight, the longitudinal wave velocity in ER/SSP-2 was decreased compared to the longitudinal wave value of ER/SSP-1. The uneven distribution of the micro-filler causes the scattering that increases the transition time of longitudinal waves passing through the composite sample [64]. Thus, the decrease in the velocity of longitudinal ultrasonic waves for the ER/SSP-2 composite can be attributed to this agglomeration. On the other hand, it was determined that the longitudinal wave velocity values of the ER/SSP composite mortars increased about 12.96–23.17 % compared to neat ER.

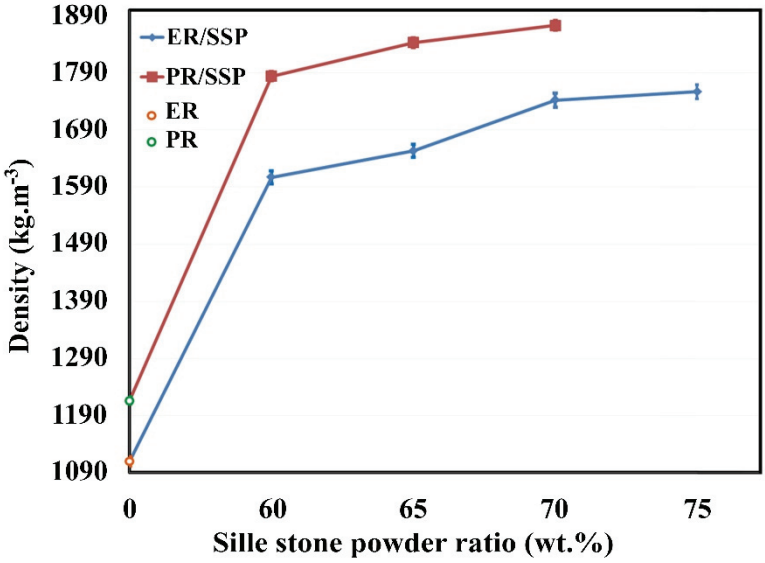

Figure 5 - Variation in densities of the ER/SSP and PR/SSP composites depending on the SSP amount.

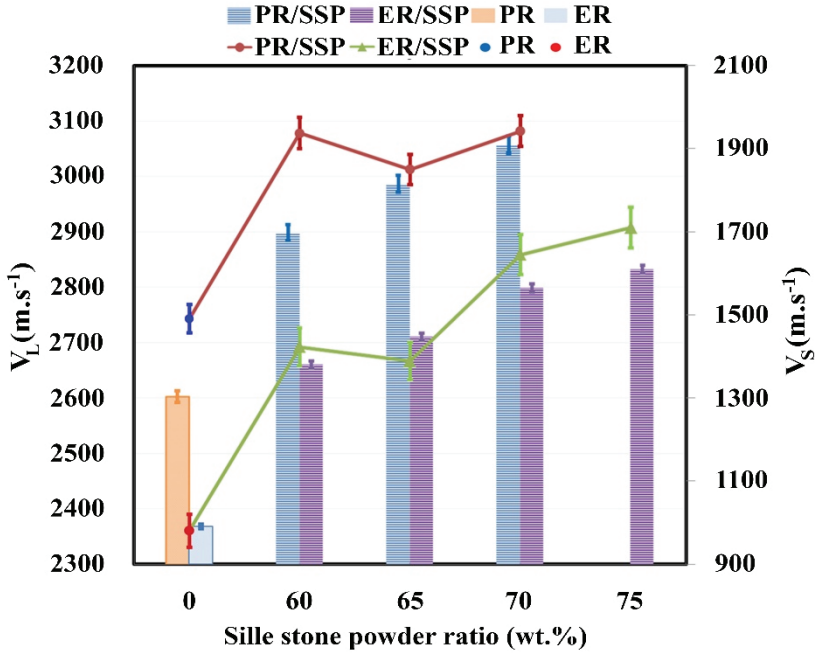

Figure 6 - Variation in ultrasonic wave velocities (V_L and V_S) of the ER/SSP and PR/SSP composites depending on the SSP amount.

Like longitudinal wave velocity values obtained for the ER/SSP composites, a linear increase in shear wave velocity was observed with the increasing amount of SSP in the ER/SSP composites. It was determined that the shear wave velocity values of the ER/SSP composite mortars increased by about 39.35–62.46 % compared to neat ER. This result shows that the contribution of SSP to neat ER increases the shear wave velocity values much more than the longitudinal wave velocity values. Since longitudinal wave velocity values are related to covalent bonds and shear wave velocity values are related to transverse interactions such as Van der Waals, these data show that the contribution of SSP to neat ER creates strong transverse bonds [65]. The higher shear wave values indicate that the outer electron clouds of adjacent atoms of the epoxy resin and SSP are quite close to each other.

Similar behavior of longitudinal ultrasonic wave velocity value of the ER/SSP composites was observed for the PR/SSP composites. The longitudinal wave velocity values of the PR/SSP composites vary between 3012.40 and 3081.60 $m.s^{-1}$, while the shear wave velocity values vary between 1698.60 and 1909.20 $m.s^{-1}$. The longitudinal wave velocity values of all PR/SSP composites were higher than those of neat PR. On the other hand, it was determined that the longitudinal wave velocity values of the PR/SSP composite mortars increased by about 9.81–12.32 % compared to neat PR. Also, a linear increase was observed in the shear wave velocity values of the PR/SSP composites with the increasing amount of SSP (see Table 4; Figure 6). The shear wave velocity values of the PR/SSP composite mortars increased by about 30.31 to 45.51% compared to neat PR. This significant increase in shear wave velocity values of the PR/SSP composites shows the effect of SSP on the shear wave velocity values of the PR/SSP composites.

The longitudinal wave velocity values measured for different kinds of composite mortars have been determined in the range of 800 $m.s^{-1}$ to 3400 $m.s^{-1}$ [34-36, 66, 67]. For example, Gupta and Vyas [68] prepared mortar mixtures (6FS, 6CS-30 and 6CS-40) using granite powder (GP), coarse river sand (CS) and fine river sand (FS) and various properties of obtained mortars were examined both by mechanical tests and ultrasonic velocity measurements. In the research conducted by Gupta and Vyas [68], it was determined that the ultrasonic velocity values of 6CS-30 and 6CS-40 mortars were 13% and 27% higher, respectively, than the control mortar (FS). The reason for this difference was shown to be that granite powders have better packaging properties than the control mortar. Thus, the measured values of ultrasonic longitudinal wave velocity are in good agreement with the related literature. To our knowledge, there is no study that measured the ultrasonic shear wave velocity of composite mortars in the related literature. In this consideration, the determination of the shear wave velocity values of the ER/SSP and PR/SSP composite mortars for the first time is quite important for the literature.

3.3. Elastic Modulus of the ER/SSP and PR/SSP Composites

The elastic properties of ER and PR at different amounts of SSP were calculated using the equations (2, 3, 4, and 6) by the measured density and ultrasonic velocity values. The results obtained are given in Table 5 and Figures 7-8.

The L, G, K, and E values of the neat ER were determined as 6.19 GPa, 1.09 GPa, 4.73 GPa, and 3.04 GPa, respectively. On the other hand, all values of the L, G, K, and E of the ER/SSP composites were determined bigger than those of the neat ER. The L, G, K, and E values of

the ER/SSP composites were determined between 11.65 and 14.87 GPa, 3.07 and 4.56 GPa, 7.56 and 8.79 GPa, and 8.10 and 11.64 GPa, respectively. Also, compared to the L, G, K, and E values of the neat ER, the L, G, K, and E values of the ER/SSP composite mortars increased about 88.21-140.23%, 181.65-318.35%, 50.74-85.84 %, and 166.45-282.89 %, respectively.

Table 5 - The elastic properties of materials obtained in this research.

Samples' ID	L(GPa)	G(GPa)	K(GPa)	E(GPa)
ER	06.19±0.06	1.09±0.01	4.73±0.05	3.04±0.04
ER/SSP-1	11.65±0.11	3.07±0.03	7.56±0.10	8.10±0.07
ER/SSP-2	11.76±0.06	3.47±0.02	7.13±0.06	8.95±0.04
ER/SSP-3	14.24±0.63	4.27±0.07	8.56±0.57	10.97±0.23
ER/SSP-4	14.87±0.94	4.56±0.09	8.79±0.88	11.64±0.30
PR	09.16±0.30	2.07±0.08	6.40±0.20	5.60±0.21
PR/SSP-1	16.90±0.09	5.15±0.03	10.04±0.12	13.19±0.06
PR/SSP-2	16.73±0.19	6.08±0.14	8.62±0.19	14.76±0.24
PR/SSP-3	17.79±0.50	6.83±0.19	8.69±0.31	16.23±0.43

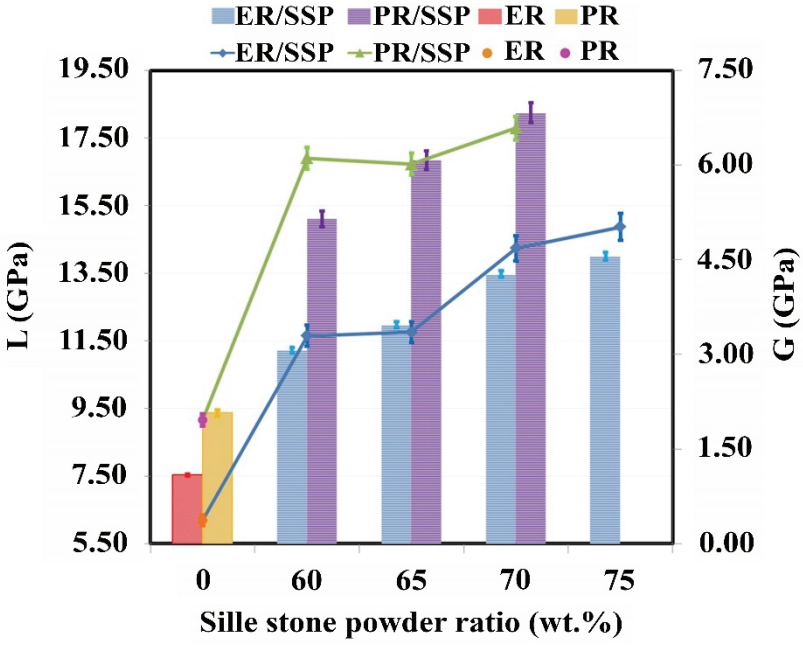

Figure 7 - L, G modulus values of the ER/SSP and PR/SSP composites depending on the SSP amount.

The L, G, K, and E values of the neat PR were determined as 9.16 GPa, 2.07 GPa, 6.40 GPa, and 5.60 GPa, respectively. On the other hand, all values of the L, G, K, and E of the PR/SSP composites were determined bigger than those of the neat PR as well. The L, G, K, and E values of the PR/SSP composites were determined between 16.90 and 17.79 GPa, 5.15 and 6.83 GPa, 8.62 and 10.04 GPa, and 13.19 and 16.23 GPa, respectively. Also, compared to the L, G, K, and E values of the neat PR, the L, G, K, and E values of the PR/SSP composite mortars increased about 84.50 to 94.21%, 148.79 to 229.95%, 34.69 to 56.88%, and 135.54 to189.82%, respectively.

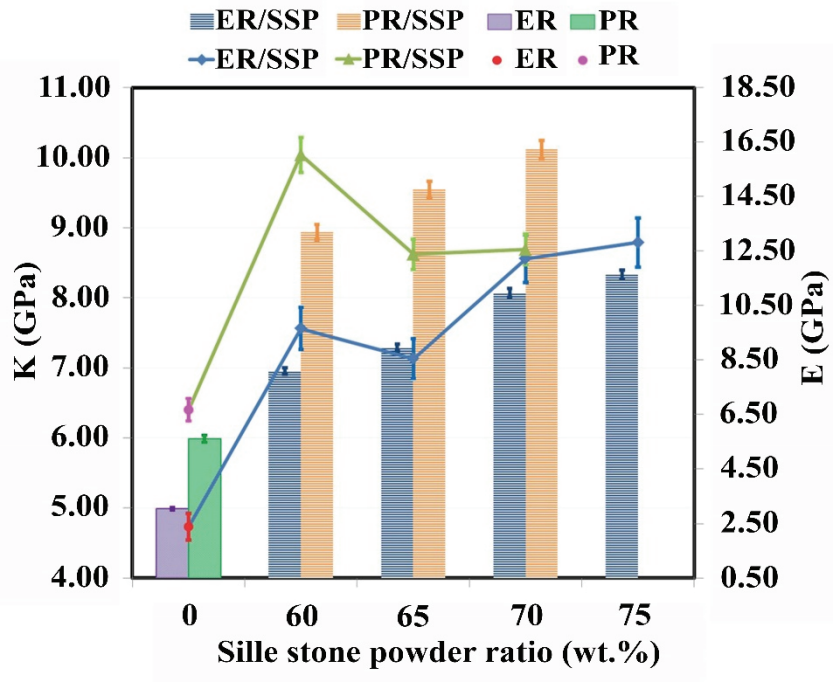

Figure 8 - K, E modulus values of the ER/SSP and PR/SSP composites depending on the SSP amount.

When the literature on restoration mortars is examined, it is seen that there are some studies that measured the ultrasonic longitudinal velocity to determine the durability of produced mortars[34-36, 66, 67]. For instance, Gupta and Vyas [68] determined that the dynamic elasticity modulus of mortars (CS-30 and CS-40) obtained with granite powder and coarse river sand at 1:4 ratios using ultrasonic velocity values and they reported an increase about 29% and 64% in the dynamic elasticity modulus of mortars, respectively, compared to the control mortar (FS). Wu, Liu, Sun and Zhang [69] added peach shell (PS) and apricot shell (AS) to concrete instead of normal weight aggregate (NWA) and sand to obtain environmentally friendly concrete. As a result of the research, it was determined that the elasticity modulus (10.91 GPa to 15.93 GPa) of concretes obtained with PS and AS additives were lower than those of NWA concretes. The low elastic modulus values of the new

concretes are attributed to the fact that the hardness of PS and AS is lower than that of NWA. Also, it is seen that the mechanical properties of the mortars were generally realized by destructive methods such as tensile and compression tests as well [36-38, 63, 70-74]. The elastic modulus values of these restoration mortars measured by mechanical methods are between 0.3 and 18.2 GPa. It is seen that the highest elastic modulus values were determined for the cement-based restoration mortars.

The ratio of fillers in the matrix is effective on the mechanical properties of the composites. The durability of the composites increases with the increasing amount of fillers in the matrix at a certain rate. When the ratio of fillers in the matrix exceeds this certain ratio, the mechanical properties of the composites decrease. Because the increase in the amount of filler after a certain ratio causes the interfacial area that weakens the strength of the composite [75]. Also, adding more than a certain amount of filler to the matrix of a composite decreases the mechanical properties of composites due to agglomeration in the composite [76, 77]. On the other hand, studies show that as the fineness of the aggregate increases, the bond between brick and mortar weakens [78], and therefore the mortar prepared with coarse sand will have greater tensile strength than the mortar prepared with fine sand. It has been reported that the tensile bond strength between brick and mortar decreases as fineness of aggregate increases [79].

3.4. Poisson's Ratio, Ultrasonic Micro-Hardness, and Acoustic Impedance

In this part of the research, Poisson's ratio (μ), ultrasonic micro-hardness (H), and acoustic impedance (Z) values of the neat ER, ER/SSP, neat PR, and PR/SSP composites were calculated using Equations (5, 7, and 8). The results obtained are given in Table 6, and Figures 9-10. As seen in Table 6 and Figure 9, the Poisson's ratio values of the neat ER and PR were measured as 0.393 and 0.354, respectively. Additionally, the Poisson ratio values of the ER/SSP and PR/SSP composites were obtained from 0.278 to 0.321, and 0.188 to 0.281, respectively.

Table 6 - Poisson's ratio (μ), ultrasonic micro-hardness (H), and acoustic impedance (Z) values of materials obtained in this research.

Samples' ID	μ	H (GPa)	Z (MRayl)
ER	0.393±0.001	0.15±0.00	2.62±0.02
ER/SSP-1	0.321±0.003	0.64±0.01	4.33±0.03
ER/SSP-2	0.291±0.002	0.81±0.01	4.41±0.03
ER/SSP-3	0.286±0.011	1.01±0.03	4.98±0.12
ER/SSP-4	0.278±0.017	1.10±0.06	5.11±0.16
PR	0.354±0.002	0.37±0.02	3.34±0.06
PR/SSP-1	0.281±0.003	1.23±0.02	5.49±0.02
PR/SSP-2	0.215±0.009	1.71±0.06	5.55±0.04
PR/SSP-3	0.188±0.007	2.00±0.06	5.77±0.08

As it is seen from these results, Poisson's ratio values of the ER/SSP and PR/SSP composites are smaller than those of the neat ER and PR. It was determined that the Poisson's ratios of the ER/SSP composites obtained because of the incorporation of SSP into the neat ER at increasing rates, were lower than those of the neat ER by about 18.32% to 29.26%. A similar decrease of about 20.62% to 46.89% in Poisson's ratio of the neat PR was determined by adding increasing amounts of SSP to neat PR. Since the smaller Poisson's ratio values indicate the enhancement in the mechanical properties of materials, it can be stated that all composite mortars have better mechanical properties than the neat ER and PR resins.

According to the data given in Table 6 and Figure 9, a linear increase was determined in the ultrasonic micro-hardness values of the ER/SSP and PR/SSP composites obtained by increasing the amount of SSP in neat ER and PR resins compared to the micro-hardness value of the neat ER, and PR resins. The ultrasonic micro-hardness values of the ER/SSP and PR/SSP composites were measured between 0.64 GPa to 1.10 GPa and 1.23 GPa to 2.00 GPa, respectively. On the other hand, compared to the H values of the neat ER and PR matrices, an increase of 326.67 % to 633.33% was observed in the H values of the ER/SSP composite mortars while an increase of 232.43% to 440.54% was observed in the H values of the PR/SSP composite mortars. These results are like the results of ultrasonic wave velocities and the elastic properties of ER/SSP and PR/SSP composites. When the ultrasonic micro-hardness values of the obtained ER/SSP and PR/SSP composites are compared, it is seen that the bonds formed because of the interaction of the SSP filler with the neat PR matrix are stronger than those of the bonds formed due to the interaction between the SSP filler and the neat ER. Because the increase in the ultrasonic micro-hardness values in the composite is due to the strong atomic or molecular bonds between the matrix and the fillers.

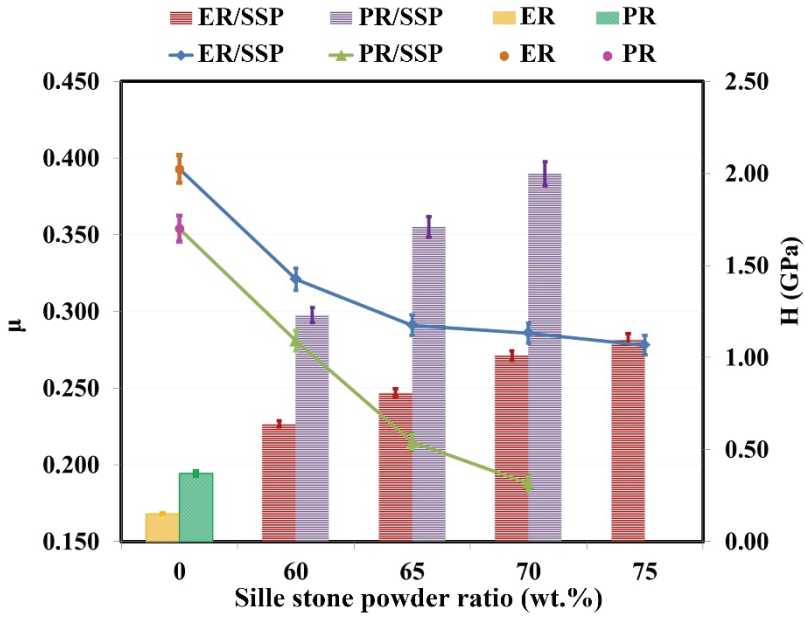

Figure 9 - Change in ER and PR different amounts of SSP Poisson's ratio (μ), and ultrasonic micro-hardness (H).

On the other hand, the acoustic impedance (Z) values of the neat ER and PR were measured as 2.62 MRayl and 3.34 MRayl, respectively. The acoustic impedance (Z) values of the ER/SSP and PR/SSP composites were determined in a range of 4.33 MRayl to 5.11 MRayl and 5.49 MRayl to 5.77 MRayl, respectively (see Table 6; Figure 10). Thus, a significant increase was observed for Z values of neat ER, and PR. Because compared to neat ER, and PR matrices, an increase was seen in a range of 65.27% to 95.04% and 64.37% to 72.75% was observed in the Z values of the ER/SSP, and PR/SSP composites, respectively. As seen in Figure 10, a linear increase was observed in Z values of both neat ER and PR matrices by increasing the amount of SSP. As with all other elastic properties, the Z values of the neat PR matrix, and PR/SSP composites were determined higher than those of the neat ER matrix, and ER/SSP composites. Therefore, it can be stated that adding the SSP filler to the PR matrix provides composites that have higher Z values compared to the ER/SSP composites obtained by adding the SSP filler to the ER matrix.

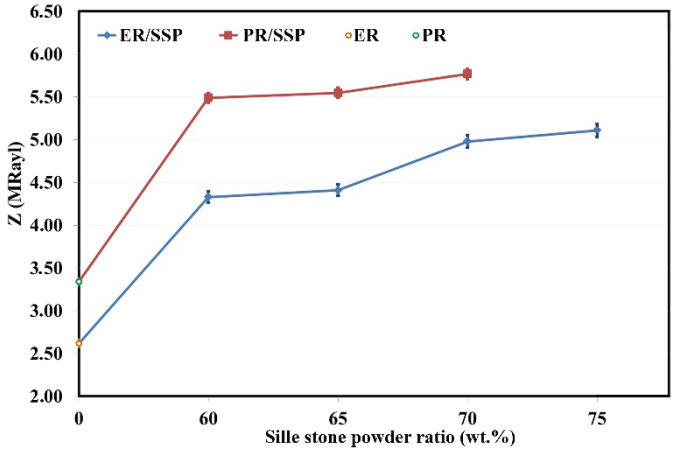

Figure 10 - Change in ER and PR different amounts of SSP acoustic impedance (Z) values.

Although material density is an important factor affecting ultrasonic wave velocity [80, 81], it is not the only factor affecting ultrasonic wave velocity in composite materials. Because moisture content, porosity degree of the material and discontinuities within the material can also affect the materials properties such as ultrasonic wave velocity in composites [70, 82-85]. Ultrasonic wave velocity is also directly related to the density and elastic properties of the material [86]. There are various reasons why the density of materials affects the ultrasonic wave velocity in composites (Elastic modulus, acoustic impedance, packing of particles, homogeneity). For example, ultrasonic wave velocity is frequently directly proportional to the materials' Young's modulus and hardness, both of which depend on the material density [87]. Therefore, if the Young's modulus and hardness value of a material are high, the ultrasonic wave velocity in that material may also be high. On the other hand, acoustic impedance, which is a measure of the ability to transfer ultrasonic wave energy from one medium to another, also affects the ultrasonic wave velocity. Because acoustic impedance is a physical material property that depends on both density and ultrasonic velocity, and a high acoustic impedance causes an increase in ultrasonic velocity. The tight packing of particles

such as sand, cement and aggregate added into the matrix in mortar may cause fewer voids in the resulting composite, which causes an increase in both the density of the resulting composite and the ultrasonic wave velocity. Because there are fewer gaps in the resulting composite, it causes ultrasonic waves to travel in the medium in a shorter time.

Since higher density can be achieved in materials with more homogeneous distribution, ultrasonic wave velocity may also be higher in a more homogeneous environment. Achieving the desired homogeneity in composites depends on the composite components and the applications in the production process. Proper mixing time and intensity are very important to ensure homogeneity in mechanical mixing. It is possible to ensure homogeneous distribution of the components by breaking up the lumps by applying appropriate mechanical force during mixing. Sometimes, homogeneous distribution can be achieved by improving the compatibility between these fillings and the matrix material by treating the surfaces of the filling materials with coupling agents or chemical treatments. In some cases, the homogeneity of the matrix and components of the mixture can be supported by the addition of surfactants or dispersants. Making composite mixtures at appropriate temperature and pressure, reducing the size of the particles added to the composite, and adding them to the mixture in the appropriate order can also help in the homogeneous distribution of the composite components. On the other hand, one of the best ways to improve the homogeneity of composite mortars at the production process is to use ultrasonic homogenizer which uses ultrasonic waves.

3.5. Cost Analysis

A cost analysis was conducted to evaluate the feasibility of using the composite mortars produced in this study in the restoration of historical buildings. In the cost analysis, prices of epoxy and polyester resin materials are based on data available on commercial websites [49, 50, 88]. In calculating the cost analysis of these materials, 20% goods and services tax was added to the market price. Additionally, for imported goods, a shipping fee of $65 per ton has been added. Average unit prices of various restoration mortars are given in Table 7.

Table 7 - Average unit prices of various restoration mortars.

Composite mortars abbreviations	Unit price ($ per ton)
Pozzolanic lime-based mortar	628
Natural hydraulic lime mortar	601
Khorasan mortar	732
Gypsum mortar	147
Composite mortar obtained in this research	240–600

According to the data in Table 7, it is seen that the composite mortars produced within the scope of this study have lower costs than other traditional restoration mortars, except gypsum mortar. On the other hand, composite mortars are cheaper than pozzolanic lime mortar,

natural lime mortar, and Khorasan mortar by approximately 4.46% to 61.78%, 0.16% to 60.07% and 18.03% to 67.21% respectively. However, composite mortars obtained in this research are approximately 63.27% to 308.16% more expensive than gypsum mortar.

4. CONCLUSIONS

In this research, epoxy, and polyester matrix-based repair mortars were developed by utilizing the recycling of Sille Stone Powder (SSP) to be used in the restoration of old historical buildings such as madrasas, mosques, palaces, libraries, fountains, and caravanserais and in new generation construction buildings. The physical and mechanical properties of these new polymer-based mortars were determined non-destructively by ultrasonic method, while their morphology was analyzed by SEM. SEM images revealed that SSP showed a more homogeneous distribution in PR resin compared to ER. The findings of the research showed that except the values of Poisson's ratio, the values of density, ultrasonic longitudinal wave velocity, ultrasonic shear wave velocity, ultrasonic micro-hardness, acoustic impedance, and elastic modulus (L, G, K, E) of the ER/SSP, and PR/SSP composites are higher than those of the values of neat ER, and PR. In addition, it was determined that the most suitable combination ratio between ER and SSP in the ER/SSP composite mortars was 25:75, and the most appropriate combination ratio between PR and SSP in the PR/SSP composite mortars was 30:70. One of the most important results of the research is that the costs of the repair mortars obtained are more affordable than traditional repair mortars. In conclusion, this research showed that the ultrasonic testing method can be used as a beneficial method in the characterization of composite mortars and the evaluation of their elastic properties. For this reason, it may be recommended to conduct similar research using SSP and other environmentally polluting wastes such as SSP with other polymer matrices such as polystyrene and polyurethane, as in ER and PR, and characterizing these new repair mortars with non-destructive ultrasonic methods.

Acknowledgments

This study was prepared from the first author's PH.D. thesis. This thesis study was supported by the Scientific Research Projects Commission of the Konya Technical University within the scope of Ph.D. (Project number: 211120045). The authors are grateful for the support provided by Konya Technical University (Türkiye). Experimental studies of this research were carried out in laboratories of the Science and Technology Research and Application Center (BITAM) at Necmettin Erbakan University. We would like to thank the staff of BITAM for their assistance as well.

References

[1] Saheb D. N., Jog J. P., Natural Fiber Polymer Composites: A Review, Advances in Polymer Technology, 18(4), 351-363, 1999.

[2] Humphreys M. F., The Use of Polymer Composites in Construction, International Conference on Smart and Sustainable Built Environment, Australia, 2003.

[3] Pendhari S. S., Kant T., Desai Y. M., Application of Polymer Composites in Civil Construction: A General Review, Composite Structures, 84(2), 114-124, 2008.

[4] Jain A., Polymer Concrete: Future of Construction Industry, International Journal of Scientific Research, 2(11), 201-202, 2012.

[5] Van Gemert D., Czarnecki L., Maultzsch M., Schorn H., Beeldens A., Łukowski P., Knapen E., Cement Concrete and Concrete–Polymer Composites: Two Merging Worlds: A Report from 11th ICPIC Congress in Berlin, 2004, Cement and Concrete Composites, 27(9-10), 926-933, 2005.

[6] Pascal S., Alliche A., Pilvin P., Mechanical Behaviour of Polymer Modified Mortars, Materials Science and Engineering: A, 380(1-2), 1-8, 2004.

[7] Hwang E.-H., Ko Y. S., Comparison of Mechanical and Physical Properties of SBR-Polymer Modified Mortars Using Recycled Waste Materials, Journal of Industrial and Engineering Chemistry, 14(5), 644-650, 2008.

[8] Buyuksagis I. S., Uygunoglu T., Tatar E., Investigation on The Usage of Waste Marble Powder in Cement-Based Adhesive Mortar, Construction and Building Materials, 154, 734-742, 2017.

[9] Marvila M. T., Alexandre J., de Azevedo A. R. G., Zanelato E. B., Evaluation of The Use of Marble Waste in Hydrated Lime Cement Mortar Based, Journal of Material Cycles and Waste Management, 21, 1250-1261, 2019.

[10] Vardhan K., Siddique R., Goyal S., Strength, Permeation and Micro-Structural Characteristics of Concrete Incorporating Waste Marble, Construction and Building Materials, 203, 45-55, 2019.

[11] Srivastava A., Singh S. K., Utilization of Alternative Sand for Preparation of Sustainable Mortar: A Review, Journal of Cleaner Production, 253, 119706, 2020.

[12] Eren Y., Stratigraphy of Autochthonous and Cover Units of the Bozdağlar Massif NW Konya, Geological Bulletin of Turkey, 36, 7-23, 1993.

[13] Aksoy R., Demiröz A., The Konya Earthquakes of 10–11 September 2009 and Soil Conditions in Konya, Central Anatolia, Turkey, Natural Hazards and Earth System Sciences, 12, 295-303, 2012.

[14] Aksoy R., Extensional Neotectonic Regime in West-Southwest Konya, Central Anatolia, Turkey, International Geology Review, 61(14), 1803-1821, 2019.

[15] Sprenger S., Epoxy Resin Composites with Surface-Modified Silicon Dioxide Nanoparticles: A Review, Journal of Applied Polymer Science, 130(3), 1421-1428, 2013.

[16] Doan T. T. L., Brodowsky H. M., Gohs U., Mäder E., Re-use of Marble Stone Powders in Producing Unsaturated Polyester Composites, Advanced Engineering Materials, 20, 1701061, 2018.

[17] Ramadan N., Taha M., La Rosa A. D., Elsabbagh A., Towards Selection Charts for Epoxy Resin, Unsaturated Polyester Resin and Their Fibre-Fabric Composites with Flame Retardants, Materials, 14(5), 1181, 2021.

[18] Ying G.-G., Song C., Ren J., Guo S.-Y., Nie R., Zhang L., Mechanical and Durability-Related Performance of Graphene/Epoxy Resin and Epoxy Resin Enhanced OPC Mortar, Construction and Building Materials, 282, 122644, 2021.

[19] Debska B., Lichołai L., Miąsik P., Assessment of the Applicability of Sustainable Epoxy Composites Containing Waste Rubber Aggregates in Buildings, Buildings, 9(2), 31, 2019.

[20] Abenojar J., Martínez M. A., de Armentia S. L., Paz E., del Real J. C., Velasco F., Mechanical Properties and Fire-Resistance of Composites with Marble Particles, Journal of Materials Research and Technology, 12, 1403-1417, 2021.

[21] Barros M. M., de Oliveira M. F. L., da Conceição Ribeiro R. C., Bastos D. C., de Oliveira M. G., Ecological Bricks from Dimension Stone Waste and Polyester Resin, Construction and Building Materials, 232, 117252, 2020.

[22] Lee C. H., Jo Y. H., Correlation and Correction Factor Between Direct and Indirect Methods for the Ultrasonic Measurement of Stone Samples, Environmental Earth Sciences, 76, 477, 2017.

[23] Ahmad A., Pamplona M., Simon S., Ultrasonic Testing for The Investigation and Characterization of Stone–A Non-Destructive and Transportable Tool, Studies in Conservation, 54, 43-53, 2009.

[24] Favaro M., Mendichi R., Ossola F., Russo U., Simon S., Tomasin P., Vigato P. A., Evaluation of Polymers for Conservation Treatments of Outdoor Exposed Stone Monuments. Part I: Photo-Oxidative Weathering, Polymer Degradation and Stability, 91(12), 3083-3096, 2006.

[25] Alameri I., Oltulu M., Mechanical Properties of Polymer Composites Reinforced by Silica-Based Materials of Various Sizes, Applied Nanoscience, 10, 4087-4102, 2020.

[26] Ghassemi P., Toufigh V., Durability of Epoxy Polymer and Ordinary Cement Concrete in Aggressive Environments, Construction and Building Materials, 234, 117887, 2020.

[27] Jafari K., Toufigh V., Experimental and Analytical Evaluation of Rubberized Polymer Concrete, Construction and Building Materials, 155, 495-510, 2017.

[28] Kılıç A., Teymen A., Determination of Mechanical Properties of Rocks Using Simple Methods, Bulletin of Engineering Geology and the Environment, 67, 237-244, 2008.

[29] Ye G., Lura P., Van Breugel K., Fraaij A. L. A., Study on The Development of The Microstructure in Cement-Based Materials by Means of Numerical Simulation and Ultrasonic Pulse Velocity Measurement, Cement and Concrete Composites, 26(5), 491-497, 2004.

[30] Mesquita E., Martini R., Alves A., Antunes P., Varum H., Non-Destructive Characterization of Ancient Clay Brick Walls by Indirect Ultrasonic Measurements, Journal of Building Engineering, 19, 172-180, 2018.

[31] de Araújo Freitas V. L., de Albuquerque V. H. C., de Macedo Silva E., Silva A. A., Tavares J. M. R., Nondestructive Characterization of Microstructures and

Determination of Elastic Properties in Plain Carbon Steel Using Ultrasonic Measurements, Materials Science and Engineering: A, 527(16-17), 4431-4437, 2010.

[32] Adamus K., Janina A., Lacki J., Ultrasonic Testing of Thin Walled Components Made of Aluminum Based Laminates, Composite Structures, 202, 95-101, 2018.

[33] Sun H., Zhu J., Nondestructive Evaluation of Steel-Concrete Composite Structure Using High-Frequency Ultrasonic Guided Wave, Ultrasonics, 103, 106096, 2020.

[34] Xu S., Wang J., Jiang Q., Zhang S., Study of Natural Hydraulic Lime-Based Mortars Prepared with Masonry Waste Powder as Aggregate and Diatomite/Fly Ash as Mineral Admixtures, Journal of Cleaner Production, 119, 118-127, 2016.

[35] Branco F. G., Belgas M. d. L., Mendes C., Pereira L., Ortega J. M., Mechanical Performance of Lime Mortar Coatings for Rehabilitation of Masonry Elements in Old and Historical Buildings, Sustainability, 13(6), 3281, 2021.

[36] Autiero F., Ramesh M., Azenha M., Di Ludovico M., Prota A., Lourenço P. B., Experimental Analysis of Lime Putty and Pozzolan-Based Mortar for Interventions in Archaeological Sites, Materials and Structures, 54, 148, 2021.

[37] Grazzini A., Zerbinatti M., Fasana S., Mechanical Characterization of Mortars Used in the Restoration of Historical Buildings: an Operative Atlas for Maintenance and Conservation, IOP Conference Series: Materials Science and Engineering, 629, 012024, 2019.

[38] Ramesh M., Azenha M., Lourenço P. B., Quantification of Impact of Lime on Mechanical Behaviour of Lime Cement Blended Mortars for Bedding Joints in Masonry Systems, Construction and Building Materials, 229, 116884, 2019.

[39] Aliabdo A. A. E., Elmoaty A. E. M. A., Reliability of Using Nondestructive Tests to Estimate Compressive Strength of Building Stones and Bricks, Alexandria Engineering Journal, 51(3), 193-203, 2012.

[40] Ozdemir A., Capillary Water Absorption Potential of Some Building Materials, Geological Engineering, 26(1), 19-32, 2002.

[41] Kekec B., Unal M., Investigation of The Texture, Physical and Mechanical Properties of Some Rocks Used as Building Stone, 7-Th International Multidisciplinary Scientific Geoconference SGEM, 2007.

[42] Saydan M., Unal A., Keskin U. S., Kansun G., An Investigation of the Current Situation of the Mısırlıoğlu Bridge and Possible Damages After Freeze-Thaw by Using Finite Elements Analysis, Sille–Konya (Central Anatolia, Turkey), Engineering Failure Analysis, 117, 104788, 2020.

[43] Zedef V., Kocak K., Doyen A., Ozsen H., Kekec B., Effect of Salt Crystallization on Stones of Historical Buildings and Monuments, Konya, Central Turkey, Building and Environment, 42(3), 1453-1457, 2007.

[44] Fener M., İnce İ., Effects of the Freeze–Thaw (F–T) Cycle on the Andesitic Rocks (Sille-Konya/Turkey) Used in Construction Building, Journal of African Earth Sciences, 109, 96-106, 2015.

[45] Korkanç M., Hüseyinca M. Y., Hatır M. E., Tosunlar M. B., Bozdağ A., Özen L., İnce İ., Interpreting Sulfated Crusts on Natural Building Stones Using Sulfur Contour Maps and Infrared Thermography, Environmental Earth Sciences, 78, 378, 2019.

[46] Öztürk Ç., Akpınar S., Tarhan M., Investigation of the Usability of Sille Stone as Additive in Floor Tiles, Journal of the Australian Ceramic Society, 57, 567-577, 2021.

[47] Öztürk Ç., Physicochemical Properties of Heat Treated Sille Stone for Ceramic Industry, Open Chemistry, 16(1), 1134-1142, 2018.

[48] Güyer F., Günaydın A. B., Akbulut İ., Ak S., Kurtman T., Demirci A. R., Akarsu B., Emre Ö., Durdu M., Karakaş M., Üyüklü A., Yıldız H., Konya İli Çevre Jeolojisi ve Doğal Kaynaklar, No: 42149, MTA Rap., Ankara, 1998.

[49] Url1, https://www.kompozitpazari.com/ (Accessed 13.09.2023), 2023.

[50] Url2, https://brtr-kimya-as.business.site/ (Accessed 13.09.2023), 2023.

[51] Standard A., ASTM D638-14. Standard Test Method for Tensile Properties of Plastics, ASTM International: West Conshohocken, PA, 2014.

[52] Dong J., Kim B., Locquet A., McKeon P., Declercq N., Citrin D. S., Nondestructive Evaluation of Forced Delamination in Glass Fiber-Reinforced Composites by Terahertz and Ultrasonic Waves, Composites Part B: Engineering, 79, 667-675, 2015.

[53] Hellier C. J., Handbook of Nondestructive Evaluation, Blacklick, OH, 2nd ed. McGraw-Hill Education, 2013.

[54] Nanekar P. P., Shah B. K., Characterization of Material Properties by Ultrasonics, BARC Newsletter, 249, 25-38, 2003.

[55] Perepechko I. I., Acoustic Methods of Investigating Polymers (Translated from Russian by G. Leib), Moscow, Mir Publishers, 1975.

[56] Shah A. A., Ribakov Y., Zhang C., Efficiency and Sensitivity of Linear and Non-Linear Ultrasonics to Identifying Micro and Macro-Scale Defects in Concrete, Materials & Design, 50, 905-916, 2013.

[57] Fang Y., Lin L., Feng H., Lu Z., Emms G. W., Review of The Use of Air-Coupled Ultrasonic Technologies for Nondestructive Testing of Wood and Wood Products, Computers and Electronics in Agriculture, 137, 79-87, 2017.

[58] Vasconcelos G., Lourenço P. B., Alves C. A. S., Pamplona J., Ultrasonic Evaluation of The Physical and Mechanical Properties of Granites, Ultrasonics, 48(5), 453-466, 2008.

[59] Noor-E-Khuda S., Albermani F., Mechanical Properties of Clay Masonry Units: Destructive and Ultrasonic Testing, Construction and Building Materials, 219, 111-120, 2019.

[60] Lafhaj Z., Goueygou M., Djerbi A., Kaczmarek M., Correlation Between Porosity, Permeability and Ultrasonic Parameters of Mortar with Variable Water/Cement Ratio and Water Content, Cement and Concrete Research, 36(4), 625-633, 2006.

[61] Trtnik G., Kavčič F., Turk G., Prediction of Concrete Strength Using Ultrasonic Pulse Velocity and Artificial Neural Networks, Ultrasonics, 49(1), 53-60, 2009.

[62] Hirsekorn S., Van Andel P. W., Netzelmann U., Ultrasonic Methods to Detect and Evaluate Damage in Steel, Nondestructive Testing and Evaluation, 15(6), 373-393, 1998.

[63] Aggelakopoulou E., Bakolas A., Moropoulou A., Properties of Lime–Metakolin Mortars for the Restoration of Historic Masonries, Applied Clay Science, 53(1), 15-19, 2011.

[64] Garbacz A., Garboczi E. J., Ultrasonic Evaluation Methods Applicable to Polymer Concrete Composites, US Department of Commerce, Technology Administration, National Institute of Standards and Technology, 2003.

[65] Oral I., Determination of Elastic Constants of Epoxy Resin/Biochar Composites by Ultrasonic Pulse Echo Overlap Method, Polymer Composites, 37(9), 2907-2915, 2016.

[66] Bulut Ü., Tanaçan L., Perlitin Puzolanik Aktivitesi (Pozzolanic Activity of Perlite) İtüdergisi/a Mimarlık, Planlama, Tasarım, 8(1), 81-89, 2009.

[67] Topçu İ. B., Gökbel S., Işıkdağ B., Genleştirilmiş Perlitin Horasan Harçlarında Kullanılması (Using Expanded Perlite in Khorasan Mortars), 2nd International Sustainable Building Sympodium, Ankara, Turkey, 133-137, 2015.

[68] Gupta L. K., Vyas A. K., Impact on Mechanical Properties of Cement Sand Mortar Containing Waste Granite Powder, Construction and Building Materials, 191, 155-164, 2018.

[69] Wu F., Liu C., Sun W., Zhang L., Mechanical Properties of Bio-Based Concrete Containing Blended Peach Shell and Apricot Shell Waste, Materiali in Tehnologije, 52(5), 645-651, 2018.

[70] Eren F., Keskinateş M., Felekoğlu B., Tosun Felekoğlu K., Mineral Katkı İkamesinin Kalsiyum Alümina Çimentolu Harçların Taze Hal ve Zamana Bağlı Sertleşmiş Hal Özelliklerine Etkileri, Turkish Journal of Civil Engineering, 34(3), 139-162, 2023.

[71] Haach V. G., Vasconcelos G., Lourenço P. B., Influence of Aggregates Grading and Water/Cement Ratio in Workability and Hardened Properties of Mortars, Construction and Building Materials, 25(6), 2980-2987, 2011.

[72] Iucolano F., Liguori B., Colella C., Fibre-Reinforced Lime-Based Mortars: A Possible Resource for Ancient Masonry Restoration, Construction and Building Materials, 38, 785-789, 2013.

[73] Oğuz C., Türker F., Koçkal N. U., Andriake Limanı'nda Roma, Bizans ve Selçuklu Dönemi Harçların Özellikleri, İMO Teknik Dergi, 429, 6993-7013, 2015.

[74] Papatzani S., Paine K., Nanomontmorillonite Reinforced Fibre Cements and Nanomontmorillonite-Nanosilica Reinforced Mortars, Turkish Journal of Civil Engineering, 34(3), 43-60, 2023.

[75] Sahu R., Gupta M. K., Chaturvedi R., Tripaliya S. S., Pappu A., Moisture Resistant Stones Waste Based Polymer Composites with Enhanced Dielectric Constant and Flexural Strength, Composites Part B: Engineering, 182, 107656, 2020.

[76] Awad A. H., El-Gamasy R., Abd El-Wahab A. A., Abdellatif M. H., Assessment of Mechanical Properties of HDPE Composite with Addition of Marble and Granite Dust, Ain Shams Engineering Journal, 11(4), 1211-1217, 2020.

[77] Awad A. H., El-gamasy R., Abd El-Wahab A. A., Abdellatif M. H., Mechanical Behavior of PP Reinforced with Marble Dust, Construction and Building Materials, 228, 116766, 2019.

[78] Kabeer K. I. S. A., Vyas A. K., Utilization of Marble Powder as Fine Aggregate in Mortar Mixes, Construction and Building Materials, 165, 321-332, 2018.

[79] Reddy B. V. V., Gupta A., Influence of Sand Grading on the Characteristics of Mortars and Soil–Cement Block Masonry, Construction and Building Materials, 22(8), 1614-1623, 2008.

[80] Afifi H., Hasan E., Annealing Effect on Microhardness and Elastic Constants of PMMA, Polymer-Plastics Technology and Engineering, 42(4), 543-554, 2003.

[81] Afifi H. A., Ultrasonic Pulse Echo Studies of the Physical Properties of PMMA, PS, and PVC, Polymer-Plastics Technology and Engineering, 42(2), 193-205, 2003.

[82] Ali M. G. S., Elsayed N. Z., Eid A. M., Ultrasonic Attenuation and Velocity in Steel Standard Reference Blocks, Romanian Journal of Acoustics and Vibration, 10(1), 33-38, 2013.

[83] Hirose S., Hatakeyama T., Hatakeyama H., Glass Transition and Thermal Decomposition of Epoxy Resins from the Carboxylic Acid System Consisting of Ester-Carboxylic Acid Derivatives of Alcoholysis Lignin and Ethylene Glycol with Various Dicarboxylic Acids, Thermochimica Acta, 431(1-2), 76-80, 2005.

[84] Kocaman S., Soydal U., Ahmetli G., Influence of Cotton Waste and Flame-Retardant Additives on the Mechanical, Thermal, and Flammability Properties of Phenolic Novolac Epoxy Composites, Cellulose, 28, 7765-7780, 2021.

[85] Zakriya M., Ramakrishnan G., Gobi N., Palaniswamy N. K., Srinivasan J., Jute-Reinforced Non-Woven Composites as a Thermal Insulator and Sound Absorber–A Review, Journal of Reinforced Plastics and Composites, 36, 206-213, 2017.

[86] Amin V. R., Ultrasonic Attenuation Estimation for Tissue Characterization, Retrospective Theses and Dissertations, Ames, Iowa State University, 1989.

[87] Oral I., Guzel H., Ahmetli G., Gur C. H., Determining The Elastic Properties of Modified Polystyrenes by Sound Velocity Measurements, Journal of Applied Polymer Science, 121(6), 3425-3432, 2011.

[88] Url3, https://kvmgm.ktb.gov.tr/Eklenti/116937,kultur-ve-turizm-bakanligi-2023-2-birim-fiyatlaripdf.pdf?0 (Accessed 13.09.2023), 2023.

Turkish Journal of Civil Engineering, 2024 47-70, Paper 769, ***Research Article***

Protection of Reinforced Concrete Columns from Pounding-Induced Effects in Adjacent Buildings

Sueda ALTAN OYMANLI[1*]
Özgür AVŞAR[2]

ABSTRACT

The pounding damage is one of the most common seismic damage types observed after past earthquakes in adjacent reinforced concrete (RC) buildings having insufficient gap in-between. Particularly in highly populated regions, there are numerous adjacent RC buildings, in which pounding can cause severe damage or total collapse. Many previous reconnaissance reports following earthquakes have emphasized severe column damage due to pounding with the slab of adjacent building. In this paper, a retrofitting method is presented to reduce the seismic damage caused by pounding on existing RC structural elements in cases where collision is unavoidable. Pounding effects are investigated by using 4- and 7-story RC buildings with unequal floor elevations. As a retrofitting solution for pounding, steel columns and neoprene rubber pads are placed at the mid-height of the story so that the pounding takes place between the neighbouring slab and added steel columns instead of existing RC columns. The mid-column pounding of existing RC buildings with and without retrofitting are numerically investigated. In the numerical model, buildings are connected by link elements to produce the pounding in-between. Nonlinear response history analyses are performed using 11 different real ground-motion records. Pounding forces, peak floor accelerations, inter-story drift ratios, story shear force distributions, and plastic hinge distributions are obtained and compared for each of the pounding conditions. The analysis results reveal that the proposed retrofitting method protects the existing RC columns from brittle type of shear failure and reduces the destructive effects of pounding.

Keywords: Pounding, seismic damage, retrofitting, adjacent buildings, reinforced concrete, link element.

Note:
- This paper was received on April 10, 2023 and accepted for publication by the Editorial Board on December 22, 2023.
- Discussions on this paper will be accepted by July 31, 2024.
- https://doi.org/10.18400/tjce.1280691

1 Eskisehir, Türkiye
sueda.altan19@gmail.com - https://orcid.org/0000-0001-8872-0544

2 Eskisehir Technical University, Department of Civil Engineering, Eskisehir, Türkiye
ozguravsar@eskisehir.edu.tr - https://orcid.org/0000-0001-7246-9631

* Corresponding author

1. INTRODUCTION

Earthquakes are one of the most common natural disasters that result in loss of life and property in the seismically active regions. Adjacent buildings can collide due to the insufficient seismic gap between them or due to their out-of-phase vibrations [1,2].

This phenomenon is referred to as pounding, which is one of the common causes of damage observed during earthquakes. Especially in metropolitan cities, there are numerous buildings with insufficient seismic gap between them, and these adjacent buildings are under the risk of structural damage due to pounding in future earthquakes. Therefore, it is necessary to minimize the risks arising from earthquake-induced pounding damage.

Leaving sufficient seismic gaps ensuring that a collision does not occur between adjacent buildings is the most effective method for preventing the occurrence of pounding. Therefore, a minimum seismic gap that shall be placed between two buildings has been specified to avoid pounding in building design codes. In the Turkish Building Earthquake Code (TBEC-2018) [3], the minimum size of gap shall not be less than the value obtained by multiplying the coefficient (α) by the square root of the sum of squares of displacements obtained in adjacent buildings for each floor. If all floor levels of adjacent buildings are the same at all stories, the coefficient (α) is 0.25R/I; otherwise, the coefficient is 0.5R/I. R and I represent the structural system behaviour factor and importance factor, respectively. In addition, gap distance shall not be less than 30 mm up to 6.0 m height and shall be increased by 10 mm for each additional 3.0 m above 6.0 m and shall be arranged to allow independent movement of building blocks in all earthquake directions. In some studies, the adequacy of the seismic gap specified in building codes is investigated [2,4]. There are other studies conducted to determine the minimum seismic gap required to prevent a collision [5-9].

Mostly, during the construction stage, the seismic gap calculated according to the earthquake design code requirements is neither considered nor inspected properly between adjacent buildings.

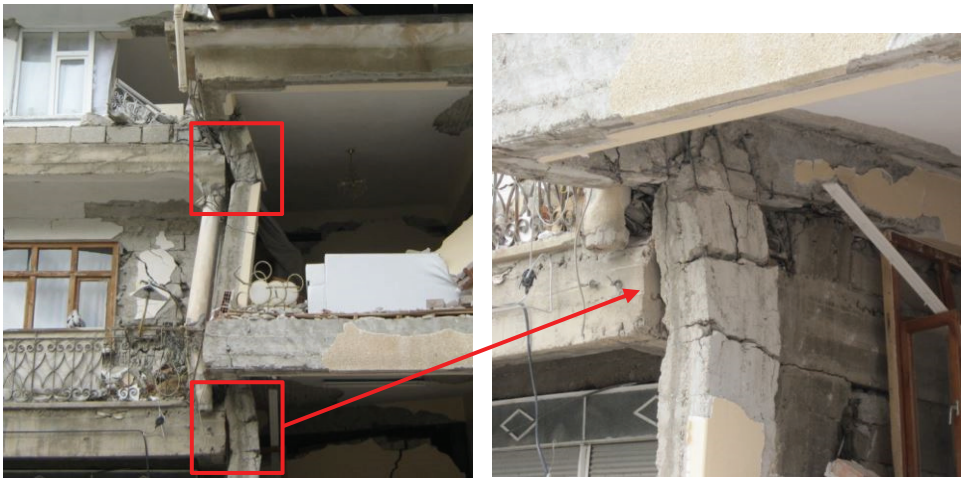

Fig. 1 – Examples of Pounding failures. [13]

The collision between buildings can cause local damages or total collapse. Slab to column collision is much more critical due to large shear forces imposed on the columns as a result of pounding [10-12]. The shear capacity of the columns can be exceeded as a result of the impact of the adjacent slab that has very high in-plane stiffness and capacity. As a result, occurrence of column shear damage can lead to partial or total collapse of the buildings as shown in Fig. 1.

Pounding has been observed in many past earthquakes. Following the 1985 Mexico City Earthquake, it was reported that 40 percent of the buildings collided with each other, and pounding damages were observed in 15 percent of the severely damaged buildings [14]. The same phenomenon was observed in Loma Prieta Earthquake (1989), which affected over 500 buildings and caused pounding damage in over 200 buildings [15]. After the 1999 Kocaeli Earthquake in Turkey, severe column damage was reported as a result of a collision between a six-story building and a two-story neighbouring building [16]. Following the earthquake, reconnaissance studies and reports revealed that the pounding caused significant damage to the RC buildings [17–21]. Many experimental and numerical studies have also show that pounding affects the seismic behaviour of buildings [22-29].

Thus, retrofitting methods to avoid the pounding have been the topic of many previous studies.

Anagnostopoulos [30] proposed the placement of impact-absorbing materials between the reinforced concrete structures to reduce the pounding effects. Many studies investigated the effect of use of impact-absorbing materials on the response of colliding buildings [31-35].

Using supplemental energy dissipation devices reduces the maximum lateral displacements of the building. However, such supplemental energy dissipation devices may not be sufficient to prevent pounding in all conditions. Structural pounding can be avoided by increasing the stiffness of the buildings using shear walls and bracing systems [36,37]. Shear walls reduce the lateral displacements by increasing the stiffness of the building. If the displacements could not be sufficiently reduced to the point where the collision is prevented, pounding is inevitable and existing frame elements that collide with the adjacent building will be severely damaged. Another mitigation measure proposed in the literature is to connect adjacent buildings with links to keep structural vibrations in phase without causing pounding [38,39]. Abdel-Mooty and Ahmed [40] proposed a retrofitting solution using localized interconnections between adjacent parts of the structure. In this case, seismic damage is especially localized in the connection points of these link elements at existing building components. Fluid viscous dampers and friction dampers have also been used to mitigate the pounding effects in adjacent buildings [41]. Pargoo et al. [42] suggested implementing viscous wall dampers in adjacent structures to reduce the pounding-induced effects.

Many studies have indicated that the most efficient method of preventing pounding is to leave a sufficient gap between the buildings or to upgrade the stiffness of the structural system by introducing structural walls in order to minimize the structural displacements to avoid pounding. The adequacy of the proposed retrofitting methods in terms of preventing pounding phenomenon includes several uncertainties such as the approximations in calculating the inelastic displacements. However, there is no retrofitting method or published study for preventing pounding-induced structural damage for existing buildings that have already been constructed without sufficient seismic joint, and where pounding is

unavoidable. This study aims to minimize the seismic damage caused by pounding on existing RC structural elements in cases where collision is unavoidable. For this purpose, existing adjacent RC buildings are retrofitted with steel columns and neoprene rubber pads which are added to the existing structural system of buildings. Therefore, pounding will take place between the added steel columns and the slab of the adjacent building. By this retrofitting approach, existing RC columns can be protected by diverting the collision to the steel columns. Then the pounding forces will be transferred from the pin connected steel columns to the slabs, whose in-plane capacity is the largest compared to the capacity of any other structural component of the exiting substandard RC buildings. Like the capacity design principles adopted in the seismic design of buildings, the proposed retrofitting approach receives use of the capacity of the strongest link, which is the in-plane capacity of slabs, in the existing substandard RC building when pounding takes place.

2. PROPOSED RETROFITTING METHOD

The proposed retrofitting approach is intended to prevent column damage when pounding is unavoidable. In order to protect the existing RC columns from pounding effects, steel columns are placed at each story of the buildings by partially removing the infill wall and pounding is ensured in these elements instead of existing substandard RC columns. Steel columns added to the structural system of the buildings are shown in Fig. 2. The additional steel columns are placed such that the pounding first takes place with them by extending steel beam elements at the pounding level. Therefore, added steel columns by means of the proposed retrofitting approach can only be effective in the case of floor-to-column pounding.

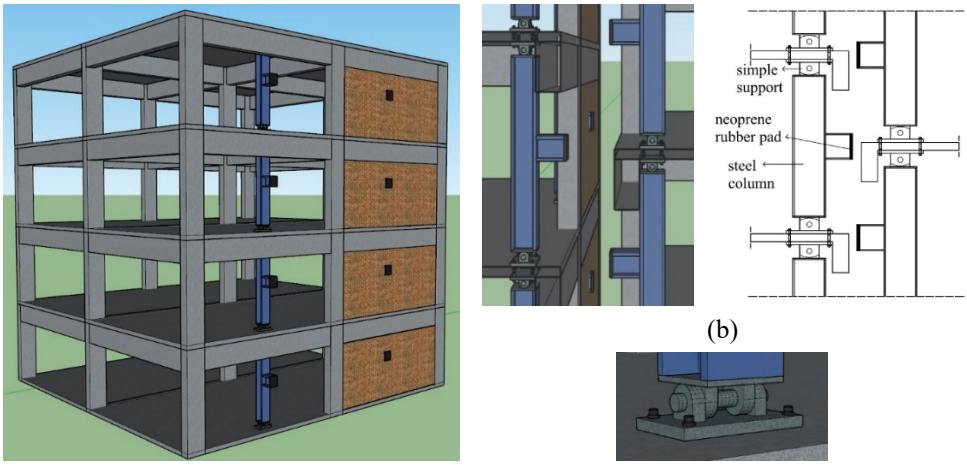

Fig. 2 - (a) Proposed retrofitting method, (b) sectional view of columns, (c) connection detail.

The steel columns are connected to the floor with a simple support at both ends (Fig. 2(c)). With this connection detail, only axial loads are transferred to the floors where the steel column is supported. The floors that have very high in-plane stiffness and capacity distribute the impact forces to the vertical structural members in accordance with their stiffness. Furthermore, neoprene rubber pads are placed on the steel columns to provide additional damping in the system during the collision and to prevent local damage that may occur on steel columns and the concrete slab.

3. BUILDING FEATURES AND MODELING

3.1. Properties of Adjacent Buildings

Low and mid-rise RC buildings constitute a significant portion of Turkey's existing building stock. Therefore, the study focused on 4- and 7-story RC buildings that represent typical members of the existing building stock. Building models are determined from an inventory study that is investigated about 500 RC buildings by Inel et al. [43]. 4- and 7-story buildings are designed according to previous seismic codes. The reason for selecting these two RC buildings is that the pounding phenomenon can take place due to their different dynamic characteristics ensuring that their vibration modes will not be in phase and pounding can take place in between.

Buildings have RC frame system constituted by beams and columns with no structural wall. Plan view of ground story for both buildings is shown in Fig. 3. In both buildings, the sizes of the structural system elements are smaller at the upper floors. The column and beam dimensions of 4- and 7- story buildings are given in *Table 1*.

4-story building has a total length of 15 m in the x-direction, 10 m in the y-direction. 7-story building has a total length of 19.5 m in the x-direction, 13 m in the y-direction. Story heights in both building models are 2.8 m. In the design of both buildings, as per TBEC-2018, the importance factor of both buildings and the soil class is taken as “1” and ZC (very dense sand, gravel, or very stiff clay), respectively.

Concrete compressive strength of both building models is 16 MPa. Nominal yield strength of both longitudinal and transverse reinforcements of 4- and 7-story buildings are 420 MPa and 220 MPa, respectively.

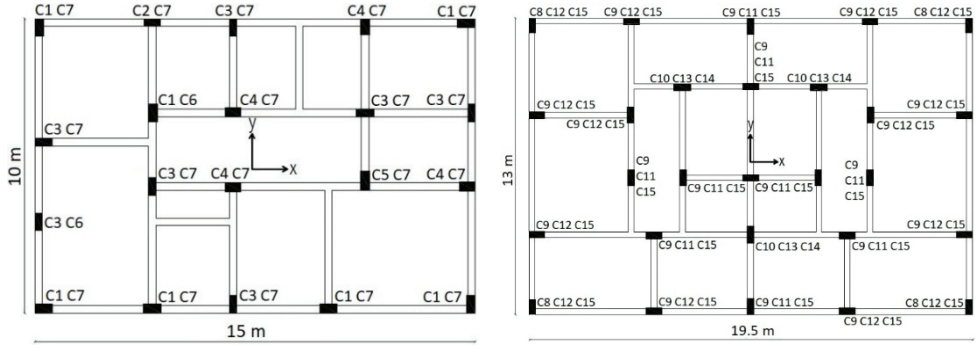

(a) (b)

Fig. 3 - Plan view of ground story for buildings (a) 4-story, (b) 7-story.

Table 1 - The column and beam sizes of 4- and 7- story buildings.

Building model	Story level	Column label	Column size (cm)	Beam size (cm)
4-story	from 1 to 2	C1	30×60	25×60
		C2	25×55	
		C3	25×60	
		C4	30×55	
		C5	30×65	
	from 3 to 4	C6	25×50	
		C7	25×55	
7-story	from 1 to 2	C8	30×65	25×60
		C9	30×70	
		C10	30×75	
	from 3 to 4	C11	30×60	
		C12	25×60	
		C13	30×70	
	5	C11	30×60	25×50
		C12	25×60	
		C13	30×70	
	from 6 to 7	C14	30×60	
		C15	25×50	

Steel columns that are placed in the mid-bays on the collision surface of RC buildings are made of S235 (structural steel with a nominal yield strength of 235 MPa). Columns section is HE500M of standard European sections. Neoprene rubber pads have dimensions of 200×200×25 mm. The nominal hardness of the rubber bearings is 60 on the Shore A scale, which has the shear modulus, G of 1.1 MPa. The design of all components of the retrofitting scheme including the connection details to the RC slab is made such that they will not be exposed to any seismic damage under the impact forces during collision.

3.2. Nonlinear Modeling of Buildings

Three dimensional numerical models are developed for both buildings in SAP2000 [44]. The base of the columns is assumed to be fully restrained. Slabs are considered to be rigid diaphragms for the in-plane behaviour due to their larger cross-sectional area. The rigid diaphragm constraint is employed to reflect this behaviour of the slabs. In the nonlinear calculation method, effective stiffness coefficient values used for cracked sections of reinforced concrete sections are considered as per TBEC-2018.

Plastic hinges have been defined at both ends of columns and beams in reflecting non-linear behaviour in building models. P-M2-M3 plastic hinge is assigned for columns to consider the interaction between bi-axial flexure and normal force, whereas M3 plastic hinge is employed for beams. User-defined hinge properties are used in this study. The moment-plastic rotation relationship of the plastic hinges defined in the SAP2000 is given in Fig. 4. 'A', 'B', 'C', 'D', and 'E'. Moment-rotation relation of each plastic hinge are determined according to section geometry, material properties of reinforcement steel, confined and unconfined concrete, and axial load level on the RC members.

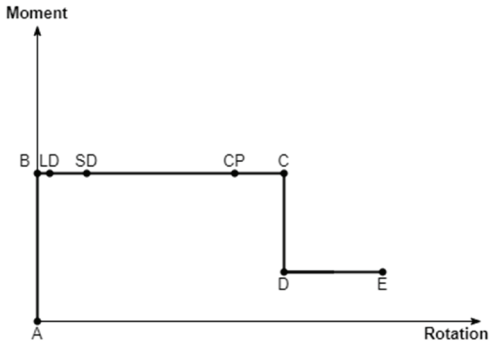

Fig. 4 - Moment-rotation relationship of the plastic hinge.

Mander's model is selected for concrete material models to define unconfined concrete and confined concrete [45]. Modulus of elasticity of concrete is taken as 20000 MPa according to TBEC-2018 for concrete class C16. The strain corresponding to the maximum strength of unconfined concrete is 0.002, the crushing strain is 0.0035, and the spalling strain is 0.005. The characteristics of the confined concrete model vary depending on the cross-sectional characteristics of the RC members and the detailing of the longitudinal and transverse reinforcement.

Two different grades of steel, which are S420 and S220, have been considered. Modulus of elasticity of reinforcement steel is taken as 200000 MPa. Yield strength, ultimate strength, failure strain, and yield strain values are given in *Table 2*.

Table 2 - Mechanical properties of reinforcement.

Reinforcement class	Yield Strength (MPa)	Ultimate Strength (MPa)	Yield Strain, ε_y	Failure Strain, ε_{su}
S220	220	264	0.0011	0.12
S420	420	550	0.0021	0.08

The moment-curvature relationship of the RC members is obtained using the cross-section analysis conducted in XTRACT [46]. The obtained moment-curvature values are used in the definition of plastic hinges to be lumped at critical sections of RC members. P-M2-M3

interaction and M3 hinges are assigned at the ends of columns and beams, respectively to identify the attainment of their capacities during the nonlinear analysis. The performance limits of Limited Damage (LD), Significant Damage (SD), and Collapse Prevention (CP) for the flexural hinges are specified from section analysis and the requirements of TBEC-2018. *Table 3* shows the damage levels for flexural response in terms of material strains specified in TBEC-2018. In the definition of moment-rotation relation, the plastic hinge length is considered to be the half of the section depth ($L_p = H/2$) as recommended in TBEC-2018.

Table 3 - Strain based damage levels as per TBEC-2018.

Damage Levels	Concrete Limit Condition	Steel Limit Condition
Limited Damage (LD)	$\varepsilon_c^{LD} = 0.0025$	$\varepsilon_s^{LD} = 0.0075$
Significant Damage (SD)	$\varepsilon_c^{SD} = 0.75\varepsilon_c^{CP}$	$\varepsilon_s^{SD} = 0.75\varepsilon_s^{CP}$
Collapse Prevention (CP)	$\varepsilon_c^{CP} = 0.0035 + 0.04\sqrt{\omega_{we}} \leq 0.018$	$\varepsilon_s^{CP} = 0.40\varepsilon_{su}$

where ε_c is concrete compressive strain, ε_s is the steel strain and ε_{su} steel strain at the maximum tensile stress and ω_{we} is the ratio of mechanical reinforcement of the effective stirrup. ω_{we} is calculated according TBEC-2018 as;

$$\omega_{we} = \alpha_{se}\rho_{sh,min}\frac{f_{ywe}}{f_{ce}} \tag{1}$$

$$\alpha_{se} = \left(1 - \frac{\sum a_i^2}{6b_o h_o}\right)\left(1 - \frac{s}{2b_o}\right)\left(1 - \frac{s}{2h_o}\right) \quad ; \quad \rho_{sh} = \frac{A_{sh}}{b_k s} \tag{2}$$

where α_{se} is the efficiency coefficient of transverse reinforcement, ρ_{sh} is volumetric ratio of transverse reinforcement, $\rho_{sh,min}$ is the minimum of the volumetric ratio of the transverse reinforcement in two horizontal directions, f_{ywe} is the yield strength of transverse reinforcement, f_{ce} is compressive strength of concrete, α_i is lateral distance between the axes of the longitudinal bars, which are supported by the transverse reinforcement, b_o and h_o are size of the cross-section between the axes of the transverse reinforcement of core concrete, s is the spacing of transverse reinforcement, A_{sh} is area of transverse reinforcement for rectangular section, b_k is cross section dimension of concrete core of column (distance between the centers or outermost rebars).

Shear hinges are also assigned to each frame member to determine whether its shear capacity has been attained during the analysis. Due to its brittle nature, only ultimate state limit is specified for the shear hinges assigned at the mid-span of the members to distinguish the shear hinges with the flexural hinges.

Flexural and shear hinges are assigned to steel columns placed on the pounding surface. In this way, the demands that will occur on the steel column are monitored. Plastic moment strength (M_p) and nominal shear strength (V_n) of steel columns are calculated according to Turkish Structural Steel Code [47] as follows;

$$M_p = F_y W_{px} \tag{3}$$

$$V_n = 0.6 F_y A_w C_{v1} \tag{4}$$

where F_y is the yield strength of structural steel, W_{px} is the plastic section modulus about x-axis, A_w is the area of the web, C_{v1} is the web shear strength coefficient, which is 1.0.

3.3. Examined Pounding Cases

Although there are buildings adjacent to the neighbouring building having the same floor elevations, the majority of the existing buildings are adjacent to the neighbouring building with different floor elevations. In this case, pounding takes place between the floor of one building and the columns of the other building. Story heights of both building models are 2.8 m. One of the buildings is moved in vertical direction in the numerical model so that pounding occurs in the mid-height of the columns. Slab-to-column collision models are established by connecting building models with link elements. Then, slab-to-steel column collision model is established by placing the steel columns in the mid-bays on the collision surface of 4-story and 7-story buildings. Moreover, individual 4-story and 7-story buildings where no pounding takes place are also examined for comparison purposes. Pounding models and link elements are presented in *Fig. 5*.

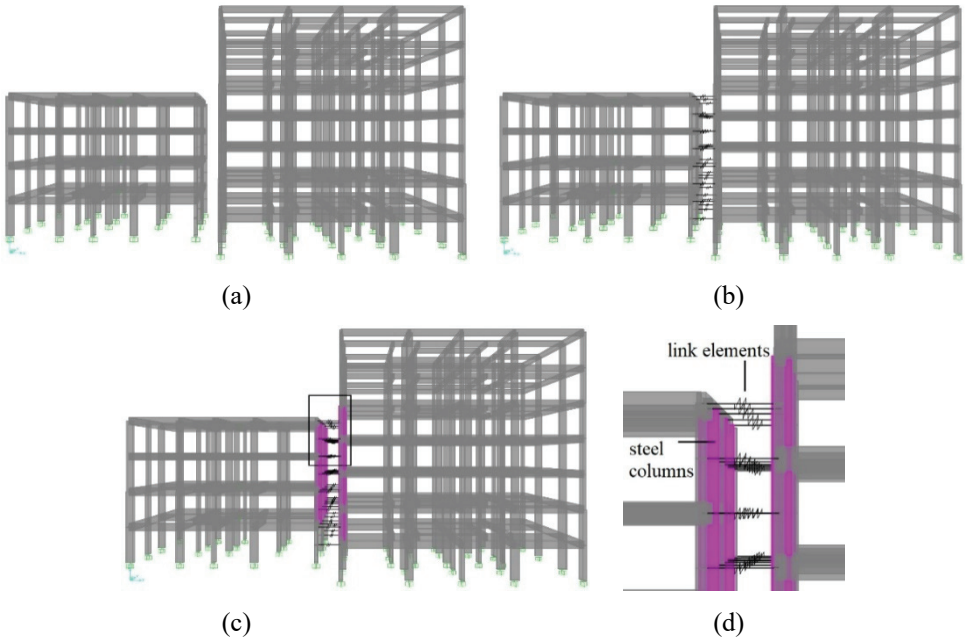

Fig. 5 - Pounding cases for (a) no collision, (b) pounding model of non-retrofitted buildings, (c) pounding model of retrofitted buildings, (d) link elements.

Several impact models are used to simulate the pounding between colliding buildings in literature [48–50]. Because of its simplicity and ease, the linear elastic spring model is commonly used in previous studies. In the linear elastic spring model, linear spring with a high stiffness is used to simulate impact once the gap between adjacent buildings closes. The spring is only activated when the calculated relative distance in the closing direction is greater or equal to the specified gap distance. In such a case, pounding takes place and spring stiffness becomes effective. The force-displacement relationship of a link element is shown in Fig. 6.. The impact force *F(t)*, based on linear elastic spring model is determined as follows;

$$F(t) = \begin{cases} k(\delta(t) - d), & \delta(t) - d > 0 \\ 0, & \delta(t) - d \leq 0 \end{cases} \tag{5}$$

$$\delta(t) = u_j(t) - u_i(t) \tag{6}$$

where k is the stiffness of the spring, $\delta(t)$ is the depth of interpenetration, $u_j(t)$ and $u_i(t)$ are the displacements of the two adjacent buildings and d is the gap distance.

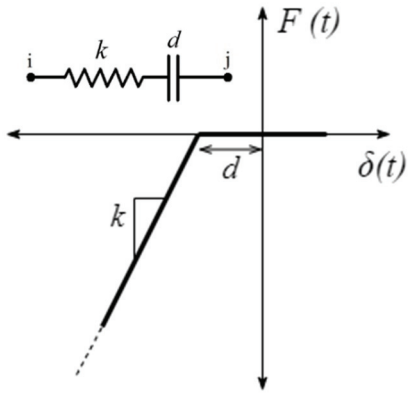

Fig. 6 - Force-displacement relationship for linear elastic spring model

The impact model is simulated by using nonlinear link element in SAP2000. When the gap distance closes during motion, the axial stiffness of the slab triggers in the stiffness matrix. The axial stiffness of the building's floor slab in the pounding direction is used to calculate the stiffness of the link element. The stiffness of link elements (k) is recommended to be greater than the axial stiffness of the slab of the adjacent buildings [30,51,52]. Based on the study of Altınel [53], the stiffness for the link elements is chosen as 35 times the axial stiffness corresponding to the effective area on the slab section where the pounding takes place. Hence k is calculated as;

$$k = \frac{EA}{L} \times 35 \tag{7}$$

where E is the modulus of elasticity of concrete, A is the effective cross-sectional area of the slab, L is the length of the slab in the direction perpendicular to the contact surface.

The gap distance between the adjacent buildings is defined in the link element. If pounding occurs, the gap distance is critical in the seismic response of both buildings. Although gap distance is variable in existing buildings, a constant gap distance of 40 mm is selected in this study to reflect an insufficient gap distance specified by TBEC-2018 to observe pounding. In order to make consistent comparisons, the same gap distance, 40 mm, is also considered in the retrofitted buildings, which includes steel columns and neoprene rubber pads. However, in real life applications of the proposed retrofitting approach, the additional steel column and neoprene rubber pad reduce the gap between the existing adjacent buildings.

The link elements defined in SAP2000 are used to model the neoprene rubber pad that will be added to the collision surface of the steel columns. The neoprene rubber pad is modeled as a spring connected in series to the link element. The axial stiffness of neoprene rubber pads adopted from Naeim and Kelly [54] calculated as follows:

$$K_v = \frac{E_c A}{t_r} \tag{8}$$

$$E_c = 6.73GS^2 \tag{9}$$

$$S = \frac{a}{4t} \tag{10}$$

where K_v is axial stiffness, E_c is elasticity modulus, A is the area of neoprene pad, t_r is the neoprene pad thickness, G is shear modulus, S shape factor, a is the side dimension of the square pad.

4. GROUND MOTION SELECTION AND SCALING

Real ground motion records obtained during earthquakes are used in nonlinear time history analyses. Recorded ground motions are selected and scaled with respect to the requirements of TBEC-2018. TBEC-2018 requires the selection of a minimum of 11 ground motion recordings, where at most three ground motion records can be selected from the same earthquake event. The selected ground motion records are scaled such that the average of the response spectra values should be greater than the ordinates of the TBEC-2018 target spectrum between the period range $0.2T_p$ and $1.5T_p$, where T_p is the natural period of the building model.

In this study, the PEER (Pacific Earthquake Engineering Research) strong ground motion database has been used for selecting the ground motion records (https://ngawest2.berkeley.edu/). Table 4 shows the main characteristics of the selected earthquake records. Since the analyses is performed along the x axis where the pounding takes place, only one of the horizontal components of the earthquakes is used. The component with the highest PGV value is chosen.

Table 4 - The properties of the selected earthquake records.

Record No	Earthquake Name	Station	Magnitude	Component	PGA (g)	PGV (cm/s)	PGD (cm)
RSN-879	Landers	Lucerne	7.28	260°	0.73	133.40	113.92
RSN-821	Erzincan, Turkey	Erzincan	6.69	NS	0.39	107.14	31.99
RSN-180	Imperial Valley-06	El Centro Array #5	6.53	230°	0.38	96.90	75.22
RSN-529	N. Palm Springs	North Palm Springs	6.06	210°	0.69	65.99	16.17
RSN-1602	Duzce, Turkey	Bolu	7.14	90°	0.81	65.88	13.10
RSN-959	Northridge-01	Canoga Park - Topanga Can	6.69	196°	0.39	63.29	13.17
RSN-183	Imperial Valley-06	El Centro Array #8	6.53	140°	0.61	54.49	41.78
RSN-1052	Northridge-01	Pacoima Kagel Canyon	6.69	360°	0.43	51.38	7.22
RSN-767	Loma Prieta	Gilroy Array #3	6.93	90°	0.37	45.43	24.11
RSN-727	Superstition Hills-02	Superstition Mtn Camera	6.54	135°	0.84	43.50	5.23
RSN-1165	Kocaeli, Turkey	Izmit	7.51	90°	0.23	38.29	24.29

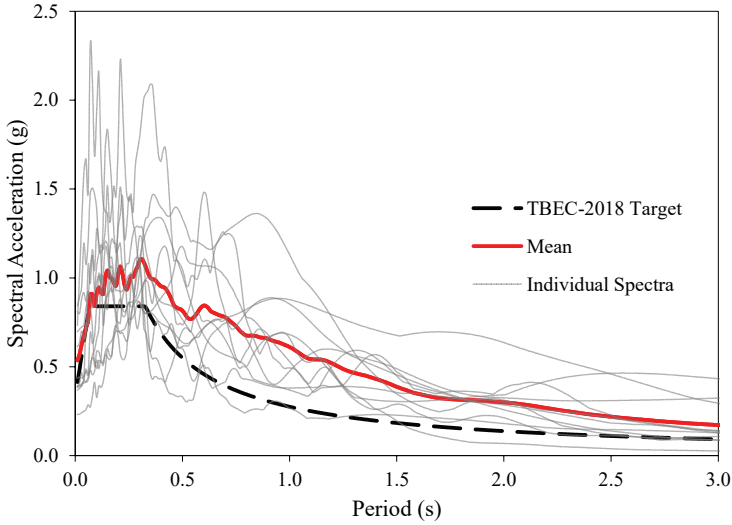

Fig. 7 - Elastic response spectra of the selected ground motion records.

The target design spectrum is defined by considering the coordinates, the soil type, and the earthquake ground motion level of the buildings. This information is used in the seismic hazard map of Turkey (https://tdth.afad.gov.tr) to obtain the design spectrum for the

investigated buildings. The target design spectrum corresponds to the seismic hazard level (DD-2) with 10 percent probability of exceedance in 50 years in TBEC-2018 for the specific location in Eskişehir city center with latitude coordinate of 39.763946°N and longitude coordinate of 30.514724°E. The soil type is ZC (very dense sand, gravel, or very stiff clay). *Fig. 7* shows the elastic response spectra of the selected ground motion records with a damping ratio of 5 percent. As shown in *Fig. 7*, since the average response spectrum is greater than the considered target design spectrum, the scale factor is taken as "1" for all earthquake records satisfying the criteria specified by TBEC-2018. Therefore, original ground motion records are employed in the analyses without interfering with their content.

5. ANALYSIS RESULTS AND DISCUSSION

Nonlinear response history analyses are performed for four numerical models using the selected 11 earthquake ground motion records. Four numerical models are composed of two individual numerical models of 4-story and 7-story buildings termed as "reference", pounding model of the existing adjacent buildings termed as "non-retrofitted", and finally pounding model of the retrofitted adjacent buildings termed as "retrofitted". Pounding forces, peak floor accelerations, inter-story drift ratios, and story shear force distributions obtained from the nonlinear time history analysis are recorded. The response of the original buildings and retrofitted buildings with steel columns are compared based on the selected engineering demand parameters. Comparisons are made for the average results of the selected 11 ground motion records for each of the numerical models. Plastic hinge distribution caused by the pounding effects of both buildings is also investigated for a specific ground motion record.

5.1. Pounding Forces

When the specified gap between the two buildings closes, the stiffness of the link elements activate and pounding forces develop in the link elements. Thus, the time and the pounding force can be determined for each link element when the collision occurs. Fig. 8 shows the variation of the pounding forces in both retrofitted and non-retrofitted models for the two ground motion records. In the retrofitted model, collision occurred at each floor in all earthquake ground motion records. Pounding took place only on the steel columns. There was no collision in the existing RC columns. The pounding-induced demands were prevented from being accumulated at a specific floor level by distributing the pounding effects throughout the building height by the applied retrofitting technique. As a result, a relatively more uniform distribution of pounding-induced seismic effects is ensured throughout the floors of the retrofitted building compared to the non-retrofitted one. Pounding forces reduce at the lower floors of the retrofitted building as a result of the decreasing displacement demands at the lower stories. The pounding forces are much greater in the non-retrofitted building. On the fourth floor of non-retrofitted building, pounding force was 3.13 times greater for Imperial Valley Earthquake record. The largest pounding forces took place on the fourth floor of both retrofitted and non-retrofitted buildings for Superstition Hills Earthquake record, which are almost the same. Seismic damage, on the other hand, is mostly localized in the fourth floor of the non-retrofitted building, resulting in brittle type shear failure in existing RC columns.

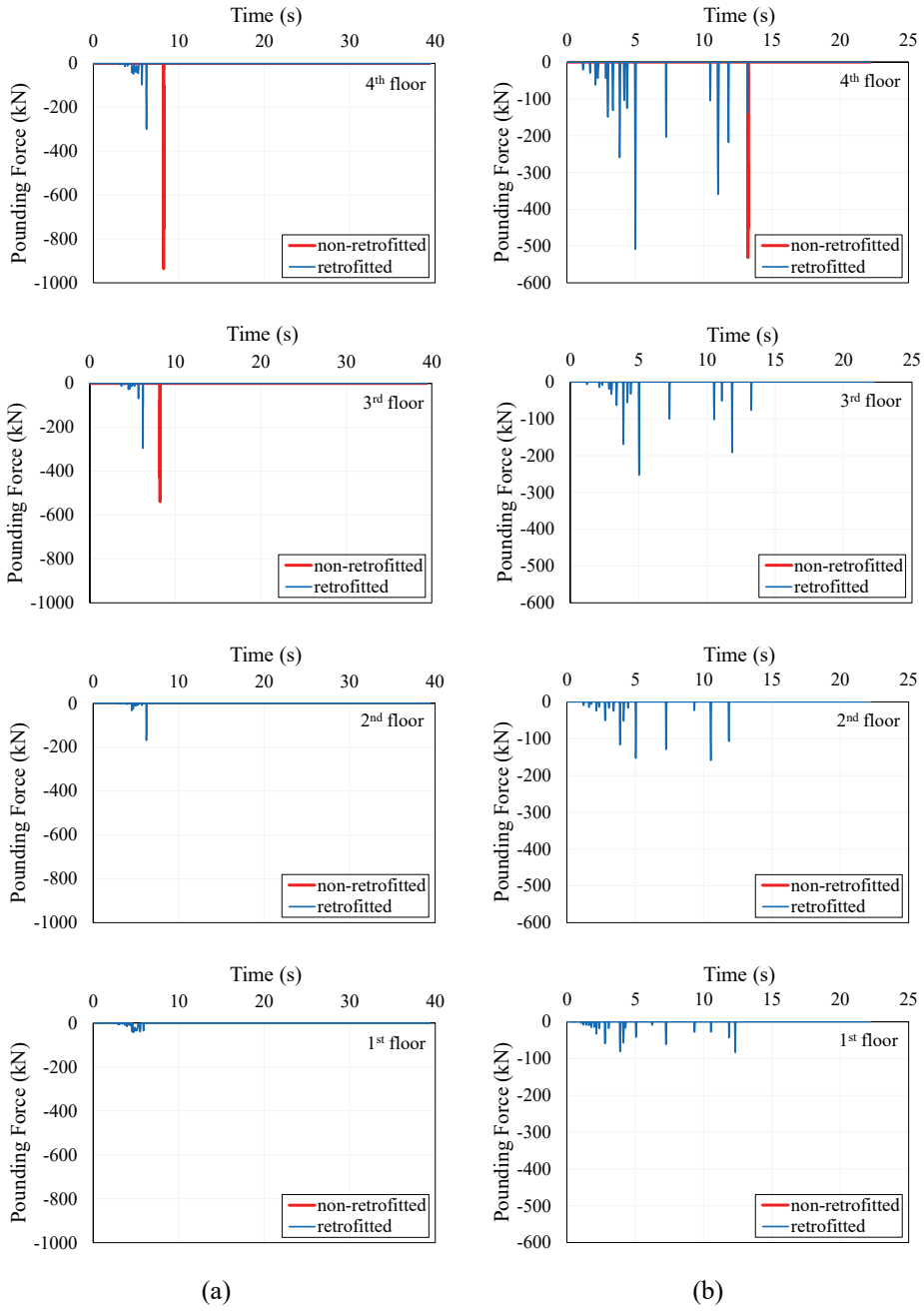

Fig. 8 - Variation of pounding forces at each floor (a) for Imperial Valley Earthquake record (Array #5), (b) for Superstition Hills Earthquake record.

5.2. Peak Floor Accelerations

Peak floor acceleration is an important engineering demand parameter for the safety of the building's contents and the comfort of its residents [55]. Peak floor acceleration values provide information about the seismic forces that will impose on the structural and nonstructural components. Fig. 9 shows the average peak acceleration values at each floor for all pounding models. For both buildings, pounding increases the floor accelerations at each floor. In 4-story building, the maximum average peak floor acceleration values of pounding models occurred in fourth floor of the building due to larger displacements. The maximum peak floor acceleration in retrofitted building is less than that in non-retrofitted building. In 4-story building, the maximum peak floor acceleration of the retrofitted and non-retrofitted building is 1.72 and 2.08 times larger than the reference building, respectively. In 7-story building, the maximum peak floor acceleration of the retrofitted and non-retrofitted building is 1.69 and 1.94 times larger than the reference building, respectively. In general, the pounding takes place in all floors of the retrofitted buildings. However, in non-retrofitted buildings, the pounding localized mostly in a single floor where the pounding first takes place. Because the pounding demands are distributed throughout the retrofitted models rather than localized in one floor as in the case of non-retrofitted building, the floor accelerations of retrofitted building are lower than the ones for non-retrofitted building. There is a jump even in the average peak floor accelerations at the fourth floor of both 4-story and 7-story non-retrofitted buildings. As also observed in the pounding force variations in *Fig. 8*, pounding took place mostly in the fourth floor only for the non-retrofitted building. This caused the localization of pounding effects at the fourth floor of both non-retrofitted buildings. On the other hand, as the pounding occurred in all floors of the retrofitted models, there is no distinct jump in the average peak floor acceleration values.

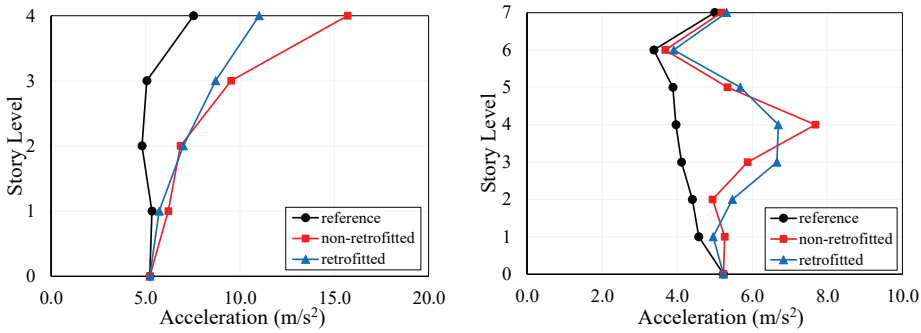

Fig. 9 - Average peak floor accelerations for buildings (a) 4-story, (b) 7-story.

5.3. Inter-Story Drift Ratios

Inter-story drift ratio (ISDR), a fundamental indicator for seismic damage for structural and non-structural components, plays a critical role in structural performance. During an earthquake, if the ISDR is excessive, both structural and non-structural components will be damaged. Thus, the ISDR is restricted to a certain limit in building design codes in order to

protect the components of the buildings. Fig. 10 shows the variation of ISDR in 4- and 7-story buildings.

The effect of pounding on the variation of ISDR is not as pronounced as in the case of peak floor acceleration distribution. Compared to the reference 4-story building, the maximum increase in ISDRs at the fourth story of the retrofitted 4-story building is 21.8 percent, while it is 15.4 percent at the fourth story of the non-retrofitted 4-story building. Compared to the reference 7-story building, the maximum increase in ISDRs at the sixth story of the retrofitted 7-story building is 27.6 percent, while it is 15.0 percent at the sixth story of the non-retrofitted 7-story building. In retrofitted buildings, the increase in ISDR values is greater. Since pounding did not cause any brittle type of shear failure to the columns of the retrofitted building, retrofitted building has more ductile behaviour and has more displacement capacity for additional displacement demands.

The maximum increase in ISDR occurs on the sixth story level of the 7-story building and the fourth story level of the 4-story building. When buildings collide, the floors below the fourth floor, where the pounding takes place, of the 7-story building have reduced ISDR than the reference building. The 4-story building reduces the displacement of the first 4 floors of the 7-story building. However, the floors above the pounding floor of the 7-story building displaced more by the impact of the post-collision. Thus, for the 7-story building, there is an increase in ISDRs at the floors above the pounding floor whereas the ISDRs are reduced in the floors below the pounding floor. This response is clearly observed in *Fig. 10*(b) referred as the whiplash effect, which causes changes in the displacements below and above the pounding floor [2,11,56]. On the other hand, ISDR of the 4-story reference building is less than the others when the pounding takes place. In both 4-story and 7-story buildings, the retrofitted buildings have increased ISDR values at each story than the non-retrofitted buildings. When the brittle type of RC column shear failure is prevented by the introduction of steel columns for retrofitting purposes, the overall behaviour mode of the buildings is dominated by the flexural response of the columns.

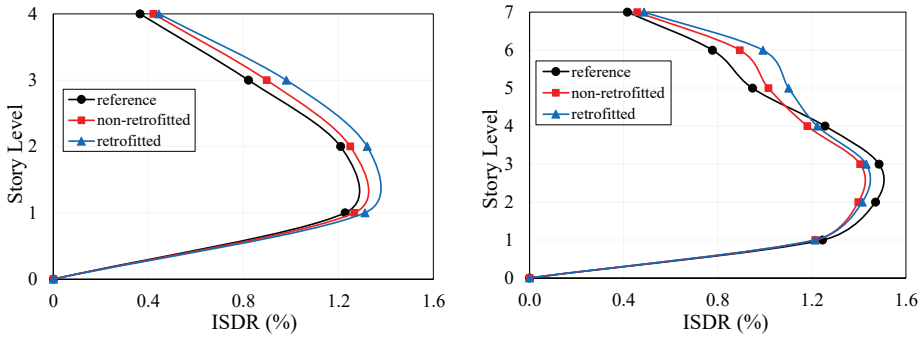

Fig. 10 - Average ISDR distribution for buildings (a) 4-story, (b) 7-story.

5.4. Story Shear Force

Maximum story shear force distributions are given in *Fig. 11* for the two buildings. The presented average values are the peak value of the sum of the shear forces in the vertical structural elements at each story under each earthquake record. The increase in the story shear force is evident at the stories above and below the pounding level. In the 7-story building, the increase in the shear forces at the floor above the pounding elevation is obvious due to whiplash effect. The maximum increase in the story shear force of the retrofitted 4-story building is 36.2 percent at the fourth story, while it is 43.6 percent in the non-retrofitted 4-story building. The maximum increase in the story shear force of the retrofitted 7-story building is 22.2 percent at the fifth story, while it is 13.2 percent in the non-retrofitted 7-story building. Story shear forces have increased in retrofitted buildings. This is due to the fact that pounding has not caused shear damage to existing RC columns with the addition of steel columns for retrofitting purposes. Thus, the displacement of the columns increases so does the shear force demands in the columns.

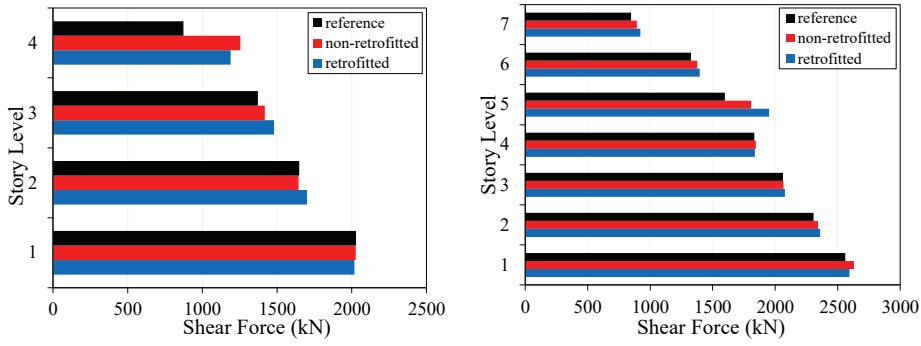

Fig. 11 - Average story shear force distributions for the buildings (a) 4-story, (b) 7-story.

5.5. Plastic Hinge Distributions

Plastic hinge distribution is examined under the Erzincan Earthquake ground motion record where the greatest pounding force occurs among the other selected records. Plastic hinge distributions of the buildings are presented in Fig. 12. Damage state of the assigned plastic hinges is determined according to the colored scale shown on the right side of Fig. 12. On the colored scale, “B” is the beginning of nonlinear behaviour and “E” is the ultimate point, beyond which the member failure takes place. (IO) corresponds to the limited damage, (LS) corresponds to the significant damage, and (CP) corresponds to collapse prevention limit states in TBEC-2018. Pounding significantly changes the plastic hinge distribution of both buildings. There is an increase in the number of damaged column and beam members at the upper floors of the buildings after pounding.

When Fig. 12 (b) and (c) are compared with Fig. 12 (a), it is observed that the plastic rotation demands in ground story beams and columns of 4-story building have increased, whereas the plastic rotation demands in ground story beams and columns of 7-story building have decreased. This result is consistent with the fact that pounding causes an increase in the

ISDRs of 4-story building and a decrease in the ISDRs of a 7-story building below the pounding floor as shown in Fig. 10.

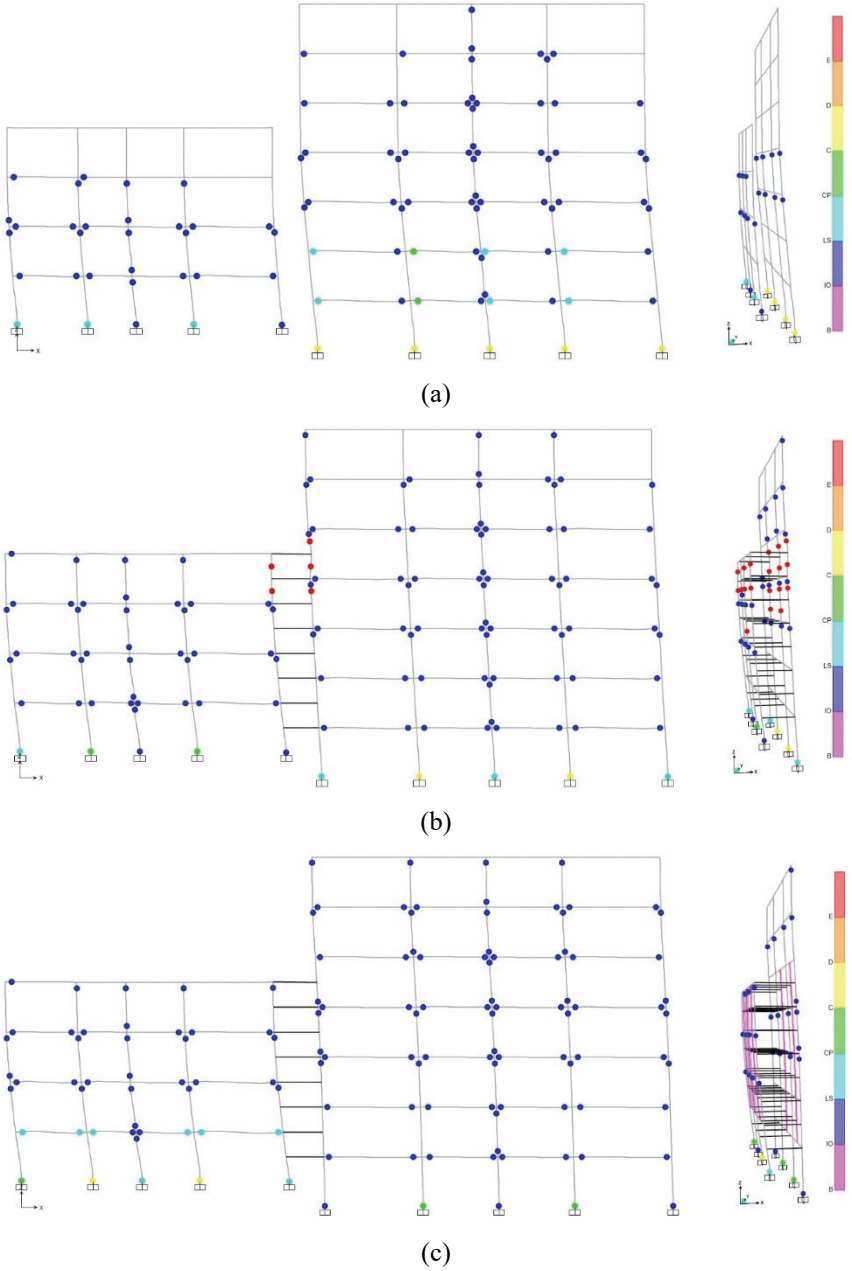

Fig. 12 - Plastic hinge distribution for the Erzincan Earthquake record (a) reference buildings, (b) non-retrofitted buildings, (c) retrofitted buildings.

As shown in Fig. 12 (b), shear failure in several columns of the non-retrofitted buildings has been observed at the stories where pounding takes place. In the retrofitted building, although the pounding takes place in each story, no shear failure is observed in the added steel columns or in the existing RC columns. Therefore, by introducing steel columns for retrofitting purposes, the existing RC columns are protected from any brittle type of shear failure. This leads to more ductile behaviour with increased ISDRs, and plastic rotation demands in the lower stories. Therefore, the detrimental effects of collision between adjacent buildings are minimized and the overall seismic response of the buildings is improved by eliminating the column shear failures.

6. CONCLUSIONS

In this paper, the effectiveness of the proposed retrofitting strategy for protecting existing RC columns against pounding effects has been investigated. Firstly, 3D numerical models of the 4- and 7-story RC buildings representing the existing building stock are developed in SAP2000 program. Then, steel columns with neoprene rubber pads were introduced in the retrofitted buildings. Nonlinear time-history analyses were conducted with 11 different real ground-motion records. The variations in pounding force, peak floor accelerations, ISDRs, story shear forces, plastic hinge distributions are examined for all pounding cases. The analysis results for each engineering demand parameter are compared for reference buildings, non-retrofitted buildings, and retrofitted buildings. Following conclusions were drawn based on the results of this study:

- With the introduction of steel columns in retrofitted buildings, pounding takes place in each story with reduced pounding forces. This enables a relatively more uniform distribution in the pounding-induced seismic effects along the height of the building. Whereas, in the non- retrofitted building, pounding forces are much larger and the seismic damage is mostly localized in the pounding story causing brittle type of shear failure in RC columns.
- The peak floor accelerations are observed to be increased due to pounding. The increase in peak accelerations at floors with larger displacements is especially pronounced as a result of pounding. Because pounding demands are distributed throughout the retrofitted building, the increase in peak floor accelerations is less in retrofitted buildings compared to the non-retrofitted buildings. Distinct jumps in the average peak floor accelerations were observed in the non-retrofitted building as a result of localization of pounding in a single floor.
- The variation in the ISDR is not as significantly affected by pounding as it is in the case of peak floor accelerations. There is an increase in the ISDR of 4-story building with pounding. Because of the change in the dynamic response of the 7-story building, ISDRs have increased at floors above the fourth story, at which the pounding takes place. However, in the lower stories of the 7-story building, ISDRs have decreased due to pounding with the 4-story building.
- Story shear forces have been increased due to pounding. There is greater increase, particularly in the retrofitted building because the existing columns could resist more lateral force without shear damage. The largest increase of shear forces took place in

the pounding stories, which are the roof story of the 4-story building and the fifth story of the 7-story building.

- The distribution of plastic hinges is one of the most significant indicators for the effectiveness of the proposed retrofitting strategy against pounding. Pounding caused a significant change in the damage profile of the buildings with an increase in the number of damaged members. The shear capacity of RC columns in the non-retrofitted buildings was exceeded during collision, and shear failure was observed in several columns at the pounding elevation. The existing RC columns in the retrofitted building did not exhaust their shear capacity because no collision occurred in existing RC columns. Thus, pounding impact spread throughout the structural members. The proposed retrofitting method protects the existing RC columns from brittle type of shear failure as a result of pounding.

The results are valid only for the 4- and 7-storey buildings used in this study. The retrofitting method can be used by extending the findings to other buildings. Future studies can be extended to investigate the effectiveness of the proposed retrofitting approach for the adjacent buildings at which the collision can take place at different column elevations rather than the column mid-point as is the case in this paper.

Acknowledgments

This work was supported by The Scientific and Technological Research Council of Turkey (TÜBİTAK) [grant number 120M877]

References

[1] Maison BF, Kasai K. Analysis for a Type of Structural Pounding. J Struct Eng 1990; 116(4):957–77.

[2] Anagnostopoulos SA, Spiliopoulos KV. An investigation of earthquake induced pounding between adjacent buildings. Earthq Eng Struct Dyn 1992;21:289–302.

[3] TBEC-2018. Turkish Building Earthquake Code. Ankara, Turkey: 2018.

[4] Jeng V, Kasai K, Maison BF. A Spectral Difference Method to Estimate Building Separations to Avoid Pounding. Earthq Spectra 1992;8:201–23. https://doi.org/10.1193/1.1585679.

[5] Kamal M, Inel M. Simplified approaches for estimation of required seismic separation distance between adjacent reinforced concrete buildings. Eng Struct 2021:113610. https://doi.org/10.1016/j.engstruct.2021.113610.

[6] Favvata MJ. Minimum required separation gap for adjacent RC frames with potential inter-story seismic pounding. Eng Struct 2017;152:643–59. https://doi.org/10.1016/j.engstruct.2017.09.025.

[7] Kamal M, Code-based new approaches for determining the minimum required separation gap. Structures 2022;46:750-764. https://doi.org/10.1016/j.istruc.2022.10.075.

[8] Khatami SM, Naderpour H, Razavi SMN, Barros RC, Sołtysik B, Jankowski R. An ANN-Based Approach for Prediction of Sufficient Seismic Gap between Adjacent Buildings Prone to Earthquake-Induced Pounding. Applied Sciences 2020;10:3591. https://doi.org/10.3390/app10103591.

[9] Khatami SM, Naderpour H, Barros RC, Jankowski R. Verification of Formulas for Periods of Adjacent Buildings Used to Assess Minimum Separation Gap Preventing Structural Pounding during Earthquakes. Advances in Civil Engineering 2019:1–8. https://doi.org/10.1155/2019/9714939.

[10] Anagnostopoulos S. Building pounding Re-examined: How Serious a Problem Is It? Elev World Conf Earthq Eng Acapulco, Mex June 23-28, 1996 1996:Paper 2108.

[11] Karayannis CG, Favvata MJ. Earthquake-induced interaction between adjacent reinforced concrete structures with non-equal heights. Earthq Eng Struct Dyn 2005;34:1–20. https://doi.org/10.1002/eqe.398.

[12] Karayannis CG, Naoum MC. Torsional behavior of multistory RC frame structures due to asymmetric seismic interaction. Eng Struct 2018;163:93–111. https://doi.org/10.1016/j.engstruct.2018.02.038.

[13] Korkmaz SZ. Observations on the Van Earthquake and Structural Failures. J Perform Constr Facil 2015;29:04014033. https://doi.org/10.1061/(ASCE)CF.1943-5509.0000456.

[14] Rosenblueth E, Meli R. The 1985 Earthquake: Causes and Effects in Mexico City. Concr Int 1986;8(5):23–34.

[15] Kasai K, Maison BF. Building pounding damage during the 1989 Loma Prieta earthquake. Eng Struct 1997;19:195–207. https://doi.org/10.1016/S0141-0296(96)00082-X.

[16] Youd TL, Bardet JP, Bray JD. Kocaeli, Turkey, earthquake of August 17, 1999. Oakland, California: Earthquake Engineering Research Institute; 2000.

[17] Yurdakul Ö, Duran B, Tunaboyu O, Avşar Ö. Field reconnaissance on seismic performance of RC buildings after the January 24, 2020 Elazığ-Sivrice earthquake. Nat Hazards 2021;105:859–87. https://doi.org/10.1007/s11069-020-04340-x.

[18] Inel M, Ozmen HB, Akyol E. Observations on the building damages after 19 May 2011 Simav (Turkey) earthquake. Bull Earthq Eng 2013;11:255–83.

[19] Sharma K, Deng L, Noguez CC. Field investigation on the performance of building structures during the April 25, 2015, Gorkha earthquake in Nepal. Eng Struct 2016;121:61–74. https://doi.org/10.1016/j.engstruct.2016.04.043.

[20] Cole GL, Dhakal RP, Turner FM. Building pounding damage observed in the 2011 Christchurch earthquake. Earthq Eng Struct Dyn 2012;41:893–913. https://doi.org/10.1002/eqe.1164.

[21] Romão X, Costa AA,a , Paupério E, Rodrigues H, Vicente R, Varum H, Costa A. Field observations and interpretation of the structural performance of constructions after the 11 May 2011 Lorca earthquake. Eng. Fail. Anal. 2013;34:670-692. https://doi.org/10.1016/j.engfailanal.2013.01.040.

[22] Papadrakakis M, Mouzakis HP. Earthquake simulator testing of pounding between adjacent buildings. Earthq Eng Struct Dyn 1995;24:811–34. https://doi.org/10.1002/eqe.4290240604.

[23] Filiatrault A, Wagner P, Cherry S. Analytical prediction of experimental building pounding. Earthq Eng Struct Dyn 1995;24:1131–54. https://doi.org/10.1002/eqe.4290240807.

[24] Chau KT, Wei XX, Guo X, Shen CY. Experimental and theoretical simulations of seismic poundings between two adjacent structures. Earthq Eng Struct Dyn 2003;32:537–54. https://doi.org/10.1002/eqe.231.

[25] Jankowski R. Earthquake-induced pounding between equal height buildings with substantially different dynamic properties. Eng Struct 2008;30:2818–29.

[26] Inel M, Cayci T, Kamal M, Altınel O. Structural Pounding of Mid-Rise RC Buildings During Earthquakes, Proceedings of the second European conference on earthquake engineering and semiology; 2014.

[27] Raheem SA, Fooly MY, Shafy AA, Abbas YA, Omar M, Latif MMSA, Mahmoud S. Seismic pounding effects on adjacent buildings in series with different alignment configurations. Steel and Composite Structures 2018;28(3):289-308.

[28] Raheem SEA, Fooly MY, Omar M, Zaher AKA. Seismic pounding effects on the adjacent symmetric buildings with eccentric alignment. Earthq Struct 2019;16(6):715-726.

[29] Raheem SEA, Alazrak T, AbdelShafy AG, Ahmed MM, Gamal YA. Seismic pounding between adjacent buildings considering soil-structure interaction. Earthquakes and Structures 2021;20(1): 55-70.

[30] Anagnostopoulos SA. Pounding of buildings in series during earthquakes. Earthq Eng Struct Dyn 1988;16:443–56.

[31] Rezavandi A, Moghadam AS. Experimental and Numerical Study on Pounding Effects and Mitigation Techniques for Adjacent Structures. Adv Struct Eng 2007;10:121–34. https://doi.org/10.1260/136943307780429752.

[32] Polycarpou PC, Komodromos P, Polycarpou AC. A nonlinear impact model for simulating the use of rubber shock absorbers for mitigation the effect of structural pounding during earthquakes. Earthq Eng Struct Dyn 2013;42:81–100. https://doi.org/10.1002/eqe.

[33] Sołtysik B, Falborski T, Jankowski R. Preventing of earthquake-induced pounding between steel structures by using polymer elements-experimental study. Procedia Eng 2017;199:278–83. https://doi.org/10.1016/j.proeng.2017.09.029.

[34] He J, Jiang Y, Xue Q, Zhang C, Zhang J. Effectiveness of Using Polymer Bumpers to Mitigate Earthquake-Induced Pounding between Buildings of Unequal Heights. Adv Civ Eng 2018;2018:1–14.

[35] Raheem SEA. Mitigation measures for earthquake induced pounding effects on seismic performance of adjacent buildings. Bull Earthquake Eng 2014;12:1705–1724. https://doi.org/10.1007/s10518-014-9592-2.

[36] Anagnostopoulos SA, Karamaneas CE. Use of collision shear walls to minimize seismic separation and to protect adjacent buildings from collapse due to earthquake-induced pounding. Earthq Eng Struct Dyn 2008;37:1371–88.

[37] N.K. A, Neeraja N. Evaluation of Seismic Pounding between Adjacent Buildings. Int J Innov Res Sci Technol IJIRST 2016;3:138–47. https://doi.org/10.15224/978-1-63248-105-4-24.

[38] Noman M, Alam B, Fahad M, Shahzada K, Kamal M. Effects of pounding on adjacent buildings of varying heights during earthquake in Pakistan. Cogent Eng 2016;3:1225878. https://doi.org/10.1080/23311916.2016.1225878.

[39] Jankowski R, Mahmoud S. Linking of adjacent three-storey buildings for mitigation of structural pounding during earthquakes. Bull Earthq Eng 2016;14:3075–97. https://doi.org/10.1007/s10518-016-9946-z.

[40] Abdel-Mooty MAN, Ahmed NZ. Pounding Mitigation in Buildings using Localized Interconnections. Adv Struct Eng Mech (ASEM17), 28 August-1 Seprember, 2017, Ilsan (Seoul), Korea 2017.

[41] Nishath PV, Abhilash PP. Mid-Column Pounding Effects On Adjacent Tall Buildings and Its Mitigation Using Viscous Dampers and Friction Dampers. Int J Sci Eng Res 2017;8:168–73.

[42] Pargoo NS, Hejazi F, Jabbar S. Preventing Seismic Pounding of Adjacent Structures Using Viscous Wall Damper Device. GCEC 2017 Proc. 1st Glob. Civ. Eng. Conf., 2019, p. 561–77. https://doi.org/10.1007/978-981-10-8016-6_44.

[43] Inel M, Ozmen HB, Şenel ŞM, Kayhan AH. Mevcut Betonarme Binaların Yapısal Özelliklerinin Belirlenmesi. International Earthquake Symposium of Sakarya, Turkey 2009 [in Turkish].

[44] SAP2000. Integrated Finite Element Analysis and Design of Structures. Bekeley (CA, USA): Computer and Structures Ins.

[45] Mander JB, Priestley MJN, Park R. Theoretical Stress-Strain Model for Confined Concrete. J Struct Eng 1988;114:1804–25.

[46] XTRACT. Cross Sectional Analysis of Components, Imbsen Software System. Sacramento.

[47] Çelik Yapıların Tasarım, Hesap ve Yapım Esaslarına Dair Yönetmelik. Ministry of Environment and Urban Planning, Ankara, Turkey 2018.

[48] Anagnostopoulos SA. Equivalent viscous damping for modeling inelastic impacts in earthquake pounding problems. Earthq Eng Struct Dyn 2004;33:897–902. https://doi.org/10.1002/eqe.377.

[49] Jankowski R. Non-linear viscoelastic modelling of earthquake-induced structural pounding. Earthq Eng Struct Dyn 2005;34:595–611. https://doi.org/10.1002/eqe.434.

[50] Muthukumar S, DesRoches R. A Hertz contact model with non-linear damping for pounding simulation. Earthq Eng Struct Dyn 2006;35:811–28. https://doi.org/10.1002/eqe.557.

[51] Naserkhaki S, Abdul Aziz FNA, Pourmohammad H. Parametric study on earthquake induced pounding between adjacent buildings. Struct Eng Mech 2012;43:503–26. https://doi.org/http://dx.doi.org/10.12989/sem.2012.43.4.503503.

[52] Jameel M, Saiful Islam ABM, Hussain RR, Hasan SD, Khaleel M. Non-linear FEM analysis of seismic induced pounding between neighbouring Multi-storey Structures. Lat Am J Solids Struct 2013;10:921–39.

[53] Altınel O. Investigation of Pounding Effects on Seismic Performance of Existing Sequential Buildings. MSc Thesis. Pamukkale University. Denizli, Turkey 2015 [in Turkish]

[54] Naeim F, Kelly JM. Design of seismic isolated structures: from theory to practice. John Wiley & Sons, Inc; 1999.

[55] Çerçevik AE, Avşar Ö, Dilsiz A. Optimal Placement of Viscous Wall Dampers in RC Moment Resisting Frames Using Metaheuristic Search Methods. Engineering Structures 2021;249:113108. https://doi.org/10.1016/j.engstruct.2021.113108.

[56] Naserkhaki S, El-Rich M, Abdul Aziz FNA, Pourmohammad H. Pounding between adjacent buildings of varying height coupled through soil. Struct Eng Mech 2014;52:573–93. https://doi.org/10.12989/sem.2014.52.3.573.

Turkish Journal of Civil Engineering, 2024 71-94, Paper 770, ***Research Article***

Energy-Based Assessment of Liquefaction Behavior of a Non-Plastic Silt Based on Cyclic Triaxial Tests

Alper SEZER[1]
Çağlar KUMAŞDERE[2]
Nazar TANRINIAN[3]
Eyyüb KARAKAN[4*]

ABSTRACT

Earthquakes cause cyclic shear deformations in soil and build-up of excessive pore water pressure as a result of undrained loading, accompanied with rearrangement of soil particles and degradation in stiffness of the soil due to decrease in effective stresses. During loading, the onset of soil liquefaction is defined as a stress state in which the excess pore water pressure is equalized to the total stress. From this point of view, assessment of the pore water pressure development pattern under cyclic loading has been one of the most salient research topics in geotechnical and earthquake engineering. In this study, results of a series of cyclic triaxial tests on non-plastic silt specimens consolidated under 100 kPa effective isotropic consolidation pressure were used to question the modelling ability of pore pressure development models previously proposed for sands. Tests were performed on specimens of 6 different initial relative densities (D_r) ranging between 30-80% and 10 different cyclic stress ratios (CSR). The key parameters of pore water pressure development and shear deformation in the energy-based model used are relative density, cyclic stress ratio and number of cycles. The results revealed that, these energy-based models have a strong potential in evaluation of pore water pressure development pattern of non-plastic silts. Test results also show that the increase in relative density and decrease in CSR causes a ladderlike behavior among pore water pressure and cyclic shear strain, which is relevantly rendered by energy-based models.

Keywords: Pore water pressure, silt, cyclic triaxial tests, energy-based models.

Note:
- This paper was received on April 17, 2023 and accepted for publication by the Editorial Board on December 22, 2023.
- Discussions on this paper will be accepted by July 31, 2024.

• https://doi.org/10.18400/tjce.1283189

1 Ege University, Department of Civil Engineering, Izmir, Türkiye
alper.sezer@ege.edu.tr - https://orcid.org/0000-0002-2663-2028

2 Ege University, Department of Civil Engineering, Izmir, Türkiye
caglar.kumasdere@gmail.com - https://orcid.org/0000-0003-2133-6796

3 DNV France Sarl, Paris, France
ntanrinian@gmail.com - https://orcid.org/0000-0002-5929-0757

4 Kilis 7 Aralik University, Department of Civil Engineering, Kilis, Türkiye
eyyubkarakan@kilis.edu.tr - https://orcid.org/0000-0003-2133-6796

* Corresponding author

1. INTRODUCTION

It is a well-known fact that, during earthquake loading, soils may completely lose their strength and imitate the viscous behavior of a "liquid". Identified as liquefaction, this phenomenon is one of the reasons causing severe damage during seismic action. Many liquefaction cases were reported in the past, particularly in San Francisco (1906), Alaska (1964), Niigata (1964), San Fernando (1971), Kocaeli (1999) as reported in literature [1]. Evaluation of the pore water pressure development mechanisms triggering liquefaction has become one of the most important and interesting topics in geotechnical earthquake engineering [1]. Liquefaction leads to loss of shear strength caused by the build-up of excessive pore water pressure. Liquefaction can cause loss of bearing capacity, floating of buried structures, ground subsidence, settlement of embankments, lateral displacement of slopes and retaining walls [2-3].

Excess pore pressures in a soil during cyclic loading can be divided into two components, transient and residual. Transient pore water pressures in saturated soils occur due to changes in the applied average normal stresses resulting from dynamic loading [4-5]. Since the resulting pore water pressures are equal to the change in the total stress acting on the soil, transient excess pore pressures will have an inconsiderable effect on the effective stresses acting on the soil. Conversely, residual pore water pressures result from gradual collapse of the soil skeleton (i.e. plastic deformations) and therefore change the effective stresses acting on the soil. As a result, residual pore water pressures directly affect the strength and stiffness of the soil. During stress controlled cyclic tests, the residual pore pressures are those that are present when the applied deviator stress equals to (or exceeds) zero [6-7]. Residual pore pressures are often measured as the residual pore water pressure ratio. Pore water pressure ratio (r_u) defined as the ratio of the residual pore water pressure (u_{xs}) to the initial effective confining stress (σ'_o) acting on the soil. This ratio ranges from zero (i.e. no residual pore pressure) to one (i.e. complete transfer of load to pore water or "liquefaction") and thus provides more information than just the magnitude of the residual pore pressure.

In the literature, much effort is given on understanding the cyclic pore water pressure development pattern; these can be classified as stress-based [8,9], deformation-based [10, 11], energy-based [7, 12], and plasticity-based [13] models.

Four stress-based models can be used to predict pore water pressure generation for a non-plastic silt subjected to dynamic loading. The first model was developed by the empirical solution of Seed et al. [8]. In the sequel, a simplified alternative model was proposed by Booker et al. [9]. Three decades later, Polito et al. [14] revisited the method proposed by Seed et al. [1] with the help of statistics. Lastly, Baziar et al. [15] proposed an alternative closed form solution for silts using statistical software based on Seed et al.'s [8] methodology.

An empirical model considering excess pore-water pressure ratio (r_u) and ratio of number of cycles to liquefaction (N/N_{liq}) was suggested by Lee and Albaisa [16]. Seed et al. [8] proposed an empirical formula as given in Equation (1) based on data from De Alba et al. [17]:

$$R_u = \frac{1}{2} + \frac{1}{\pi} * \arcsin\left[2 * \left(\frac{N}{N_{liq}}\right)^{\frac{1}{\alpha}} - 1\right] \quad (1)$$

where α is a function of soil properties and testing conditions (α=0.7; and N=number of equivalent uniform loading cycles). Recently, Polito et al. [14] revised Seed et al.'s [8] method by use of statistical approaches and suggested that the model coefficient alpha (α) is dependent on several factors including cyclic stress ratio (CSR), fines content (FC), and relative density (D_r):

$$\alpha = 0.01166 * FC + 0.007397 * D_r + 0.01034 * CSR + 0.5058 \quad (2)$$

Equation (2) is valid for coarse grained soils with fines content (FC) less than 35%. For clean sands (FC=0), the effect of CSR on results is relatively insignificant, and it is evident that relative density has a remarkable effect on α. It is estimated that α should be between 0.73 to 1.14 [3]. Seed et al. [8] developed an empirical equation for assessment of excess pore-water pressure ratio (r_u) as a function of cycle ratio. This expression was subsequently simplified by Booker et al. [9] and is given as:

$$R_u = \frac{2}{\pi} arcsin\left[\left(\frac{N}{N_{liq}}\right)^{\frac{1}{2\alpha}}\right] \quad (3)$$

Equation (3) is composed of two calibration parameters, namely, number of cycles to liquefaction (N_{liq}) and empirical constant (α), which is to be determined by stress-controlled testing. For a certain soil, N_{liq} increases with increasing relative density (D_r) and decreases with increasing cyclic stress ratio (CSR); α is a constant-a function of soil type and test conditions. Baziar et al. [15] proposed the correlation given in Equation (4) based on model of Booker et al. [9]:

$$R_u = \frac{2}{\pi} arcsin\left[\left(\frac{N}{N_{liq}}\right)^{\frac{1}{2\alpha}}\right] + \sqrt[\beta]{\left(1 - \left(2 * \frac{N}{N_{liq}} - 1\right)^2\right)} \quad (4)$$

In Equation 4, α and β are two constants which are identified for different types of soils based on their silt content.

Early efforts on evaluation of dynamic characteristics of soil utilize slow and rapid transient loading on soil specimens by impact loading on a spring [18]. However, cyclic triaxial testing by analysis of stress reversals for assessment of liquefaction susceptibility and dynamic characteristics of soils were introduced by studies of Seed & Fead [19] and Seed [20]. During the past decade the test device, thanks to developments of data acquisition and measurement technology, use of the test has steadily increased, and it has been the most commonly used laboratory test for evaluating dynamic response of soils. The test has even broadened its use to analysis of response of foundations of offshore structures. However, sometimes, the difficulties in obtaining undisturbed specimens, imitation of loading and stress conditions come up with the need of modeling efforts. In this regard, an empirical energy-based excess pore pressure generation model has been developed that accurately approximates residual pore pressure generation in cohesionless soils under stress-controlled cyclic loading. The energy-based model has a simple mathematical form and a single calibration parameter (PEC), which facilitates its implementation and calibration.

Energy based pore water pressure development models are beneficial for understanding the pore water pressure development pattern during seismic loading. Some researchers developed models considering deformation energy and established relationships among change in excess pore pressure and energy absorbed per unit soil volume for a certain loading cycle [21]. They proposed an equation establishing a relationship between the volume change of dry sand and pore water pressure, considering an energy-based model. Further attempts were based on theoretical studies, mainly focusing on developing experimental models using empirical data [22-28]. A comprehensive summary of previous studies is presented by Green [28] along with a new set of calibration parameters. Additionally, Green et al. [7] presented a compilation of previous studies along with a new set of calibration parameters. The following model is proposed by Green et al. [7]:

$$r_u = \sqrt{\frac{W_s}{PEC}} \leq 1 \tag{5}$$

Here; W_s is the energy dissipated per unit volume of soil divided by initial effective confining pressure and PEC is the Pseudo Energy Capacity, which is a calibration parameter. An infinitesimal increase in W_s can be linked to state of stress and changes in strain (Equations 6 and 7).

$$dW_s = \frac{(\sigma'_v\, d\varepsilon_v + 2\sigma'_h\, d\varepsilon_h + \tau_{vh}\, d\gamma_{vh} + \tau_{hv}\, d\gamma_{hv})}{\sigma'_{m0}} \tag{6}$$

where; dW_s is the dissipated energy increase normalized by the initial mean effective stress; σ'_{m0} is the initial mean effective stress; $\boldsymbol{\sigma'_v}$ is the vertical effective stress; $\mathbf{d\varepsilon_v}$ is the change in vertical strain; $\boldsymbol{\sigma'_h}$ is the horizontal effective stress; $\mathbf{d\varepsilon_h}$ is the change in radial strain; $\boldsymbol{\tau_{vh}}$ is the horizontal shear stress acting on a plane with a vertical normal; $\mathbf{d\gamma_{vh}}$ is the change in shear strain due to change in τ_{vh}; $\boldsymbol{\tau_{hv}}$ is the vertical shear stress acting on a plane with a horizontal normal and $\mathbf{d\gamma_{hv}}$ is the change in shear strain due to change in $\boldsymbol{\tau_{hv}}$;

$$W_s = \frac{1}{2\sigma'_0} \sum_{i=1}^{n-1} \left[\left(\sigma_{d,i+1} + \sigma_{d,i} \right) . \left(\varepsilon_{a,i+1} - \varepsilon_{a,i} \right) \right] \tag{7}$$

In Equation 7, n is the number of load increments to liquefaction; $\sigma_{d,i}$ and $\sigma_{d,i+1}$ are applied deviator stress at load increments "i" and "i+1", respectively; $\varepsilon_{a,i}$ and $\varepsilon_{a,i+1}$ are the axial strains at load increment "i" and "i+1", respectively.

In energy-based models, there is no need for definition of an equivalent number of cycles for introduction of a seismic action. With energy-based models, the stress or strain profile can be conveniently obtained based on the pore water pressure ratio (r_u)-cyclic shear strain (γ) relationship. One limitation of energy-based models is the need for information about complete stress-deformation history, which influences selection of convenient constitutive model [29]. However, under uniform and non-uniform loading conditions, the energy-based approach is a viable tool for evaluation of liquefaction [30-35]. Based on an experimental framework, Baziar et al. [36] developed a model to analyze strain energy-based liquefaction resistance based on parameters including initial effective overburden pressure, relative density and mean grain size. Xu et al. [37] also used the energy-based approach to analyze

the liquefaction potential of both loose and medium-density sand samples. Zhang et al. [38] performed a series of soil liquefaction tests and developed multivariate adaptive regression splines to find out the energy threshold triggering the liquefaction in sand and silt. Yang and Pan [39] studied cyclic resistance and pore water pressure generation in consolidated anisotropic sand samples using the Green, Mitchell and Polito Model (GMP) in conjunction with energy dissipation theory. Several experimental studies in the literature question the parameters affecting liquefaction behavior of silts and sands. Kokusho [40] evaluated the liquefaction potential of Futtsu sand using stress and energy-based methods with reference to varying relative densities and fines contents. Karakan et al. [32] performed cyclic triaxial tests on a non-plastic silt specimen of different relative densities. Varying cyclic strain levels were applied to observe the excess pore pressure development patterns, and also liquefaction behavior.

The residual pore pressures computed by the energy-based model and the experimental results are in good agreement. However, contrary to stress-based models, energy-based models do not require the conversion of randomized loads to an equivalent number of uniform load cycles. Moreover, the energy-based models are plausible alternatives to stress-based models for prediction of residual excess pore pressure generation patterns of cohesionless soils subjected to cyclic loading. Energy dissipation theory is a favorable tool in understanding the parameters influencing the liquefaction and pore water pressure generation behaviors in non-plastic silts. However, limited number of studies investigate the liquefaction phenomenon in pure non-plastic silts, based on energy-based models. In the present study, results of a series of stress-controlled consolidated undrained cyclic triaxial tests were analyzed to investigate the pattern and amount of dissipated energy threshold for the onset of liquefaction of a non-plastic silt. Relative density (D_r) and cyclic stress ratio (CSR) were determined to be the major influencing factors affecting the dissipated energy.

2. MATERIALS AND METHODS

2.1. Experimental Data

As mentioned before, results of cyclic triaxial tests performed by authors were used, and these studies report properties of non-plastic silt tested [32-33]. The specific gravity of non-plastic (NP) silt is 2.65 and the particle size distribution is given in Figure 1. The maximum and minimum void ratios in accordance with ASTM D4253 [41] and D4254 [42] standards were determined as 1.352 and 0.894, respectively. Cyclic triaxial tests were performed on samples prepared at six different relative densities ranging from 30% to 80%. For specimens prepared at different initial relative densities, 10 different cyclic triaxial tests of different CSRs were performed, which makes a total of 61 experiments (Data available in [32-33]).

Stress-controlled cyclic triaxial tests were performed to analyze the relationships among cyclic stress ratio (CSR), pore water pressure and double amplitude of axial strain. The device is equipped with a single column load frame, including a servo-pneumatic actuator with external displacement transducer. The servo-valve is able to apply a sinusoidal vibration frequency between 0.001 to 10 Hz. The device is capable of measuring axial displacement and load up to 50 mm. and 2 kN, respectively, by use of relevant transducers inside the cell. Volume change of specimens was measured by a double burette type volume change device, which is equipped with a transducer having a stroke of 25 ml (Figure 2).

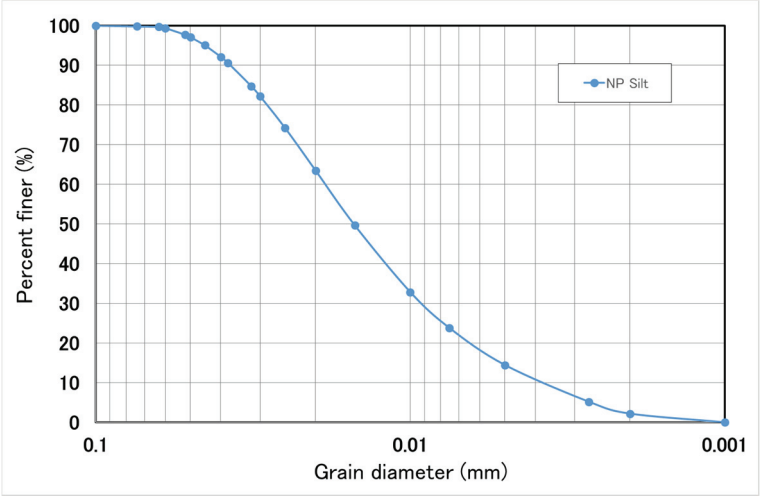

Figure 1 - Grain size distribution of non-plastic silt [45]

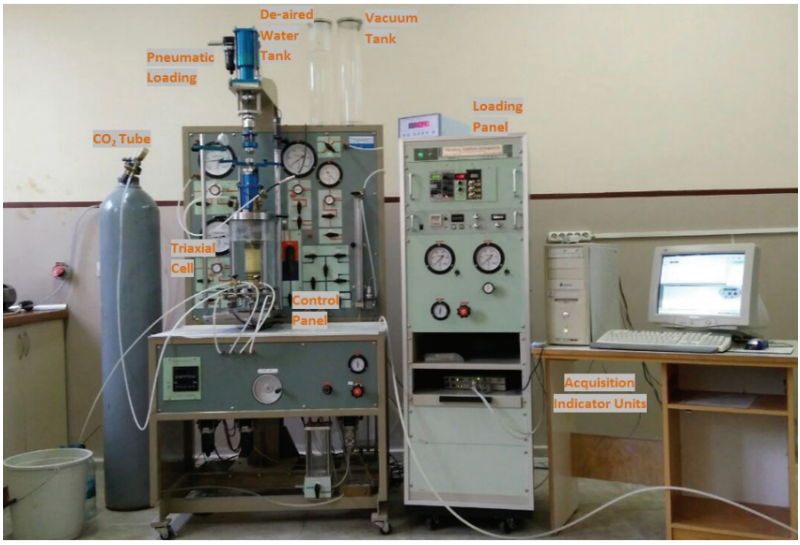

Figure 2 - Dynamic triaxial testing system

The tests were applied on specimens having dimensions of 50×100 mm (diameter×height), which were prepared and tested in accordance with JGS 0520-2000 and JGS 0541-2000 standards, respectively [43-44]. During specimen preparation, a vacuum of -20 kPa was applied to the specimen, in order to obtain a constant cross-sectional area throughout its height and prevent membrane penetration. Afterwards, the confining pressure was gradually increased as the vacuum pressure is also gradually decreased at a same rate. Later, carbon dioxide and de-aired water were circulated through the specimen. Saturation of specimens

were ensured by application of cell and back pressures. Consolidation under a confining pressure of 100 kPa was initiated after obtaining a Skempton's pore water pressure (B) value greater than 0.96. The next phase was application of undrained cyclic loading, and the liquefaction assessments were made until the specimens were exposed to 20 cycles of loading or when the double amplitude axial strain exceeds 5% [32]. During cyclic loading, excess pore water pressure, cyclic axial strain and cyclic deviator stresses were recorded simultaneously. After the loading stage, drainage valves are opened to drain the water in the soil sample. The water in soil specimen is transferred to volume change burette, enabling measurement of volume change due to post-liquefaction settlement. A series of tests on the required number of homogeneous specimens were performed, by gradually increasing the amplitude of cyclic load. Table 1 includes the details of the experiments including consolidation pressure, range of relative densities, CSR values, cyclic stress, pore water pressure ratios, volumetric strain, cyclic axial strain, double amplitude axial strain, factor of safety, number of tests and corresponding number of cycles to liquefaction. For providing a systematic approach, relative density of specimens was changed from 30% to 80%. Also, the specimens were subjected to different amplitudes of sine wave loading, by changing cyclic stress ratio (CSR) values. For specimens of 80% relative density, CSR values ranging between 0.173 and 0.226 caused higher strain levels up to 16%. Literally, a very low number of cycles between 0.5 to 1.5 caused liquefaction of silt, when subjected to higher CSR values. For 50% relative density, strain levels of specimens subjected to CSR values ranging between 0.149 and 0.186 are on the order of 12%. The specimens were completely liquefied after 2 to 7 cycles of loading, in other words, pore water pressure ratio has reached 100% and large strains were observed. For specimens having an initial relative density of 40%, strains corresponding to CSR values of 0.137 to 0.190 were approximately 9% whereas the soil lost its strength completely after 3 to 6 cycles. For specimens of 30% initial relative density, strains were recorded between 3.3% to 5% for CSR values between 0.123 and 0.166, with corresponding number of cycles from to 1 to 3.

In brief, the specimens, which were subjected to stress-controlled cyclic loading, were initially consolidated at 100 kPa under isotropic conditions. The dynamic loading pattern was a sine wave with a frequency of 0.1 Hz. As a result, excess pore water pressure (u), cyclic axial strain (ε_c), and cyclic deviatoric stresses were recorded continuously. Results of tests on a liquefied and a non-liquified sample are given in Figures 3 and 4, respectively. Here, the differences in stress path, change in stress path due to cyclic axial strain, and the change in number of cycles with pore water pressure ratio and cyclic axial strain by application of varying CSR levels on identical specimens of 60% relative density were presented. In this regard, a specimen of 60% relative density liquified after 13 cycles under a CSR value of 0.112 (Figure 3). In detail, Figure 3a presents the application of sine wave load of ±50 N for 13 cycles. Figure 3b shows the cyclic axial strain with number of cycles. It is evident that the specimen reaches 0.3%, 1.5% and 10% cyclic axial strains after application of 6, 11 and 12 cycles, respectively. Investigation of the change in pore water pressure with cyclic axial strains (Figure 3c), 6, 11 and 12 cycles come up with r_u values of 0.4, 0.65 and 0.75 and cyclic axial strains of 0.35%, 0.75% and 10%, respectively. Nevertheless, Figure 3d shows the variation of stress path, where maximum amplitude of principal stress difference is ±5.60 kPa. It is clearly observed that the mean effective stress of 100 kPa decreases to 0 after 13 cycles.

Table 1- Details of testing program

Test Number	Relative Density D_r (%)	Skempton value, B	Consolidation Pressure (kPa)	Cyclic Stress (kPa)	Cyclic stress ratio, CSR	Number of Cycles N	Pore Water Pressure Ratio	Cyclic Axial Strain $(\varepsilon_a)_{ss}$ (%)	Double amplitude of axial strain (%)	Cumulative $\sqrt{W_S}$	PEC	R^2	RMSE
0	80	1.00	99	2.18	0.011	20	0.02	0.009	0.018	Not liquified			
1	80	1.00	100	4.34	0.022	20	0.02	0.007	0.013	Not liquified			
2	80	1.00	99.8	8.31	0.042	20	0.04	0.019	0.039	Not liquified			
3	80	1.00	100	13.79	0.069	20	0.10	0.045	0.089	Not liquified			
4	80	1.00	99.6	20.13	0.101	20	0.23	0.086	0.173	Not liquified			
5	80	0.97	99.3	21.62	0.109	20	1.00	3.273	6.547	8.11	73.10	0.974	0.013
6	80	0.98	99.6	28.33	0.142	6	1.00	11.836	23.672	17.39	41.73	0.982	0.030
7	80	0.98	99.9	34.63	0.173	3	1.00	15.525	31.050	20.05	48.72	0.999	0.007
8	80	0.98	99.7	37.53	0.188	1.5	1.00	18.083	36.167	14.51	207.36	0.997	0.019
9	80	0.98	99.3	39.01	0.196	1	1.00	15.405	30.810	16.60	273.90	1.000	0.000
10	80	0.99	99.8	45.17	0.226	0.5	1.00	17.396	34.792	26.40	784.00	1.000	0.000
11	70	0.97	100	4.39	0.022	20	0.02	0.013	0.027	Not liquified			
12	70	0.99	99.6	9.32	0.047	20	0.06	0.019	0.039	Not liquified			
13	70	1.00	99.9	13.76	0.069	20	0.09	0.058	0.116	Not liquified			
14	70	1.00	98.9	17.24	0.087	20	0.23	0.127	0.254	Not liquified			
15	70	0.89	99	26.62	0.134	20	0.51	0.219	0.438	Not liquified			
16	70	0.98	99	29.00	0.146	6	1.00	11.060	22.120	9.48	31.14	0.994	0.014
17	70	0.94	99.2	34.26	0.173	3	1.00	14.565	29.130	8.99	37.45	0.991	0.027
18	70	0.98	99.2	37.73	0.190	1	1.00	11.962	23.924	16.08	284.93	0.999	0.016
19	70	1.00	100	40.31	0.202	0.8	1.00	18.053	36.106	25.53	748.57	0.022	0.997
20	70	1.00	99.5	41.26	0.207	0.5	1.00	18.046	36.092	25.21	635.04	1.000	0.000
21	60	0.98	99	4.45	0.022	20	0.03	0.016	0.031	Not liquified			
22	60	0.99	99.8	8.93	0.045	20	0.06	0.031	0.062	Not liquified			
23	60	1.00	99.5	13.79	0.069	20	0.14	0.074	0.147	Not liquified			
24	60	0.99	100	17.51	0.088	20	0.20	0.141	0.283	Not liquified			
25	60	1.00	100	21.67	0.108	13	1.00	9.101	18.202	6.73	48.44	0.987	0.012
26	60	0.90	100	25.61	0.128	3	1.00	11.944	23.889	16.28	16.00	0.975	0.043
27	60	0.97	99	34.47	0.174	1	0.90	7.221	14.441	11.60	70.56	0.996	0.036
28	60	1.00	99	38.24	0.193	0.7	1.00	8.922	17.843	13.08	171.61	1.000	0.001
29	60	1.00	98	42.51	0.217	0.5	1.00	10.021	20.041	14.15	198.81	1.000	0.000
30	60	1.00	99.9	37.88	0.190	0.8	1.00	18.085	36.171	23.72	561.69	1.000	0.000
31	50	1.00	99.2	2.21	0.011	20	0.01	0.011	0.022	Not liquified			
32	50	1.00	99	4.66	0.024	20	0.03	0.015	0.030	Not liquified			
33	50	1.00	99.6	9.46	0.048	20	0.06	0.031	0.061	Not liquified			
34	50	1.00	99.3	12.25	0.062	20	0.09	0.042	0.083	Not liquified			
35	50	0.90	99	13.82	0.070	20	0.08	0.056	0.113	Not liquified			
36	50	1.00	100	18.17	0.091	20	0.26	0.147	0.294	Not liquified			
37	50	1.00	100	23.64	0.118	18	1.00	7.109	14.218	9.16	58.22	0.980	0.036
38	50	1.00	99	29.55	0.149	7	1.00	11.616	23.232	11.59	38.32	0.990	0.040
39	50	0.93	99	32.26	0.163	5	1.00	12.733	25.466	18.35	121.00	0.983	0.025
40	50	1.00	99.6	36.95	0.186	2	1.00	11.534	23.067	17.97	30.36	1.000	0.020
41	40	1.00	100	2.16	0.011	20	0.02	0.012	0.023	Not liquified			
42	40	0.98	99.5	4.53	0.023	20	0.01	0.021	0.041	Not liquified			
43	40	1.00	99.9	9.47	0.047	20	0.06	0.029	0.058	Not liquified			
44	40	1.00	99.5	11.68	0.059	20	0.07	0.046	0.093	Not liquified			
45	40	1.00	99.7	13.99	0.070	20	0.09	0.059	0.118	Not liquified			
46	40	1.00	99.9	18.49	0.093	20	0.21	0.147	0.293	Not liquified			
47	40	0.99	99.5	24.65	0.124	20	0.46	0.306	0.612	Not liquified			
48	40	1.00	99.7	27.38	0.137	6	1.00	9.227	18.454	14.30	29.70	0.994	0.052
49	40	1.00	99.7	33.63	0.169	4	1.00	6.725	13.451	13.20	49.00	0.987	0.050
50	40	0.92	99.6	37.77	0.190	3	1.00	9.098	18.197	9.53	71.40	0.963	0.083
51	30	0.97	100	2.03	0.010	20	0.01	0.012	0.024	Not liquified			
52	30	0.97	99.8	4.46	0.022	20	0.02	0.020	0.041	Not liquified			
53	30	0.97	99.8	8.92	0.045	20	0.04	0.031	0.062	Not liquified			
54	30	1.00	99.9	11.37	0.057	20	0.07	0.046	0.092	Not liquified			
55	30	0.98	99.9	13.52	0.068	20	0.10	0.072	0.145	Not liquified			
56	30	0.96	100	17.42	0.087	20	0.35	0.188	0.376	Not liquified			
57	30	0.98	99.7	20.77	0.104	15	1.00	1.310	2.620	9.50	92.16	0.976	0.091
58	30	0.98	99.7	24.52	0.123	3	1.00	4.963	9.925	8.31	44.89	0.971	0.125
59	30	0.94	99.8	30.81	0.154	2	0.93	4.250	8.500	8.91	110.25	0.995	0.040
60	30	1.00	99.9	33.21	0.166	1	0.98	3.357	6.713	8.12	83.72	0.995	0.050

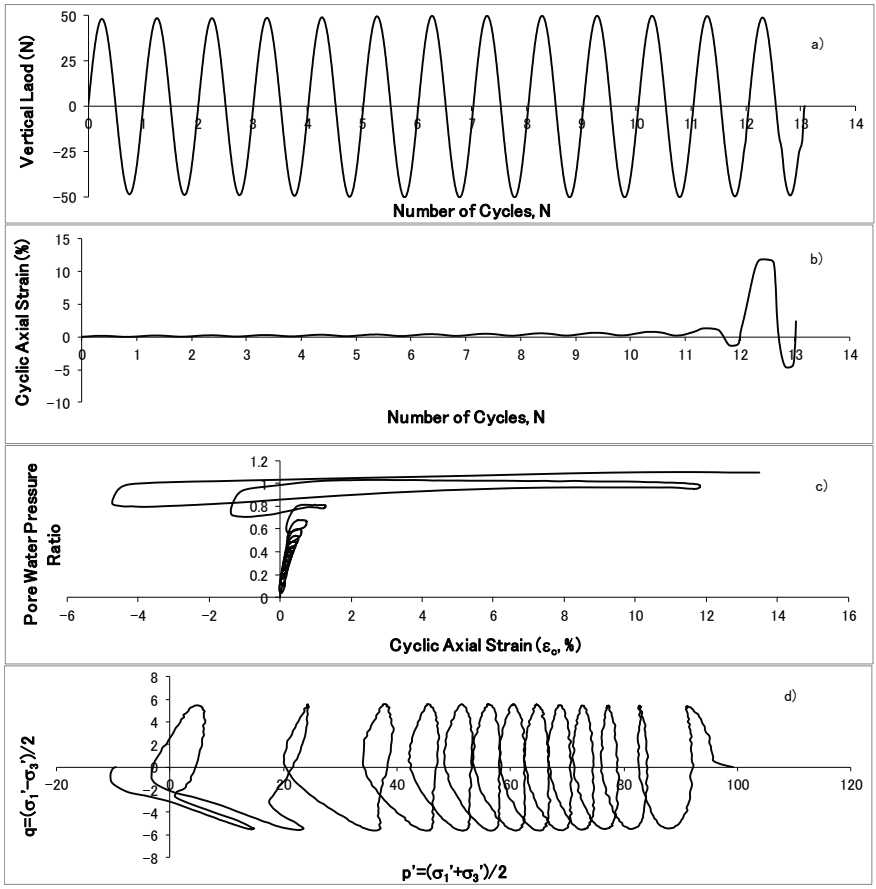

Figure 3 - Test results on a liquified specimen of 60% relative density under a CSR value of 0.112 (a) Change of sine wave load with number of cycles, (b) Change of cyclic axial strain with number of cycles, (c) Change of pore water pressure ratio with cyclic axial strain, (d) Stress path.

On the other hand, results of tests on a non-liquified specimen of 60% relative density are also shown in Figure 4. The specimen did not liquefy after 20 cycles under a CSR of 0.09, corresponding to a sine wave load of ±41 N. Figure 4b presents the variation of cyclic axial strain by number of cycles. Strictly speaking, the strains reach to 0.28%, after 20 cycles of loading. The non-liquified specimen reaches a pore water pressure ratio and axial strain of 0.25 and 0.28%, respectively (Figure 4c). Finally, Figure 4d shows the variation of stress path, where maximum amplitude of principal stress difference is ±4.50 kPa. It is evident that the mean effective stress of 100 kPa decreases by a relatively small value, down to 82 kPa.

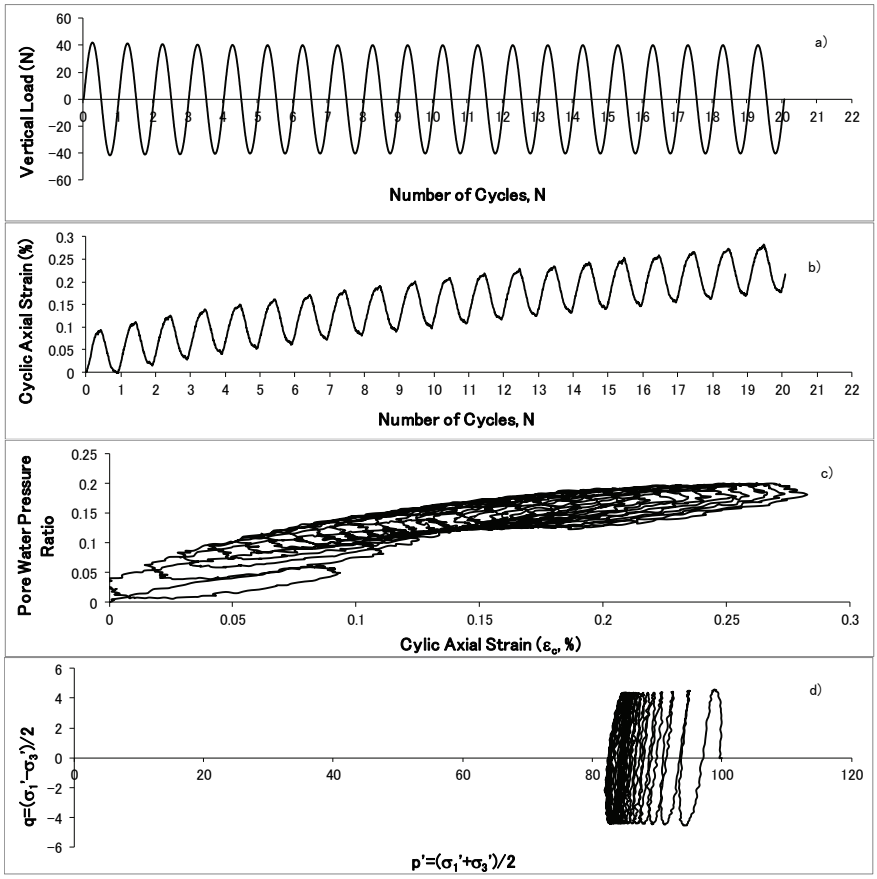

Figure 4 - Test results on a non-liquified specimen of 60% relative density under a CSR value of 0.09 (a) Change of sine wave load with number of cycles, (b) Change of cyclic axial strain with number of cycles, (c) Change of pore water pressure ratio with cyclic axial strain, (d) Stress path.

2.2. Calculation of Energy Dissipated Per Unit Volume

The method proposed by Green et al. [7], which is previously introduced in "Introduction" was used as a guide. The analyses were employed on liquified test results, which are presented in Table 1. In this regard, the energy-based pore water pressure calculation procedure was not applied for 33 non-liquified tests. For example, for 80% relative density, in experiment #3 in Table 1, for CSR=0.069 after 20 cycles, the PWP was 10.28%, while in experiment #4 for CSR=0.101 after 20 cycles, the PWP was 22.89%. These values clearly demonstrate that liquefaction did not occur in these tests.

The change in excess pore water pressure corresponding to energy absorbed per unit volume (W_s) for a certain loading cycle can be calculated by use of the calculating the ratio of energy

dissipated per unit soil volume to the initial average effective stress. Defined in Equation (3), physical meaning of W_s is given in Figure 5.

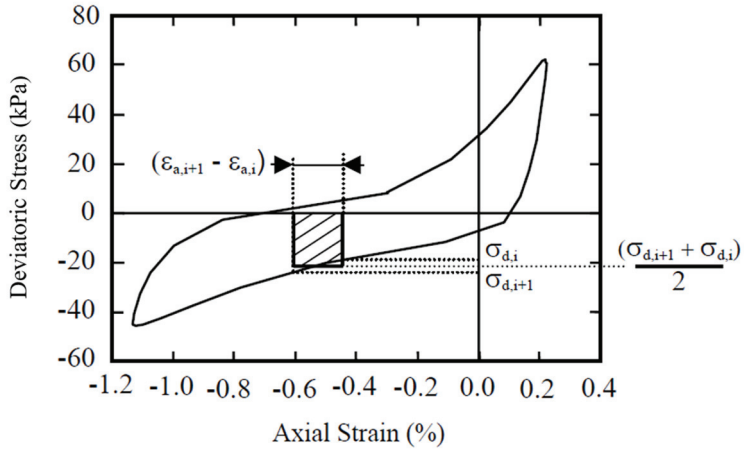

Figure 5 - Hysteresis loop of a cycle as a result of cyclic loading [7]

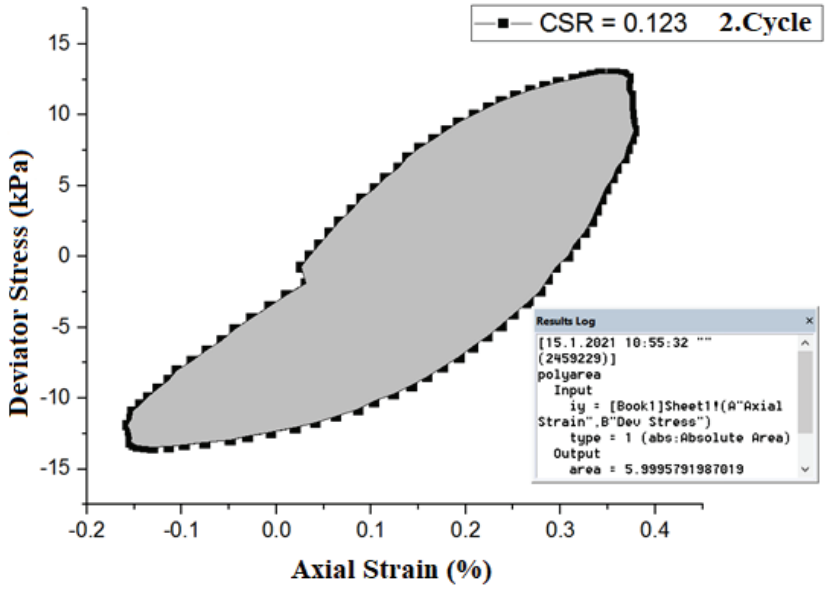

Figure 6 - Calculation of the hysteresis loop area in 2nd cycle of Test #58 with CSR = 0.123

During cyclic loading, the energy consumed per unit volume for a soil sample is defined as the area covered a by deviatoric stress-strain hysteresis cycle [7]. In a certain test, a hysteresis

loop corresponding to each cycle is drawn, and the energy consumed (W_s) in that cycle is the area limited by the relevant cycle. Therefore, the variation of deviatoric stress by axial strain were plotted for each cycle. The areas covered by certain cycles in deviatoric stress-axial strain plots were calculated. An example of the hysteresis loop area calculation is shown in Figure 6.

2.3. Pseudo Energy Capacity (PEC) Calculations

The pseudo-energy capacity (calibration parameter) calculation called PEC is as important as the W_s (energy consumed) in the r_u formulation given in Equation (1) as shown in Figure 7.

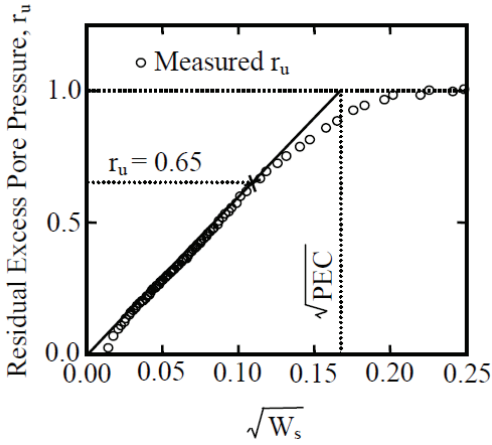

Figure 7 - An illustration of determination of PEC from dynamic triaxial test results [7].

To determine the PEC value of each experiment, first of all, $\sqrt{W_s}$ from each cycle are cumulatively calculated and plotted in abscissa (Figure 8).

Afterwards, experimental r_u value at the end of the relevant cycle is plotted on ordinate and the variation of r_u with $\sqrt{W_s}$ is obtained. A line is drawn (dashed line) from r_u = 0.65, intersecting the curve formed by the resulting r_u - $\sqrt{W_s}$ data. Next, the red line in the figure is drawn, between the origin and the curve, corresponding to a r_u value of 0.65. Finally, this red line is extended to the the horizontal line of r_u = 1.00 and the abscissa of the intersection of these two lines is $\sqrt{\text{PEC}}$. Calculated PEC values are given in Table 1. Numerically, this procedure simplifies to Equation 8:

$$\text{PEC} = \frac{W_{s,r_u=0.65}}{0.4225} \tag{8}$$

where $W_{s,ru=0.65}$ is the value of W_s corresponding to r_u = 0.65. The term “pseudo energy capacity” or PEC is used to label the calibration parameter to give a certain amount of

physical significance to it over just a general curve fit parameter. PEC is approximately equal to the energy dissipated per unit volume normalized by the initial effective confining pressure in a sample up to the point of initial liquefaction.

Afterwards, W_s and PEC values were substituted in Equation 1 to calculate r_u values. Lastly, experimental and calculated pore water pressure ratio (r_u) values were plotted against number of cycles (N).

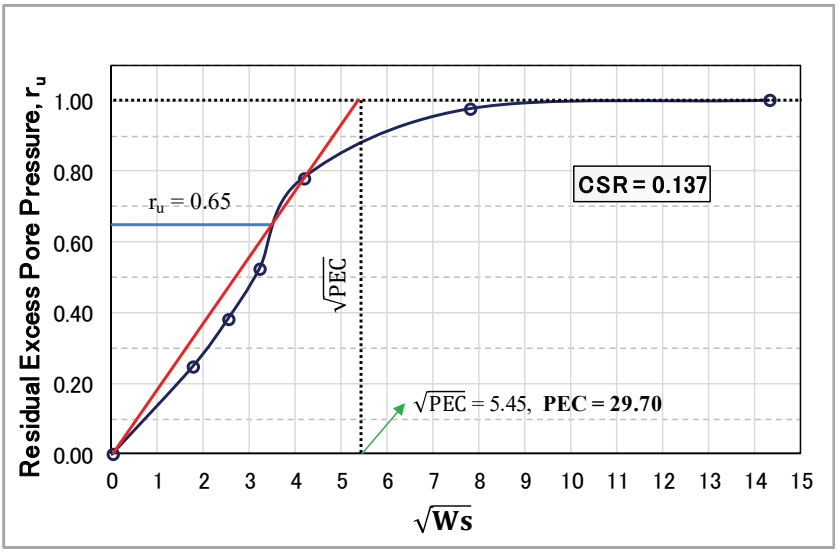

Figure 8 - A sample PEC calculation for CSR = 0.137

3. RESULTS AND DISCUSSION

Using the procedure explained above, application of energy-based pore water pressure models for sands on evaluation of pore water pressure development behavior of non-plastic silts were analyzed. Figure 9 shows the pore water pressure ratio (r_u) – number of cycles (N) relationship for a test with cyclic stress ratio (CSR) *of* 0.119 at a relative density (D_r) of 50%. As can be observed, with increasing number of cycles, modeled r_u values reaches 1 after application of approximately 17 cycles. As can be observed, with increasing number of cycles, modeled r_u values reach to 1 after approximately 16.5 cycles. However, experimental data show that same r_u value was obtained after 17th cycle.

3.1. Comparison of calculated and experimental r_u values

The relationship between pore water pressure ratio (r_u) and number of cycles (N) for liquefied tests on specimens with relative densities ranging between 30% to 80% are given in Figure 10. Analyzing results of test performed under a CSR of 0.104, while the energy based r_u values were higher than experimentally obtained r_u values until the 14th cycle, it is clear that

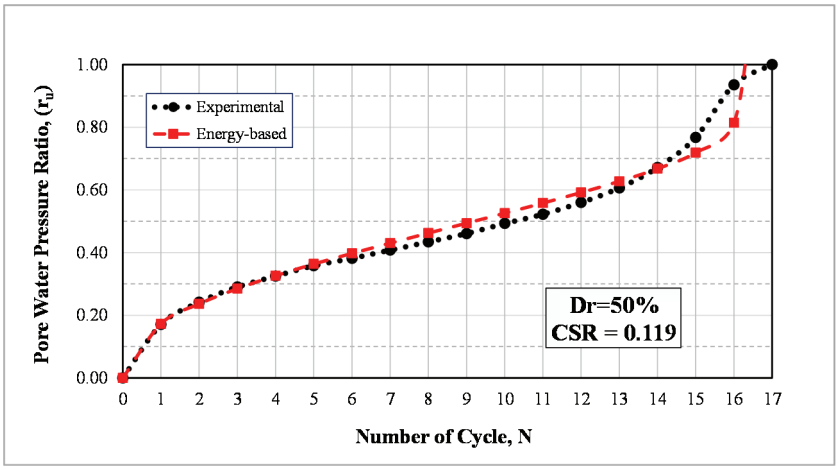

Figure 9 - An example of comparison of experimental and energy-based r_u values.

the r_u values converge from 14th to 15.2nd cycle (Figure 10a). When CSR was increased to 0.123, it is observed that the modeled r_u value reaches 1 after 2.6 cycles, while the experimental r_u value reaches 1 at the end of the 3rd cycle. Under a CSR of 0.154, it is understood that the experimental r_u value can rise up to 0.93 and liquefaction is evident, while the model results show that soil liquefies at an r_u value of 1. Similarly, the maximum of modeled r_u value for CSR = 0.166 is determined to be 0.88-which is also experienced in reality (Figure 10a). As seen in Figure 10a, for D_r = 30%, the number of cycles required for r_u to reach 1.0 decreased as the CSR value increased. For instance, the number of cycles required for liquefaction for CSR values of 0.166 and 0.104 are 1 and 15, respectively.

Considering results of test of CSR = 0.137, it is observed that the onset of liquefaction is at 2nd cycle during the experiment, and the model shows that the specimen liquifies at 1.7th cycle. For CSR = 0.168, liquefaction is observed after 4th and 3.2nd cycle, according to experimental and model outcomes (Figure 10b). Likewise, for CSR = 0.190, although it is seen that it liquefied after 5.1st cycle in reality, modeling results show that the soil liquefied after 4.5th cycle (Figure 10b).

Analyzing results obtained from liquefied tests on specimens of D_r=50%, although r_u value calculated as a result of the energy-based analysis in all four liquefied tests shows a similar trend with experimental results, it is seen that the model outcomes show liquefaction before experimental outcomes (Figure 10c). Although it is found that the modeled r_u value in the CSR = 0.119 test reached 1 in the 16.5th cycle, in reality, it is evident that the soil liquefies after 17th cycle. For CSR = 0.149, r_u value increased up to 1 after 6 cycles, model outcomes state that r_u increased up to 1 after 5.2 cycles. In tests with CSR = 0.163 and CSR = 0.183, experimental and modeled r_u values rise to 1, and the model and real behaviors are in agreement with each other. In Figure 10c, analyzing behavior of specimen of D_r = 50%, for CSR = 0.183, the pore water pressure ratio reaches 1.00 after just one cycle.

Focusing on Figure 10d, for CSR = 0.112, liquefaction is initiated after 12th cycle and the model outcomes show that r_u value reaches 0.97 after same number of cycles. At CSR =

0.131, the experimental and model results show that the r_u value reaches 1 after 3rd and 2.1st cycles, respectively. At CSR = 0.172, while it is observed that the experimental r_u value reaches a level of 0.90 and liquefies in the 1.27th cycle, it is calculated that modeled r_u values reach to 1.0 even after 1.15th cycle. In the three liquefied tests with CSR values greater than 0.172, the r_u values found as a result of the experimental and energy-based analysis follow a similar trend, and liquefied around 1st cycle. In Figure 10d, the number of cycles required for the r_u to reach 1.0 for both CSR = 0.217 and CSR = 0.193 has been determined as 1. When CSR = 0.172, the number of cycles required for the r_u to reach 1.00 is just over 1. For all three liquefied specimens with D_r=70% and applied CSR greater than 0.188; the number of cycles in which r_u values reaches 1.0 were same for energy-based model and experimental outcomes (Figure 10e). For D_r = 70%, the number of cycles required for r_u to reach 1.0 for CSR values of 0.211, 0.208 and 0.194 are equal to 1. In this case, as the CSR value increases with the increasing relative density, it was shown that one cycle is sufficient when the number of cycles required for liquefaction exceeds a certain CSR value.

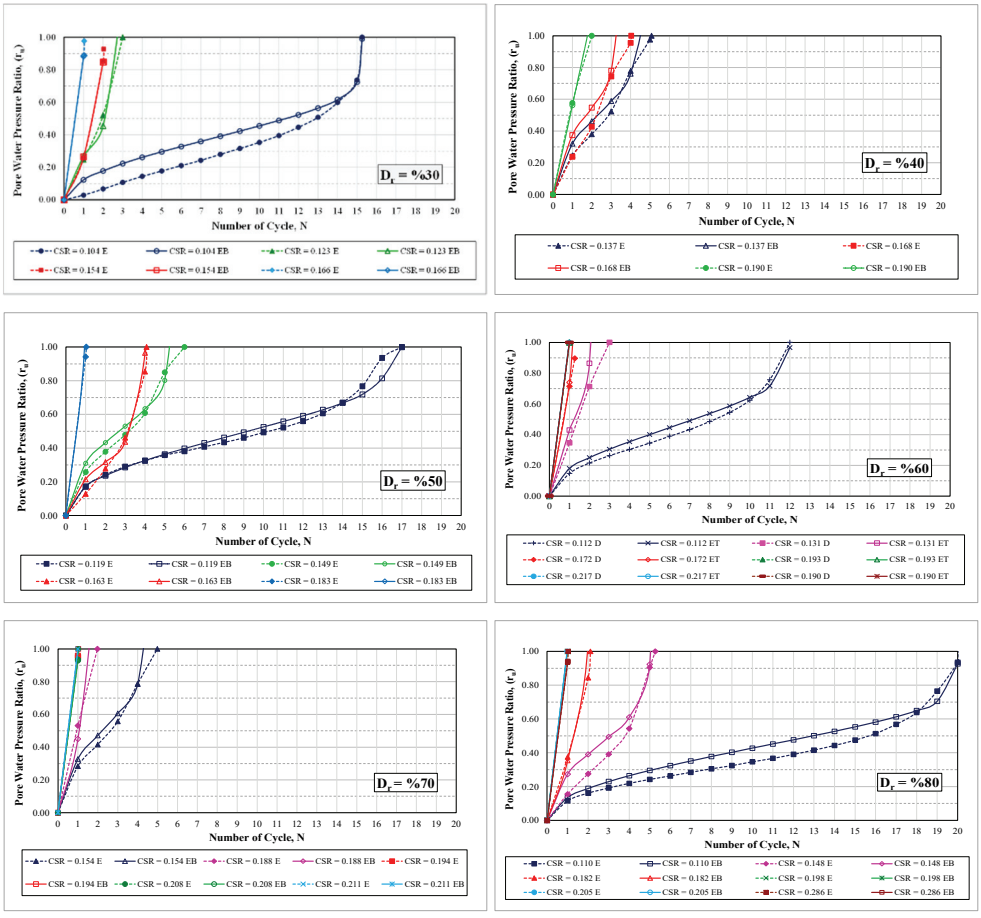

Figure 10- The relationship between r_u and number of cycles - liquefied tests with D_r=30% to 80% (E = Experimental, EB = Energy-based)

Results of test performed under CSR = 0.110 revealed that the r_u value escalated up to 1 in the 20.1st cycle (Figure 10f). However, energy-based analysis concludes that the real r_u value reaches a maximum of 0.95 in the relevant cycle, and liquefaction is initiated. At a CSR of 0.148, while the r_u value reached 1 in the 5.27th cycle during testing, model outcomes reveal that r_u value reaches 1 after 5 cycles. For a CSR of 0.182; r_u reached 1 after 2.11 cycles, while in the model outcomes, a value of 1 is reached after 1.95 cycles. When CSR exceeds 0.182, all three specimens of D_r=80% liquefied in the first cycle, and the model outcomes are in accordance with experimental values. For dense specimens, when CSR is above 0.198, the number of cycles needed for liquefaction is less than 1. At a constant CSR value, the number of cycles required for liquefaction and pore water pressure ratio increased with increasing relative density values.

3.2. Dependence of Cumulative $\sqrt{W_s}$ on r_u Values

In Figure 11, for six relative density values ranging from 30% to 80%, the variation of cumulative √(Ws) at different CSR values with pore water pressure ratios was obtained. For loose specimens, at smaller CSR amplitudes, increasing number of cycles causes a stepwise increase $\sqrt{W_s}$ values, causing r_u values ascend to 1. Nevertheless, results of four experiments in Figure 11 show different trends from those of the rest. In detail, the first test of Dr=60% and CSR=0.190 liquified after one single cycle, and √(Ws) is calculated as 23.72. In the next two tests on specimens with a D_r value of 70%, under CSRs of 0.211 and 0.208, number of cycles required to initiate liquefaction are 1 and 1.3, respectively. Corresponding √(Ws) values are 25.20 and 25.53, respectively. In the fourth test, a high CSR value of 0.286 was applied on specimen of highest relative density (Dr=80%), it expectedly liquified after one cycle, and the √(Ws) value was calculated as 26.40. Considering common aspects of the last four tests, high CSR values caused liquefaction of dense to very dense specimens after very low number of cycles.

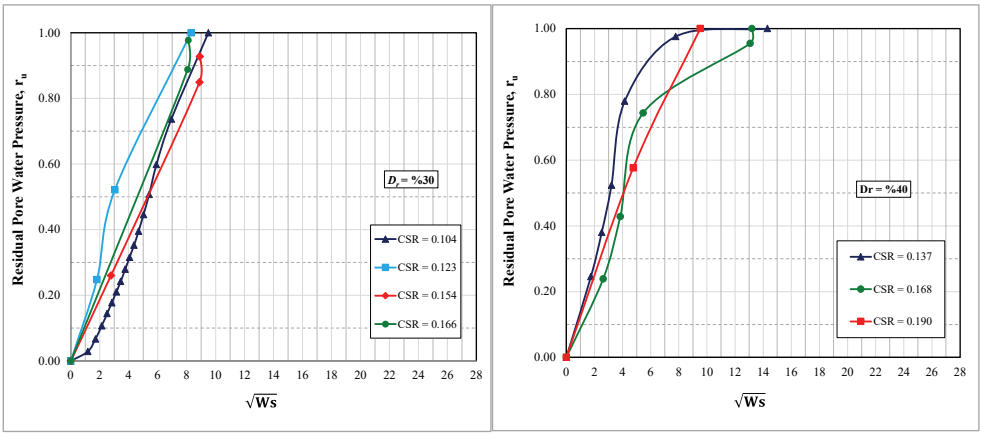

Figure 11- The relationship between pore water pressure ratio and cumulative number √Ws for liquefied tests with relative densities ranging between 30% to 80% and varying CSR

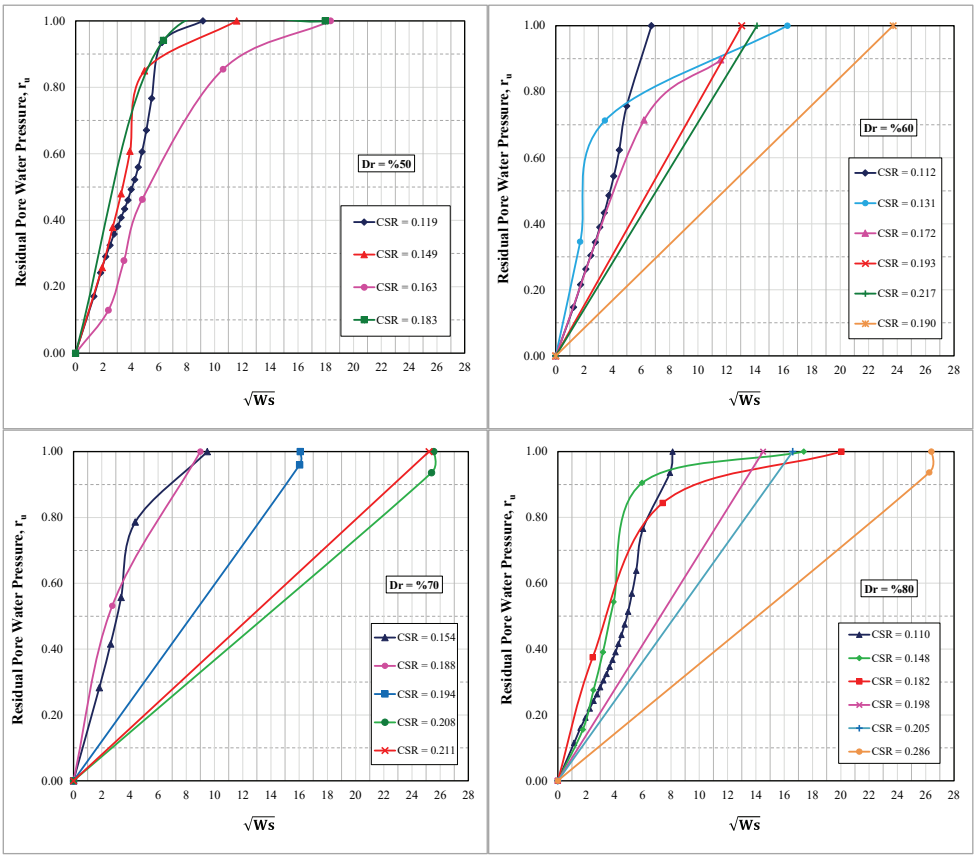

Figure 11- The relationship between pore water pressure ratio and cumulative number √Ws for liquefied tests with relative densities ranging between 30% to 80% and varying CSR (continued)

3.3. Variations of Accumulative Dissipated energy with the Number of Cycles

According to Yang and Pan [39] and Kokusho [40] and the dissipated energy (W_s) during cyclic undrained loading can be calculated by finding the hysteretic area of each individual stress–strain loop. In Figure 12, change of W_s by increasing N by increasing CSR is presented for a wide range of relative densities, starting from 30% to 80%. As shown in Figure 12a, when the non-plastic silt is at a very loose state, accumulated energy after 15 cycles is 0.483 kJ/m^3. Further increase in CSR decreased number of cycles below 2, and corresponding accumulated energy is between 0.6 and 0.8 kJ/m^3. When D_r=40% and CSR=0.137, accumulated energy after 5 cycles is 2.045 kJ/m^3 (Figure 12b). For medium dense specimens (D_r=50% and 60%), similar behaviors were observed. For instance, when CSR=0.119, while 17 cycles cause accumulation of an energy of 0.84 kJ/m^3 (Figure 12c), 12 cycles under a CSR of 0.112 accumulate an energy of 0.45 kJ/m^3 (Figure 12d). Without hesitation, increasing CSR caused decrease in number of cycles, while increasing accumulated energy at this

density level. For dense specimens (Dr=70%), high CSR values of 0.211 and 0.208 caused liquefaction before one single cycle and accumulated energy was calculated as 6.40 and 7.50 kJ/m^3 (Figure 12e). At densest state, six CSR levels were applied ranging from 0.110 to 0.286. Accumulated energy for CSR of 0.110 after 20 cycles and CSR of 0.286 after one cycle were obtained as 0.628 and 6.89 kJ/m^3.

Figure 12 presents the variation in the accumulative dissipated energy with *N* for typical tests for relative densities ranging from 30% to 80%. For the nonplastic silt under isotropic consolidation, Figures 12(a) to 12(f) shows that the energy accumulation is insignificant at the beginning but accelerates when the cyclic strain starts to develop rapidly for CSR=0.183 (Figure 12c) and reaches a value of 3.28 kJ/m^3 when cyclic failure occurs with 5% double amplitude axial strain. In Fig. 11d, although a larger energy dissipation is required for failure for D_r=60% (W_f = 4.018 kJ/m^3), *W–N* relationship exhibits a similar upward concave tendency as that of dense samples (Dr=70% and 80%).

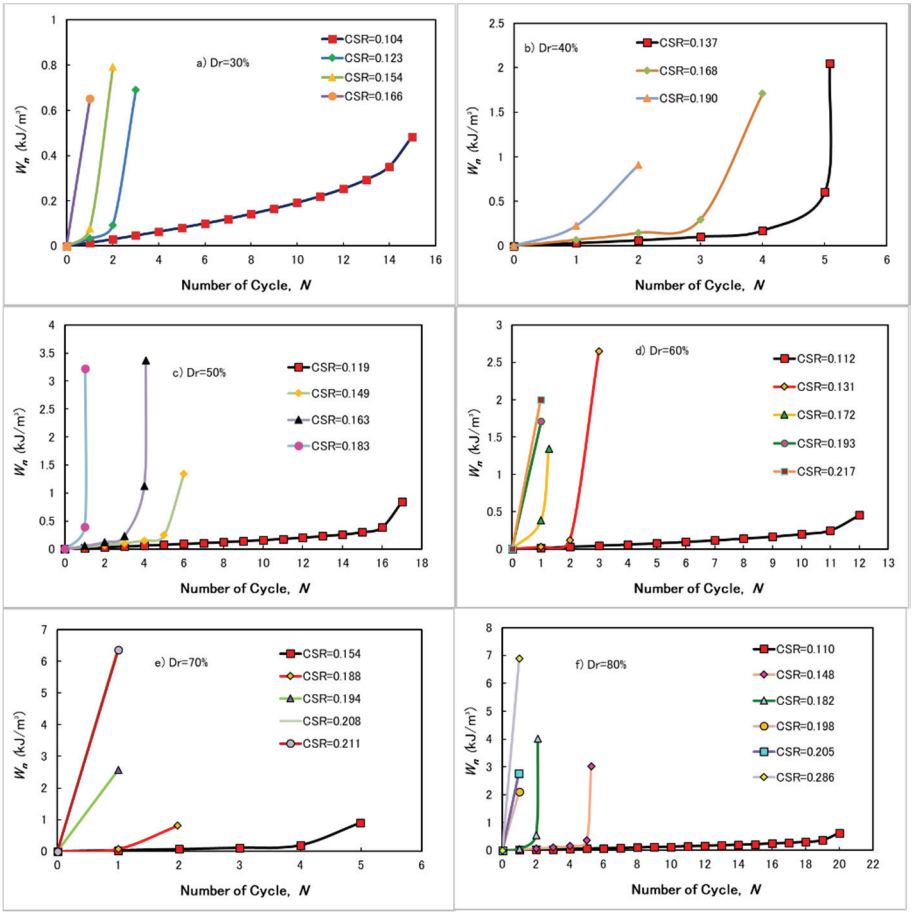

Figure 12 - Variations of accumulative dissipated energy with the number of cycles for 30% to 80% relative densities and different CSR values

The constraints of the model are limited by the conditions enlisted in Table 1. A wide range of relative densities from 30% to 80% were used, use of relative density values out of this range is inconvenient. The soil is a commercially available silt, which is free of coarse-grained content. These results cannot be used for modeling silt behavior of different plasticity levels. For each relative density, the tests were initiated by selecting a very small CSR value and then the cyclic stress ratio was gradually increased until number of cycles to liquefaction drops to one. Thus, the variation of CSR values could be analyzed in a very wide range. About the potential sources of error, calculation of area covered by deviatoric stress-axial strain plot is not prone to errors. However, the empirical approach for calculation of PEC can be discussed. Since it is empirical, we found that this approach can be used for evaluation of pore pressure development pattern of silts. Therefore, sources of error in modeling can be associated with PEC value, further studies can discuss the method for obtaining PEC, by performing cyclic tests on different types of soils. The changes in coefficient of determination (R^2) and root mean square error (RMSE) values for each modeling attempt is calculated and tabulated in Table 1. Analyzing the results, it is observed that the performance of model is higher for increasing CSR values, which can be observed by decreasing RMSE and increasing R^2 values, regardless of the relative density (D_r) value.

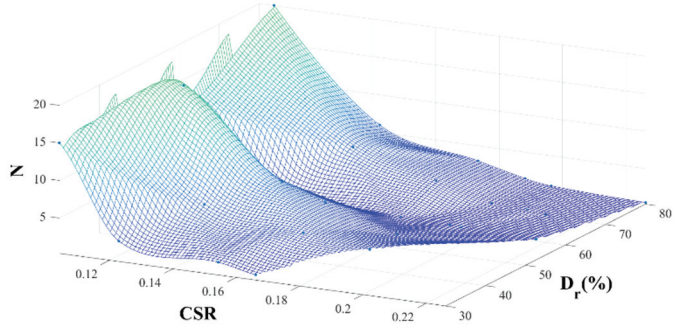

(a)

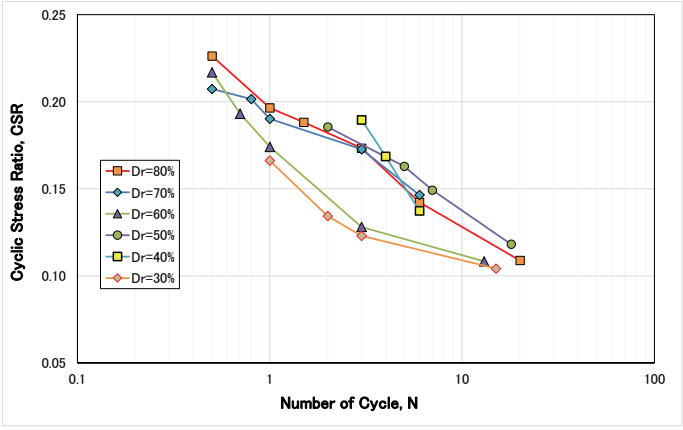

(b)

Figure 13 - a) Variation of number of cycles to liquefaction with varying CSR and D_r b) Biaxial representation of data

Lastly, Figure 13a presents a 3D plot of CSR, D_r and N. It is clear that at lower relative density and higher CSR values, the specimen liquifies after a lower number of cycles. On the other hand, it was also observed that, for a certain CSR value, increasing relative density causes an increase in number of cycles to liquefaction. Figure 13b also show that as the cyclic stress ratio increases for any sample, the number of cycles to reach initial liquefaction decreases.

5. CONCLUSIONS

In this study, the applicability of a previously proposed energy-based model for analysis of the pore pressure development in sands on a nonplastic silt was questioned. In this regard, by use of a previously published data set consisting of 61 cyclic triaxial test results was utilized. The tests were performed at 6 different relative densities (D_r) *ranging from 30% to 80%* and 10 different cyclic stress amplitude ratios (CSR). In the current energy-based model, the key parameters of pore water pressure development and shear deformation were determined as relative density, cyclic stress ratio and number of cycles. In order to analyze these behaviors, areas covered by 852 deviator stress–axial strain hysteresis loops of from these tests were calculated. After calculation of area, PEC (Pseudo Energy Capacity) values were obtained in order to calculate the energy-based pore water pressure ratio (r_u). Afterwards, the variation of pore water pressure ratio with number of cycles in 28 liquefied test were obtained and comparative pore water pressure – number of cycle plots of liquefied tests at each relative density were presented. Following conclusions can be drawn from this study:

- The energy-based pore pressure behavior models proposed so far were mostly applied for analysis of dynamic test results on clean sands. Applying the model by use of test results on non-plastic silt specimens (28 liquefied tests from a total of 61), the concordance among the model outcomes and experimental r_u values were provided.
- In 28 liquified tests, the model-based development pattern of energy-based pore pressure ratios were in a similar trend with experimental records.
- In 50% (14/28) of the specimens liquefied, the modeled r_u values reached 1 at lower number of cycles, compared to experimental outcomes.
- When liquefied experiments with six different relative densities were examined; particularly the specimens liquefied within the first cycle, the number of cycles in real and model outcomes to reach a value of $r_u = 1$ are approximately the same. For this reason, a comparison of the experimental and energy-based r_u revealed that, differences between the number of cycles to reach liquefaction state was not remarkable. However, the performance of energy-based model was better for samples liquefied after 1 cycle. It should be noted that, the specimens liquefied in earlier number of cycles, with reference to the experimental records.
- As the CSR values are reduced, it is observed that the modeling ability of energy-based model is increased.

- The energy-based pore pressure development model, which was previously proposed for clean sand soils, can be reliably applied to analyze behavior of non-plastic silts.
- Methods of estimating pore water pressure with constitutive models require a large number of input parameters that are not easy to determine in the absence of advanced laboratory test results. For this reason, it is thought that empirical or semi-empirical models will be used more widely for a while. However, in cases where laboratory test results are sufficient, energy-based pore pressure calculation yields very efficient results.
- The limitation of energy-based pore pressure modeling is that the test data should be firm, and the entire stress-strain history of specimens should be known. However, the advantage of energy-based studies is that there is no need to convert the earthquake wave motion to equivalent number of cycles in stress-based studies.
- Analyzing past studies, it was observed that experimental efforts are concentrated on testing clean sands and sand-silt mixtures. This study demonstrates that the energy-based pore water pressure model can also be used to simulate the pore pressure generation behavior of non-plastic silts. Comparison of the test results with model outcomes reveal that energy-based pore water pressure models are viable tools for simulation of pore water pressure development pattern of non-plastic silts, within a certain confidence interval. It should be emphasized that use of the model is limited to only non-plastic silts, more effort is needed to prove the applicability of method to a wide range of grain sizes, shapes, size distributions and plasticity indices.

References

[1] Kramer, S. L., Geotechnical earthquake engineering, Prentice-Hall Civil Engineering and Engineering Mechanics Series, Upper Saddle River, NJ: Prentice Hall. 1996.

[2] Towhata, I., Geotechnical earthquake engineering. Berlin Heidelberg: Springer – Verlag, 2008.

[3] Amini, P. F., and Noorzad, R., Energy based evaluation of liquefaction of fiber-reinforced sand using cyclic triaxial testing. Soil Dynamics and Earthquake Engineering, 104, 2018.

[4] Scott, R. F., Principles of soil mechanics, Addison-Wesley, Reading, Mass. 1963.

[5] Lambe, T. W., and Whitman, R. V., Soil mechanics, Wiley, New York. 1969.

[6] Dobry, R., Ladd, R. S., Yokel, F. Y., Chung, R. M., and Powell, D., Prediction of pore-water pressure buildup and liquefaction of sands during earthquakes by the cyclic strain method. National Bureau of Standards Building Science Series 138, National Bureau of Standards, U.S. Dept. of Commerce, Washington, D.C. 1982.

[7] Green, R. A., Mitchell, J. K., and Polito, C. P., An energy-based excess pore-water pressure generation model for cohesionless soils. Proc., John Booker Memorial Symp.-Developments in Theoretical Geomechanics, D. W. Smith and J. P. Carter, eds., Balkema, Rotterdam, Netherlands, 383–390, 2000.

[8] Seed, H.B., Martin, P.P., and Lysmer, J. (1975). The generation and dissipation of pore water pressures during soil liquefaction. Rep. No. EERC 75-26, Univ. of California, Berkeley.

[9] Booker, J.R., Rahman, M.S., and Seed, H.B. (1976). GADFLEA—A computer program for the analysis of pore pressure generation and dissipation during cyclic or earthquake loading. Rep. No. EERC 76-24, Earthquake Engineering Research Center, Univ. of California at Berkeley, Berkeley, California.

[10] Dobry, R., Ladd, R., Yokel, F., Chung, R., and Powell, D. (1982). Prediction of pore water pressure buildup and liquefaction of sands during earthquakes by the cyclic strain method. NBS Building Science Series 138, National Bureau of Standards, U.S. Dept. of Commerce.

[11] Cetin K.O, and Bilge, H.T. (2012). Cyclic Large Strain and Induced Pore Pressure Models for Saturated Clean Sands. Journal of Geotechnical and Geoenvironmental Engineering, 138 (3).

[12] Jafarian Y, Towhata I., Baziar M.H., Noorzad A. and Bahmanpour A., (2012). Strain energy based evaluation of liquefaction and residual pore water pressure in sands using cyclic torsional shear experiments. Soil Dynamics and Earthquake Engineering. 35, 13–28.

[13] Elgamal, A., Yang, Z., Parra, E. and Ragheb, A. (2003). Modeling of cyclic mobility in saturated cohesionless soils. Int. J. Plast., 19(6), pp. 883–905.

[14] Polito, C.P., Green, R.A., and Lee, J. (2008). Pore pressure generation models for sands and silty soils subjected to cyclic loading. J. Geotech. Geoenviron. Eng., 134(10), 1490–1500.

[15] Baziar M.H., Shahnazari H., and Sharafi H., (2011). A laboratory study on the pore pressure generation model for Firouzkooh silty sands using hollow torsional test International Journal of Civil Engineering, 9 (2).

[16] Lee, K., and Albaisa, A. (1974). Earthquake induced settlements in saturated sands. J. Geotech. Eng. Div., 100(4), 387–405.

[17] De Alba, P., Chan, C.K., and Seed, H.B. (1975). Determination of soil liquefaction characteristics by large scale laboratory tests. EERC Rep. No. 75-14, Univ. of California, Berkeley, CA.

[18] Seed, H.B. and Lundgren R. "Investigation or the effect or transient loading on the strength and deformation characteristics of saturated sands",· Proc ASTM, vol. 54, pp 1288-1306.

[19] Seed, H.B. and Fead, J.W.N. (1959) "Apparatus for Repeated Load Tests on Soils" Special Technical Publication No 204 ASTM Philadelphia.

[20] Seed, H.B. (1960). Soil Strength During Earthquakes, Proceedings of World Conference of Earthquake Engineering, vol I, pp 183-194.

[21] Nemat-Nasser, S., and Shokooh, A., A unified approach to densification and liquefaction of cohesionless sand in cyclic shearing. Can. Geotech. J., 16(4), 1979.

[22] Davis, R. O., and Berrill, J. B., Energy dissipation and seismic liquefaction in sands. Earthquake Eng. Struct. Dyn., 10(1), 1982.

[23] Davis, R. O., and Berrill, J. B., Pore pressure and dissipated energy in earthquakes—Field verification. J. Geotech. Geoenviron. Eng., 127(3), 2001.

[24] Yamazaki, F., Towhata, I., and Ishihara, K., Numerical model for liquefaction problem under multi-directional shearing on horizontal plane. Proc., 5th Int. Conf. on Numerical Methods in Geomechanics, Vol. 1, Taylor & Francis Group, London, 1985.

[25] Law, K. T., Cao, Y. L., and He, G. N., An energy approach for assessing seismic liquefaction potential. Can. Geotech. J., 27(3), 1990.

[26] Hsu, H. L., Study on the relationship between shear work and pore-water pressure for saturated sand in undrained test. First Int. Conf. on Earthquake Geotechnical Engineering, K. Ishihara, ed., Vol. 1, Balkema, Rotterdam, Netherlands, 1995.

[27] Wang, G. J., Takemura, J., and Kuwano, J., Evaluation of excess pore-water pressures of intermediate soils due to cyclic loading by energy method. Computer methods and advances in geomechanics, J. X. Yuan, ed., Balkema, Rotterdam, Netherlands, 1997.

[28] Green, R. A., Energy-based evaluation and remediation of liquefiable soils. Ph.D. dissertation, Civil Engineering, Virginia Polytechnic Institute and State Univ., Blacksburg, VA, 2001.

[29] Cetin, K. O., and Bilge, H. T., Cyclic large strain and induced pore pressure models for saturated clean sands. Journal of Geotechnical Geoenvironmental Engineering. 2012.

[30] Polito, C., Green, R. A., Dillon, E., Sohn, C., Effect of load shape on relationship between dissipated energy and residual excess pore pressure generation in cyclic triaxial tests. Can Geotech J. 50(11):1118–28, 2013.

[31] Azeiteiro, R.J.N. Coelho, P. A. L. F., Taborda, D. M. G., Grazina, J. C. D., Energy based evaluation of liquefaction potential under non-uniform cyclic loading. Soil Dynam Earthq Eng. 92:650–65, 2017.

[32] Karakan, E., Tanrınıan, N., and Sezer A., Cyclic undrained behavior and post liquefaction settlement of a nonplastic silt, Soil Dynamics and Earthquake Engineering, 120, 2019a.

[33] Karakan, E., Sezer A., and Tanrınıan N., Evaluation of effect of limited pore water pressure development on cyclic behavior of a nonplastic silt, Soils and Foundations, 59(5), 2019b.

[34] Pan, K., Yang, Z. X., Evaluation of the liquefaction potential of sand under random loading conditions: equivalent approach versus energy-based method. Journal of earthquake engineering. 24 (1) :59–83.2020.

[35] Karakan, E., Validation of pore water pressure model calibration parameters for non-plastic silt. *Fresenius environmental bulletin*, *29*(12), 2020.

[36] Baziar, M.H., Sharafi, H., Assessment of silty sand liquefaction potential using hollow torsional tests—an energy approach. Soil Dynam Earthq Eng. 31(7), 2011.

[37] Xu, C., Feng, C., Du, X., Zhang, X., Study on liquefaction mechanism of saturated sand considering stress redistribution. Engineering Geology. 264, 2020.

[38] Zhang, W., Goh, A., Zhang, Y. M., Chen, Y. M., Xiao, Y., Assessment of soil liquefaction based on capacity energy concept and multivariate adaptive regression splines. Eng Geol. 188:29–37, 2015.

[39] Yang, Z. X., Pan, K., Energy-based approach to quantify cyclic resistance and pore pressure generation in anisotropically consolidated sand. J Mater Civ Eng. 30 (9), 2018.

[40] Kokusho T., Liquefaction potential evaluations: energy-based method versus stress based method. Can Geotech J 2013;50(10) 2013.

[41] ASTM, Standard Test Methods for Maximum Index Density and Unit Weight of Soils Using a Vibratory Table: D4253-16e1, American Society for Testing and Materials, 14p. 2016.

[42] ASTM, Standard Test Methods for Minimum Index Density and Unit Weight of Soils and Calculation of Relative Density: D4254-16, American Society for Testing and Materials, 9p. 2016.

[43] JGS 0520-2000, Preparation of Soil Specimens for Triaxial Tests.

[44] JGS 0541-2000, Method for Cyclic Undrained Triaxial Test on Soils.

[45] Tanrınıan, N., Post-Liquefaction Settlement Behavior of Non-Plastic Silts, Master Thesis, Ege University, İzmir. 2018.

Turkish Journal of Civil Engineering, 2024 95-123, Paper 771, ***Research Article***

Investigation of the Performance of Bio-Oils from Three Different Agricultural Wastes as Rejuvenators for Recycled Asphalt

Beyza FURTANA YALCIN[1*]
Mehmet YILMAZ[2]

ABSTRACT

The aim of this study was to investigate the possibility of using bio-oil obtained from pinecones, olive mill pomace, and wheat straw as rejuvenators for the reuse of aged asphalt binders. Additionally, the biomass used for bio-oil production was selected from waste materials. Therefore, it makes great contributions to both the environment and the economy. B50/70 bitumen was selected as the neat binder. The bio-oils used in the study were obtained as a result of pyrolysis. Bio-oil rejuvenators at 5%, 10% and 20% by the weight of the binder were added to the aged binder obtained from recycled asphalt mixtures to obtain bioregenerated asphalts. The physical and rheological properties of bioregenerated asphalts were investigated and not compared on neat and aged binders through penetration, softening point, rotational viscometer and dynamic shear rheometer tests. In addition, the effects of temperature and biooil content on complex modulus properties were examined using response surface methods. It was found that while the bio-oils increased the penetration values of the aged binders, they also decreased the softening point and viscosity values. The bio-oils significantly modified rutting resistance of the aged binder. The addition of bio-oil improved the viscous components and can rejuvenate the viscoelastic properties of aged asphalt binders to that of almost the original level. In addition, response surface methods results showed that the interactions between both independent variables were effective. Finally, high coefficient of determination (R^2) values indicated good agreement between the actual and predicted values. It was recommended as a result of the study that 20% concentration of bio-oil should be used to rejuvenate the aged asphalt binder for reuse in pavement construction.

Keywords: Bio-oil, rejuvenator, aged asphalt, rheological properties, response surface methodology.

Note:
- This paper was received on June 26, 2023 and accepted for publication by the Editorial Board on December 22, 2023.
- Discussions on this paper will be accepted by July 31, 2024.
- https://doi.org/10.18400/tjce.1320185

1 Firat University, Department of Civil Engineering, Elazığ, Türkiye
bfyalcin@firat.edu.tr - https://orcid.org/0000-0003-4565-7324

2 Firat University, Department of Civil Engineering, Elazığ, Türkiye
mehmetyilmaz@firat.edu.tr - https://orcid.org/0000-0002-2761-2598

* Corresponding author

1. INTRODUCTION

The consumption of bitumen used in road construction and maintenance has paved the way for prices of bitumen obtained from petroleum crude to significantly increase [1-4]. In addition, a trend to sustain environmentally friendly coating has started [2, 5-8]. Environmentally friendly pavement is the reuse of recycled pavement. Thus, instead of traditional bitumen, alternative binders have been investigated. In this sense, reclaimed asphalt pavement (RAP) is among the effective ways to decrease bitumen consumption [9]. Aging of asphalt binders during construction and service time poses a significant problem in pavement engineering [10-12]. Oxidation and loss of volatile substances are the primary reasons for aging of asphalt binders. They lead asphalt binders to increase in viscosity and to be harder than fresh asphalt binders [13, 14]. In order to overcome these problems, many types of rejuvenating RAP binders have been used [9, 15-19].

Of a number of renewable energy sources, bio-oil draws a considerable attention as a result of its advantages such as wide range of sources, high efficiency and low prices [2, 20, 21]. Therefore, agricultural and natural biomass resources are of crucial importance. Although grain, legumes, fruits and vegetables are the primary foods in human nutrition, they also lead to a large amount of waste. Among them, wheat is one of the most common grain produced in the world and in Turkey. The wastes of grain such as stem, straw, and stubble are called agricultural waste [22]. These wastes produced as a result of their harvesting and processing or left in the cultivated area cannot be utilized appropriately [23, 24]. The use of these wastes for fuel is a widely practiced method. However, their burning results in greenhouse gases which cause global warming. It is reported that only in Spain, 11 Tg (1 Tg=109 kg) of carbon dioxide, 23 Gg (1 Gg=106 kg) of nitrogenous compounds and 80 Gg particulate matter are released into the atmosphere annually due to the burning of grain wastes [25]. In addition, many animals will be burned as a result of the burning of stubble. Therefore, the use of straw waste as a rejuvenator will offer great benefits to the economy, environment and ecosystem. Wheat straw is obtained as a plentiful by-product of wheat, which is produced 529 million tons/year worldwide. Asia provides 43% of global wheat production and is the largest production region. The typical harvest of wheat straw is 1.3-1.4 kg per kg of wheat grain. Having an area of 78 million hectares, Turkey has a rich ecological diversity. Forests have a remarkable place in this richness in terms of species and composition. As of 2020, forest areas covered 29.4% of the country's area. In addition, the pine forests in Turkey cover 54,000 ha^2. The General Directorate of Forestry reported that the total pine cone production was approximately 3500 tons in 2006. In the world, extensive amounts of cone are produced every year in pine fields grown especially for the pulp and paper industry [26]. Olive mill pomace is a by-product from olive oil factories and is an important biomass in Mediterranean countries. It is a solid waste which is composed of olive seeds and pulp as a result of olive oil production. In olive oil production, “oil-free olive mill pomace” is obtained by removing the 2-12% of oil in “crude olive mill pomace”. In world olive oil production, Turkey follows Spain, Italy and Greece. In Turkey, 1.000.000 tons of olives and olive oil are produced annually and approximately 450,000 tons of olive mill pomace is obtained. Similar to other wastes, olive mill pomace is generally used as fertilizer or for fuel in industry [27]. Bio-oil is mainly produced through biomass pyrolysis process. Pyrolysis are divided into two types as slow pyrolysis and fast pyrolysis. The difference between slow and fast pyrolysis is the residence time in the pyrolysis process. Although the residence time of the latter is less than 10 seconds and the residence time of the former differs from 5 minutes to 12 hours [28]. As

a result of pyrolysis, three main components are produced, including biochars, gases and liquids. The liquid is considered bio-oil [29-31]. Bio-oils have been increasingly used to modify or partially replace asphalt binders [2, 32, 33].

Previous studies revealed that bio-oils are able to soften asphalt binders and contribute to enhancing their low temperature performance [34, 35]. Furthermore, some researchers focused on the potential of reclaimed asphalt pavement to be restored to its original condition. Several types of bio-oil such as waste vegetable oil, organic oil and distilled oil can be used as rejuvenators. The rejuvenation effects differ depending on the types of resource. In particular, it rejuvenated the aged binder by reducing the performance grade of the aged binder with a waste vegetable oil content of 12 wt% from PG 94-12 to PG 64-22. Therefore, the cracking resistance of the binder decreased [17]. By adding 1.75–2% by weight to the aged binder, the bio-oil rejuvenator obtained from biodiesel residue increases the crack resistance at low temperature by compensating for the loss of light components of the aged binder [36]. Waste cooking oil with a concentration of 3-4% by weight can rejuvenate the physical and rheological properties of bitumen with a penetration degree of 40/50 by approximating those with a penetration degree of 80/100 [37]. In their study, Rzek et al. obtained rejuvenator through the waste tires pyrolysis. They added the rejuvenators to the recycled asphalt mixtures at three different rates. They concluded that the addition of a recently developed alternative rejuvenator at the rate of 20% increased the utilization rate of the reclaimed asphalt. The standard mechanical tests and rheological tests applied to the asphalt mixtures showed that the addition of this alternative rejuvenator to the asphalt mixtures could increase the recycled asphalt ratio up to 60% [38]. Avsenik et al. investigated the effect of bio-oils produced as a result of the pyrolysis of waste tires on aged bitumen. They used lab-aged bitumen with a penetration degree of 50/70 using reference short- and long-term aging procedures. They evaluated the effect of rejuvenating addition at four different rates (3%, 5%, 10% and 20%) on aged and unaged bitumen through standard mechanical and rheological tests. The mechanical and rheological experiments indicated that the rejuvenator was suitable for the modification of aged bitumen [39]. Nizamuddin et al. used bio-oil produced from hydrothermal liquefaction of waste plastic films (linear low-density polyethylene - LLDPE) for the rejuvenation of laboratory aged bitumen. The neat binder caused the aged binder to harden; however, they determined that bio-oil rejuvenator significantly softened the aged binder [40]. Mirhosseini et al. conducted a laboratory-based research study evaluating the performance of asphalt mixtures prepared with binders modified with palm kernel oil (DSO) containing different components. They determined that while the rutting performance of the mixtures deteriorated, the addition of DSO increased the fatigue life of samples containing 20% RAP by up to 15% [41].

Mostly, the properties of bio-rejuvenators rely on the biomass. To the best of the researchers knowledge, there are no studies on rejuvenation of RAP binder in which a bio-oil produced from wheat straw, pine cone and olive mill pomace is used as a rejuvenator. The usage of bio-oil as a rejuvenator to recycle the aged binder allows the reuse of waste biomass resources and waste construction materials, which contributes to the environment and sustainable development. In this study, the physical and rheological properties of bio-rejuvenated binders were examined. To do this, bio-based rejuvenators obtained from wheat straw, pine cone and olive mill pomace were used to rejuvenate the aged binder of RAP. In addition, the effect of these three different biorejuvenators on the aged binder was evaluated by comparison. In addition, the effect of these three different biorejuvenators on the aged binder was compared.

2. MATERIAL AND METHODS

2.1. Neat binder and reclaimed asphalt pavement

B50/70 grade bitumen obtained from TÜPRAŞ Batman Refinery was used in the study. The general properties of the bitumen are shown in Table 1. In addition, single-source reclaimed asphalt pavement (RAP) obtained from Elazig Municipality, Turkey was used. It was stored in sealed containers to prevent environmental effect. The reason for using this RAP material was that B50/70 grade bitumen was used in the initial production phase. The aim of this study was to add rejuvenators to the RAP binder and restore the initial hardness of bitumen. Therefore, B50/70 grade bitumen was preferred as neat bitumen. In order to choose HMA mixing and compaction temperatures, equiviscous temperature ranges are also established using the rotational viscometer [42]. Viscosity-temperature graphs are used to calculate mixing and compaction temperatures.

Table 1 - General features of bitumen

Properties	Unit	Standard	Results
Penetration	dmm	EN 1426	56
Softening point	°C	EN 1427	53.3
Flash Point	°C	EN ISO 2719	245
Density	g/cm^3	ASTM D70 - 18a	1.015
Elastic Recovery	%	EN 13398	30
Viscosity 135°C /165°C	cP	ASTM D4402	737.5/225
Mixing temperature range	°C	-	159-165
Compaction temperature range	°C	-	145-151

2.2. Biomass

In the study, ground wheat straw, ground pine cone and olive mill pomace were used as biomass sources. The materials were obtained from Çanbaylar company located in the province of Elazig. In order to use material with the same granule size, the materials passing through No. 30 sieve were used. Thus, it was aimed that the size of the biomass did not have an influence on the experimental results.

2.3. Properties of the Reclaimed Asphalt Pavement (RAP) Material

The RAP used in the study was made on the RAP taken from the Elazığ central highway. This RAP material is milled from a highway that has been used for 10 years. The bitumen properties of this RAP material used 10 years ago were taken from the 8th Regional Directorate of Highways. For this reason, the reference 50/70 bitumen was chosen. Sampling of the RAP material was carried out in line with the EN 932-1 standard [43]. An extraction experiment was performed to examine the gradation of the reclaimed asphalt pavement material (Figure 1a). As a result of the extraction experiment, the amount of bitumen in the

RAP material was determined as 4.6%. The aged binder separated from the reclaimed asphalt binder through extraction was recovered using a rotary evaporator consistent with the TS EN 12697-3+A standard [44] (Figure 1b). The bitumen content was determined by performing 50 extraction experiments. Throughout the study, reclaimed aged binder was used.

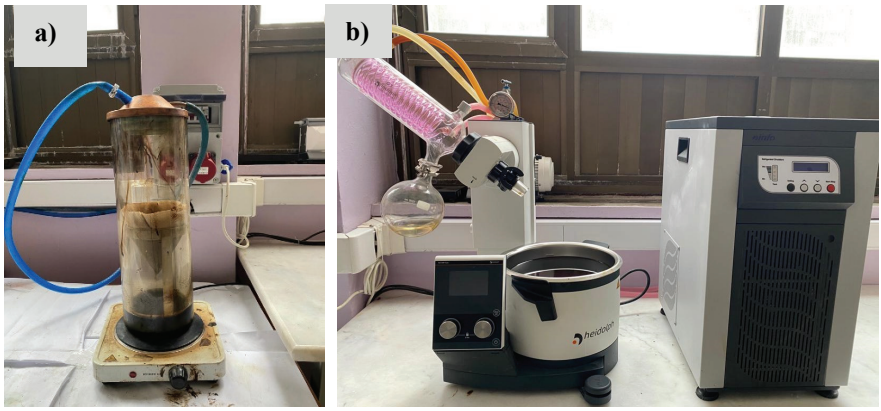

Figure 1 - a) Extraction device b) Rotary evaporator

2.4. Bio-oil Production

Three different rejuvenators obtained from bio-based agricultural products were used. Accordingly, wheat straw, pine cone and olive mill pomace bio-oil were used in the study. In order to use material with the same granule size, they were sieved through No. 30 sieve. Thus, the size of the biomass was selected so that it prevents affecting the experimental results. A slow device was used for the pyrolysis of biomass. The slow pyrolysis experimental setup consisted of a high temperature resistant cylindrical vessel with an inner diameter of 150 mm and a height of 240 mm in which the biomass was placed, a programming device box where the test temperature could be adjusted, a water-cooling system and a chamber where the biogas was condensed into oil after cooling. The slow pyrolysis experimental setup is shown in Figure 2a.

In the study, 1000 grams of biomass was placed in the chamber of the device each time in order to eliminate the effect of biomass amount on the carbonization. Accordingly, 1000 grams of dried biomass sample was exposed to pyrolysis at 500°C in a fixed bed slow pyrolysis setup shown in Figure 2b. This temperature was preferred on the basis of the studies in the literature [45]. Liquid pyrolysis product (bio-oil) was obtained as a result of condensing the pyrolysis vapors in a water-cooled condenser. In addition, non-condensable pyrolysis gases were burned and disposed of in a fume hood at the exit of the setup. The pyrolysis process was continued until the gas output stopped. The obtained liquid pyrolysis product and pyrolysis residue biochar were cooled and then weighed. By subtracting the total weight of the products from the amount of dry biomass used initially, the amount of non-condensed gas product was calculated. The results are presented in Table 2. The liquid products (Figure 2) were subjected to a vacuum evaporation (Heidolph rotary evaporator) process at 80°C and 200 mmHg pressure in order to separate the water and organic acids from the oil phase in a vacuum rotary evaporator since they contained a high percentage of water (Figure 1). As a

result, high viscosity oil products were obtained for pine cone, olive mill pomace and wheat straw, in which organic acids such as water and acetic acid were removed at a rate of 12.75%, 11.56% and 10.95% by weight, relative to the amount of dried biomass.

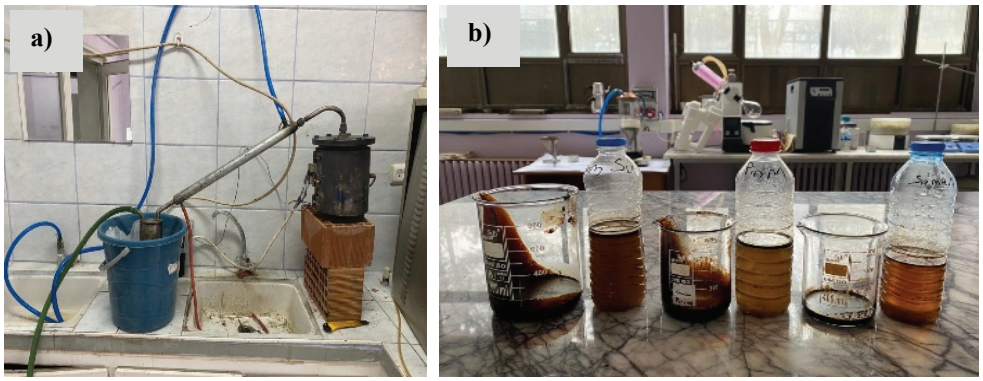

Figure 2 - a) The slow pyrolysis experimental setup, b) Bio-oil and water samples obtained as liquid product as a result of pyrolysis

Table 2 - Yields of liquid bio-oil, bio-char and non-condensed gas obtained as a result of pyrolysis of biomass

Biomass	% Bio-oil yield	% Bio-char yield	% Gas yield
Pine cone	37.92	32.09	29.99
Olive pomace	31.83	32.52	35.65
Wheat straw	27.13	31.57	41.30

2.5. Preparation of Modified Bitumen

In the study, it was aimed to bring the traditional and rheological properties of aged bitumen closer to the traditional and rheological properties before aging. The purpose of using the three ratios in the study is to capture the traditional and rheological properties of the aged binder and the traditional and rheological properties of the unaged binder. Three different ratios (5%, 10% and 20%) were used for the bio-oils. The modified bitumen used in the study was prepared as stated below.

First, the aged binder obtained from RAP was heated in a vacuum furnace at 140±5°C for 30 minutes to become fluid. The fluidized bitumen was poured into the metal chamber of the mixer as 400 grams and placed inside the thermal jacket on the heater source conditioned at 140±5°C to provide a homogeneous heat source, and then waited until the heater reached thermal equilibrium. Rejuvenators at different percentages by weight of the determined bitumen were added into the hot bitumen and mixed with a mechanical mixer operating at 500 rpm for 40 minutes, and modified bitumen was obtained. The same procedure was followed for all rejuvenators. This modification was preferred on the basis of the studies in the literature [13].

After the mixing process was completed, the obtained modified bitumen was transferred to the glass beaker. The same procedure was adopted for mixing each time in order to avoid its interference the test results [45]. Two sets of modified bitumen were prepared for each modification process. Three samples were prepared for each experiment. The abbreviations used for bituminous binders are shown in Table 3.

Table 3 - The abbreviations used for bituminous binders

Biomass	**Bio-oil content (%)**			
	0	5	10	20
Pine cone		K5	K10	K20
Olive pomace		P5	P10	P20
Wheat straw		S5	S10	S20
Neat binder	SB			
Recycled aged binder	RAP			

2.6. Conventional Properties Test

Conventional physical properties of the asphalt binder were determined, including penetration (ASTM D5) and softening point (ASTM D36) at 25°C.

2.7. Rotational Viscometer Test

The rotational viscometer (RV) test is used to determine the viscosity characteristics of bituminous binders at high temperatures. The rotational viscometer values of bituminous binders were determined using a Brookfield DV-III device according to ASTM D44402 standards. In the study, viscosity values of neat binder samples and samples of binders with waste oils were measured at two different temperatures (135°C and 165°C).

2.8. Dynamic Shear Rheometer Test

Determination of complex shear modulus (G*) and phase angle (δ)

Dynamic shear rheometer (DSR) is a test method used to characterize viscous and elastic behaviors of bituminous binders and moderate and high temperatures. In the DSR test, the complex shear modulus (G*) and phase angle (δ) of binders are determined. Permanent deformation is controlled by limiting them to 1.0 kPa for unaged original binders [46]. The tests were conducted by using Bohlin DSR-II rheometer on neat and modified bitumen according to ASTM D7175 standards. The tests were also conducted with a plate with 25 mm diameter and 1 mm plate clearance at 1.59 Hz frequency value, and at 52°C, 58°C, 64°C, 70°C, 76°C, 82°C and 88°C.

Multiple stress creep recovery (MSCR) test

In this study, the multiple stress creep recovery (MSCR) test was conducted according to AASHTO T350 standards on neat binders and binders with waste oils, which were prepared according to T315 [47] standards, by using 25 mm plates at 64°C, 70°C, 76°C, 82°C and 88°C. The test is conducted by applying 10 cycles of 0.1 kPa stress and 10 cycles of 3.2 kPa stress at different temperatures (Figure 3). Each cycle consists of 1 second of shear stress application and 9 seconds of the recovery period. However, this characterization contradicts the purpose of the MSCR test, where non-recoverable strain accumulates gradually at both loading rates. Therefore, 0.1 kPa cannot represent the LVE behavior of the material. With this test, whether the rejuvenators in neat binders affect the elastic recovery and rutting characteristics is determined. With the MSCR test, two parameters are obtained according to AASHTO M332. These are the percentage of recovery (R) and permanent creep compliance (J_{nr}) values. For bituminous binders, the mean recovery rates (R) of binders are calculated according to formulas 1 and 2 at 0.1 ($R_{0.1}$) and 3.2 ($R_{3.2}$) kPa shear stress levels [48].

$$R_{0.1} = \frac{\sum_{N=11}^{20} [\varepsilon_r(0.1, N)]}{10} \tag{1}$$

$$R_{3.2} = \frac{\sum_{N=1}^{10} [\varepsilon_r(3.2, N)]}{10} \tag{2}$$

Here, ε_r (0.1, N) and ε_r (3.2, N) represent the percentage of recovery at N number of cycles and 0.1 and 3.2 kPa stress levels, respectively while N represents the number of cycles at any level of stress. It was determined that the J_{nr} parameter provided a better correlation with rutting resistance according to Superpave PG criteria [49, 50]. The calculations of the fit values for permanent creep for 0.1 kPa (J_{nr} 0.1) and 3.2 kPa (J_{nr} 3.2) were presented in Formulas 3 and 4 while the calculations of the J_{nrdiff} value were presented in Formula 5.

$$J_{nr0.1} = \frac{\sum_{N=11}^{20} [Jnr(0.1, N)]}{10} \tag{3}$$

$$J_{nr3.2} = \frac{\sum_{N=1}^{10} [Jnr(3.2, N)]}{10} \tag{4}$$

$$J_{nrdiff} = \frac{(J_{nr3.2} - J_{nr0.1})}{J_{nr0.1}} * 100 \tag{5}$$

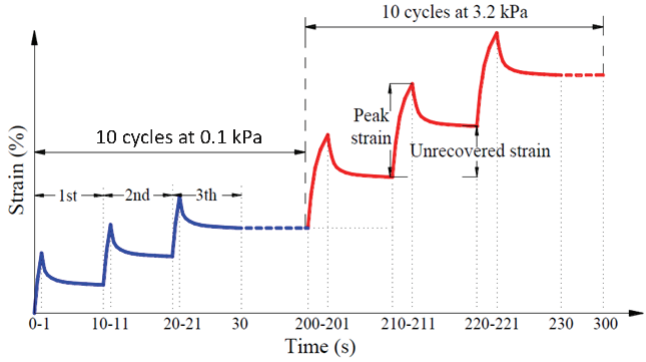

Figure 3 - Schematic representation of the MSCR system

2.9. Method of Analysis and Design of Experiments Using RSM

Response surface methodology (RSM) is a statistical instrument used in the design of experiments to increase relationships between a number of independent factors and one or more responses via mathematical concepts. In addition, it can be used to optimize the variable of response within factors in the experiment. Although RMS choice is based on the number of experimental factors and the variation level of each factor, central composite design (CCD) is largely used for its appropriateness in sequential experiments and providing the best quality predictions through the whole design space [51, 52]. In order to develop an experimental design, to provide mathematical models and statistical analysis of responses and to obtain optimal solutions for the parameters, Design-Expert v12 was used. Finally, it is calculated depending on the input parameters using the RSM, which is then evaluated for the choice of the most appropriate model that fits the correlation between the input and output parameters [36]. In this study, the effects of two input parameters, namely bio-oil in the range of 5-20% and temperature between 52°C and 88°C, were analyzed. It was calculated based on central composite design (CCD). Related studies and preliminary results in the literature were applied to reveal input parameters and corresponding domains of significance [20,21,29,37-41]. CCD is the most frequent and effective method used to statistically evaluate the interaction between independent variables and responses over the experimental range [26,27,42]. Based on the input parameters, five center point replicates were performed to allow robust evaluation of errors, with the RSM running in random order for the individual responses analyzed. Linear models developed through RSM were used for data design and analysis. The numerical variables of the experiments are converted into coded form using the following equation.

$$X_i = \frac{X_i - X_0}{\Delta X} \quad (6)$$

Here, X_i is the ith independent factor coded value, X_i, X_0, are the actual values of the center point; here ΔX, represents the step change for the ith variable. The appropriate quadratic

polynomial model suggested in the literature was used for the prediction of optimal conditions as shown in the following equation [53, 54]:

$$Y = \beta_0 + \sum_{i=1}^{n} \beta_i x_i + \sum_{i=1}^{n} \beta_{ii} x_i^2 + \sum_{i=1}^{n} \sum_{j=1}^{n} \beta_{ij} x_i x_j + \varepsilon \quad (7)$$

Y is the calculated response, β_0 is the constant value. Independent variables in coded form are defined as x_i and x_j. The coefficients β_i and β_{ii} are linear and quadratic terms. β_{ij} is the coefficient of interaction term, ε is the random error and the number of factors is defined as n. In addition, analysis of variance (ANOVA) was run to examine the appropriateness of the proposed model. The coefficients of determination (R^2 and R^2_{adj}) express the goodness of fit to the suggested model. These values can be determined using the equations below [43]:

$$R^2 = 1 - \frac{SS_{residual}}{SS_{model} + SS_{residual}} \quad (8)$$

$$R^2_{adj} = 1 - \frac{SS_{residual} / DF_{residual}}{(SS_{model} + SS_{residual}) / (DF_{model} + DF_{residual})} \quad (9)$$

where R_2 and R^2_{adj} represent the determination coefficients; SS_{res}, SS_{mod}, and DF_{res}, DF_{mod} represent the sum of squares and degrees of freedom for residual and models, respectively. The F-test was used at a 95% confidence level for the proposed models that were statistically appropriate and represented based on the p-value. Also, the F test was used to verify the adequate precision (AP) of the model, and the data-set variability was controlled through Standard Deviation (SD).

3. RESULTS AND DISCUSSION

3.1. Conventional Properties

Figure 4 shows the penetration and softening point values of the binders. Penetration values of bio-oil modified bitumen increased linearly with increasing additive content. The neat binder provided the highest penetration value and RAP binder provided the lowest penetration value. All the bio-oils rejuvenated the aged bitumen. It was found that the most effective bio-oil was the one obtained from the pine cone. Compared to the RAP binder, 5% bio-oil content did not significantly increase the penetration value. Penetration values of K5, K10 and K20 binders increased by 1.5, 2.1 and 3 times, respectively, compared to the penetration value of RAP binder. It was also found that the penetration values of P5, P10 and P20 binders increased by 1.3, 1.7 and 2.5 times, respectively, compared to the penetration value of RAP binder. Finally, compared to the penetration value of the RAP binder, the penetration values of S5, S10 and S20 binders were found to increase by 1.4, 1.9 and 2.4 times, respectively. As a result, it was found that the aged bitumen softened due to the addition of rejuvenators to the aged bitumen obtained from the recycled bitumen mixture.

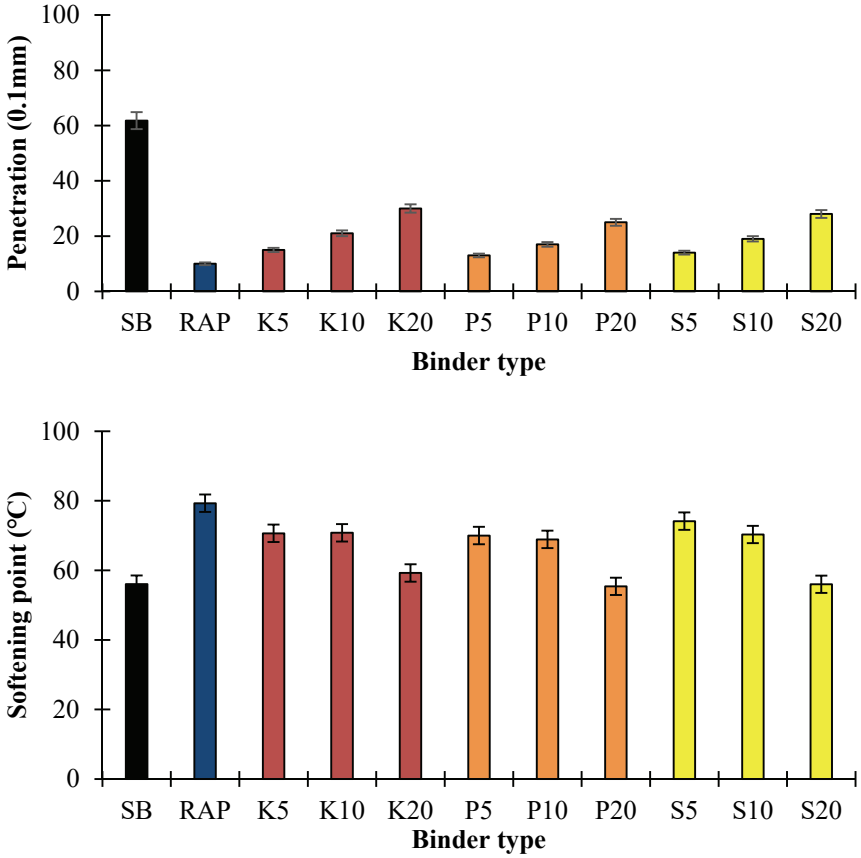

Figure 4 - Conventional properties of asphalt binders

There was a linear relationship between softening point values and biooil content. It was revealed that the softening point values of the RAP binder decreased with the addition of rejuvenators to the RAP binder. Additive contents of 20% provided almost similar softening point values. Especially after 10% additive content, softening point values of bio-oil modifications differed. The softening point value of the bitumen obtained from the recycled asphalt mixture was 1.41 times higher than that of the neat binder. This value decreased because of the fact that the rejuvenators had the feature of softening the bitumen. With the addition of 5%, 10% and 20% of the bio-oil additive obtained from pine cone to the bitumen, the softening point values decreased by 10.8%, 10.72% and 25.2%, respectively, compared to the RAP binder. The softening point values of P5, P10 and P20 binders decreased by 11.72%, 13.11% and 30.14%, respectively, compared to those of the RAP binder. Finally, softening point values of S5, S10 and S20 binders decreased by 6.43%, 11.34% and 29.38%, respectively, compared to the RAP binder. Among the three bio-oils, the most effective bio-oil in the softening point values was the one obtained from olive mill pomace. As a result, it was revealed that all three bio-oils had softening properties on the aged binder. When added

to the aged binder (RAP binder) at a rate of approximately 20% from all three bio-oils, it was seen that it reached the softening value before aging (neat binder).

3.2. Viscosity and Workability Requirement

The variation in the viscosities of the neat and modified binders at 135 °C and 165 °C are shown in Figure 5, respectively. As the additive content of biooil modified bitumen increased, a decrease was observed in viscosity values at both 135 °C and 165 °C. It was found that the viscosity value of the RAP binder at 135°C was 6338 cP which is 2.11 times the standard condition of 3000cP. In addition, negative effect on workability was revealed. Although the viscosity value of the unaged binder at 135°C was 675 cP, the viscosity value of the binder as a result of aging was 6338 cP, which indicated the effect of aging. The change in viscosity trend was similar for 135°C and 165°C. The addition of rejuvenators to the aged binder removed this problem. As the amount of bio-oil added to the aged binder increased, the viscosity values of the aged binder decreased and reached almost the pre-aging viscosity value. Compared to the aged binder at 135ºC, bitumen modified with the biooil obtained from pine cone at the rate of 5%, 10% and 20% provided 52.67%, 54.43% and 83.83% lower viscosity values, respectively. At 165 °C, it provided 35.52%, 39.47% and 69.74% lower viscosity values than the RAP binder, respectively. Bitumen modified with the biooil obtained from 5%, 10% and 20% olive mill pomace had 46.54%, 57.98% and 87.18% lower viscosity, respectively, than the aged binder at 135ºC. At 165 °C, it gave 30.26%, 43.42% and 72.37% lower viscosity values than the RAP binder, respectively. Bitumen modified with the biooil obtained from 5%, 10% and 20% wheat straw provided lower viscosity values of 38.86%, 57.59% and 86.59%, respectively, compared to the aged binder at 135ºC. At 165°C, it gave 28.95%, 42.11% and 71.84% lower viscosity values than the RAP binder, respectively. As a result, it was revealed that the use of bio-oil obtained from pine cone, olive mill pomace and wheat straw as a rejuvenator decreased the viscosity value of the aged binder and almost restored the original viscosity value. Among the bio-oils, the most effective bio-oil for viscosity values was pine cone at 5%, and olive mill pomace at 10% and 20%.

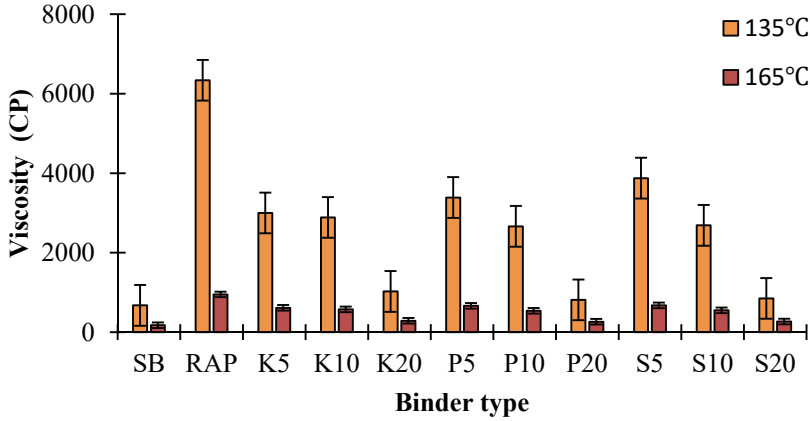

Figure 5 - Viscosity values of binders

The enhanced fluidity of the biooil and the higher content of light compounds in the biooil may play a role in the reduced viscosity of the aged binder. All the viscosity tests indicated that the biorejuvenators can reduce the stiffness of the aged binder. It was concluded that a concentration of 20% bio-rejuvenator is sufficient to rejuvenate the aged asphalt binder to be reused in pavement construction. The findings in the literature is in line with this conclusion [55-57].

3.3. Complex Shear Modulus (G*) and Phase Angle (δ)

Figure 6 shows the change in shear modulus of neat and modified binders with increasing temperature. As the temperature increased, the shear modulus decreased logarithmically, and this decrease showed a similar trend for all connector types. Accordingly, the shear modulus decreased by about 50% for every 6 degrees of temperature increase, while the G*/sinδ value of the SB binder decreased below 1000 Pa at 76 ºC, the K20, P20 and S20 binders provided 1623 Pa, 1092 Pa and 1658 Pa G*/sin δ values at 76 ºC, respectively. On the other hand, the RAP binder gave a G*/sinδ value of 21270 Pa at 76°C. Except for the neat binder, all binders do not fall below the limit condition of 1000 Pa at 88°C. Except for the neat binder, all binders did not decrease below 1000 Pa at 88°C which is the limit condition. After 76°C, the G*/sinδ values approximated to each other. It was determined that all three bio-oils reduced the high temperature performance level of bituminous binders, which is an indication of rejuvenating effect. The rejuvenation rate of the aged binder increased with the increase in the amount of bio-oil. The most effective results were obtained from pine cone at 5%, and olive mill pomace at 10% and 20%.

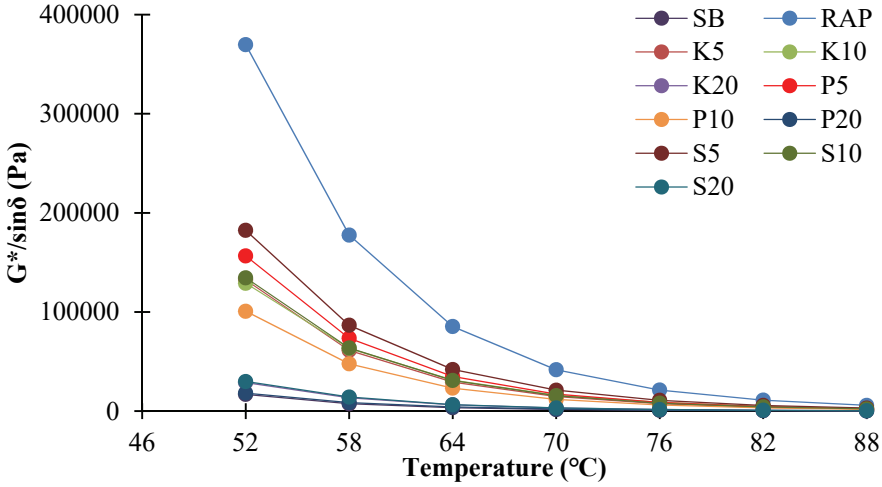

Figure 6 - Change in the G/sinδ considering temperature of the bituminous binders*

The results revealed that the properties of unaged bitumen were acquired by adding bio-oils to the aged binder, which suggests that bio-oils can be used as rejuvenating agents. The rutting parameter (G*/sinδ) is used to determine the asphalt binder's resistance to permanent

deformation at high temperature. As shown in Figure 6, after the addition of all three bio-oils to the aged binder G*/sinδ values decreased compared to the aged binder. As the amount of added biooil increased, the decrease in G*/sinδ values increased. G*/sinδ values of RAP, K20, P20, S20 and SB binders at 88°C were found to be 41750, 3167, 2108, 3267 and 1658, respectively. The higher light components and viscous content in the bio-oil are capable of stabilizing the chemical components of the aged binders and thus restoring rutting resistance to a great extent. The results of this study showed that bio-oils rejuvenated the aged bitumen and approached the G*/sinδ value of the bitumen to that of unaged bitumen (50/70). In addition, the results also indicated the positive results of the bio-oils obtained from the three waste products. The studies in the literature support the results of this study [56, 57].

Figure 7 shows the change in the phase angles of the binders with temperature. The phase angle is used to characterize the viscoelastic properties of asphalt binders. The larger the phase angle is, the more viscous components present in the asphalt binder. The phase angles of all binders increase with the increase in temperature and they exhibit a more viscous behavior. The changes in the phase angle values of the three bio-oil modifications were comparable. It was observed that the phase angle values of the bio-oil rejuvenators increased as the temperature increased. A further increase in phase angle values was observed after 10% biooil content. Oxidation and evaporation of some light compounds paved the way for the aged asphalt binder to have less viscous components than the untreated asphalt binder. As the bio-oil content in the aged binder increased, the phase angle value also increased. The phase angle value of the aged bitumen obtained from the recycled asphalt mixture was 62.01 at 70°C and the phase angle value before aging was 81.97. The aged binder provided 1.32 times higher phase angle value than the unaged binder due to the effects such as environmental, climate and traffic in asphalt mixtures. Phase angle values of SB, RAP, K5, K10, K20, P5, P10, P20, S5, S10 and S20 binder at 52°C were 72.06, 52.96, 59.01, 59.12, 67.49, 58.38, 59.87, 71.08, 56.51, 59.00 and 63.52, respectively. 58.38, 59.87, 71.08, 56.51, 59.00 and 63.52phase angle values at 88°C were 88.7, 71.13, 76.72, 76.65, 82.00, 75.95, 76.58, 84.53, 73.44, 75.99 and 80.11, respectively. The examination of the values indicated that binders with 20% bio-oil content provided approximately the phase angle value of the

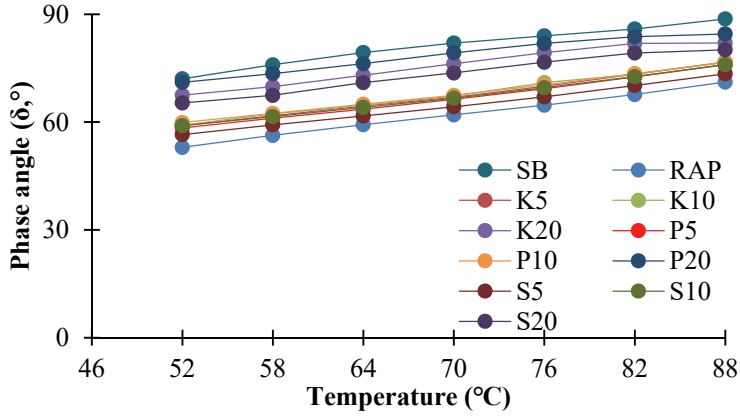

Figure 7 - Change in the phase angles considering temperature of the bituminous binders

unaged neat binder. As a result, it was found that the addition of bio-oil improved the viscous components and could rejuvenate the viscoelastic properties of aged asphalt binders to the similar level as that of the original bitumen. This is also one of the reasons why the viscosities of binders rejuvenated with bio-oils are much lower than that of aged asphalt binders. The results were in line with rotational viscosity results. Similar results were reported by Zhang et al. [57]. It was found that the most effective bio-oil was the one obtained from olive mill pomace.

Figure 8 shows the changes in the shear modulus corresponding to the phase angle of the three bio-oil modifications for different temperatures. As the amount of bio-oil used in the aged binder increased, the phase angle values increased and the G*/sinδ values decreased. P20 binder provided the closest values to that of the unaged binder (SB). These results suggest that bio-oils can be used as rejuvenators in aged bitumen.

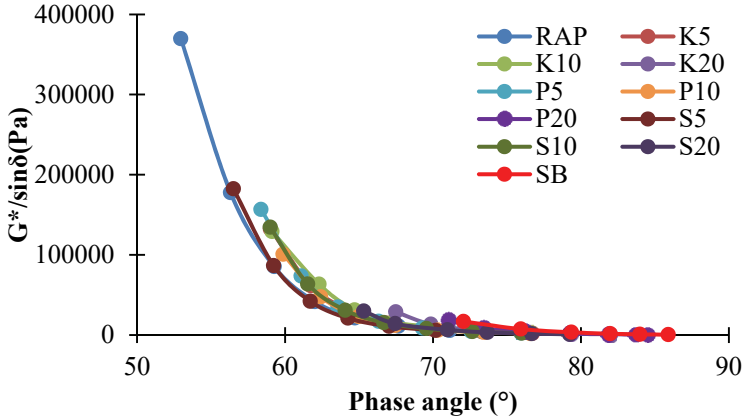

Figure 8 - Change in shear modulus versus phase angle

3.4. MSCR Test and Results

Figure 9 shows the variation of $J_{nr0.1}$ values of K, P and S added binders with temperature. The $J_{nr0.1}$ values of the binders increased with the increase in the temperature. The increase was significant after 76ºC. In the study, the J_{nr} values of the S20 binder increased the most. The RAP binder had the lowest J_{nr} value. However, with the addition of bio-oils to the RAP binder, J_{nr} values increased. Adding 10% bio-oils approached the J_{nr} values of the RAP binder to that of the SB binder. As a result of the addition of 5% and 10% bio-oil to the RAP binder, J_{nr} values provided comparable results. S20 was the fastest increasing binder after 76ºC. At 64°C, J_{nr} values of all binder were close to each other. The J_{nr} values of RAP binders with 5% and 10% content have different values, especially at high temperatures. In all three modifications, it was observed that the J_{nr} values increased significantly with the increase in the additive content. Especially after 10% additive content, there was a significant increase in J_{nr} value. At low additive contents such as 5% K, 5% P and 5% S, J_{nr} values did not change significantly. $J_{nr0.1}$ values increased with the increase in the temperature. The highest increase in $J_{nr0.1}$ values occurred in wheat straw bio-oil. The J_{nr} values of binders with 20% S additives increased by 5.22, 4.75, and 5.71 times at 64°C, 70°C and 76°C, compared to the SB binder.

The J_{nr} values increased by 4.20, 4.10, and 4.99 times in 20% P added binder and 1.91, 1,88, and 2.90 times in 20% K added binder. The highest $J_{nr0.1}$ value was observed at 88ºC for all added binders. K-added binders had the lowest $J_{nr0.1}$ values.

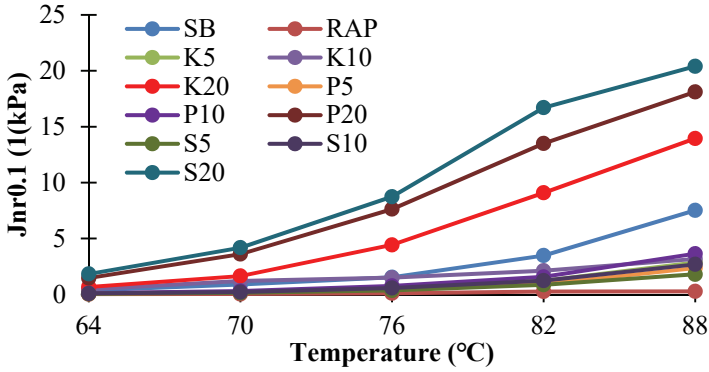

Figure 9 - Change in the $J_{nr0.1}$ considering temperature of the bituminous binders

The change in the additive content and J_{nr} values of the binders at the high shear stress level (3.2 kPa) at 64ºC is shown in Figure 10. At this stress level, a rapid increase in Jnr values was observed with the increase of bio-oil content. As the load applied to the binder increased, the Jnr values decreased. The J_{nr} values of binders containing 20% bio-oil were close to each other until 82°C. With the increase in temperature, the $J_{nr3.2}$ values also increased. S20 binder had the highest $J_{nr3.2}$ value and RAP binder had the lowest $J_{nr3.2}$ value. Binders containing 10% bio-oil had $J_{nr3.2}$ value close to that of unaged binder (SB). Different $J_{nr3.2}$ values were observed in all three additive types at 88ºC. Although the additive content did not have a considerable effect on $J_{nr3.2}$ at low temperatures, it produced an effect at high temperatures (82°C).

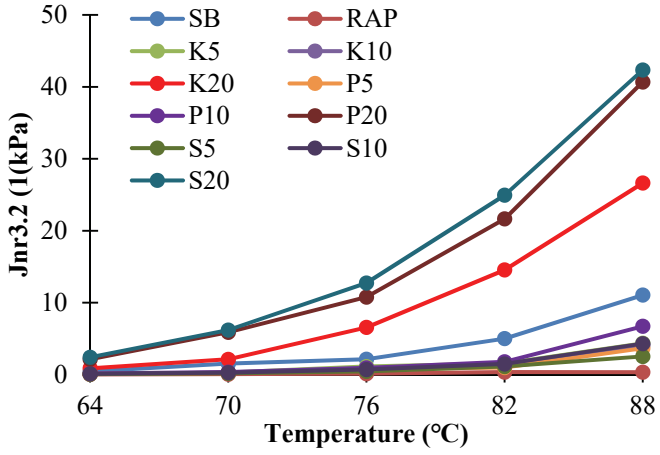

Figure 10 - Change in the $J_{nr3.2}$ considering temperature of the bituminous binders

Binders with 5% and 10% additive content provided comparable $J_{nr3.2}$ values at all temperatures except 88°C. There was a sudden increase in $J_{nr3.2}$ values in the contents after 10% biooil content. $J_{nr3.2}$ values increased at high temperatures. Accordingly, the effect of additive ratios on $J_{nr3.2}$ was greater at high temperature in all three modifications. With the increase in temperature, both $J_{nr3.2}$ values and the difference between $J_{nr3.2}$ values increased significantly.

The elastic recovery values of all binders decreased with the increase in the temperature (Figure 11). The elastic recovery values of the RAP binder decreased as the amount of biooil added to the RAP binder increased. RAP binder provided the highest elastic recovery value and S20 binder gave the lowest elastic recovery value. Especially, the elastic recovery values of P20 and S20 binders were close to those of the unaged neat binder (SB). The elastic recovery values of RAP binders containing 5% and 10% bio-oil were between 50% and 60%. It was found that the elastic recovery value of the RAP binder at 76°C increased 5.3 times compared to the neat binder (SB). These results revealed that there was an increase in the elastic recovery values of the aging bitumen and that the added bio-oil rejuvenated the aged binder. The addition of 20% wheat straw bio-oil to the RAP binder at 76°C decreased the elastic recovery value from 53% to 8%. Similarly, addition of 20% P bio-oil to the aged binder decreased the elastic recovery value 50% to 8%, restoring it to that of SB binder. These results verified the rejuvenation of the aged binder. At 82ºC, the elastic recovery value of the K20, P20 and S20 binders decreased by 68.2%, 86.6% and 86.6%, respectively, compared to the $R_{0.1}$% values of the RAP binder.

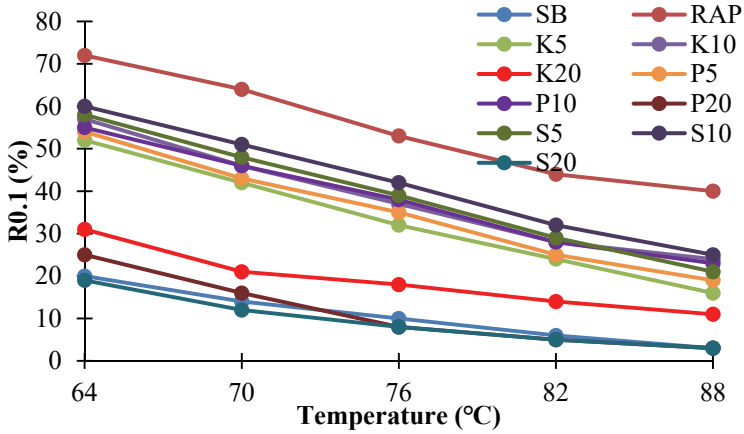

Figure 11 - %R – temperature relationship at 0.1 stress level

Figure 12 shows the change in elastic recovery values of K, P and S modified binders at 3.2 stress level with temperature. The decrease in the %R values with the increase in temperature was more evident in P and S modification. Although there was a rapid decrease until 76ºC, the rate of decrease declined after 76ºC. RAP binder had the highest elastic recovery value and the P20 and S20 binders had the lowest values. When the temperature increases from 64ºC to 76ºC, binders with 20% K, 20% P and 20% S lost 54.5%, 100% and 100% of their flexibility, respectively. As at low stress level, elastic recovery values of all modified binders decreased with the increase in temperature at high stress level. In all three modifications, the

elastic recovery values decreased when the stress increased from 0.1 kPa to 3.2 kPa. High additive ratios were more effective at high stresses than at low stresses. In contrast, the elasticity values decreased with increasing stresses. Although the elasticity of the P20 binder at 0.1 kPa stress level was 38% at 76 ºC, it decreased to 19% at 3.2 kPa stress level. Under the same conditions, the elasticity of K20 and S20 binders decreased from 37% and 42% at 0.1 kPa stress level to 12% and 27% at 3.2 kPa stress level.

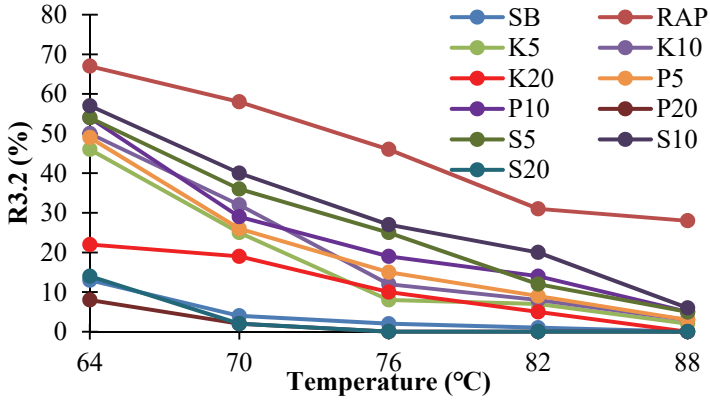

Figure 12 - %R – temperature relationship at 3.2 stress level

The fact that the difference (J_{nrdiff}) between the creep recovery of the binders at 0.1 and 3.2 kPa stress levels was greater than 75% indicated sensitivity to rutting. The change in J_{nrdiff} values of the binders is given in Figure 13. There was not a significant change in the J_{nrdiff} values for all modifications. The J_{nrdiff} values increased as the biooil content increased. With the increase in temperature, J_{nrdiff} values increased in all three modifications and when the additives were used together. The binders, except for P20, did not satisfy the 75% limit requirement at 82°C. At 88°C, K10, K20, P10, P20 and S20 met the limit requirement. RAP had the lowest J_{nrdiff} value and P20 had the highest value.

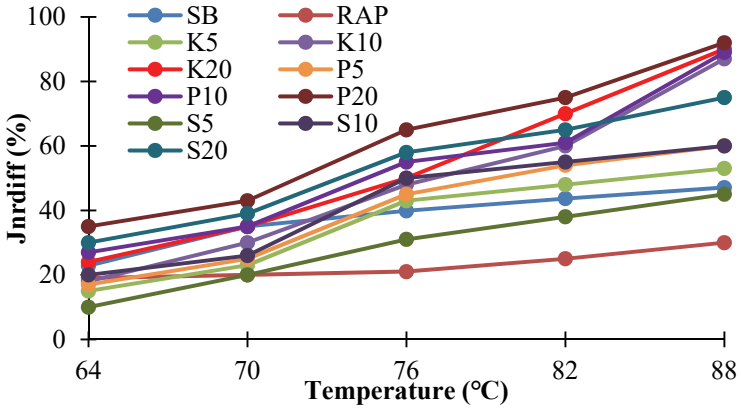

Figure 13 - Change in J_{nrdiff} values of binders

Table 4 - Overview of the binder grading according to PG and MSCR systems

Binder Type and Test Temperature (°C)		G*/sinδ (kPa)	AASHTOT315	$J_{nr3.2}$ (1/kPa)	AASHTO T350	
		Aged with RAP	PG		J_{nrdiff}	PG
	64	85310		0,02	19	64-E
	70	41750		0,05	20	70-E
Neat	76	21270	88	0,12	21	76-E
	82	11100		0,34	25	82-E
	88	5815		0,33	30	88-E
	64	29310		0,11	15	64-E
	70	14670		0,28	23	70-E
K5	76	7450	82	1,12	43	76-H
	82	3882		1,56	48	82-H
	88	2083		4,36	53	88-S
	64	31270		0,1	18	64-E
	70	15860		0,25	30	70-E
K10	76	8928	88	0,9	48	76-V
	82	4626		1,31	60	82-V
	88	2492		4,58	87	-
	64	6395		0,87	24	64-E
	70	3167		2,12	35	70-S
K20	76	1623	70	6,56	50	-
	82	871		14,55	70	-
	88	420		26,63	90	-
	64	34890		0,08	17	64-E
	70	17120		0,24	25	70-E
P5	76	8760	88	0,75	45	76-V
	82	4522		0,98	54	82-V
	88	2458		3,66	60	88-S
	64	23170		0,14	27	64-E
	70	11810		0,35	35	70-E
P10	76	6144	82	0,92	55	76-V
	82	3277		1,78	61	82-H
	88	1781		6,72	89	-
	64	4223		2,14	35	64-S
	70	2108		5,88	43	-
P20	76	1092	70	10,78	65	-
	82	606		21,64	75	-
	88	347		40,68	92	-
	64	42010		0,06	10	64-E
	70	21120		0,17	20	70-E
S5	76	10940	88	0,45	31	76-E
	82	5751		1,12	38	82-H
	88	3073		2,53	45	88-S
	64	30940		0,1	20	64-E
	70	15550		0,27	26	70-E
S10	76	8016	88	0,7	50	76-V
	82	4252		1,48	55	82-H
	88	2295		4,3	60	88-S
	64	6469		2,41	30	64-S
	70	3267		6,19	39	-
S20	76	1658	70	12,73	58	-
	82	912		24,94	65	-
	88	448		42,34	75	-

An overview of the binder grades based on conventional and MSCR systems is shown in Table 4. The J_{nrdiff} values obtained using the T350 approach showed that the non-recoverable creep compliance performed well. The results of the investigation demonstrated that the additions considerably improved the binders' capacity to withstand high temperatures. Some changes can withstand high traffic conditions at this temperature, according to T350. The asphalt binders' resistance to rutting rises with the amount of elastomer they include.

3.5. Statistical Analysis and Model Development

The Quadratic model was the recommended regression model for all dependent variables and the models were in good agreement with the examined parameters. The numerical variables (A, B) of the predicted models were determined using Equation 10-12. Only significant impact variables were included in the equations. The synergistic and antagonistic effects of each factor on the dependent variables are specified with a sign (negative or positive) in front of the terms in the equation. A represents temperature and B represents bio-oil content.

$$K_{\text{Complex modulus}} = 7.73*10^{5} - 18073.83A - 8429.96B + 146.86AB + 102.61A^{2} - 138.29B^{2} \quad (10)$$

$$P_{\text{Complex modulus}} = 7.96*10^{5} - 17648.40A - 15821.64B + 182.80AB + 97.20A^{2} + 34.96B^{2} \quad (11)$$

$$S_{\text{Complex modulus}} = 9.49*10^{5} - 21409.66A - 15920.59B + 203.46AB + 119.25A^{2} - 28.69B^{2} \quad (12)$$

In a situation where the model fit is not satisfactory, the model functions will result in inappropriate responses. Therefore, it is of crucial importance to check the model adequacy as part of the data analysis [58-60]. Hence, ANOVA was performed to examine the adequacy and appropriateness of the proposed models. Other statistical results are also presented in the table. The degree of appropriateness of the proposed models was investigated through the coefficient of determination (R^2). The R^2 values for the dependent variables $K_{\text{Complex modulus}}$, $P_{\text{Complex modulus}}$ and $S_{\text{Complex modulus}}$ were 0.9267, 0.9254 and 0.9349, respectively. A higher R^2 value suggests stronger agreement between the expected and actual values. High R^2 values in this study indicated stronger agreement between the predicted and actual values. In addition, the predicted coefficients of determination were in acceptable agreement with the adjusted coefficients of determination which refers to an inconsistency of less than 0.2. Sufficient precision reveals the signal-to-noise ratio for comparison between the various quantities calculated at the design points and the average prediction error. The signal-to-noise ratios for the dependent variables of $K_{\text{Complex modulus}}$, $P_{\text{Complex modulus}}$ ve $S_{\text{Complex modulus}}$ were 20.0660 20.8163 and 22.0569, respectively. All of them were greater than 4, indicating that they provide an adequate signal. The results showed that all bio-oils can be used to navigate the design space. In the analysis, the confidence level was at 95% with a p-value less than 0.05. P-values less than 0.05 for the models also indicated that there was only a 0.0001 probability of an F-value of this magnitude due to noise [61].

2D contour and 3D graphical diagnostic plots of the relationship between independent variables and complex modulus values are shown in Figure 14. The figure shows that there

is a perfect interaction between the variables and response of the bio-oil-added asphalt mixtures. The addition of bio-oil to aged bitumen decreased the complex modulus values. The binders' complex modulus values decreased with the increase of bio-oil content. As the rate of rejuvenation affecting the aged binder increased with the increase in the amount of bio-oil, a further decrease was observed in the complex modulus values. In addition, as the temperature applied to the binders increased, the complex modulus values decreased. Especially at high temperatures, the complex modulus values decreased significantly. Among the bio-oils used in the study, olive mill pomace was found to be the most effective bio-oil. The decrease in the complex modulus values with the increase of bio-oil in the aged binder can be seen in both 2D contour and 3D graph.

In Figure 14, the intensity red color in the 2D and 3D graphics changes, which indicates that the relationship between the variables is good. The effect of bio-oils on complex modulus values was determined. Accordingly, the redness in the graphs decreases as the bio-oil increases, which shows the positive effect on the complex modulus. As the amount of bio-oil used in the aged binder increases, the oils decrease the viscosity of the bituminous binders as they reduce the gravity force between the molecules. In addition, a decrease in the complex modulus value was observed with the increase in temperature, showing that the rising temperature increased the fluidity of the binders. This is due to the fact that bio-oils contain light components (i.e. aromatic solvents) that can dissolve asphaltenes, and as a result make the binders softer.

Graphs of predicted values and actual quantities were used to obtain a clear interpretation of the satisfaction of the proposed models. Figure 15 displays the plots of the predicted against the actual values of all the responses. It shows that almost all the points are distributed fairly close to the equality line. This means that the proposed models have a good agreement with the data. In addition, the distributions of all the points on the straight line showed a strong correlation between the predicted values and the experimental values. Finally, the results confirmed that the proposed prediction models can adequately navigate the design space defined by CCD.

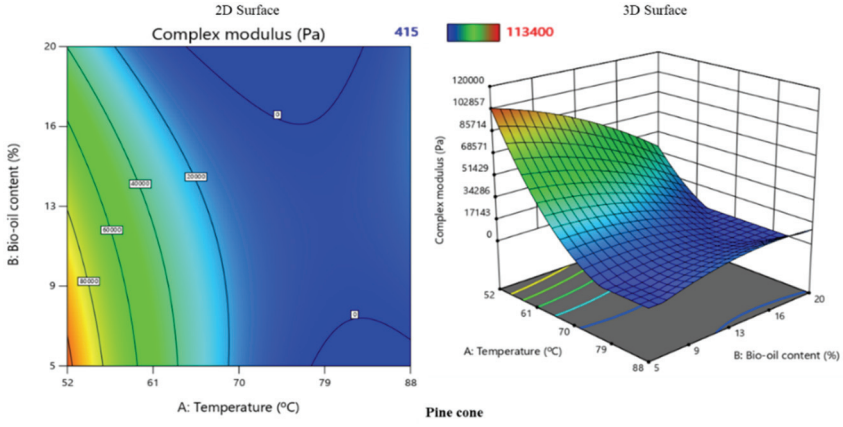

Figure 14 - Effect of fat content and temperature on complex modulus

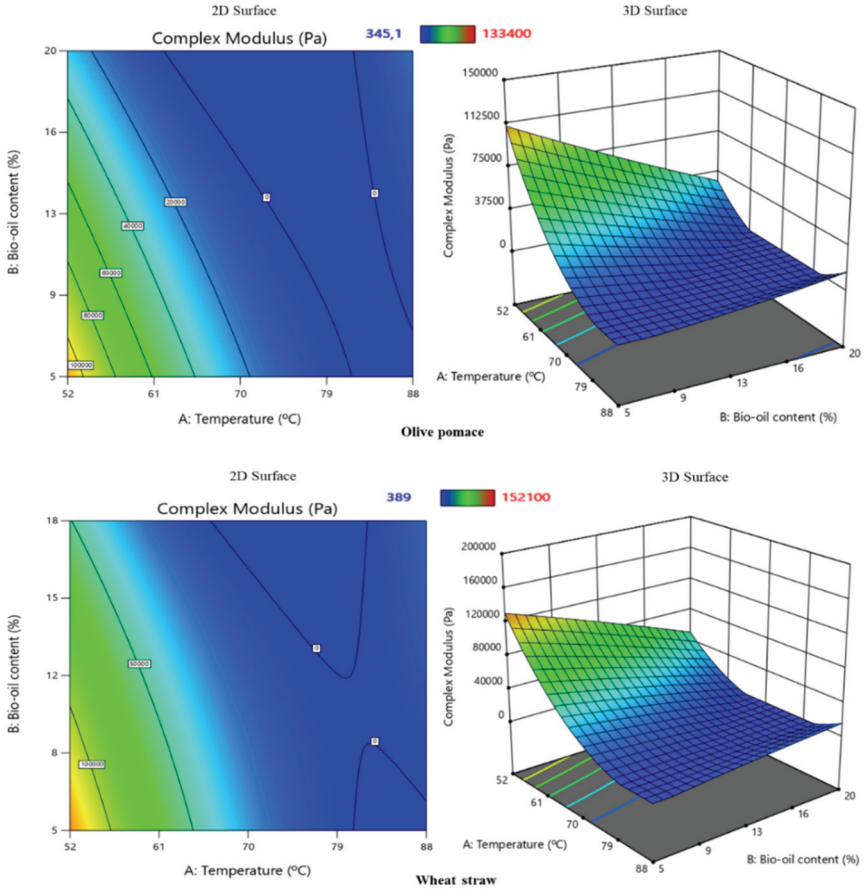

Figure 14 - Effect of fat content and temperature on complex modulus (continue)

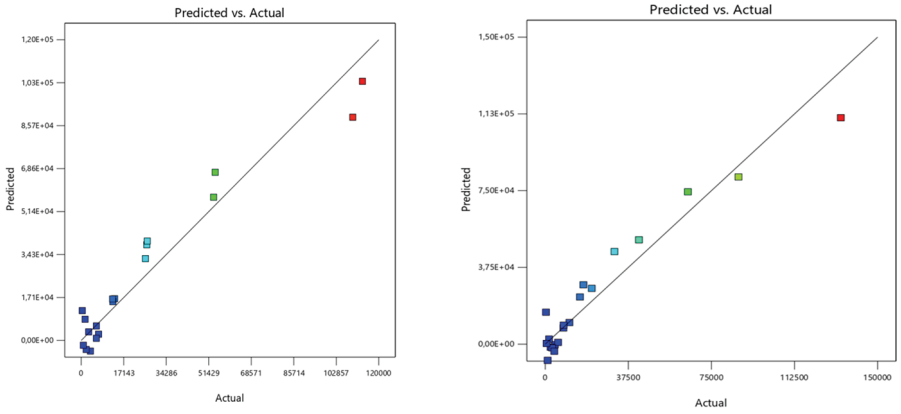

Figure 15 - Trace plot of complex modulus

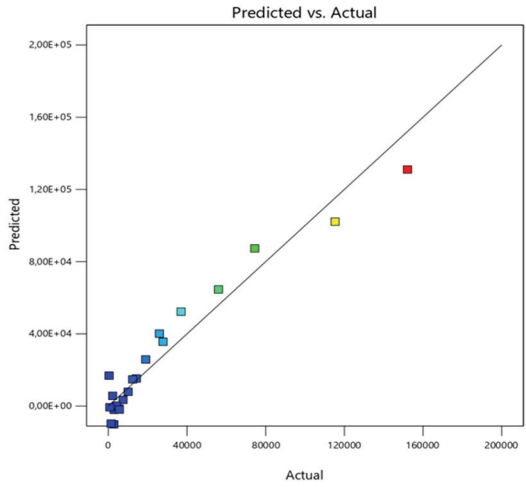

Figure 15 - Trace plot of complex modulus (continue)

4. CONCLUSIONS

In this study, physical and rheological properties of binders were investigated by adding three different bio-oils obtained as a result of pyrolysis to aged bitumen obtained from recycled asphalt mixture. The following conclusions can be drawn:

- The addition of rejuvenators to the aged bitumen obtained from the recycled bitumen mixture increased the penetration value of the aged bitumen. It was determined that all three bio-oils had softening properties on the aged binder. The addition of approximately 20% of all three bio-oils to the aged binder (RAP binder) restored the softening value to the initial value of unaged (neat binder).
- Viscosity tests showed that biorejuvenators can alleviate the stiffness of aged binder. A concentration of 20% bio-rejuvenator was considered to be approximately sufficient to rejuvenate the aged asphalt binder to be reused in pavement construction.
- The higher light components and viscous content in the bio-oil are able to stabilize the chemical components of aged binders and consequently restore rutting resistance to a great extent. The results revealed that bio-oils rejuvenated the aged bitumen and approached its G*/sinδ value to that of the unaged bitumen (50/70). permanent creep compliance
- It was observed that the J_{nr} values increased significantly with the increase in the additive content in all three modifications. Especially after 10% additive content, there was a significant increase in J_{nr} value. The elastic recovery values of the RAP binder decreased with the increase in the amount of biooil added to the RAP binder. Although RAP binder provided the highest elastic recovery value, S20 binder provided the lowest value. There was no significant change in the J_{nrdiff} values for

all modifications. As the bio-oil content increased, the J_{nrdiff} values increased. With the increase in temperature, J_{nrdiff} values increased in all three modifications and when additives were used together.

- High R^2 values indicated stronger agreement between predicted and actual values. The intensity of the red color in 2D and 3D graphics changed which indicated that the relationship between the variables was good. The distributions of all the points on the straight line in the graphs showed a strong correlation between the predicted and the experimental values.

This study recommends that 20% concentration bio-oil should be used to rejuvenate the aged asphalt binder for reuse in pavement construction. In addition, future studies should investigate the mechanical properties of the regenerated asphalt mixtures.

Acknowledgements

This study was carried out within the scope of the Scientific and Technological Research Council of Turkey (TUBITAK). We gratefully acknowledge the financial support provided by TUBITAK to the Research Project 122M042.

Credit authorship contribution statement

Beyza Furtana Yalcin: Methodology, Writing – original draft, Investigation, Data curation, Result presentation, Resources. **Mehmet Yilmaz:** Writing – review & editing, Supervision, Result presentation, Validation, Conceptualization.

Data Availability

Some or all data, models, or code that support the findings of this study are available from the corresponding author upon reasonable request.

Declaration of competing interest

The authors declare that they have no known competing financial interests or personal relationships that could have appeared to influence the work reported in this paper.

References

[1] Chailleux, E., Audo, M., Bujoli, B., Queffelec, C., Legrand, J., Lepine, O.: Workshop alternative binders for sustainable asphalt pavements. In: Alternative Binder from Microalgae: Algoroute Project. pp. 7–14 (2012)

[2] Zhang, R., Wang, H., Gao, J., You, Z., Yang, X.: High temperature performance of SBS modified bio-asphalt. Constr. Build. Mater. 144, 99–105 (2017). https://doi.org/10.1016/j.conbuildmat.2017.03.103

[3] Lv, S., Liu, C., Yao, H., Zheng, J.: Comparisons of synchronous measurement methods on various moduli of asphalt mixtures. Constr. Build. Mater. 158, 1035–1045 (2018). https://doi.org/10.1016/j.conbuildmat.2017.09.193

[4] Lee, K.W., Brayton, T.E., Mueller, M., Singh, A.: Rational Mix-Design Procedure for Cold In-Place Recycling Asphalt Mixtures and Performance Prediction. J. Mater. Civ. Eng. 28, 04016008 (2016). https://doi.org/10.1061/(ASCE)MT.1943-5533.0001492

[5] Onochie, A., Fini, E., Yang, X., Mills-Beale, J., You, Z.: Transportation research board 92nd annual meeting. Rheological Characterization of Nano-particle based Bio-modified Binder, Washington DC (2013)

[6] Zhang, R., Wang, H., Gao, J., Yang, X., You, Z.: Comprehensive Performance Evaluation and Cost Analysis of SBS-Modified Bioasphalt Binders and Mixtures. J. Mater. Civ. Eng. 29, 04017232 (2017). https://doi.org/10.1061/(ASCE)MT.1943-5533.0002098

[7] Ge, D., Yan, K., You, Z., Xu, H.: Modification mechanism of asphalt binder with waste tire rubber and recycled polyethylene. Constr. Build. Mater. 126, 66–76 (2016). https://doi.org/10.1016/j.conbuildmat.2016.09.014

[8] Zhang, R., Wang, H., Jiang, X., You, Z., Yang, X., Ye, M.: Thermal Storage Stability of Bio-Oil Modified Asphalt. J. Mater. Civ. Eng. 30, 04018054 (2018). https://doi.org/10.1061/(ASCE)MT.1943-5533.0002237

[9] Wang, H., Zhang, R., Chen, Y., You, Z., Fang, J.: Study on microstructure of rubberized recycled hot mix asphalt based X-ray CT technology. Constr. Build. Mater. 121, 177–184 (2016). https://doi.org/10.1016/j.conbuildmat.2016.05.166

[10] Bell, C.A., Wieder, A.J., Fellin, M.J.: Laboratory aging of asphalt-aggregate mixtures, Field Validation. , Washington, DC (1994)

[11] Said, S.: Aging Effect on Mechanical Characteristics of Bituminous Mixtures. Transp. Res. Rec. J. Transp. Res. Board. 1901, 1–9 (2005). https://doi.org/10.3141/1901-01

[12] Ramadan, K.Z., Saad, A.A.: Effect of Superpave Short-Term Aging on Binder and Asphalt Mixture Rheology. Period. Polytech. Transp. Eng. 45, 196 (2017). https://doi.org/10.3311/PPtr.10477

[13] G. Holleran, T. Wieringa, T. Tailby: Rejuvenation treatments for aged pavements. In: Transit New Zealand and New Zealand Institute of Highway Technology (NZIHT) Annual Conference. , Auckland, New Zealand (2006)

[14] Zhang, R.H., Zhao, T.S., Tan, P., Wu, M.C., Jiang, H.R.: Ruthenium dioxide-decorated carbonized tubular polypyrrole as a bifunctional catalyst for non-aqueous lithium-oxygen batteries. Electrochim. Acta. 257, 281–289 (2017). https://doi.org/10.1016/j.electacta.2017.10.097

[15] Nahar, S.N., Qiu, J., Schmets, A.J.M., Schlangen, E., Shirazi, M., van de Ven, M.F.C., Schitter, G., Scarpas, A.: Turning Back Time. Transp. Res. Rec. J. Transp. Res. Board. 2444, 52–62 (2014). https://doi.org/10.3141/2444-06

[16] Yu, X., Zaumanis, M., dos Santos, S., Poulikakos, L.D.: Rheological, microscopic, and chemical characterization of the rejuvenating effect on asphalt binders. Fuel. 135, 162–171 (2014). https://doi.org/10.1016/j.fuel.2014.06.038

[17] Zaumanis, M., Mallick, R.B., Poulikakos, L., Frank, R.: Influence of six rejuvenators on the performance properties of Reclaimed Asphalt Pavement (RAP) binder and 100% recycled asphalt mixtures. Constr. Build. Mater. 71, 538–550 (2014). https://doi.org/10.1016/j.conbuildmat.2014.08.073

[18] Xie, Z., Tran, N., Julian, G., Taylor, A., Blackburn, L.D.: Performance of Asphalt Mixtures with High Recycled Contents Using Rejuvenators and Warm-Mix Additive: Field and Lab Experiments. J. Mater. Civ. Eng. 29, 04017190 (2017). https://doi.org/10.1061/(ASCE)MT.1943-5533.0002037

[19] Tran, N., Xie, Z., Julian, G., Taylor, A., Willis, R., Robbins, M., Buchanan, S.: Effect of a Recycling Agent on the Performance of High-RAP and High-RAS Mixtures: Field and Lab Experiments. J. Mater. Civ. Eng. 29, 04016178 (2017). https://doi.org/10.1061/(ASCE)MT.1943-5533.0001697

[20] Lei, Z., Bahia, H., Yi-qiu, T.: Effect of bio-based and refined waste oil modifiers on low temperature performance of asphalt binders. Constr. Build. Mater. 86, 95–100 (2015). https://doi.org/10.1016/j.conbuildmat.2015.03.106

[21] Yang, X., You, Z.-P., Dai, Q.-L.: Performance evaluation of asphalt binder modified by bio-oil generated from waste wood resources. Int. J. Pavement Res. Technol. 6, 431–439 (2013). https://doi.org/10.6135/ijprt.org.tw/2013.6(4).431

[22] López, S., Davies, D.R., Giráldez, F.J., Dhanoa, M., Dijkstra, J., France, J.: Assessment of nutritive value of cereal and legume straws based on chemical composition andin vitro digestibility. J. Sci. Food Agric. 85, 1550–1557 (2005). https://doi.org/10.1002/jsfa.2136

[23] Wang, M., Hettiarachchy, N.S., Qi, M., Burks, W., Siebenmorgen, T.: Preparation and Functional Properties of Rice Bran Protein Isolate. J. Agric. Food Chem. 47, 411–416 (1999). https://doi.org/10.1021/jf9806964

[24] Wang, J., Sun, B., Cao, Y., Wang, C.: In vitro fermentation of xylooligosaccharides from wheat bran insoluble dietary fiber by Bifidobacteria. Carbohydr. Polym. 82, 419–423 (2010). https://doi.org/10.1016/j.carbpol.2010.04.082

[25] Ortiz de Zárate, I., Ezcurra, A., Lacaux, J.P., Van Dinh, P., de Argandoña, J.D.: Pollution by cereal waste burning in Spain. Atmos. Res. 73, 161–170 (2005). https://doi.org/10.1016/j.atmosres.2004.07.006

[26] Ayrilmis, N., Buyuksari, U., Dundar, T.: Waste pine cones as a source of reinforcing fillers for thermoplastic composites. J. Appl. Polym. Sci. 117, 2324–2330 (2010). https://doi.org/10.1002/app.32076

[27] McCready, N.S., Williams, R.C.: The Utilization of Agriculturally Derived Lignin as an Antioxidant in Asphalt Binder. In: Proceedings of the 2007 Mid-Continent Transportation Research Symposium. , Ames (2007)

[28] Li, Y., Xing, B., Ding, Y., Han, X., Wang, S.: A critical review of the production and advanced utilization of biochar via selective pyrolysis of lignocellulosic biomass. Bioresour. Technol. 312, 123614 (2020). https://doi.org/10.1016/j.biortech.2020.123614

[29] Akhtar, J., Kuang, S.K., Amin, N.S.: Liquefaction of empty palm fruit bunch (EPFB) in alkaline hot compressed water. Renew. Energy. 35, 1220–1227 (2010). https://doi.org/10.1016/j.renene.2009.10.003

[30] Bridgwater, A.: Fast pyrolysis processes for biomass. Renew. Sustain. Energy Rev. 4, 1–73 (2000). https://doi.org/10.1016/S1364-0321(99)00007-6

[31] Mohan, D., Pittman, C.U., Steele, P.H.: Pyrolysis of Wood/Biomass for Bio-oil: A Critical Review. Energy & Fuels. 20, 848–889 (2006). https://doi.org/10.1021/ef0502397

[32] Asli, H., Ahmadinia, E., Zargar, M., Karim, M.R.: Investigation on physical properties of waste cooking oil – Rejuvenated bitumen binder. Constr. Build. Mater. 37, 398–405 (2012). https://doi.org/10.1016/j.conbuildmat.2012.07.042

[33] You, Z., Mills-Beale, J., Fini, E., Goh, S.W., Colbert, B.: Evaluation of Low-Temperature Binder Properties of Warm-Mix Asphalt, Extracted and Recovered RAP and RAS, and Bioasphalt. J. Mater. Civ. Eng. 23, 1569–1574 (2011). https://doi.org/10.1061/(ASCE)MT.1943-5533.0000295

[34] Wang, H., Sun, M., Yang, H., Tian, X., Tong, Y., Zhou, T., Zhang, T., Fu, Y., Guo, X., Fan, D., Yu, A., Fan, M., Wu, X., Xiao, W., Chui, D.: Hypoxia-inducible factor-1α mediates up-regulation of neprilysin by histone deacetylase-1 under hypoxia condition in neuroblastoma cells. J. Neurochem. 131, 4–11 (2014). https://doi.org/10.1111/jnc.12795

[35] Yang, X., You, Z.: High temperature performance evaluation of bio-oil modified asphalt binders using the DSR and MSCR tests. Constr. Build. Mater. 76, 380–387 (2015). https://doi.org/10.1016/j.conbuildmat.2014.11.063

[36] Gong, M., Yang, J., Zhang, J., Zhu, H., Tong, T.: Physical–chemical properties of aged asphalt rejuvenated by bio-oil derived from biodiesel residue. Constr. Build. Mater. 105, 35–45 (2016). https://doi.org/10.1016/j.conbuildmat.2015.12.025

[37] Zargar, M., Ahmadinia, E., Asli, H., Karim, M.R.: Investigation of the possibility of using waste cooking oil as a rejuvenating agent for aged bitumen. J. Hazard. Mater. 233–234, 254–258 (2012). https://doi.org/10.1016/j.jhazmat.2012.06.021

[38] Ržek, L., Ravnikar Turk, M., Tušar, M.: Increasing the rate of reclaimed asphalt in asphalt mixture by using alternative rejuvenator produced by tire pyrolysis. Constr. Build. Mater. 232, 117177 (2020). https://doi.org/10.1016/j.conbuildmat.2019.117177

[39] Avsenik, L., Klinar, D., Tušar, M., Perše, L.S.: Use of modified slow tire pyrolysis product as a rejuvenator for aged bitumen. Constr. Build. Mater. 120, 605–616 (2016). https://doi.org/10.1016/j.conbuildmat.2016.05.140

[40] Nizamuddin, S., Baloch, H.A., Jamal, M., Madapusi, S., Giustozzi, F.: Performance of waste plastic bio-oil as a rejuvenator for asphalt binder. Sci. Total Environ. 828, 154489 (2022). https://doi.org/10.1016/j.scitotenv.2022.154489

[41] Foroutan Mirhosseini, A., Tahami, S.A., Hoff, I., Dessouky, S., Ho, C.-H.: Performance evaluation of asphalt mixtures containing high-RAP binder content and bio-oil rejuvenator. Constr. Build. Mater. 227, 116465 (2019). https://doi.org/10.1016/j.conbuildmat.2019.07.191

[42] Technical, A.I., Bulletin: Laboratory Mixing and Compaction Temperatures, http://www.asphaltinstitute.org/superpav/mixcompt.html, accessed 8/19/01

[43] TS EN 932-1: Test For General Properties of Aggregates part 1 methods for sampling. (1997)

[44] TS EN 12697-3+A1: Bituminous mixtures - Test methods for hot mix asphalt - Part 3: Bitumen recovery: Rotary evaporator. (2019)

[45] Çeloğlu, M.E.: Investigation of the Usability of Biochars Obtained from the Pyrolysis of Different Biomasses in Bitumen and Bituminous Hot, (2020)

[46] Ganter, D., Mielke, T., Maier, M., Lupascu, D.C.: Bitumen rheology and the impact of rejuvenators. Constr. Build. Mater. 222, 414–423 (2019). https://doi.org/10.1016/j.conbuildmat.2019.06.177

[47] AASHTO T315: Standard Method of Test for Determining the Rheological Properties of Asphalt Binder Using a Dynamic Shear Rheometer (DSR). AASHTO, USA (2019)

[48] AASHTO M332: D8239 Standard specification for Performance-Graded Asphalt Binder using Multiple Stress Creep Recovery (MSCR) Test. AASHTO, USA (2015)

[49] Wasage, T.L.J., Stastna, J., Zanzotto, L.: Rheological analysis of multi-stress creep recovery (MSCR) test. 8436, (2011). https://doi.org/10.1080/10298436.2011.573557

[50] Behnood, A., Shah, A., McDaniel, R.S., Beeson, M., Olek, J.: High-Temperature Properties of Asphalt Binders: Comparison of Multiple Stress Creep Recovery and Performance Grading Systems. Transp. Res. Rec. 2574, 131–143 (2016). https://doi.org/10.3141/2574-15

[51] Khodaii, A., Haghshenas, H.F., Kazemi Tehrani, H.: Effect of grading and lime content on HMA stripping using statistical methodology. Constr. Build. Mater. 34, 131–135 (2012). https://doi.org/10.1016/j.conbuildmat.2012.02.025

[52] Montgomery, D.C.: Design and analysis of experiments. Wiley, New York (2012)

[53] Montgomery, D.C.: Design and analysis of experiments,. Wiley, New York (2001)

[54] Myers, R.H., Douglas C. Montgomery, Christine M. Anderson-Cook: Response surface methodology: process and product optimization using designed experiments. Wiley, New York (2016)

[55] Fang, Y., Zhang, Z., Yang, J., Li, X.: Comprehensive review on the application of bio-rejuvenator in the regeneration of waste asphalt materials. Constr. Build. Mater. 295, 123631 (2021). https://doi.org/10.1016/j.conbuildmat.2021.123631

[56] Zhou, X., Moghaddam, T.B., Chen, M., Wu, S., Zhang, Y., Zhang, X., Adhikari, S., Zhang, X.: Effects of pyrolysis parameters on physicochemical properties of biochar and bio-oil and application in asphalt. Sci. Total Environ. 780, 146448 (2021). https://doi.org/10.1016/j.scitotenv.2021.146448

[57] Zhang, R., You, Z., Wang, H., Chen, X., Si, C., Peng, C.: Using bio-based rejuvenator derived from waste wood to recycle old asphalt. Constr. Build. Mater. 189, 568–575 (2018). https://doi.org/10.1016/j.conbuildmat.2018.08.201

[58] Baghaee Moghaddam, T., Soltani, M., Karim, M.R., Baaj, H.: Optimization of asphalt and modifier contents for polyethylene terephthalate modified asphalt mixtures using response surface methodology. Measurement. 74, 159–169 (2015). https://doi.org/10.1016/j.measurement.2015.07.012

[59] Myers, R.H., Montgomery, D.C., Anderson-Cook, C.M.: Response Surface Methodology: Process and Product Optimization Using Designed Experiments. John Wiley & Sons (2016)

[60] Körbahti, B.K., Rauf, M.A.: Application of response surface analysis to the photolytic degradation of Basic Red 2 dye. Chem. Eng. J. 138, 166–171 (2008). https://doi.org/10.1016/j.cej.2007.06.016

[61] Hosseinpour, V., Kazemeini, M., Mohammadrezaee, A.: Optimisation of Ru-promoted Ir-catalysed methanol carbonylation utilising response surface methodology. Appl. Catal. A Gen. 394, 166–175 (2011). https://doi.org/10.1016/j.apcata.2010.12.036

Turkish Journal of Civil Engineering, 2024 125-147, Paper 772, ***Research Article***

Computational Modelling of Damage Progression in Unreinforced Masonry Walls via DEM

Bora PULATSU[1*]
Kagan TUNCAY[2]

ABSTRACT

Unreinforced masonry (URM) walls are the common load-bearing elements for old masonry buildings and heritage structures. As witnessed from the past and recent earthquakes, URM walls may demonstrate various collapse mechanisms along with different crack patterns influenced by the wall aspect ratio, vertical pre-compression load, opening size and ratio, among many other factors. Typically, the mortar joints and unit-mortar interfaces are the weak planes where we expect to observe most failures, such as sliding, cracking and joint opening. However, it is not a straightforward task to simulate the structural behaviour and the failure mechanism of URM walls, including the crack localizations and propagation through the mortar joints, using the standard continuum-based computational models given the composite and highly nonlinear nature of the material. In this context, the present research offers a discontinuum-based approach to simulate the damage progression in URM walls subjected to combined shear-compression loading using the discrete element method (DEM). The masonry walls are represented via distinct elastic blocks interacting through point contacts to their surroundings. It is aimed to present the effect of the local fracture mechanism on the macro response of the masonry walls via validated DEM-based numerical models that can address all possible fracture mechanisms occurring at the unit-mortar interfaces. An innovative damage monitoring technique relying on the stress state at the point contacts is implemented and utilized to explore the associated damage progression in URM walls. The results show the great potential of the adopted modelling strategy to better understand the mechanics of URM walls and indicate the effect of strength properties of masonry constituents on the overall in-plane capacity of the load-bearing walls.

Keywords: Discrete element method, contact mechanics, masonry, in-plane behaviour, fracture mechanisms.

Note:
- This paper was received on July 7, 2023 and accepted for publication by the Editorial Board on December 28, 2023.
- Discussions on this paper will be accepted by July 31, 2024.
- https://doi.org/10.18400/tjce.1323977

1 Carleton University, Department of Civil and Environmental Engineering, Ottawa, Canada
bora.pulatsu@carleton.ca - https://orcid.org/0000-0002-7040-0734

2 Middle East Technical University, Department of Civil Engineering, Ankara, Türkiye
tuncay@metu.edu.tr - https://orcid.org/0000-0002-4523-2388

* Corresponding author

1. INTRODUCTION

The unreinforced masonry (URM) constitutes the vast majority of old building inventory in major cities and rural areas, including historic buildings and most landmark structures. Specifically, masonry refers to a construction technique where the discrete units (or blocks) are laid on top of each other with or without using a binding material (i.e., cement or lime-based mortar) to construct a load-bearing wall system. Often, the bricks (or stone blocks) are stronger and stiffer than the mortar and unit-mortar interfaces; hence, the cracks are most likely to develop and propagate through the joints (referred to as strong brick weak joint combination). Given the considerable difference in the mechanical properties of masonry constituents in URM walls, various crack patterns and failure mechanisms can develop under lateral seismic forces such as rocking, sliding and diagonal tensile failure [1]. It is worth noting that there may be an interaction between the failure modes when a URM wall starts to displace and get damaged [2]. In other words, the structural behaviour of masonry walls may demonstrate progressive damage by switching from one mechanism to another with increased lateral displacement.

With the advances in computational power, different numerical approaches and modelling strategies have been proposed to simulate the in- and out-of-plane response of masonry walls [3]. By and large, continuum-based methods (such as standard Finite Element Analysis, FEA) are commonly used in the structural analysis of URM walls (also referred to as macro-modelling), offering a practical solution with low computational cost and requiring a relatively lower number of input parameters. In macro models, homogenized material properties are used with no distinction among masonry units and mortar, where the material failure is smeared out through the continuous medium [4–7]. Although this approach provides valuable information regarding the overall performance of large-scale buildings and load-bearing wall systems, it may not capture the local mechanisms and crack patterns that are also related to the morphological features of URM walls. Alternatively, discontinuum-based methodologies can be adopted in the seismic analysis or performance assessment of masonry structures. Among different discontinuum-based analyses, the discrete element method (DEM) has been the one that has attracted the most attention from the academic community and industry for the last several decades (*e.g.*, [8–15]). In DEM, the discontinuous texture of masonry is represented explicitly, considering masonry units via rigid or deformable blocks that can interact with each other along their boundaries, as shown in Figure 1. Moreover, the bond between the mortar and the masonry units is denoted as zero-thickness interfaces without including the mortar joint in the numerical formulation (see Figure 1b), which is called simplified micro-modelling (SMM) in the literature [16]. This approach offers a good compromise in accuracy and computational cost that mainly requires reliable input data regarding the bond (or unit-mortar interface) parameters and unit properties. In SMM, the cracking of masonry units is addressed by defining a potential crack surface between adjacent blocks representing a masonry unit, which is also illustrated in Figure 1c. It is important to highlight that the consideration of potential crack surfaces in masonry units, implementation of sophisticated material models, and contact constitutive laws in DEM-based models (both in two- and three-dimensional settings) are driven by expectations from computational predictions. The available studies adopting DEM as a predictive numerical model (e.g., [17–20]) consist of different improvements and simplifications related to the necessities stemming from physical realities. A review article

focusing on the differences between available DEM-based computational models and their application to masonry structures is discussed in [21].

This research follows the SMM approach implemented within the DEM framework, where elastic blocks are used for bricks that can mechanically interact at the contact points to better understand the progressive damage mechanism in unreinforced masonry walls. While previous studies have discussed the accuracy of the DEM-based computational models and the predicted failure mechanisms, they rarely explore the damage progression at the units and the unit-mortar interfaces. To this end, we aim to provide a deeper understanding of the mechanics of URM walls using validated discrete element models and offer a generalized perspective regarding the accumulated damage and its correlation with the lateral load carrying capacity.

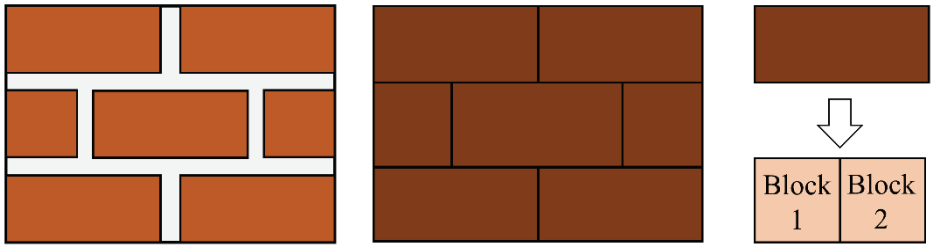

Figure 1 - Representation of masonry wall within the DEM framework; (a) a masonry wall texture, (b) SMM realization and (c) potential crack line (or surface in 3D) for a single block in DEM.

The present study includes the mathematical background of the adopted computational model and validation of the implemented approach by comparing the numerical findings against two experimental results. Then, a detailed investigation is performed to explore the damage progression under the increasing lateral deflection, together with comprehensive sensitivity analyses. Finally, the proposed modelling strategy is applied to simulate the damage progression of a masonry panel with an opening under vertical loading.

2. SIMPLIFIED MICRO-MODELLING VIA DISCRETE ELEMENT METHOD (DEM)

The adopted discontinuum-based approach was initially proposed by Cundall to solve slope stability and rock fragmentation problems [22]. Later, the DEM was used to analyze masonry structures subjected to quasi-static and dynamic loading, among other subjects related to various engineering disciplines. This study performs DEM-based analysis to simulate different URM walls under combined compression-shear loading and predict their structural behaviour from the elastic regime up to failure. A commercial three-dimensional discrete element code, 3DEC developed by Itasca Consulting Group [23], is used during the analyses. The proposed computational modelling approach utilizes elastic blocks, discretized into constant strain tetrahedral (CST) volumes (each consists of four nodes – or gridpoints), and

their mechanical interaction is predicted by computing action/reaction forces at the point contacts (also called sub-contacts) defined along the contact surface, as shown in *Figure 2*.

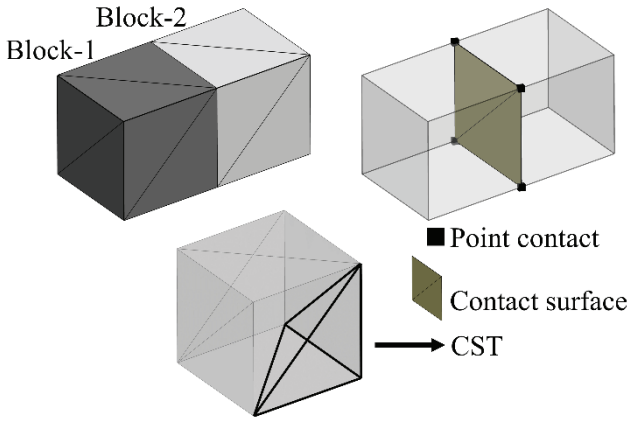

Figure 2 - Two deformable blocks and the contact surface.

The block deformation is computed by solving the equations of motion for each gridpoint (or node) using the central difference algorithm. New nodal velocities are obtained following compact expression at each time step, given in Equation 1. Note that the quasi-static solutions are obtained by adopting Cundall's local damping formulation [24], and the nodal velocities ($\dot{u}_i$) are evaluated at the mid-time intervals (*i.e.*, Δt: time step, $t^+ = t + \Delta t/2$, $t^- = t - \Delta t/2$).

$$\dot{u}_i^{t+} = \dot{u}_i^{t-} + \frac{\Delta t}{m}\left(\Sigma F_i^t - \alpha|\Sigma F_i^t|sgn(\dot{u}_i^{t-})\right) \tag{1}$$

where ΣF_i, m and α are the total force vector, nodal mass (the total mass of a tetrahedron divided by four) and the non-viscous damping constant (default value is 0.8). The sum of forces includes gravity loads, external loads, contact forces (if any), and nodal contribution of the internal stress in the zones adjacent to the gridpoint. Once the new nodal velocities are obtained, nodal displacements are calculated (*i.e.*, $u_i^{t+} = u_i^t + \Delta t(\dot{u}_i^{t+})$), later utilized to predict the block deformation and the relative point contact displacements among the adjacent blocks. In *Figure 3*, the relative displacement of two elastic blocks, in normal and two shear directions, are illustrated. It is worth noting that the point contacts are defined at the vertices of the tetrahedral elements associated with the contact planes. At each contact point, three orthogonal springs are assigned, and the action/reaction forces are computed in the normal and shear directions accordingly. Elastic response at the contact points is governed by the normal and shear contact stiffnesses (k_n, k_s), whereas the failure is controlled by the given tensile (f_t) and compressive (f_m) strength in the normal direction, cohesion (c) and friction angle (θ) in the shear directions. It is important to recall that the normal (σ) and shear (τ) contact stresses are functions of relative normal (u_n) and shear ($u_{s,i}$) displacements. The contact stresses are obtained by first computing elastic increments (*i.e.*, $\Delta\sigma = k_n\Delta u_n$, $\Delta\tau_i = k_s\Delta u_{s,i}$), which are then added to contact stresses computed in the previous time step. Next,

they are corrected (if required) following the defined failure criterion and multiplied with the associated sub-contact area to get forces that are finally used in the equations of motion (Equation 1).

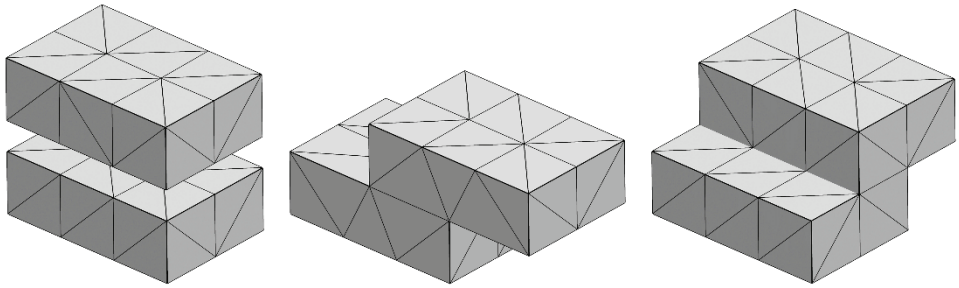

(a) *(b)* *(c)*

Figure 3 - Relative displacement of two blocks: (a) pure tension and (b-c) shear directions.

Throughout this work, recently developed fracture energy based elasto-softening contact constitutive models are used [25]. A bilinear stress-displacement behaviour is implemented in tension, shear and compression regimes, considering the mode-I, mode-II and compressive fracture energy, respectively. The readers can find the graphical representation of implemented contact models in Figure 4a and Figure 4b. The strength reduction (or damage) is imposed in tension, compression and shear strength depending on the recorded relative displacement at the associated point contacts in the normal and shear directions. A single damage parameter is considered to couple tension and shear failure, whereas one-way coupling is considered between shear and compression. The readers are referred to the reference study for a comprehensive discussion and mathematical background of the implemented contact constitutive law [25].

The adopted contact model in the normal direction represents the bond behaviour when subjected to tension, whereas it corresponds to masonry composite behaviour in compression. Therefore, the parameters f_t and f_m denote the bond tensile strength and the compressive strength of the masonry composite, respectively. Upon failure in tension or compression, contact stiffness degradation is considered in the unloading response, which returns to the origin, similar to standard continuum damage mechanics formulation. In shear, the Mohr-Coulomb failure criterion is used, in line with similar studies published in the literature (e.g., [26–30]) that can fairly address the bond shear capacity, where initial and residual bond shear strength (τ_0, τ_{res}) is calculated using cohesion and friction angle parameters (*i.e.*, $\tau_0 = c_0 + tan\theta_0\sigma,\ \tau_{res} = c_{res} + tan\theta_{res}\sigma$). No stiffness degradation is considered for shear stiffness in the pre- and post-peak behaviour. The compression-shear interaction is controlled by the Cap Model, proposed in [31], which is implemented in the DEM framework and presented in *Figure 4*c. The adopted composite yield surface includes tension, compression, and shear failure surfaces, as shown in *Figure 4*.

The explicit solution scheme of DEM is executed in a cyclic manner, such that quasi-static solutions are obtained once the unbalanced force (ΣF) is below the pre-defined threshold (*e.g.*, $|\Sigma F| < 1e-5$ N) or monitored displacements converge to a specific value. Note that

the adopted central difference algorithm only provides stable solutions if the time steps are smaller than the critical value. This condition is automatically satisfied in 3DEC, using sufficiently small time steps, detailed in the reference [32]. On the other hand, the mentioned contact models are implemented in the visual studio environment and compiled as DLL (dynamic link library) in 3DEC. In the following section, the benchmark studies and the application of the DEM are presented.

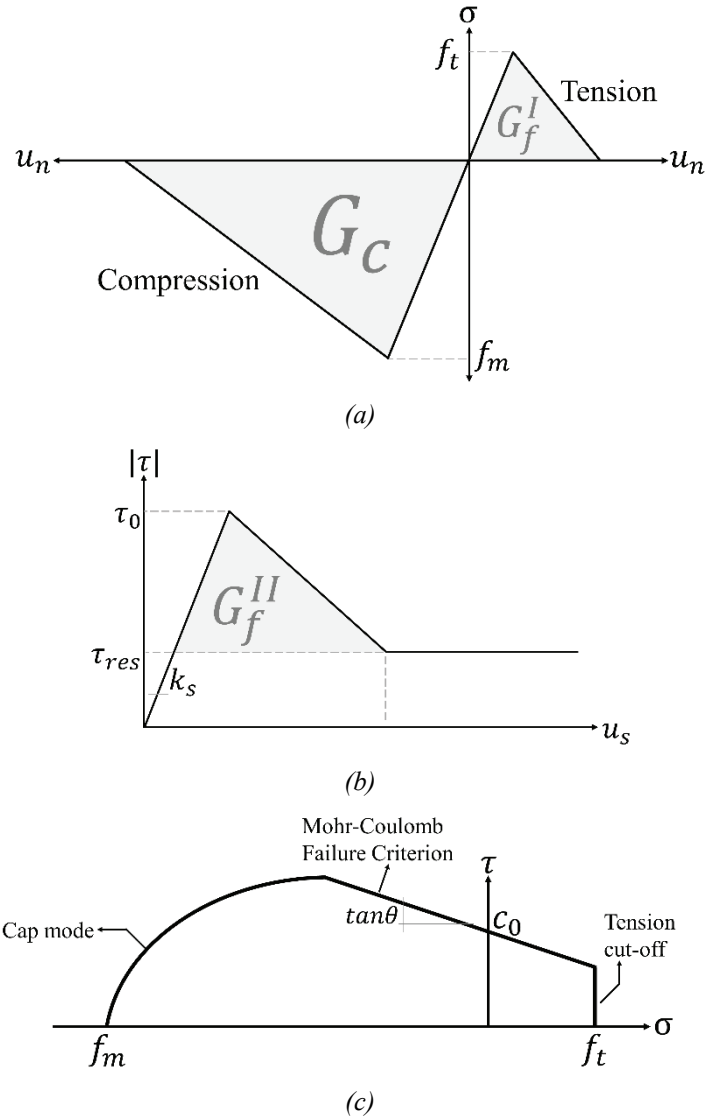

Figure 4 - (a) Contact constitutive law in tension and compression, (b) shear and (c) adopted composite yield surface.

3. VALIDATION STUDIES AND DISCONTINUUM-BASED ANALYSIS

This section presents the experimental studies used as benchmarks to validate the proposed computational modelling strategy. The first reference test was performed by Vermeltfoort et al. [33], exploring the lateral response of URM wall panels ($0.99 \times 1.00 \times 0.098\, m^3$) subjected to combined compression-shear loading with different vertical pressures. Once the vertical loads were applied at the top section of the masonry walls using a solid loading beam, the lateral loads were introduced incrementally by controlling the lateral displacement at the top. No rotation was allowed at the top beam during the lateral loading. This test was already used as validation in an earlier study [20]. Therefore, only a summary of this validation case will be presented here.

In order to study the effect of the local fracture mechanism on the behaviour of masonry walls more precisely, a new validation case was needed to show that the DEM has the capacity to predict damage progression for walls with different aspect ratios. The second benchmark study was presented by Ganz and Thürlimann [34], in which the URM walls consisting of a masonry panel ($3.6 \times 2.0 \times 0.15\, m^3$) and two flanges ($0.15 \times 2.00 \times 0.60\, m^3$) were tested under in-plane loading. Similar to the first reference study, different levels of vertical loads were considered during the testing campaign, causing different lateral load carrying capacities and fracture patterns. In the second benchmark study, the concrete slab was placed at the top of the specimens, where the lateral load was applied during the testing without imposing any restraint on the rotational degrees of freedom of the slab. In Figure 5, the computational models of the reference studies are illustrated. The readers are referred to the references for further details regarding the benchmark tests [33,34].

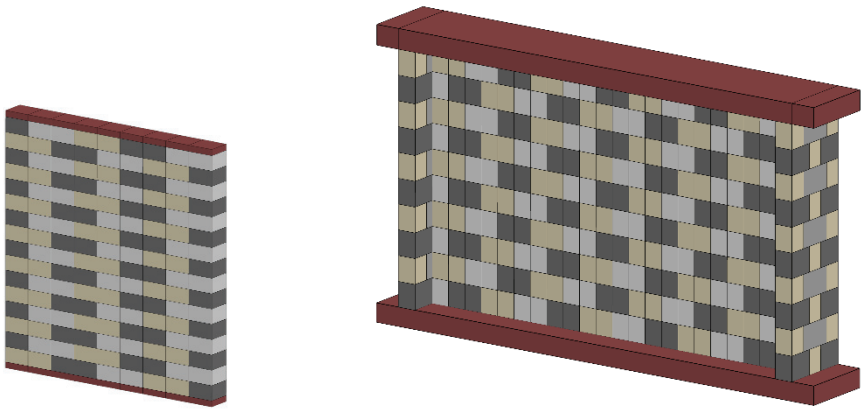

(a) *(b)*

Figure 5 - Illustration of the benchmark studies: (a) Solid wall panel – Benchmark #1, (b) URM wall with flanges – Benchmark #2.

The proposed computational models require the elastic properties of bricks (*i.e.*, Young's modulus and Poisson's ratio) and elasto-plastic properties of the unit-mortar interface (bond), mentioned earlier in Section 2. Typically, bond shear characteristics can be obtained from direct shear testing of masonry couplet or triplet, whereas bond tensile strength can be noted

via direct tension or flexural testings. In this research, brick and bond properties are taken from the provided material characterization tests or previously published academic articles that are in line with the presented modelling strategy [5,31,33–36]. In *Table 1*, assigned material and contact properties are given.

Table 1 - Material and contact properties adopted in the proposed computational models for benchmarks #1 and #2.

Benchmark Study #1					
Masonry Unit Interaction					
E, v (GPa, -)	k_n, k_s (Pa/m)	f_T (MPa)	c_0, c_{res} (MPa)	θ_0, θ_{res} (°)	G_f^I, G_f^{II} (N/m)
16.7, 0.15	820,360	2.0	$1.4f_T$, 0.0	45, 45	80, 500
Unit-Mortar Interface Properties (Bond) - $\boldsymbol{\sigma_v = 1.21, 2.12}$ **MPa**					
k_n, k_s (GPa/m)	f_T, f_m (MPa)	c_0, c_{res} (MPa)	θ_0, θ_{res} (°)	G_f^I, G_f^{II}, G_c (N/m)	C_s (-)
82, 36	0.16, 11.5	$1.4f_T$, 0.0	35, 35	12, 50, 5000	9
Unit-Mortar Interface Properties (Bond) – $\boldsymbol{\sigma_v = 0.30}$ **MPa**					
k_n, k_s (GPa/m)	f_T, f_m (MPa)	c_0, c_{res} (MPa)	θ_0, θ_{res} (°)	G_f^I, G_f^{II}, G_c (N/m)	C_s (-)
82, 36	0.25, 10.5	$1.4f_T$, 0.0	35, 35	12, 125, 5000	9
Benchmark Study #2					
Masonry Unit Interaction					
E, v (GPa, -)	k_n, k_s (Pa/m)	f_T (MPa)	c_0, c_{res} (MPa)	θ_0, θ_{res} (°)	G_f^I, G_f^{II} (N/m)
10, 0.2	100,40	1.5	$1.5f_T$, 0.0	37, 37	22.5, 225
Unit-Mortar Interface Properties (Bond) - $\boldsymbol{\sigma_v = 0.61, 1.91}$ **MPa**					
k_n, k_s (GPa/m)	f_T, f_m (MPa)	c_0, c_{res} (MPa)	θ_0, θ_{res} (°)	G_f^I, G_f^{II}, G_c (N/m)	C_s (-)
20, 8	0.15, 7.6	$1.5f_T$, 0.0	37,37	2.25,150,11500	9

The same loading procedure is applied in the discontinuum models for both benchmark studies, where a constant lateral displacement rate (*i.e.*, 0.005 m/s) is prescribed at the top loading beam after the equilibrium is reached under the self-weight and the vertical pre-compression forces. The base reaction is recorded during the analyses by summing up the shear forces at the springs defined between the supporting block and the bottom course of masonry. In the first benchmark study, three pre-compression loads were considered (*e.g.*,

$\sigma_v = 0.3, 1.21$ and 2.12 MPa). The predicted force-displacement curves and the experimental findings are presented in *Figure 6*. A good agreement is found in comparing the numerical and experimental results in terms of overall force-displacement behaviour and load-carrying capacity. The difference in ultimate lateral load is negligible for low and medium pre-compression pressures ($\sigma_v = 0.3$ MPa and $\sigma_v = 1.21$ MPa), whereas slightly higher capacity, approximately 10%, is noticed for high pre-compression pressure ($\sigma_v = 2.12$ MPa).

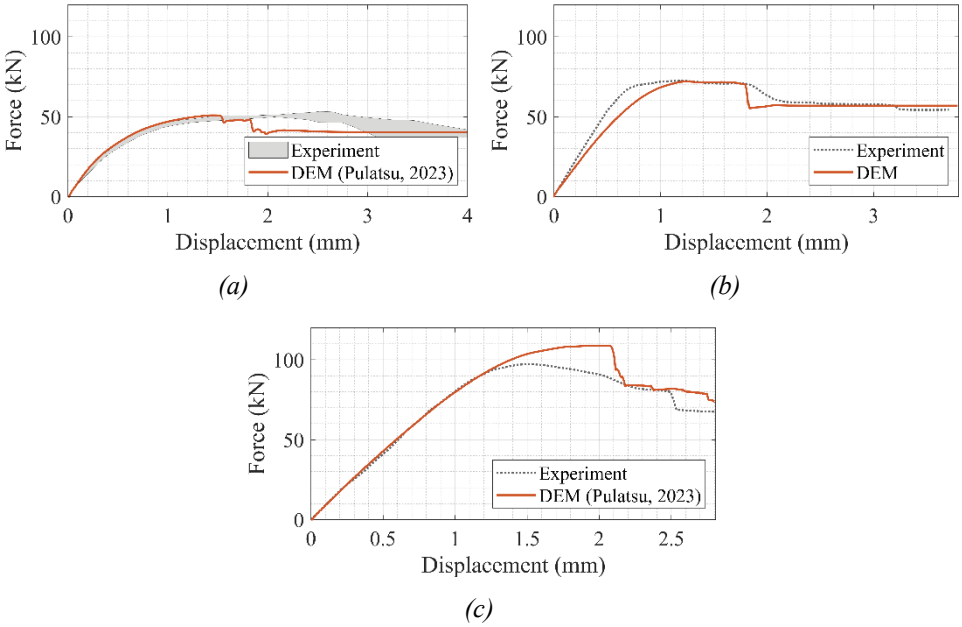

Figure 6 - Comparison of the experimental results (benchmark #1) and the discrete element models for different vertical pre-compression pressures: (a) $\sigma_v = 0.3$, (b) $\sigma_v = 1.21$ and (c) $\sigma_v = 2.12$

Furthermore, the predicted kinematic mechanisms align with the experimental findings, as shown in *Figure 7*. The obtained crack patterns are presented in *Figure 7*b for low, medium and high pre-compression pressures when the force-displacement curves at the ultimate displacement, noted as 4 mm, 3.8 mm and 2.8 mm, respectively. The overall structural behaviour is found to be influenced by the level of pre-compression pressure, which not only controls the maximum lateral load but also affects the damage in bricks (*i.e.*, cracking or combined shear and tensile failure) and the number of failures noted at the unit-mortar interfaces. In *Figure 7*b, the damage computed at the bricks and bonds is represented via points with different colours (*i.e.*, blue: brick failure, black: bond failure) at the locations where the failure occurred. The term "*failure*" is used to describe capacity loss at the point contact, which can no longer transfer action/reaction forces in tension and shear. Hence, we address a local failure at the contact planes. As seen in *Figure 7*b, the number of brick failures is almost double for a high vertical pre-compression pressure ($\sigma_v = 1.21$ MPa) and more

spread to the head joints. Conversely, a distinct localized diagonal tension crack is obtained for a low-pressure ($\sigma_v = 0.30$ MPa), shown in *Figure 7*b.

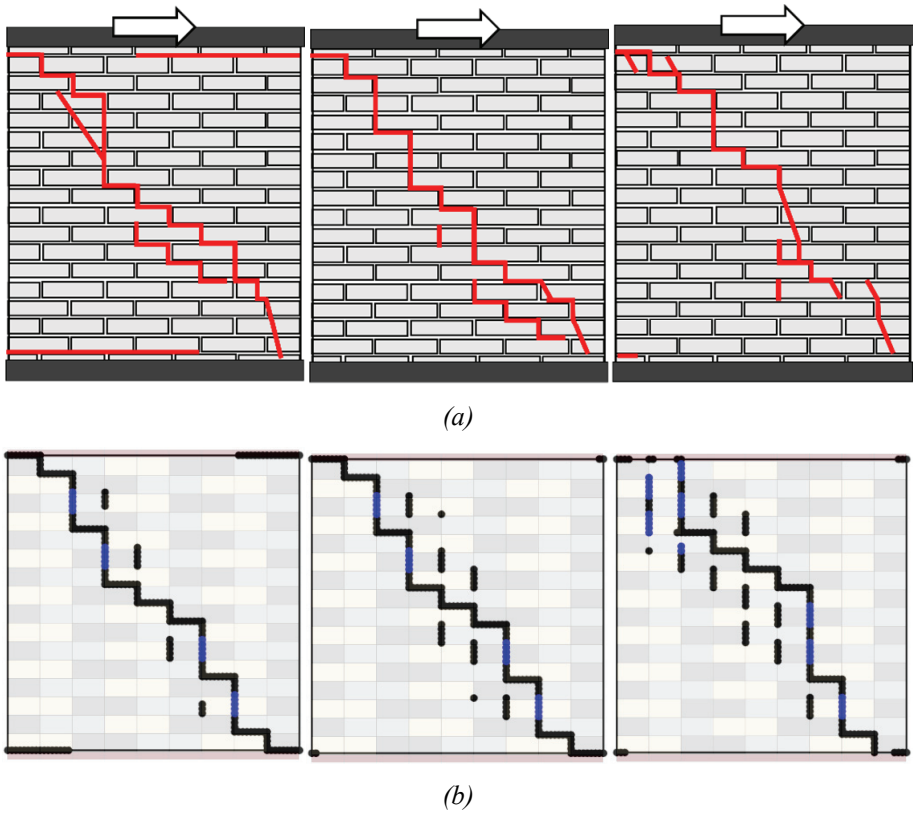

(a)

(b)

Figure 7 - Failure mechanisms obtained from numerical models and experiments (from left to right, $\sigma_v = 0.3, 1.21$ and 2.12 MPa): (a) representation of the crack pattern (test observations), (b) crack pattern obtained from DEM (blue dots indicate cracks in bricks, black dots denote bond failure).

The second benchmark study is a large-scale test and has a different configuration, including masonry wall flanges at both ends. The experimental setup is explicitly represented via the adopted three-dimensional computational model considering the same loading condition and protocol. The results of the proposed discontinuum-based models are compared against the experimental findings, as shown in *Figure 8*a, where low and high pre-compression conditions are denoted as W1 and W2, respectively. A very good match is obtained for W1 with almost no difference in ultimate lateral load, whereas a higher capacity is noted for W2 (approximately 15%) with similar force-displacement behaviour. The predicted crack pattern and the associated failure mechanisms are also given in *Figure 8*b-c, corresponding to the ultimate lateral displacement of 14 mm and 8 mm for W1 and W2, respectively. Almost no brick failure is noticed when the pre-compression pressure is low (W1, $\sigma_v = 0.61$ MPa) as

opposed to W2 that can be seen in *Figure 8*b. In both case studies, diagonal tensile failure is obtained at the final stage of the analyses. Moreover, a moderate crushing failure is also noticed at the bottom right toe in each simulation, as depicted in *Figure 8*.

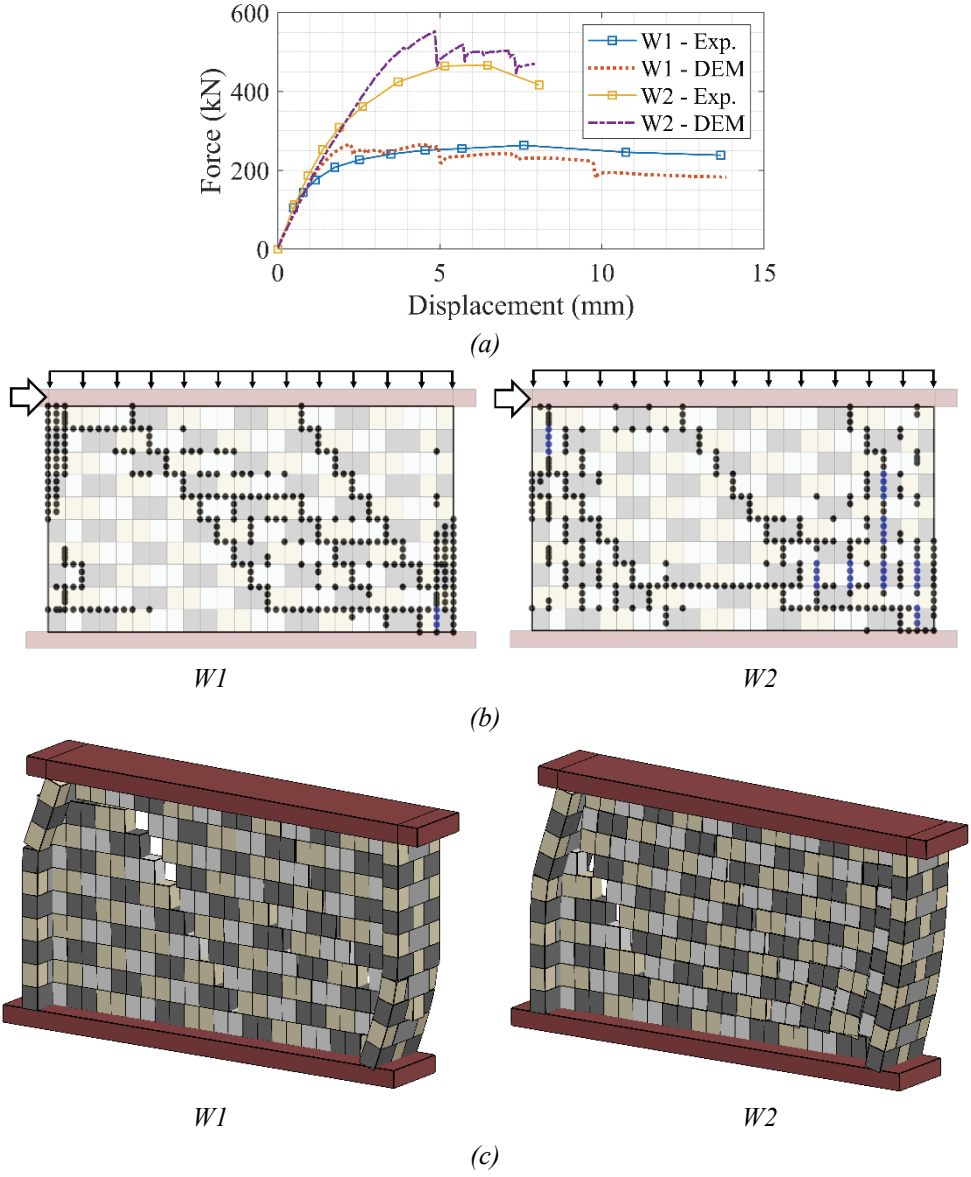

Figure 8 - Comparison of DEM results against the benchmark study #2: (a) Force-displacement curves, (b) crack pattern obtained from DEM (blue dots indicate cracks in bricks, black dots denote bond failure), and (c) predicted failure mechanisms from DEM.

4. DAMAGE PROGRESSION AND SENSITIVITY ANALYSIS

This section aims to provide a deeper understanding of the damage progression in the analyzed URM walls, referred to as benchmark #1 and #2. During the numerical analyses, the state of point contacts is recorded at every 0.2 mm displacement increment to keep track of the damage progression together with the base-shear force and maximum lateral displacement at the top corner. In *Figure 9*, the predicted point contact failures, separately denoted for units and unit-mortar interfaces, are presented for low, medium and high pre-compression pressures for benchmark study #1. The given snapshots are determined based on the observed significant events, such as changes in the crack pattern and the associated failure mechanisms. For instance, in the case of low-pressure ($\sigma_v = 0.3$ MPa), the initial significant phenomenon is noted (around $d = 0.6$ mm) at the bottom left and top right corners of the solid masonry panel, where the point contact failure is noticed for the first time due to flexural tensile stresses between the loading beam and URM wall. Then, after 1.0 mm, additional failures at the contact points corresponding to the head joints are obtained. Finally, a diagonal crack is developed, approximately at 3.0 mm, including cracks at the bricks together with the additional head and bed joints (see *Figure 9*a). Note that once the joint failures start to occur at $d = 1.6$ mm, damage at the unit-mortar interfaces accelerate and rapidly yields a diagonal tension crack, and the fully developed kinematic mechanism does not change until the end of the analysis ($d = 4.0$ mm). Different from the first case, medium pre-compression pressure ($\sigma_v = 1.21$ MPa) leads to different crack evolution, where flexural openings (or cracks) at the top right and bottom left corners are considerably less than the previous one, which is initially noticed at $d = 1.4$ mm simultaneously with several head joint openings, shown in *Figure 9*b. Next, the contact failures are spread at the head joints ($d = 1.6$ mm), and a clear diagonal tension crack is obtained when $d = 2.6$ mm. Similarly, at the initial stage of the lateral displacement, high pre-compression pressure ($\sigma_v = 2.12$ MPa) yields almost no flexural openings between the wall and the loading beam, and the cracks are initially developed at the head joints around the mid-height of the wall, displayed in *Figure 9*c. The final damage state is obtained less than a 1 mm lateral displacement after the head joint cracks are noticed. Furthermore, the results show more brick failures associated with the high vertical pre-compression load compared to the other two pre-compression loads. The given set of solutions underlines the importance of vertical pressure on the observed crack pattern, which also has a favourable influence on the lateral resistance of the URM wall. It needs to be stressed that the analyzed URM walls do not suffer from poor compressive strength, and no fully crushed contact point, meaning no force-transfer capacity in the compression, is computed in all simulations. However, this phenomenon will be an important factor for masonry walls with low compressive strength material characteristics and is out of the scope of the present research.

To quantitatively investigate the relationship between force-displacement behaviour and the associated damage evolution in the bricks and unit-mortar interfaces, they are given in the same plot for all three vertical pre-compression loads, as shown in Figure 10. As mentioned earlier, the two-way coupling mechanism is considered for tension and shear at the contact points using a single damage parameter (denoted as d^{ts}). During analysis, the stress state at the contact points is monitored, and damage at the bricks (d_B^{ts}) and bonds (d_J^{ts}) are recorded

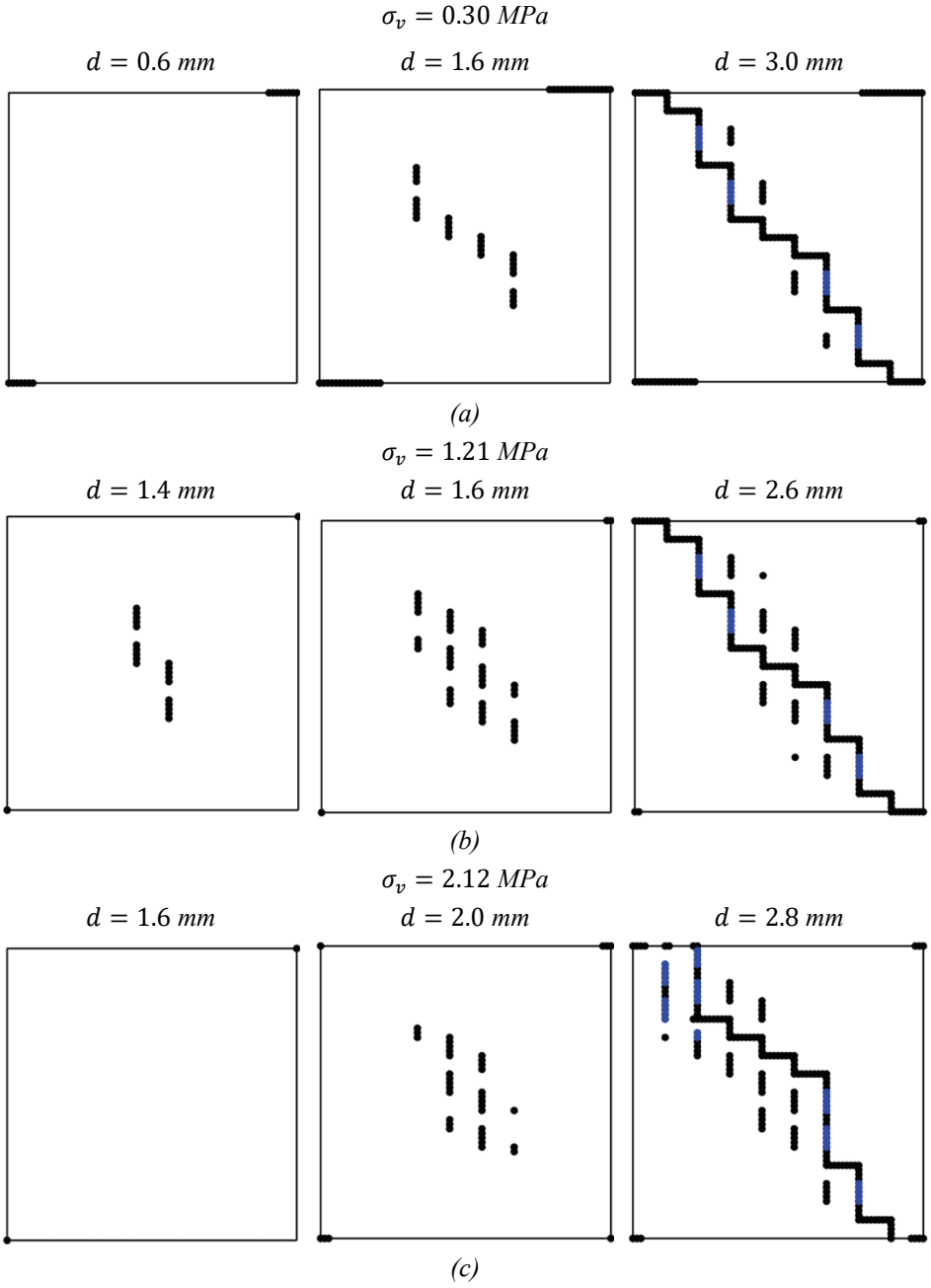

Figure 9 - Results of discontinuum analysis of URM walls (Benchmark #1) for different lateral displacements.

separately. At the end of the analysis, the total number of broken contact points (meaning that d_B^{ts} or d_J^{ts} equal to 1) is calculated, and it is used to present accumulated damage. In *Figure 10*, cumulative damage predicted at the brick and bond contact points is presented together with the force-displacement response of the URM wall. According to the results of the analyses, it is evident that the bond failures (*e.g.*, opening, sliding) start prior to the cracking of bricks, which essentially governs the force drop, hence the lateral load resistance of the URM wall. This conclusion is valid for all pre-compression loads, where the significant capacity loss coincides with the considerable extent of failure in the bricks developing rapidly upon passing the certain displacement threshold. Furthermore, it is interesting to observe that the degradation in the initial stiffness starts with the bond failure at the early stages of the lateral displacement that can be clearly noted for low pre-compression loads and relatively later stages of lateral displacement for high pre-compression loads (see *Figure 10*).

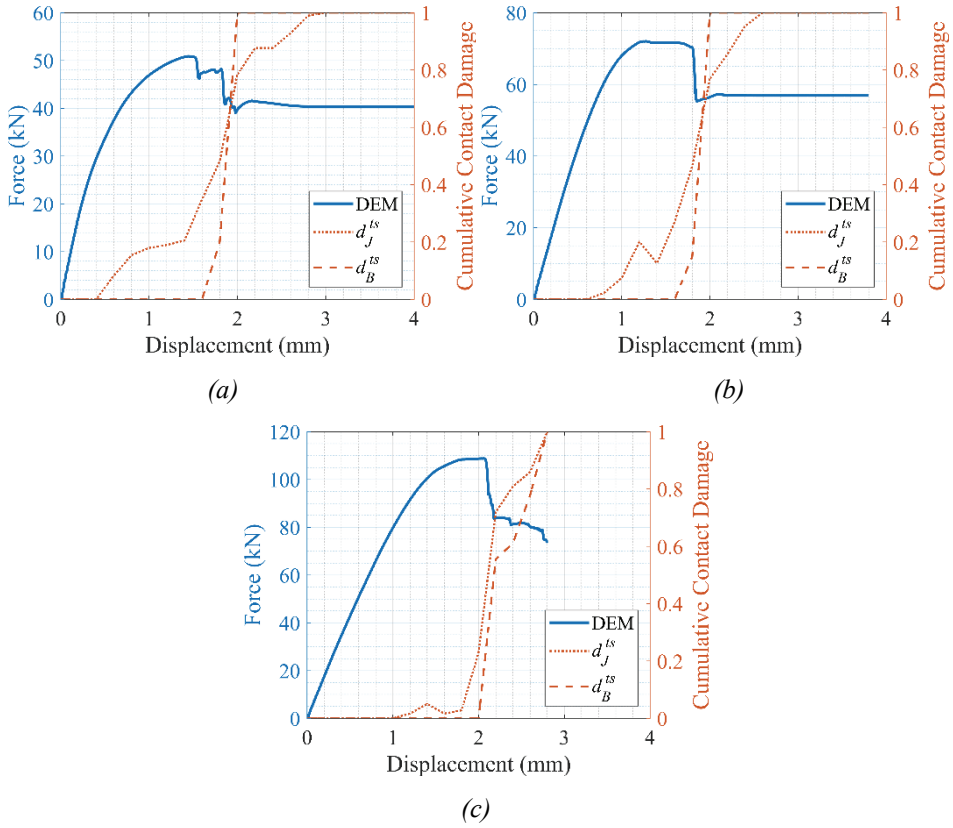

Figure 10 - Combined representation of the cumulative damage at the bricks and joints with the force-displacement behaviour of the URM walls under different vertical pressures (benchmark #1): (a) $\sigma_v = 0.30$ MPa, (b) $\sigma_v = 1.21$ MPa and (c) $\sigma_v = 2.12$ MPa.

The same methodology is applied to the second benchmark study to visualize the cumulative brick and bond damage for W1 and W2, as shown in *Figure 11*. As mentioned previously, very limited tensile cracks are observed in bricks in W1; hence, only the bond failures are displayed in *Figure 11*a. The overall ductile response of W1 and its steady strength reduction upon reaching the maximum load can be attributed to the gradual increase in the joint sliding and openings at the unit-mortar interfaces where each force drop nearly overlaps with the jump in the "*cumulative contact damage*" curve (*Figure 11*a). Similarly, the cumulative brick and bond failures are given in the same graph with the force-displacement response of W2 in *Figure 11*b. The stiffness degradation is initiated by the bond failures, and the lateral load carrying capacity is significantly affected by the brick failure, which is in line with the discussion presented earlier.

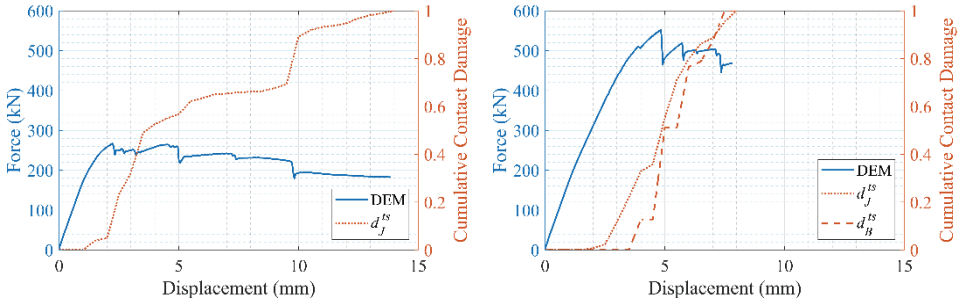

Figure 11 - Combined representation of the cumulative damage at the bricks and joints with the force-displacement behaviour of the URM walls under different vertical pressures (benchmark #2): (a) $\sigma_v = 0.61$ MPa and (b) $\sigma_v = 1.91$ MPa

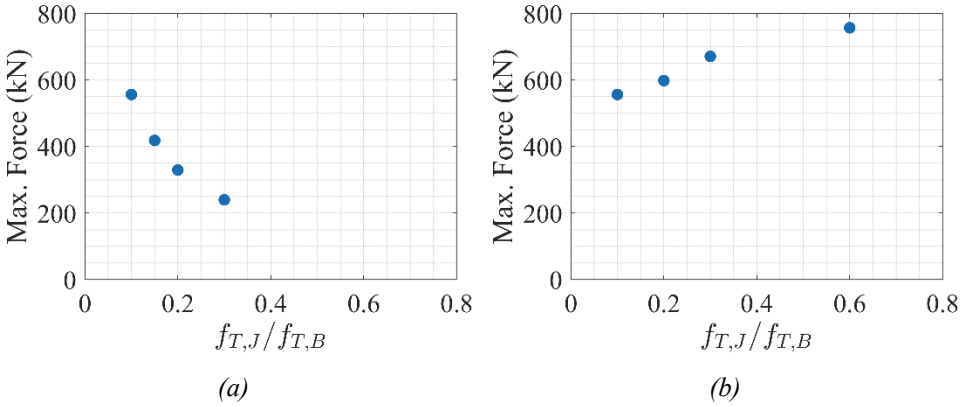

Figure 12 - Influence of the brick and mortar tensile strength on the lateral load carrying capacity of URM wall (benchmark #2): (a) Bond tensile strength ($f_{T,J}$) constant (0.15 MPa) - brick tensile strength ($f_{T,B}$) decreased ↓; (b) $f_{T,B}$ constant (1.5 MPa) - $f_{T,J}$ increased ↑

A further investigation is done using the benchmark study W2 by performing a sensitivity analysis on the brick ($f_{T,B}$) and bond ($f_{T,J}$) tensile strength to predict their effect on the overall lateral resistance of the analyzed URM wall. Two strength combination is considered. First, the brick tensile strength is reduced consistently by keeping the bond strength constant, and then brick tensile strength is kept constant, and bond strength is increased systematically. In *Figure 12*a, the detrimental effect of weak bricks is presented, where an exponential decay can be observed when the brick tensile strength gets lower. Additionally, the positive influence of a strong bond attributed to the higher bond tensile strength can be seen in *Figure 12*b. It is important to recall that no severe crushing failure is computed in the analyzed URM walls. Therefore, the main focus is given to the brick and bond failures that are predominantly related to the tension and shear fracture mechanisms.

5. APPLICATION OF THE PROPOSED STRUCTURAL ANALYSIS FRAMEWORK: URM WALL PANEL WITH AN OPENING

To further validate the implemented modelling approach and demonstrate its applicability on different URM wall sections, the proposed structural analysis framework is also applied to the URM wall panel with an opening subjected to in-plane vertical point load. The analyzed URM panel, tested by Sarhosis et al. [37] to explore the pre- and post-peak behaviour of low bond strength brickwork URM panels with an opening, is illustrated in *Figure 13*. The physical model represents a typical unreinforced brickwork panel above windows and doors in a masonry building. In the reference study, the same experimental configuration was used to perform destructive testing on four URM panels (denoted as S1, S2, S3 and S4), where the vertical loads were imposed at the mid-length of the clear span (l), as shown in *Figure 13*.

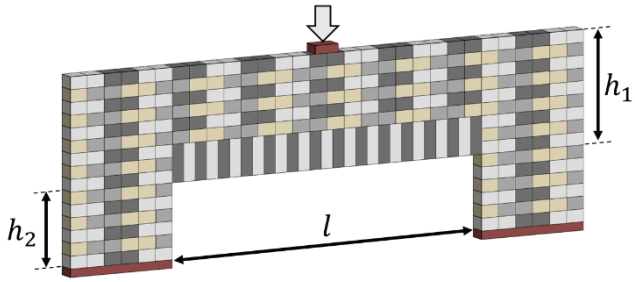

Figure 13 - Analyzed URM wall panel with an opening, where $l = 2.025$ m, $h_1 = 0.675$ m and $h_2 = 0.45$ m.

According to the experimental findings, a similar ultimate load was noted, ranging from 4.6 to 5.6 kN, except for sample S1, which failed earlier than others; hence, it is not considered here when comparing the numerical predictions against the test results. Moreover, experimental observations revealed that failures only occurred along the unit-mortar interfaces, which can be related to the lack of confinement on URM piers and low bond strength. Therefore, no potential crack plane within the masonry units is defined during the discontinuum analysis, which simplifies the computational model and reduces the number of input parameters. The adopted material and contact properties, given in Table 2, are obtained

from the provided experimental results in the reference studies and recommended values in the literature [37–39]. Elastic modulus and Poisson's ratio of the masonry units are taken as 6 GPa and 0.14, respectively. In line with previous validation studies, we utilized the coupled elasto-softening contact constitutive laws, including the mode-I and mode-II fracture energies in tension and shear regimes, respectively.

Table 2 - Material and contact properties used in a masonry panel with an opening.

Masonry Panel with an Opening					
Unit-Mortar Interface Properties (Bond)					
k_n, k_s (GPa/m)	f_T (MPa)	c_0, c_{res} (MPa)	θ_0, θ_{res} (°)	G_f^I, G_f^{II} (N/m)	C_s (-)
13.50, 5.87	0.05	f_T, 0.0	30, 30	0.75, 7.5	9

Figure 14 presents the predicted crack pattern under different load levels, corresponding to noticeable changes in the damage condition. The first crack is captured at the mid-span (above the opening), caused by the flexural tensile stresses due to the effect of vertical point load (1.6 kN), shown in Figure 14a. Upon further increase in vertical load, horizontal cracks develop along the bed joints on both sides of the URM panel (Figure 14b). Ultimately, a diagonal stair-step crack is obtained at the near collapse state of the panel, which initiates along the bed joints and progresses towards the vertical load and the flat-arch skewback, indicated in Figure 14c. The predicted mechanical behaviour of the analyzed URM wall panel with an opening aligns well with the experimental outcomes presented in Figure 14d and Figure 14e.

In addition to the qualitative assessment of the predicted crack pattern, a quantitative comparison of the computational model against the experimental results is provided in *Figure 15*. The force-displacement response obtained from DEM demonstrates a good agreement compared to the experiments, where the specific damage conditions are noted as a, b, and c associated with *Figure 14*a-c. The predicted near-collapse state of the URM panel (see *Figure 15*b) represents the similar failure mechanisms noticed during the experimental campaign.

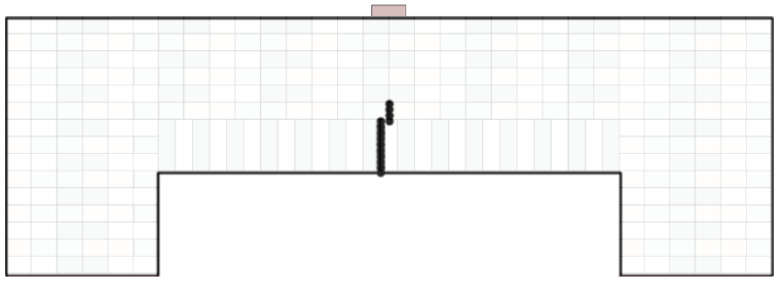

(a)

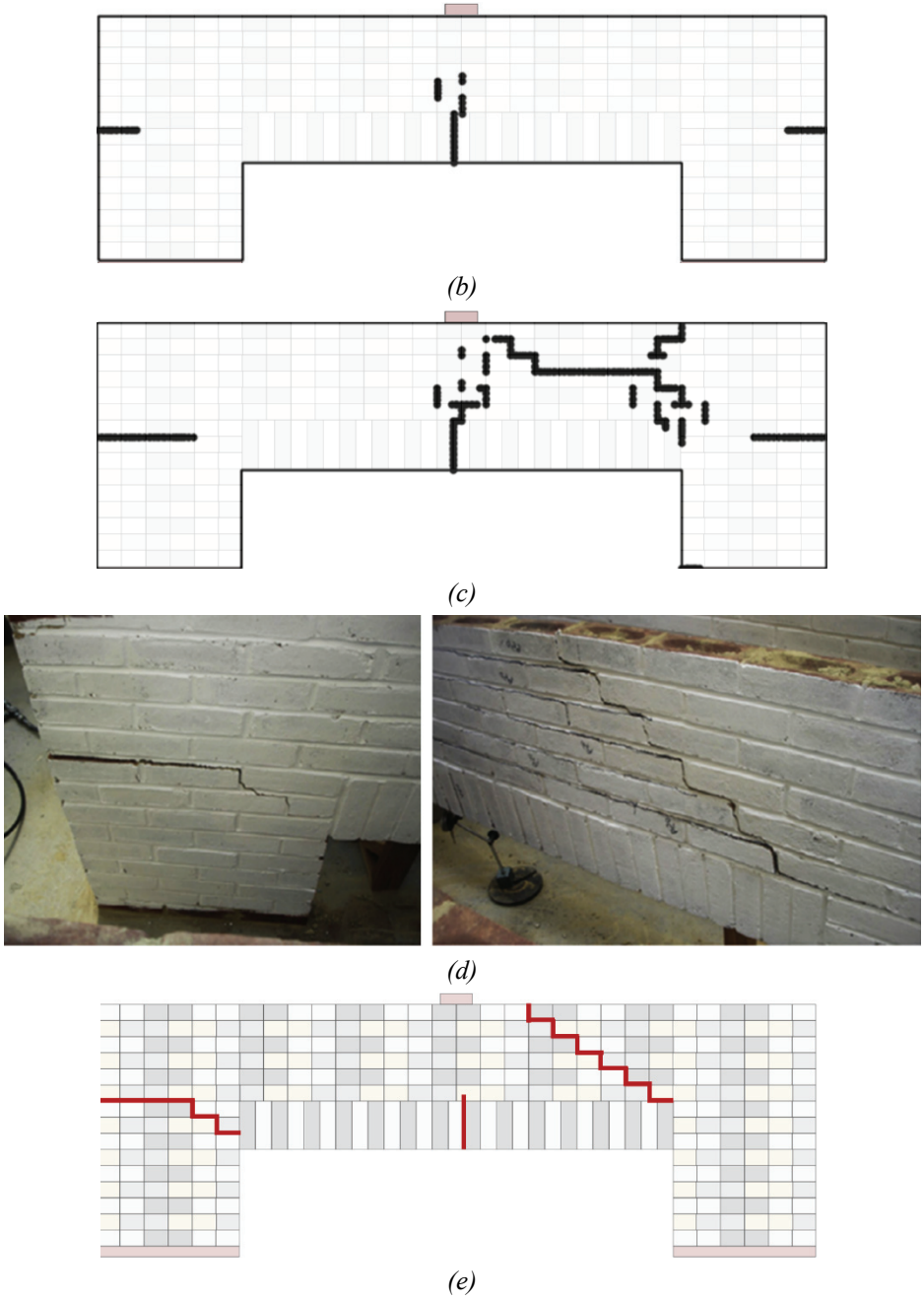

Figure 14 - Predicted damage progression using the proposed DEM-based modelling strategy under different vertical load levels: (a) 1.6 kN, (b) 3.1 kN and (c) 3.44 kN (after peak load) - (d) cracks noted during the experiments [39], (e) representation of the major cracks depicted from reference study.

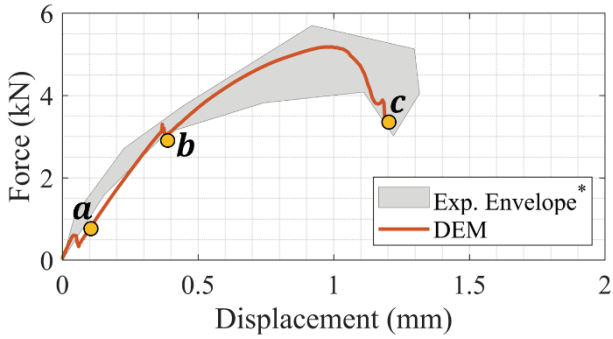

(a)

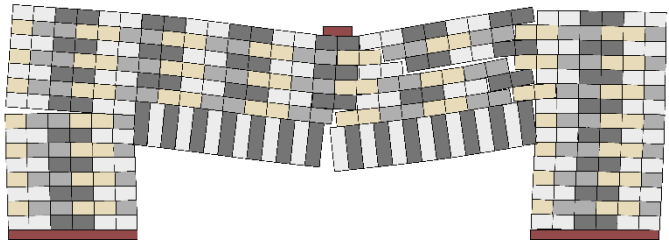

(b)

Figure 15 - (a) Comparison between experimental results denoted as envelope covering three tests (S2, S3 and S4); (b) Predicted near collapse state of the URM panel corresponding to point c in the force-displacement curve.

6. CONCLUSIONS

The present study explores the in-plane behaviour of unreinforced masonry walls via a discontinuum-based modelling strategy based on the discrete element method. The proposed approach captures all essential local failure mechanisms at the bricks and unit-mortar interfaces in tension, compression and shear regimes. The validated computational models are further used to monitor crack propagation and the associated strength reduction in the analyzed benchmark studies. The following conclusions are derived according to the results of the numerical investigations:

- The adopted discontinuum analysis framework provides reasonably accurate predictions regarding the lateral load-carrying capacity of URM walls and the corresponding collapse mechanisms by offering an explicit representation of brick and bond failures.
- The proposed post-processing approach, based on the stress state (or condition) of the contact point in DEM, suggests extracting the fully damaged contact points in tension and/or shear to be utilized in damage progression analysis. The given damage monitoring technique can visualize partially or fully developed kinematic

mechanisms and offers a better understanding of the dominant factors in strength reduction in URM walls, as illustrated in the article.

- The proposed post-processing approach utilizing the output of the adopted discontinuum-based analysis enhances the applicability of discrete element models in the structural assessment of URM walls and buildings, providing necessary information regarding the damage propagation and likely crack pattern.
- The computational investigations indicate a strong relationship between lateral load-bearing capacity and cracking of masonry units (or bricks) in URM walls, especially for medium and high pre-compression loads (*e.g.*, $\sigma_v > 1$ MPa). This phenomenon brings up the importance of brick quality and its influence on the lateral load-carrying capacity of URM walls.
- Finally, the detrimental influence of the weak bricks and the favourable effect of stronger bonds on the in-plane load-carrying capacity of URM walls is presented by performing sensitivity analyses on the brick and bond tensile strength.

As a follow-up study, the proposed DEM-based framework will be applied to more complex unreinforced masonry wall systems (*e.g.*, pier-spandrel), and the adopted post-processing approach will be utilized to assess the seismic capacity of the damaged (or *as-is*) condition of masonry walls and buildings.

References

[1] Tomaževič M. Shear resistance of masonry walls and Eurocode 6: Shear versus tensile strength of masonry. Mater Struct Constr 2009;42:889–907. https://doi.org/10.1617/s11527-008-9430-6.

[2] Betti M, Galano L, Petracchi M, Vignoli A. Diagonal cracking shear strength of unreinforced masonry panels: a correction proposal of the b shape factor. Bull Earthq Eng 2015;13:3151–86. https://doi.org/10.1007/s10518-015-9756-8.

[3] Roca P, Cervera M, Gariup G, Pela' L. Structural analysis of masonry historical constructions. Classical and advanced approaches. Arch Comput Methods Eng 2010;17:299–325. https://doi.org/10.1007/s11831-010-9046-1.

[4] Aldemir A, Erberik MA, Demirel IO, Sucuoğlu H. Seismic performance assessment of unreinforced masonry buildings with a hybrid modeling approach. Earthq Spectra 2013;29:33–57. https://doi.org/10.1193/1.4000102.

[5] Lourenço PB, Rots JG, Blaauwendraad J. Continuum model for masonry: Parameter estimation and validation. J Struct Eng 1998;124:642–52. https://doi.org/10.1061/(ASCE)0733-9445(1998)124:6(642).

[6] Gonen S, Soyoz S. Investigations on the elasticity modulus of stone masonry. Structures 2021;30:378–89. https://doi.org/10.1016/j.istruc.2021.01.035.

[7] Lourenço PB. Anisotropic softening model for masonry plates and shells. J Struct Eng 2000;126:1008–16.

[8] Foti F, Vacca V, Facchini I. DEM modeling and experimental analysis of the static behavior of a dry-joints masonry cross vaults. Constr Build Mater 2018;170:111–20. https://doi.org/10.1016/j.conbuildmat.2018.02.202.

[9] Mendes N, Zanotti S, Lemos J V. Seismic Performance of Historical Buildings Based on Discrete Element Method: An Adobe Church. J Earthq Eng 2020;24:1270–89. https://doi.org/10.1080/13632469.2018.1463879.

[10] Lemos J V. Discrete element modeling of the seismic behavior of masonry construction. Buildings 2019;9. https://doi.org/10.3390/buildings9020043.

[11] Malomo D, DeJong MJ, Penna A. Influence of Bond Pattern on the in-plane Behavior of URM Piers. Int J Archit Herit 2019;00:1–20. https://doi.org/10.1080/15583058.2019.1702738.

[12] Pulatsu B, Erdogmus E, Lourenço PB, Lemos J V., Tuncay K. Simulation of the in-plane structural behavior of unreinforced masonry walls and buildings using DEM. Structures 2020;27:2274–87. https://doi.org/10.1016/j.istruc.2020.08.026.

[13] Murano A, Mehrotra A, Ortega J, Rodrigues H, Vasconcelos G. Comparison of different numerical modelling approaches for the assessment of the out-of-plane behaviour of two-leaf stone masonry walls. Eng Struct 2023;291:116466. https://doi.org/10.1016/j.engstruct.2023.116466.

[14] Gonen S, Pulatsu B, Erdogmus E, Karaesmen E, Karaesmen E. Quasi-static nonlinear seismic assessment of a fourth century A.D. Roman Aqueduct in Istanbul, Turkey. Heritage 2021;4:401–21. https://doi.org/10.3390/heritage4010025.

[15] Mordanova A, de Felice G. Seismic Assessment of Archaeological Heritage Using Discrete Element Method. Int J Archit Herit 2020;14:345–57. https://doi.org/10.1080/15583058.2018.1543482.

[16] Lourenço PB. Computations on historic masonry structures. Prog Struct Eng Mater 2002;4:301–19. https://doi.org/10.1002/pse.120.

[17] Damiani N, DeJong MJ, Albanesi L, Penna A, Morandi P. Distinct element modeling of the in-plane response of a steel-framed retrofit solution for URM structures. Earthq Eng Struct Dyn 2023;52:3030–52. https://doi.org/10.1002/eqe.3910.

[18] Szakály F, Hortobágyi Z, Bagi K. Discrete Element Analysis of the Shear Resistance of Planar Walls with Different Bond Patterns. Open Constr Build Technol J 2016;10:220–32. https://doi.org/10.2174/1874836801610010220.

[19] de Felice G. Out-of-plane seismic capacity of masonry depending on wall section morphology. Int J Archit Herit 2011;5:466–82. https://doi.org/10.1080/15583058.2010.530339.

[20] Wilson R, Szabó S, Funari MF, Pulatsu B, Lourenço PB. A Comparative Computational Investigation on the In-Plane Behavior and Capacity of Dry-Joint URM Walls. Int J Archit Herit 2023. https://doi.org/10.1080/15583058.2023.2209776.

[21] Lemos J V. Discrete element modeling of masonry structures. Int J Archit Herit 2007;1:190–213. https://doi.org/10.1080/15583050601176868.

[22] Cundall PA. A computer model for simulating progressive, large-scale movements in blocky rock systems. Int. Symp. Rock Mech., vol. 2, Nancy: 1971, p. 47–65.

[23] Itasca Consulting Group Inc. 3DEC Three Dimensional Distinct Element Code 2013.

[24] Cundall PA, Detournay C. Dynamic relaxation applied to continuum and discontinuum numerical models in geomechanics. Rock Mech. Eng. Vol. 3 Anal. Model. Des., 2017, p. 45–90. https://doi.org/10.1201/b20402.

[25] Pulatsu B. Coupled elasto-softening contact models in DEM to predict the in-plane response of masonry walls. Comput Part Mech 2023. https://doi.org/10.1007/s40571-023-00586-x.

[26] Sarhosis V, Dais D, Smyrou E, Bal İE, Drougkas A. Quantification of damage evolution in masonry walls subjected to induced seismicity. Eng Struct 2021;243. https://doi.org/10.1016/j.engstruct.2021.112529.

[27] Saygılı Ö, Lemos J V. Investigation of the Structural Dynamic Behavior of the Frontinus Gate. Appl Sci 2020;10:5821. https://doi.org/10.3390/app10175821.

[28] Çaktı E, Saygılı Ö, Lemos J V., Oliveira CS. Discrete element modeling of a scaled masonry structure and its validation. Eng Struct 2016;126:224–36. https://doi.org/10.1016/j.engstruct.2016.07.044.

[29] Casapulla C, Mousavian E, Argiento L, Ceraldi C, Bagi K. Torsion-shear behaviour at the interfaces of rigid interlocking blocks in masonry assemblages: experimental investigation and analytical approaches. Mater Struct Constr 2021;54. https://doi.org/10.1617/s11527-021-01721-x.

[30] Pulatsu B, Gonen S, Lourenço PB, Lemos J V., Hazzard J. Computational investigations on the combined shear–torsion–bending behavior of dry-joint masonry using DEM. Comput Part Mech 2022. https://doi.org/10.1007/s40571-022-00493-7.

[31] Lourenço PB, Rots JG. Multisurface interface model for analysis of masonry structures. J Eng Mech 1997;123:660–8.

[32] Lemos J V. Block modelling of rock masses. Concepts and application to dam foundations. Rev Eur Génie Civ 2008;12:915–49. https://doi.org/10.3166/ejece.12.915-949.

[33] Vermeltfoort AT, Raijmakers T, Janssen HJM. Shear tests on masonry walls. In: Hamid AA, Harris HG, editors. 6th North Am. Mason. Conf., Philadelphia: The Masonry Society; 1993, p. 1183–93.

[34] Ganz HR, Thürlimann B. Tests on masonry walls under normal and shear loading. Zurich, Switzerland: 1984.

[35] Lourenço PB, Gaetani A. Recommended properties for advanced numerical analysis. Finite Elem. Anal. Build. Assess., New York: Routledge; 2022, p. 209–320. https://doi.org/10.1201/9780429341564-4.

[36] Wilding BV, Dolatshahi KM, Beyer K. Shear-compression tests of URM walls: Various setups and their influence on experimental results. Eng Struct 2018;156:472–9. https://doi.org/10.1016/j.engstruct.2017.11.057.

[37] Sarhosis V, Sheng Y, Garrity SW. Computational modelling of clay brickwork walls containing openings. Int Mason Soc 2010;11:1743–52.

[38] Giamundo V, Sarhosis V, Lignola GP, Sheng Y, Manfredi G. Evaluation of different computational modelling strategies for the analysis of low strength masonry structures. Eng Struct 2014;73:160–9. https://doi.org/10.1016/j.engstruct.2014.05.007.

[39] Sarhosis V, Garrity SW, Sheng Y. Influence of brick-mortar interface on the mechanical behaviour of low bond strength masonry brickwork lintels. Eng Struct 2015;88:1–11. https://doi.org/10.1016/j.engstruct.2014.12.014.

Turkish Journal of Civil Engineering (formerly Teknik Dergi)
Manuscript Drafting Rules

1. The whole manuscript (text, charts, equations, drawings etc.) should be arranged in Word and submitted in ready to print format. The article should be typed on A4 (210 x 297 mm) size paper using 10 pt (main title 15 pt) Times New Roman font, single spacing. Margins should be 40 mm on the left and right sides and 52.5 mm at the top and bottom of the page.
2. Including drawings and tables, articles should not exceed 25 pages, technical notes 10 pages.
3. Your contributed manuscript must be sent over the DergiPark system. (http://dergipark.gov.tr/tekderg)
4. The text must be written in a clear and understandable language, conform to the grammar rules. Third singular person and passive tense must be used, and no inverted sentences should be contained.
5. Title must be short (10 words maximum) and clear, and reflect the content of the paper.
6. Sections should be arranged as: (i) abstract and keywords, (ii) title, abstract and keywords in the other language, (iii) main text, (iv) symbols, (v) acknowledgements (if required) and (vi) references.
7. Both abstracts should briefly describe the object, scope, method and conclusions of the work and should not exceed 100 words. If necessary, abstracts may be re-written without consulting the author. At least three keywords must be given. Titles, abstracts and keywords must be fitted in the first page leaving ten line space at the bottom of the first page and the main text must start in the second page.
8. Section and sub-section titles must be numbered complying with the standard TS1212.
9. Symbols must conform to the international rules; each symbol must be defined where it appears first, additionally, a list of symbols must be given in alphabetic order (first Latin, then Greek alphabets) at the end of the text (before References).
10. Equations must be numbered and these numbers must be shown in brackets at the end of the line.
11. Tables, drawings and photographs must be placed inside the text, each one should have a number and title and titles should be written above the tables and below the drawings and photographs.
12. Only SI units must be used in the manuscripts.
13. Quotes must be given in inverted commas and the source must be indicated with a reference number.
14. Acknowledgement must be short and mention the people/ institutions contributed or assisted the study.
15. References must be numbered (in brackets) in the text referring to the reference list arranged in the order of appearance in the text. References must include the following information:

    If the reference is an article: Author's surname, his/her initials, other authors, full title of the article, name of the journal, volume, issue, starting and ending pages, year of publication.

    Example : Naghdi, P. M., Kalnins, A., On Vibrations of Elastic Spherical Shells. J. Appl. Mech., 29, 65-72, 1962.

    If the reference is a book: Author's surname, his/her initials, other authors, title of the book, volume number, editor if available, place of publication, year of publication.

    Example : Kraus. H., Thin Elastic Shells, New York. Wiley, 1967.

    If the reference is a conference paper: Author's surname, his/her initials, other authors, title of the paper, title of the conference, location and year.

    If the source is a thesis: Author's surname, his/her initials, thesis title, level, university, year.

    If the source is a report: Author's surname, his/her initials, other authors, title of the report, type, number, institution it is submitted to, publication place, year.
16. Discussions to an article published in Turkish Journal of Civil Engineering (formerly Teknik Dergi) should not exceed two pages, must briefly express the addressed points, must criticize the content, not the author and must be written in a polite language. Authors' closing remarks must also follow the above rules.
17. A separate note should accompany the manuscript. The note should include, (i) authors' names, business and home addresses and phone numbers, (ii) brief resumes of the authors and (iii) a statement "I declare in honesty that this article is the product of a genuinely original study and that a similar version of the article has not been previously published anywhere else" signed by all authors.
18. Copyright has to be transferred to UCTEA Turkish Chamber of Civil Engineers. The standard copyright form signed by the authorised author should therefore be submitted together with the manuscript.

CONTENTS

RESEARCH ARTICLE

UCTEA Turkish Chamber of Civil Engineers
TMMOB İnşaat Mühendisleri Odası
Necatibey St. No: 57, Kızılay, Ankara / Türkiye
Tel: +90.312.294 30 00 - Faks: 294 30 88
www.imo.org.tr